Universität Münster

Theoretische Physik

Precise Theoretical Predictions for the Dark Matter Relic Density and Neutrino Dynamics in the Early Universe

Inaugural-Dissertation
zur Erlangung des Doktorgrades
der Naturwissenschaften im Fachbereich Physik
der Mathematisch-Naturwissenschaftlichen Fakultät
der Universität Münster

vorgelegt von
Luca Paolo Wiggering
aus Ahaus

- 2024 -

Dekan	Prof. Dr. Rudolf Bratschitsch
Erster Gutachter	Prof. Dr. Michael Klasen
Zweiter Gutachter	Junior-Prof. Dr. Kai Schmitz
Tag der mündlichen Prüfung	....
Tag der Promotion	....

Abstract

The calculation of precise predictions from a given theoretical framework is of great importance, for extracting free parameters of a theory from observations as well as for determining the specific limitations of a given theory in describing our Universe. Two crucial observables in modern cosmology are the dark matter (DM) relic density $\Omega_\chi h^2$ and the effective number of relativistic degrees of freedom N_{eff}, both of which are measured within the ΛCDM model through the temperature anisotropies in the Cosmic Microwave Background (CMB) radiation.

Given that today's amount of dark matter is deduced with sub-percent level accuracy, it is one of the most stringent constraints on the valid parameter space of dark matter models. To actually profit from this experimental accuracy, theoretical predictions should be at least equally precise. Due to its predictivity and testability in current and future experiments, one of the currently most favored dark matter theories is that dark matter is made up of a new elementary particle species that has been in thermal equilibrium with the Standard Model (SM) in the early Universe, i.e., a Weakly Interacting Massive Particle (WIMP). In this setting, today's dark matter abundance is then mainly determined through all possible (co)annihilation channels of the dark matter candidate into Standard Model particles. While it is known that loop corrections to the associated annihilation cross sections can shift the predicted relic density beyond the experimental error, such calculations are so far limited in their automation due to challenges in the treatment of infrared divergences. Therefore, the dipole subtraction method designed to cancel infrared divergent pieces between virtual and real corrections while allowing for a numerical integration of the real emission contribution, is generalized in this thesis to massive initial-states. These results then allow to more easily treat dark matter annihilation beyond leading order in non-Abelian theories. To showcase the application of this generalized subtraction procedure and to study further the effect of higher-order corrections on the relic density, the complete next-to-leading order (NLO) corrections in the strong coupling α_s to stop-antistop annihilation into gluons and light quarks in the R-parity conserving Minimal Supersymmetric Standard Model (MSSM) are calculated with the lightest neutralino being the dark matter candidate. The analysis is supplemented by including the non-perturbative Sommerfeld enhancement effect from the exchange of multiple gluons between the incoming stops, finding corrections of order 10 % to the neutralino relic density. These corrections have been implemented in the software package DM@NLO which already provides the $\mathcal{O}(\alpha_s)$ corrections to many (co)annihilation channels in the MSSM besides stop-antistop annihilation. For the public release of the entire code, it has been equipped with a user-friendly interface to allow for a simple usage from within other dark matter software.

Another assumption usually entering the WIMP paradigm is that kinetic equilibrium with the Standard Model is maintained until long after chemical decoupling. However, this approach is known to fail for forbidden dark matter models since only the high momentum tail of the dark matter phase space distribution function contributes significantly to dark matter annihilations. Therefore, in this thesis, the full elastic collision term is included in the momentum-dependent Boltzmann equation as well as in a set of fluid equations that couple the evolution of the number density and dark matter temperature for a simplified model featuring forbidden dark matter annihilations into muon or tau leptons through a scalar mediator. The overall phenomenological outcome is that the updated relic density calculation results in a significant reduction of the experimentally allowed parameter space compared to the traditional approach.

While N_{eff} is also an important probe of Beyond the Standard Model (BSM) physics, its theoretical value in the Standard Model is still under debate. To date, there has been no systematic and complete study of next-to-leading order corrections in the electromagnetic coupling α_{em} to the weak scattering processes determining neutrino decoupling. To capture both vacuum and finite-temperature quantum electrodynamics (QED) corrections, the dominant $\mathcal{O}(\alpha_{\text{em}})$ contribution to the thermal neutrino interaction is computed in the Keldysh-Schwinger formalism of nonequilibrium quantum field theory (QFT). In this context, a basic introduction to (non)equilibrium QFT orientated towards practical calculations is provided for a better understanding. In particular, the Kadanoff-Baym equations and the finite-temperature Feynman rules are derived. Based on entropy conservation arguments and a solution of the Boltzmann equation in the damping approximation coupled to the continuity equation in Friedmann–Lemaître–Robertson–Walker spacetimes, the afore mentioned corrections are found to be within the error margin of the current theory benchmark $N_{\text{eff}}^{\text{SM}} = 3.0440 \pm 0.0002$.

Kurzfassung

Die Berechnung präziser Vorhersagen ist von großer Bedeutung, um zum einen freie Parameter einer Theorie aus Messungen zu extrahieren und zum anderen verlässlich testen zu können, wann eine Theorie bei der Beschreibung unseres Universums versagt. Zwei wichtige Messgrößen in der modernen Kosmologie sind die Reliktdichte der Dunklen Materie $\Omega_\chi h^2$ und die effektive Anzahl der relativistischen Freiheitsgrade N_{eff}. Beide werden im Rahmen des ΛCDM-Modells mittels der Temperaturanisotropien der kosmischen Mikrowellenhintergrundstrahlung bestimmt.

In Anbetracht der Tatsache, dass die Menge der Dunklen Materie heute mit einer Unsicherheit von weniger als einem Prozent bestimmt ist, ist dies eine der strengsten Beschränkungen auf den gültigen Parameterraum von Dunkle Materie Modellen. Um tatsächlich von dieser experimentellen Genauigkeit zu profitieren, sollten die theoretischen Vorhersagen mindestens ebenso präzise sein. Aufgrund ihrer Vorhersagbarkeit und Überprüfbarkeit in aktuellen und zukünftigen Experimenten besteht eine der derzeit beliebtesten Theorien zur Dunklen Materie darin, dass Dunkle Materie aus einer neuen Elementarteilchenspezies besteht, die sich im frühen Universum im thermischen Gleichgewicht mit den Standardmodellteilchen befand und aufgrund ihrer Eigenschaften als „Weakly Interacting Massive Particle“ bezeichnet wird. Unter diesen Bedingungen wird die heutige Reliktdichte Dunkler Materie hauptsächlich durch alle möglichen (Ko)Annihilationskanäle Dunkler Materie in Standardmodellteilchen bestimmt. Es ist zwar bekannt, dass Schleifenkorrekturen zu den zugehörigen Annihilationswirkungsquerschnitten die vorhergesagte Reliktdichte über die experimentelle Unsicherheit hinaus verschieben können, doch sind solche Berechnungen aufgrund von Problemen bei der Behandlung von infraroten Divergenzen in ihrer Automatisierung bisher begrenzt. Daher wird die „dipole subtraction method“, welche entwickelt wurde, um infrarote Divergenzen zwischen virtuellen und reellen Korrekturen zu kompensieren und gleichzeitig eine numerische Integration der reellen Korrekturen zu ermöglichen, in der vorliegenden Dissertation auf massive Anfangszustände verallgemeinert. Diese Ergebnisse ermöglichen dann eine einfachere störungstheoretische Behandlung der Annihilation Dunkler Materie jenseits der führenden Ordnung in nicht-Abelschen Theorien. Um die Anwendung dieses verallgemeinerten Subtraktionsverfahrens zu demonstrieren und die Auswirkungen von Korrekturen höherer Ordnung auf die Reliktdichte weiter zu untersuchen, werden die vollständigen Korrekturen in der starken Kopplung α_s zur Stop-Antistop Annihilation in Gluonen und leichte Quarks im minimalen supersymmetrischen Standardmodell (MSSM) mit erhaltener R-Parität berechnet, wobei das leichteste Neutralino als Kandidat für Dunkle Materie angenommen wird. Die Analyse wird ergänzt durch die Einbeziehung des nicht-perturbativen Sommerfeldeffekts, der sich aus dem Austausch mehrerer Gluonen zwischen den eingehenden skalaren Top Quarks ergibt, wobei Korrekturen in der Größenordnung von 10 % für die Neutralino-Reliktdichte gefunden werden. Diese Korrekturen wurden in das Softwarepaket

DM@NLO implementiert, das bereits $\mathcal{O}(\alpha_s)$ Korrekturen für viele (Ko)Annihilationskanäle im MSSM neben der Stop-Antistop-Annihilation bereitstellt. Für die öffentliche Freigabe des gesamten Codes wurde dieser mit einer benutzerfreundlichen Schnittstelle ausgestattet, um eine einfache Nutzung von anderen Dunkle Materie Programmen aus zu ermöglichen.

Eine weitere Annahme, die üblicherweise in die Berechnung der thermalen Reliktdichte einfließt, ist, dass das kinetische Gleichgewicht zwischen Dunkler Materie und dem Standardmodell bis lange nach der chemischen Entkopplung aufrechterhalten wird. Es ist jedoch bekannt, dass dieser Ansatz bei „forbidden dark matter“ Modellen versagt, da nur der Bereich der Phasenraumverteilungsfunktion mit hohem Impuls signifikant zur Dunkle Materie Annihilation beiträgt. Daher wird in dieser Dissertation der vollständige elastische Kollisionsterm in die impulsabhängige Boltzmann-Gleichung sowie in eine Reihe von hydrodynamischen Gleichungen aufgenommen, die gleichzeitig die Entwicklung der Teilchenzahlendichte und der Temperatur der Dunklen Materie beschreiben. Damit wird dann ein vereinfachtes Modell mit „verbotenen“ Annihilationen in Myonen oder Tau-Leptonen untersucht, welche durch ein weiteres skalares Teilchen vermittelt werden. Das phänomenologische Gesamtergebnis ist, dass die aktualisierte Berechnung der Reliktdichte zu einer signifikanten Verringerung des experimentell zulässigen Parameterraums im Vergleich zum traditionellen Ansatz führt.

Während N_{eff} auch eine wichtige Größe für Physik jenseits des Standardmodells ist, wird der zugehörige theoretische Wert im Standardmodell immer noch diskutiert, denn bisher gab es keine systematische und vollständige Untersuchung der Korrekturen in der elektromagnetischen Kopplung α_{em} zu den schwachen Streuprozessen, die für den Neutrinoentkopplungsprozess ausschlaggebend sind. Um sowohl die Vakuumkorrekturen als auch die thermalen Korrekturen der Quantenelektrodynamik zu berücksichtigen, wird der dominante $\mathcal{O}(\alpha_{\text{em}})$ Beitrag zur thermischen Neutrino-Wechselwirkungsrate im Keldysh-Schwinger Formalismus der Nichtgleichgewichts-Quantenfeldtheorie (QFT) berechnet. Zum besseren Verständis wird in diesem Kontext eine grundlegende und an praktischen Rechnungen orientierte Einführung in (Nicht)Gleichgewichts-QFT bereitgestellt. Insbesondere werden die Kadanoff-Baym Gleichungen und die Feynman-Regeln bei endlichen Temperaturen hergleitet. Auf der Grundlage von Entropieerhaltungsargumenten und einer Lösung der Boltzmann-Gleichung in der Dämpfungsannäherung mitsamt der Kontinuitätsgleichung in Friedmann-Lemaître-Robertson-Walker-Raumzeiten wird festgestellt, dass die zuvor genannten Korrekturen innerhalb der Fehlerspanne des aktuellen Theoriewerts $N_{\text{eff}}^{\text{SM}} = 3{,}0440 \pm 0{,}0002$ liegen.

Acknowledgments

I would like to thank the people who supported me during my work on this thesis. First of all, many thanks go to my supervisor Michael Klasen for offering me the possibility to obtain a PhD in his research group and to work on such a diverse number of topics as well as Alexander Kappes for being my second supervisor and for agreeing to be part of my defense committee as the third examiner. Next I would like to thank Kai Schmitz for allowing me to join the weekly particle cosmology journal club and for accepting the role as my second reviewer.

My gratitude also goes to Yvonne Wong for the hospitality at the UNSW Sydney, where I had a great time during my research stay, also thanks to the warm welcome of the local PhD students: Tobias Felkl, Adam Lackner, Giovanni Pierobon, Ameek Malhotra and Julius Wons.

Furthermore, I want to thank my collaborators over the years: Amin Aboubrahim, Marco Drewes, Yannis Georis, Björn Herrmann, Julia Harz, Sudip Jana, Karol Kovařík, Vishnu Padmanabhan Kovilakam, Mohamed Younes Sassi and Yvonne Wong.

Also I would like to thank Dominik Stöckinger for correspondence on the regularization of supersymmetric theories and Alexander Pukhov for the big help in the context of micrOMEGAs. In this context, I should also mention that all figures and Feynman diagrams have been generated using MatPlotLib [1], TikZ-Feynman [2], Numpy [3] and Scipy [4].

My thanks also go to the other students at the institute for the great time we had—also outside of the work environment: Alexander Feike, Justus Kuhlmann, Alexander Neuwirth, Pia Petrak, Johannes Pirsch, Peter Risse, Tobias Schröder and Richard von Eckardstein. In particular, I would like to thank my office mates over the years for the nice atmosphere in TP 310: Tim Huesmann, Jan Ravi Bade, Anne Poppe and Adrian Finke.

In particular, I would like to thank Amin Aboubrahim, Jan Ravi Bade, Yannis Georis, David Lübbering, Kathrin Meemken, Alexander Neuwirth and Tobias Schröder for proof reading different parts of this thesis.

I would especially like to thank Kathrin Meemken. Even though you joined my life only in the last third of my PhD journey, I hope that we will continue to experience life together. However, my biggest thanks goes to my parents. Your backing and support were and will always be of the utmost importance to me. Thank you very much for that!

List of publications

The following chronologically ordered papers are included in this thesis. The author's contributions are explained below each publication and the main authors of the papers are underlined.

I J. Harz, M. Klasen, M.Y. Sassi and L.P. Wiggering, *Dipole formalism for massive initial-state particles and its application to dark matter calculations*, *Phys. Rev. D* **107** (2023) 056020 [2210.03409].
This work was initiated within M.Y. Sassi's master's thesis supervised by J. Harz. I rederived all analytical results and extended the calculation to the previously missing cases of a massless final-state emitter and a massless final-state spectator and introduced the regularization scheme dependence. The numerical implementation was completely done by myself along with the creation of all figures and I provided a first version of the draft for this paper before finalizing it together with my co-authors.

II M. Klasen, K. Kovařík and L.P. Wiggering, *Radiative corrections to stop-antistop annihilation into gluons and light quarks*, *Phys. Rev. D* **106** (2022) 115032 [2210.05260].
This project was initiated by M. Klasen. I carried out all the analytical as well as numerical calculations and wrote the first draft of this paper before completing it together with my co-authors.

III A. Aboubrahim, M. Klasen and L.P. Wiggering, *Forbidden dark matter annihilation into leptons with full collision terms*, *JCAP* **08** (2023) 075 [2306.07753].
A. Aboubrahim proposed to consider dark matter models which require the solution of momentum-dependent Boltzmann equations. I constructed the corresponding integro partial-differential equation solver and developed the idea to look at a forbidden dark matter model where it was already known that early kinetic decoupling might be relevant. All the analytical and numerical calculations associated with this paper were then done by myself along with the preparation of a first draft which was finished together with the other co-authors.

IV J. Harz, B. Herrmann, M. Klasen, K. Kovařík and L.P. Wiggering, *Precision predictions for dark matter with DM@NLO in the MSSM*, *Eur. Phys. J. C* **84** (2024) 342 [2312.1720].
All the programming work related to this paper was done by myself. I decoupled DM@NLO from MicrOMEGAs 2.4.1, came up with the new user interface and prepared the first version of the draft. The example supersymmetric scenario was conceived in collaboration with the co-authors which also assisted in refining the available user options as well as finalizing the draft.

V M. Drewes, Y. Georis, M. Klasen, L.P. Wiggering, Y.Y.Y. Wong, *Towards a precision calculation of N_{eff} in the Standard Model III: Improved estimate of NLO contributions to the collision integral*, *JCAP* **06** (2024) 032 [`2402.18481`].

M. Drewes and Y. Wong wanted to investigate the effect of NLO contributions to the thermal neutrino interaction rate within the Keldysh-Schwinger formalism and founded the project. All calculations were performed independently, still in parallel however, by Y. Georis and myself. E.g., Y. Georis and I used different parametrizations of the collision integrals. In particular, I pointed out the divergent t-channel contribution, proposed a resummation procedure to resolve the issue and obtained the first numerically stable integration results. In addition, I created all figures and provided the first version of the draft containing the technical details of the computation. The remaining parts were written by M. Drewes and Y. Wong. The calculation of the change in N_{eff} using the momentum-dependent Boltzmann damping approximation based on Y. Georis and my interaction rates was also done by Y. Wong. All authors discussed the interpretation of the results and contributed to the final version of the manuscript.

Please note that the first two publications [**I**, **II**] are already partially contained in the author's master's thesis *Squark Annihilation Into a Pair of Gluons in the MSSM* but that the associated calculations were only completed and problems fixed during the first phase of the PhD candidacy and that the material is partially reused for completeness in Ch. 4.

The following additional publication was finished while this thesis was being written, but is not discussed in this thesis:

VI S. Jana, M. Klasen, V. P. Kovilakam, and L.P. Wiggering, *Neutrino masses and mixing from milli-charged dark matter* [`2406.18641`].

V. Kovilakam had the idea to avoid the ad-hoc imposition of a discrete $\mathbb{Z}_2$ symmetry in scotogenic models by assigning a small, but non-vanishing electric charge to the beyond the Standard Model particles. The analysis of the low-scale case was performed semi-analytically by V. Kovilakam, whereas I confirmed the results using the toolchain explained in the paper. For the high-scale scenario, we used entirely my toolchain. V. Kovilakam created all plots based on my parameter scans and wrote the first version of the draft. The introduction, however, was written by S. Jana. All authors helped to finalize the draft.

Contents

Chapter 1

Introduction

The Standard Model (SM) of particle physics and Einstein's theory of general relativity combined with standard thermodynamics form the foundation of modern (particle) cosmology. The Standard Model builds upon relativistic Quantum Field Theory (QFT) and is widely consistent with high precision experiments in describing all known elementary particles and their interactions on microscopic scales, whereas general relativity is a theory of gravity that seems to describe nature successfully on cosmological length scales. Interestingly, both theories are based on the principle of symmetry: general relativity is based on general covariance and the Standard Model on a $\mathrm{SU}(3)_c \times \mathrm{SU}(2)_L \times \mathrm{U}(1)_Y$ gauge symmetry. However, to successfully describe Cosmic Microwave Background (CMB) data, a significant amount of non-baryonic dark matter (DM) is required besides dark energy to account for the remaining energy budget. The simplest solution to the dark matter problem is to add a new elementary particle with a mass ranging from a few GeV to several TeV and with couplings to the SM at the order of the weak interaction, i.e., to add a Weakly Interacting Massive Particle (WIMP). Thermal freeze-out from the primordial Standard Model plasma then miraculously predicts the observed relic abundance. Guided by the so far successful principle of symmetry, it turned out that R-parity conserving supersymmetric extensions naturally provide with the lightest neutralino the prototypical WIMP. For a long time, the term "neutralino" was even used interchangeably with "dark matter". However, since supersymmetry (SUSY) has not shown up at the Large Hadron Collider (LHC) so far, the thermal (or WIMP) nature of dark matter is heavily reconsidered and even further the paradigm that DM is a new elementary particle is questioned. Coupled with the fact that even the simplest realistic supersymmetric models with the Minimal Supersymmetric Standard Model (MSSM) as a prime example come with $\mathcal{O}(100)$ free parameters, simplified WIMP models with only a handful of unknowns gained attention to systematically explore the WIMP scenario. That is, the Standard Model is supplemented with either a single bosonic or fermionic dark matter candidate that annihilates into SM particles via some mediator that couples to both, the SM and the "dark sector". Often times these simplified models still correspond to a certain realization of supersymmetric extensions of the SM.

To fully benefit from the experimental precision of the DM relic abundance measurement in the sub-percent regime to reliably distinguish between dark matter models from cosmology and draw conclusions on the associated parameter regions, it is of great importance to reduce theoretical uncertainties to the same precision. For this reason, the precision of relic density calculations is improved in this thesis in two ways: First, in the context of neutralino dark matter, stop-antistop annihilation into gluons and light quarks is calculated at next-to-leading order (NLO) in the strong coupling α_s and the process is implemented into the public precision code DM@NLO ("Dark Matter at Next-to-Leading Order") which already includes the $\mathcal{O}(\alpha_s)$ corrections to many important (co)annihilation processes in the MSSM. Second, in the context of a simplified dark matter model, the relic density is computed without the usual assumption of kinetic equilibrium between dark matter and the Standard Model. More precisely, the assumption that dark matter has a thermal distribution until after freeze-out is lifted requiring the numerically challenging solution of momentum-dependent Boltzmann equations.

Another important cosmological measurement and probe of Beyond the Standard Model (BSM) physics is the effective number of relativistic degrees of freedom N_{eff} at the time of photon decoupling. Its value follows from the evolution of the ratio of the photon to neutrino energy densities starting from temperatures of around 10 MeV, where the primordial plasma consisted mainly out of (anti)electrons, photons and neutrinos and was kept in thermal equilibrium through electroweak interactions. Under the most restrictive assumptions, N_{eff} evaluates to three, corresponding to the three neutrino flavors in the Standard Model. Nevertheless, to successfully find BSM physics, N_{eff} must be known precisely in the Standard Model. This requires the inclusion of higher-order corrections in the electromagnetic coupling α_{em} to the weak processes keeping neutrinos and electrons in equilibrium. For this reason, the calculation of the dominant $\mathcal{O}(\alpha_{\text{em}})$ corrections to the thermal neutrino interaction rate, and hence N_{eff}, in the closed time path formalism of finite-temperature QFT is the second major part of this thesis.

The layout of this thesis is as follows: In Ch. 2, the dynamics of Friedmann–Lemaître–Robertson–-Walker (FLRW) spacetimes is covered with a particular focus on thermodynamic aspects of the early Universe and kinetic theory. In addition, the standard computation yielding $N_{\text{eff}}^{\text{SM}} = 3$ is presented. Chapter 3 is devoted to dark matter, briefly summarizing the experimental evidence indicating its existence as well as theories of (particle) dark matter. Further, the calculation of the relic density of a single dark matter species produced through freeze-out from the Standard Model bath is explained in detail. Experimental search strategies are briefly covered as well. Next, Ch. 4 deals with the calculation of quantum chromodynamics (QCD) corrections to important (co)annihilation processes in the MSSM and their impact on today's lightest neutralino abundance. The chapter starts with a brief introduction to the MSSM, followed by a quite general introduction to the technicalities of NLO calculations with a particular emphasis on the dipole subtraction method for massive initial-states to allow for the cancellation of infrared divergences. Then, the NLO calculations to stop-antistop annihilation into gluons and light quarks are presented including the Sommerfeld enhancement effect. Finally, the user-interface to the DM@NLO code is presented with a brief introduction to the calculation of the neutralino direct detection rate. In the subsequent Ch. 5, the accuracy of the relic density calculation is improved by solving the corresponding Boltzmann equations on the level of the phase space distribution function instead, but for a simplified dark matter model and not the MSSM. Chapter 6 introduces then the basics of nonequilibrium QFT in the closed time path formalism providing the Kadanoff-Baym equations and the Feynman rules at finite-temperature. As examples, frequently encountered integrals are evaluated which are then applied to the computation of the equilibrium photon self-energy at one-loop order in the real-time formalism. Lastly, in Ch. 7, the dominant QED correction to the thermal neutrino interaction rate are computed and their impact on $N_{\text{eff}}^{\text{SM}}$ is estimated. A final summary and an outlook are given in Ch. 8.

Notation and conventions Throughout this thesis the $(+,-,-,-)$ signature of the metric tensor $g_{\mu\nu}$ is used such that a four-vector x is classified as spacelike if $x^2 < 0$ and as timelike if $x^2 > 0$. The Minkowski metric as a limiting case is denoted by $\eta_{\mu\nu}$. The spatial components of a four-vector $p^\mu = (p^0, \mathbf{p})$ are written in bold font. The "Feynman slash notation" $\not{p} = \gamma_\mu p^\mu$ is used as an abbreviation for the inner product between a four-vector p and the Dirac gamma matrices γ^μ. Physical quantities are expressed in natural units, i.e., $\hbar = c = 1$, eventually adding $k_B = 1$. Dependencies are omitted in the notation unless it enhances readability.

Chapter 2

Thermodynamics in FLRW Cosmology

The ΛCDM model is the prevailing cosmological framework that describes the large-scale dynamics of the Universe and serves by now as the standard model of cosmology. It is based on the FLRW solutions to the Einstein field equations of general relativity and is named after two of its components—Λ, representing dark energy, and CDM (Cold Dark Matter)—besides the ordinary (baryonic) matter. In the following, starting with the FLRW metric, the Boltzmann equations in an expanding Universe, equilibrium thermodynamics and a brief summary of the thermal history of the early Universe are presented. Lastly, due to its importance for Ch. 7, a naive estimate for the effective number of cosmological neutrinos in the Standard Model of particle physics $N_{\mathrm{eff}}^{\mathrm{SM}}$ is presented.

2.1 Friedmann–Lemaître–Robertson–Walker Spacetime

The foundation of modern cosmology [5, 6] is general relativity which links the geometry of space and time, encoded in the metric tensor $g_{\mu\nu}$, to the density and flux of energy and momentum throughout the Universe, all described by the stress-energy tensor $T_{\mu\nu}$, through the Einstein field equations

$$R_{\mu\nu} - \frac{1}{2} R g_{\mu\nu} + \Lambda g_{\mu\nu} = 8\pi G T_{\mu\nu} \,, \tag{2.1}$$

where $R_{\mu\nu}$ is the Ricci curvature tensor, R the scalar curvature, Λ the cosmological constant and G the Newtonian constant of gravitation.

In agreement with observations on length scales $> 100\,\mathrm{Mpc}$, the cosmological principle states that the Universe appears to be homogeneous and isotropic. Therefore, cosmological spacetimes are to a good approximation described by the maximally-symmetric FLRW metric which, in terms of the reduced circumference polar coordinates (t, r, θ, ϕ), takes the form

$$\mathrm{d}s^2 = g_{\mu\nu}\,\mathrm{d}x^\mu\,\mathrm{d}x^\nu = \mathrm{d}t^2 - a^2(t)\left(\frac{\mathrm{d}r^2}{1-kr^2} + r^2\,\mathrm{d}\Omega^2\right) \,, \tag{2.2}$$

where $a(t)$ denotes the cosmic scale factor and $\mathrm{d}\Omega^2 = \mathrm{d}\theta^2 + \sin^2\theta\,\mathrm{d}\phi^2$ the infinitesimal solid angle.

In this convention, r is dimensionless such that the scale factor has units of length and the curvature parameter k can only take on the three distinct values $\{-1, 0, +1\}$, corresponding to an open, flat or closed Universe, respectively.

One important observational consequence of FLRW Universes is that two point-like observers comoving with the cosmic fluid anywhere in the Universe move away from or towards each other with a velocity proportional to their instantaneously measured distance $L(t)$. The associated proportionality factor is given by the Hubble parameter $H = \dot{a}/a$, i.e., $\dot{L} = HL$, with a dot denoting the derivative with respect to the cosmic time. Experimentally, today's expansion rate H_0 is known to be positive $H_0 > 0$ leading to the striking observation that our Universe is constantly expanding. In reference to light whose frequency is shifted to lower values when propagating over cosmological distances, the scaling behavior of observables with $a(t)$ is also referred to as redshift.

To understand the expansion of the Universe on a quantitative level and therefore related phenomena like the aforementioned redshift of photons and how structures move apart, one has to study the dynamics of the scale factor $a(t)$ which are governed through the Einstein equations (2.1). The stress-energy tensor that sources a FLRW spacetime must be homogeneous and isotropic as well, i.e., it describes a perfect fluid and has the components

$$T_{\mu\nu} = (\rho + P) u_\mu u_\nu + P g_{\mu\nu} \,, \tag{2.3}$$

where u_μ is the four-velocity, ρ the total energy density and P the total pressure, both taken in cosmic rest frame. The resulting equations for $a(t)$ are the Friedmann equations, given by

$$H^2 = \frac{\Lambda}{3} + \frac{\rho}{3M_{\text{Pl}}^2} - \frac{k}{a^2} \,, \tag{2.4a}$$

$$\frac{\ddot{a}}{a} = \frac{\Lambda}{3} - \frac{4\pi G}{3}(\rho + 3P) \tag{2.4b}$$

with the reduced Planck mass $M_{\text{Pl}} = 1/\sqrt{8\pi G}$. The cosmological constant in modern cosmology is usually absorbed into the total energy density through the redefinitions $\rho \to \rho - M_{\text{Pl}}^2 \Lambda$ and $P \to P + M_{\text{Pl}}^2 \Lambda$. It is also useful to re-express the Friedman equation (2.4a) through the density parameter $\Omega = \rho/\rho_c$ as

$$\frac{k}{a^2 H^2} = \Omega - 1 \,, \tag{2.5}$$

where the critical density is defined by $\rho_c = 3M_{\text{Pl}}^2 H^2$. It is called the critical density as the sign of k and therefore the geometry of the Universe is determined by whether ρ is larger than, equal to, or less than ρ_c. In the following and throughout this thesis, the Universe is assumed to be flat $k = 0$ which is favored by experimental data [7], even though a priori all three possible geometries could be realized in nature.

Another important concept in cosmology is an equation of state which refers to a connection between the energy density ρ and the isotropic pressure P. The simplest and most common choice is a linear relation $P = w\rho$ with $w = \text{const}$ being independent of time. Stress-energy conservation $\nabla_\mu T^{\mu\nu} = 0$ with the covariant derivative ∇_μ leads to the continuity equation

$$\dot{\rho} + 3H(\rho + P) = 0 \,, \tag{2.6}$$

which can be integrated over time to find that the energy density in terms of the equation of state parameter w gets diluted like

$$\rho(a) = \rho(a_0) \left(\frac{a}{a_0}\right)^{-3(1+w)} . \tag{2.7}$$

In particular, this leads to the important distinction that non-relativistic fluids, known as dust or matter (m) and defined through a negligible kinetic energy compared to their rest mass, hence $w_m = 0$, dilute with the three-dimensional spatial volume $\rho_m \propto a^{-3}$, whereas relativistic fluids, referred to as radiation (r) and satisfying $w_r = \frac{1}{3}$ (see, e.g., Eq. (2.16c)), get diluted with the fourth power of the scale factor $\rho_r \propto a^{-4}$. If the cosmological constant is absorbed into the total energy density as described above and therefore corresponds to a constant contribution to the energy budget of the Universe, Eq. (2.7) implies $w_\Lambda = -1$, i.e., a negative pressure.

Another physical consequence of the presence of the scale factor in the FLRW metric compared to the Minkowskian spacetime is the resulting modification of the mass-shell relation $g_{\mu\nu}p^\mu p^\nu = m^2$ of a particle with four-momentum $p^\mu = (\omega, \mathbf{p})$ and mass m. As a result, the FLRW energy for a comoving observer in a flat geometry reads $\omega^2 = m^2 + a(t)^2\mathbf{p}^2$ such that it is sensible to call

$$\mathbf{p}_{\mathrm{ph}} = a(t)\mathbf{p} \tag{2.8}$$

the physical momentum to recover the (usual) Minkowskian energy-momentum relation $\omega^2 = m^2 + \mathbf{p}_{\mathrm{ph}}^2$. The subscript on $\mathbf{p}_{\mathrm{ph}}$ is dropped in the following.

2.2 Boltzmann Equations in an Expanding Universe

If one turns the arrow of time, the expansion of the Universe becomes a contraction. Thus, at the earliest times that we can currently describe without a working theory of quantum gravity, i.e., at times shortly after the Big Bang, the Universe was filled with a hot and dense plasma consisting of fundamental particles such as quarks, leptons, and gauge bosons.

To study the evolution of different interacting particle species in the Universe, Boltzmann equations are used [8]. These are semi-classical equations of motion describing the evolution of phase space distribution functions $f_1, \ldots, f_n$ of n (interacting) particle species in a gas. In abstract form, they are given by

$$\hat{L}[f_i] = \hat{C}[f_1, \ldots, f_n], \ i = 1, \ldots, n , \tag{2.9}$$

where the Liouville operator $\hat{L}$ alone describes the propagation in phase space for a collisionless system. In general relativity, it is of the form

$$\hat{L} = p^\mu \frac{\partial}{\partial x^\mu} - \Gamma^\mu_{\alpha\beta} p^\alpha p^\beta \frac{\partial}{\partial p^\mu} , \tag{2.10}$$

where p^μ is the conjugate momentum to the spacetime coordinate x^μ, and gravitational effects enter through the Christoffel symbols $\Gamma^\mu_{\alpha\beta}$. For a FLRW Universe, the Liouville operator becomes

$$\hat{L} = E\partial_t - H\mathbf{p}^2\partial_E , \tag{2.11}$$

where $E = |p^0|$ is the energy and $\mathbf{p}$ the associated three-momentum. As a consequence of homogeneity and isotropy, the functions f_i only depend on time t and the absolute momentum $|\mathbf{p}|$. The collision operator $\hat{C}$ on the other hand takes into account changes in the occupation number through interactions between the gas constituents. For one particular reaction $R = 1 + \dots + i + \dots + m \longleftrightarrow a + b + \dots$ involving the particle species i, whose evolution we want to follow, the corresponding collision operator (or collision term) $\hat{C}_R$, defined through

$$\begin{aligned}\hat{C}_R[f_1, \dots, f_n] = \frac{1}{2g_i} \int \prod_{\substack{j=1\\ j\neq i}}^{m} \mathrm{d}\Pi_j \, \mathrm{d}\Pi_a \, \mathrm{d}\Pi_b \dots (2\pi)^4 \delta^{(4)} \left(\sum_{k=1}^{m} p_k - p_a - p_b - \dots \right) \\ \times \Bigg[|\mathcal{M}|^2_{a+b+\dots\to 1+\dots+i+\dots+m} \, f_a \, f_b \cdots \prod_{l=1}^{m} (1 \pm f_l) \\ - |\mathcal{M}|^2_{1+\dots+i+\dots+m\to a+b+\dots} \prod_{l=1}^{m} f_l (1 \pm f_a)(1 \pm f_b) \dots \Bigg], \end{aligned} \tag{2.12}$$

describes the change of f_i at the momentum mode $|\mathbf{p}_i|$, where i carries g_i internal degrees of freedom and $\mathrm{d}\Pi = \mathrm{d}^3\mathbf{p} / [(2\pi)^3 2E]$ is the Lorentz invariant integration measure. Energy and momentum conservation are enforced through the four-dimensional Dirac distribution with $+(-)$ accounting for Bose enhancement (Pauli blocking) of the final states. In this convention, the squared S-matrix elements—$|\mathcal{M}|^2_{a+b+\dots\to 1+\dots+i+\dots+m}$ in the gain term, and $|\mathcal{M}|^2_{1+\dots+i+\dots+m\to a+b+\dots}$ in the loss term—are summed (not averaged) over both initial and final internal degrees of freedom and include the appropriate symmetry factors for identical particles in the initial or final state. For example, if there are n identical particles in either the initial or final state, the matrix element squared includes the symmetry factor $1/n!$. The total collision operator $\hat{C} = \sum_R \hat{C}_R$ is obtained by summing over all possible reactions R involving the species i, having one reaction per occurrence of i and treating particles and antiparticles as distinct from each other. To illustrate this counting procedure, the process $ii \to j$ with another species j in the final state is considered. This reaction is included twice in the summation since i can take the first and the second spot. In contrast, the process $jj \to i$ is only contained once since i appears only once.

2.3 Equilibrium Thermodynamics

From the Boltzmann equation in an expanding Universe one can deduce that as long as a species' interaction rate Γ, which is in essence the averaged collision term on the right-hand side, is larger than the Hubble rate H, this species is kept in local (in time) thermal equilibrium (LTE). This is in particular the case for a majority of the expansion history, where gauge interactions caused the SM plasma to remain in (or near) thermal equilibrium which avoids solving the complicated Boltzmann equations. Observable thermodynamic quantities such as the number density n, energy density ρ and the pressure P for a particle species with g internal degrees of freedom and mass m can be straightforwardly obtained from the associated phase space distribution function

$$n(t) = \frac{g}{(2\pi)^3} \int \mathrm{d}^3\mathbf{p} \; f(\mathbf{p}, t), \tag{2.13a}$$

$$\rho(t) = \frac{g}{(2\pi)^3} \int \mathrm{d}^3\mathbf{p} \; E f(\mathbf{p}, t), \tag{2.13b}$$

$$P(t) = \frac{g}{(2\pi)^3} \int \mathrm{d}^3\mathbf{p} \; \frac{\mathbf{p}^2}{3E} f(\mathbf{p}, t), \tag{2.13c}$$

in which $E = \sqrt{\mathbf{p}^2 + m^2}$ is the energy. Note that it is customary in the cosmological literature, to distinguish a particle from its antiparticle meaning that their contributions to thermodynamic quantities are included separately. For example, (anti)electrons, neutrinos and photons have the same number of degrees of freedom $g_e = g_\nu = g_\gamma = 2$.

For a species in kinetic equilibrium characterized through the temperature T, its phase space distribution function corresponds to the well-known Bose-Einstein or Fermi-Dirac distribution:

$$f_B(E, T, \mu) = \frac{1}{e^{(E-\mu)/T} - 1}\,, \tag{2.14a}$$

$$f_D(E, T, \mu) = \frac{1}{e^{(E-\mu)/T} + 1}\,. \tag{2.14b}$$

If the species is additionally in chemical equilibrium, its chemical potential μ can be related to the chemical potential of other species with which it exchanges energy. For example, if the species under consideration (denoted again by i) interacts with the other particle species j, k and l via the process $i + j \longleftrightarrow k + l$ with equal production and destruction rates, then $\mu_i + \mu_j = \mu_k + \mu_l$. This has the important consequence that at sufficiently large temperatures where processes like $i + i \longleftrightarrow 4i$ are possible, chemical equilibrium implies a vanishing chemical potential, $\mu_i = 0$.

For such kinetic equilibrium situations, the integrals in Eqs. (2.13a) to (2.13c) can be solved analytically in the relativistic ($T \gg m, \mu$) and non-relativistic ($m \gg T$) limit. For the relativistic case, the application of the Riemann zeta function $\zeta(s)$ is helpful since for $\mathrm{Re}(s) > 1$ it has the integral representation

$$\zeta(s) = \frac{1}{\Gamma(s)} \int_0^\infty \mathrm{d}x \, \frac{x^{s-1}}{e^x - 1}, \text{ (for bosons)}, \tag{2.15a}$$

$$= \frac{1}{(1 - 2^{1-s})\Gamma(s)} \int_0^\infty \mathrm{d}x \, \frac{x^{s-1}}{e^x + 1}, \text{ (for fermions)}, \tag{2.15b}$$

where $\Gamma(s)$ denotes the gamma function. The resulting analytical expressions are exact for a massless species with vanishing chemical potential, i.e., for $m = \mu = 0$, and read

$$n_r = \begin{cases} \frac{g\,\zeta(3)}{\pi^2} T^3 & \text{for bosons} \\ \frac{3}{4}\frac{g\zeta(3)}{\pi^2} T^3 & \text{for fermions} \end{cases} \tag{2.16a}$$

$$\rho_r = \begin{cases} \frac{g\,\pi^2}{30} T^4 & \text{for bosons} \\ \frac{7}{8}\frac{g\,\pi^2}{30} T^4 & \text{for fermions} \end{cases} \tag{2.16b}$$

$$P_r = \frac{1}{3}\rho_r, \tag{2.16c}$$

after inserting the special value $\zeta(4) = \frac{\pi^4}{90}$. Importantly, quantum statistics manifests itself through the additional factor 7/8 in the energy density for fermions compared to the bosonic case while the factor 3/4 appears for the number density. The $\rho \propto T^4$ behavior of the energy density encountered here is reminiscent of the Stefan-Boltzmann law for the total energy radiated from a black body. In the non-relativistic limit, bosons and fermions effectively obey a Maxwell-Boltzmann distribution

$$f_{\mathrm{MB}}(E, T, \mu) = \exp(-(E - \mu)/T)\,, \tag{2.17}$$

so that the distinction between particles of different spins disappears. After substituting $f_{\rm MB}$ into Eq. (2.13), one obtains

$$n_{\rm nr} = \frac{gTm^2e^{\frac{\mu}{T}}}{(2\pi)^2}K_2(m/T)\,, \tag{2.18a}$$

$$\rho_{\rm nr} = m\, n_{\rm nr}\,, \tag{2.18b}$$

$$P_{\rm nr} = T\, n_{\rm nr} \ll \rho_{\rm nr}\,, \tag{2.18c}$$

where the function $K_\nu(z)$ denotes a modified Bessel function of the second kind of positive integer degree ν. If the Maxwell-Boltzmann distribution is expanded around small momenta $|\mathbf{p}| \ll m$, using $E = m + \frac{|\mathbf{p}|^2}{2m} + \mathcal{O}(|\mathbf{p}|^4)$, one obtains a more insightful approximate expression for the number density given by

$$n_{\rm nr} \approx g\left(\frac{mT}{2\pi}\right)^{\frac{3}{2}} e^{-\frac{m-\mu}{T}}\,. \tag{2.19}$$

Here, the exponential $\sim \exp(-m/T)$ behavior is known as Boltzmann suppression and has important implications for the abundance of non-relativistic particle species in the early Universe. Another very fiducial quantity during the expansion of the Universe is the the entropy density s defined via

$$s = \frac{S}{V} = \frac{\rho + P}{T} \tag{2.20}$$

since the entropy S per comoving volume V remains conserved in LTE.

2.4 Brief Thermal History of the Universe

The following is a brief summary of our current understanding of the thermal history of the Universe. This should turn out to be useful to locate when other events, e.g., the production of dark matter, take place during the cosmological history. Note however that inflation and baryogenesis are hypothesized events whose nature must still be clarified experimentally whereas the electroweak and QCD phase transition are expected to have happened based on the Standard Model but are lacking clear experimental evidence so far.

- **Inflation**: Cosmic inflation is a hypothesized period after the Big Bang including a phase of rapid exponential expansion to cure the flatness, the horizon and the magnetic monopole problems [9,10]. In addition, inflation successfully predicts the primordial density fluctuations that are considered the seeds of structure formation. Inflation could be driven by a scalar field—the inflaton—which contains the majority of the energy density until the end of inflationary epoch where the period of reheating starts. During this phase the energy stored in the inflaton field is converted to Standard Model particles which then thermalize due to their interactions, thus, establishing a reheating temperature T_R. Our current understanding predicts reheating temperatures ranging from the GUT scale at $10^{16}\,$GeV down to $\gtrsim 5\,$MeV [11].

- **Baryogenesis**: Baryogenesis is a hypothesized process responsible for creating the baryon asymmetry in the Universe [12]. If baryons and antibaryons were equally abundant in the primordial plasma, the Universe would entirely be filled by radiation due to efficient annihilations at earlier times. However, the observable Universe is overwhelmingly composed of matter, with very little antimatter. An alternative scenario to baryogenesis is baryogenesis through leptogenesis [13] in which an asymmetry in leptons was generated first, which then was transferred to the observed baryon asymmetry through sphaleron processes.

- **Electroweak Phase Transition**: This phase transition happens in the Standard Model at a temperature of around 160 GeV [14] and is responsible for the spontaneous breaking of the $\mathrm{SU}(2)_L \times \mathrm{U}(1)_Y$ gauge symmetry down to $\mathrm{U}(1)_{\mathrm{em}}$ which gives masses to most elementary particles.

- **QCD Phase Transition**: The strong phase transition marks the moment when previously free quarks and gluons confine into colorless bound states like protons, neutrons or pions and is expected to take place at a temperature of approximately $\sim 150\,\mathrm{MeV}$ within an "analytic crossover" transition according to lattice simulations [15].

- **Neutrino Decoupling**: At temperatures $T \sim 10\,\mathrm{MeV}$ the primodial plasma was constituted out of electrons, photons and three-generations of left-handed neutrinos. Since neutrinos only interact with the Standard Model via the weak force, they decouple first from the QED plasma at temperatures of around 1 MeV. Once decoupled, their distribution function remains fixed with the neutrino temperature T_ν evolving independently of the photon temperature T. One proposal to directly detect this Cosmic Neutrino Background (CNB) is the PTOLEMY experiment [16].

- **Electron-Positron Annihilation**: When the temperature dropped below the electron mass $m_e \simeq 511\,\mathrm{keV}$, annihilation of photons into oppositely charged electrons became kinematically suppressed. As a result, the energy residing in the electron population was transferred to the photon sector through electron-positron annihilations, effectively increasing the photon energy density ρ_γ by raising the photon temperature above the neutrino temperature. The precise ratio of the energy density contained in the neutrino sector ρ_ν compared to ρ_γ in the limit $T/m_e \to 0$ is contained in the effective number of neutrino species in the Standard Model $N_{\mathrm{eff}}^{\mathrm{SM}}$ defined as
$$\frac{\rho_\nu}{\rho_\gamma}\bigg|_{T/m_e\to 0} \equiv \frac{7}{8}\left(\frac{4}{11}\right)^{4/3} N_{\mathrm{eff}}^{\mathrm{SM}}. \tag{2.21}$$
More precisely, the limit $T/m_e \to 0$ is understood to apply only to $T \gg m_i$, where m_i is the largest neutrino mass. The origin of the prefactors in Eq. (2.21) becomes clear in the next section where the value of $N_{\mathrm{eff}}^{\mathrm{SM}}$ is estimated from entropy conservation. More generally, N_{eff} is defined as the energy density residing in free-streaming, ultra-relativistic particle species relative to the photon energy density in the post-neutrino decoupling early Universe and therefore also allows to capture BSM physics [17].

- **Big Bang Nucleosynthesis**: The formation of the nuclei of light elements such as ^{2}H, ^{4}He, ^{3}Li and their isotopes out of protons and neutrons roughly started three minutes after inflation at $T \sim 0.8\,\mathrm{MeV}$ and is called Big Bang Nucleosynthesis (BBN). Heavier elements on the other hand are known to have only been formed later in the processes of stellar and supernova nucleosynthesis.

- **Recombination**: When the temperature dropped below the ionization energy of hydrogen, i.e., below 13.6 eV, long after BBN, the Universe became transparent for photons. This is because most electrons were bound within hydrogen atoms such that photons and electrons did no longer interact rapidly enough through Thomson scattering. These are the relic photons that are observed today in the Cosmic Microwave Background and allow to investigate the state of the Universe roughly 380 000 years after the end of inflation. It turns out the the CMB has an almost perfect black body spectrum with a temperature today of $T = 2.7260(13)\,\mathrm{K}$ and is isotropic to roughly one part in 10^5 [18]. These temperature fluctuations are assumed to be due to the previously mentioned primordial density inhomogenities after inflation and have been measured in a series of experiments by the COBE [19], WMAP [20] and Planck [7] satellites.

- **Reionization**: The period of reionization marks the epoch when the first stars and galaxies formed. The emitted ultraviolet light partially re-ionized the surrounding neutral hydrogen gas. This process effectively ended the cosmic "dark ages" but was not efficient enough to re-establish thermal equilibrium such that only a fraction of the CMB photons scatter off the ionized atoms and electrons. In particular, the observation of the redshifted 21 cm line of atomic hydrogen is a crucial probe of this epoch [21].

2.5 Standard $N_{\text{eff}}^{\text{SM}} = 3$ from Entropy Conservation

The naive estimation of N_{eff} in the Standard Model available in many textbooks [6, 22] relies implicitly on the following four assumptions:

- **Instantaneous decoupling approximation**: The neutrino decoupling process happens instantaneously at the decoupling temperature T_d and is not spread out over a larger time interval.
- **Ultra-relativistic approximation**: The electron gas is treated as massless even though the electron mass is non-negligible at temperatures of 1 MeV where the neutrino decoupling process is expected to take place. This is also referred to as the "neutrino-never-coupled (NNC) approximation" since treating the $e^{\pm}$ bath as ultra-relativistic is equivalent to the assumption that neutrinos decoupled in the infinite past $T_d/m_e \to \infty$.
- **Ideal gas approximation**: All relevant particles species obey either an exact Bose-Einstein or an exact Fermi-Dirac distribution such that together with the NNC approximation the neutrino, photon and electron energy densities and pressures are all given by the corresponding relativistic expressions in Eq. (2.16).
- **No energy exchange approximation**: The three species of left-handed neutrinos do not exchange energy, i.e., neutrino oscillations are neglected.

In addition, it is assumed that at temperatures relevant for the decoupling process, the photons are held in a state of thermodynamic equilibrium together with the electrons/positrons which are collectively referred to as the "QED plasma". The entropy conservation argument then posits that the comoving entropy densities in two decoupled sectors are separately conserved, i.e., for the entropy density s_{ν_α} of a decoupled neutrino species ν_α and of the QED plasma $s = s_e + s_\gamma + \sum_{\beta \neq \alpha} s_{\nu_\beta}$ plus any neutrino species ν_β that still may be in equilibrium with it one can write

$$s(a_1)a_1^3 = s(a_2)a_2^3\,, \tag{2.22a}$$

$$s_{\nu_\alpha}(a_1)a_1^3 = s_{\nu_\alpha}(a_2)a_2^3 \tag{2.22b}$$

for two different times characterized through the corresponding scale factors a_1 and a_2. After ν_α decouples instantaneously from the QED plasma at the time given by $a_1 = a_d^+$, the decoupled neutrino species and the QED plasma still share the same temperature $T_{\nu_\alpha}(a_1) = T(a_1) = T_d$. In the ideal-gas approximation and the ultra-relativistic approximation ($T_d/m_e \to \infty$) the two entropy densities are then given by

$$s(a_1) = \frac{2\pi^2}{45}\left(2 \times \frac{7}{8}g_e + g_\gamma + \frac{7}{8}\sum_\beta g_\nu\right) T_d^3(a_1)\,, \tag{2.23a}$$

$$s_{\nu_\alpha}(a_1) = \frac{7}{8}\frac{2\pi^2}{45} g_\nu T_d^3(a_1)\,. \tag{2.23b}$$

In the standard estimate, all three neutrino flavors are assumed to decouple effectively at the same time, i.e., $T_\nu(a_1) = T_{\nu_\alpha}(a_1) = T_d$, an assumption that may to some extent be justified by the observed large mixing in the neutrino sector. Therefore, the scale factor $a_1 = a_d^+$ is chosen to correspond to the time immediately after the decoupling of all neutrino flavors. In contrast, a_2 is chosen at a time significantly after the era of electron-positron annihilation such that $T(a_2) \ll m_e$ and only photons contribute to the QED entropy density while the entropy in the neutrino sector includes all flavors, i.e.,

$$s(a_2) = \frac{2\pi^2}{45} g_\gamma T(a_2)^3\,, \tag{2.24a}$$

$$s_\nu(a_2) = \sum_\alpha s_{\nu_\alpha}(a_2) = 3 \times \frac{7}{8}\frac{2\pi^2}{45} g_\nu T_d^3(a_2)\,. \tag{2.24b}$$

Comparing Eq. (2.23b) with Eq. (2.24b) via Eq. (2.22b) immediately leads to the scaling behavior $T_\nu(a_2) = (a_1/a_2)T_\nu(a_1)$. Equating furthermore Eq. (2.23a) and Eq. (2.24a) leads to the neutrino temperature

$$T_\nu(a_2) = \left(\frac{4}{11}\right)^{1/3} T(a_2)\,. \tag{2.25}$$

Using this ratio $T_\nu(a_2)/T(a_2)$ in the energy density (2.16b) yields $N_{\text{eff}}^{\text{SM}} \simeq 3$. Including the effects of a finite electron mass in the $N_{\text{eff}}^{\text{SM}}$ estimate requires the numerical evaluation of the entropy of the QED plasma which is only possible by making an assumption on the neutrino decoupling temperature. The precise calculation of the thermal neutrino interaction rate from finite-temperature field theory and therefore the decoupling temperature is the subject of Ch. 7.

Chapter 3

Dark Matter: Evidence, Candidates, Production Mechanism and Searches

There is compelling evidence from astrophysical observations that there is a yet unknown matter component called dark matter without any so far detectable interactions with light but manifests itself through its gravitational effects on baryonic matter. Nevertheless, the nature and intrinsic properties of DM remain unknown. Therefore, this chapter very briefly reviews evidence for dark matter and possible but highly speculative theories of (particle) dark matter in Secs. 3.1 and 3.2. The production of dark matter from the Standard Model bath through thermal freeze-out is discussed in depth in Sec. 3.3 due to its relevance for this thesis along with some theoretical uncertainties entering in the predictions of the abundance of such a thermal dark matter candidate. Lastly, experimental search strategies for WIMPS are discussed in Sec. 3.4. Comprehensive reviews on observational evidence for dark matter, detection strategies and theories are, e.g., available in Refs. [23–27], whereas the history of dark matter is discussed in Ref. [28].

3.1 Evidence from Galactic to Cosmological Scales

It is remarkable that within the last century, experimental evidence for dark matter has accumulated on all possible length scales, ranging from the smallest identified galaxies to the whole observable Universe.

One of the first hints towards the existence of an additional non-baryonic matter component was given through the estimation of the amount of luminous matter in the Milky Way using well-known mass to luminosity ratios [29]. The inferred mass turned out to be too little to be compatible with the relatively large velocity of stars near the galactic plane. These were measured through their Doppler shift and found to exceed the escape velocity of the gravitational pull of the luminous mass, thus, pointing to an additional mass component in the Milky Way that does not emit a sufficient amount of light or is obscured by dust. The evidence for dark matter on galactic scales strengthened further through the measurement of the rotation curve of the Andromeda galaxy which is the nearest major spiral galaxy to the Milky Way [30]. Based on Newtonian gravity and under the assumption of circular orbits, the rotational velocity v_{rot} should obey a radius and mass

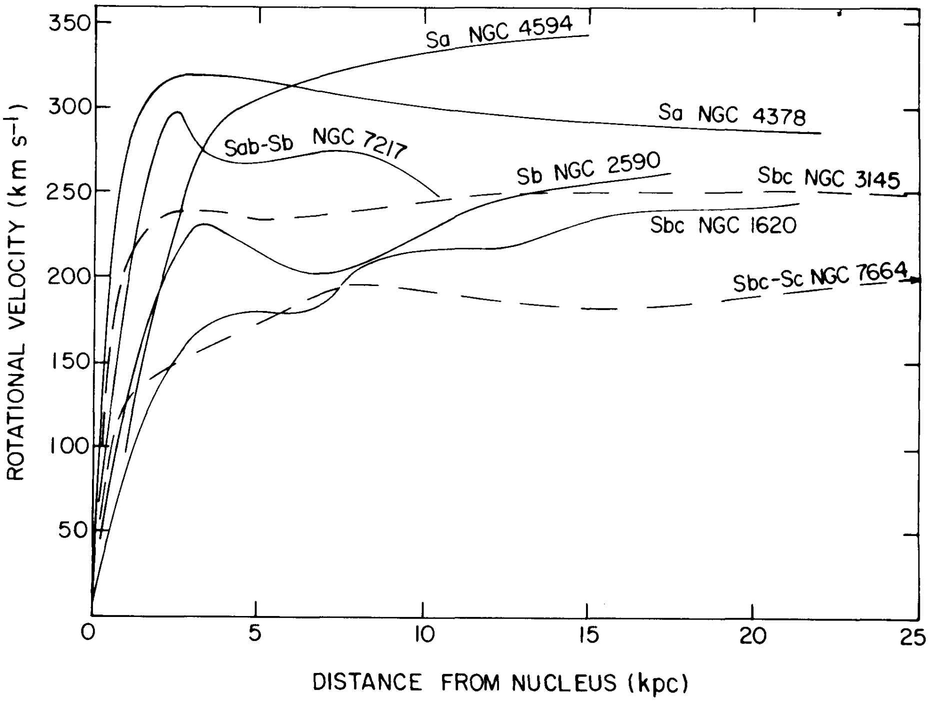

Figure 3.1: Rotation curves of seven spiral galaxies of different Hubble type, e.g., "Sa" represents an early-type spiral galaxy and "Sbc" a late-type barred spiral galaxy. Figure taken from Ref. [31].

dependence according to

$$v_{\mathrm{rot}}(r) = \sqrt{\frac{GM(r)}{r}} \tag{3.1}$$

with $M(r)$ denoting the mass enclosed in the galaxy up to the radius r. As a result, v_{rot} should decrease at the far exterior of the optical disk given the natural assumption that $M(r)$ rises slower than r in the outer region. However, spectral spectroscopy analyses showed that the observed rotational velocities remain larger than what is expected based on the measured amount of visible matter even for large distances from the galactic center. Since then, many more rotation curves have been studied, further confirming the problem of missing mass [31], some of which are displayed in Fig. 3.1.

On the scale of galaxy clusters, applications of the virial theorem, which relates the mean kinetic energy and the averaged potential, to the Coma Cluster, a large galaxy cluster consisting of over one thousand identified galaxies about 300 million light years away from Earth, yielded again the insight that the luminous mass is well below the mass obtained from the measured velocities of galaxies on the edge of the cluster [32, 33]. Besides the virial theorem, another "direct empirical proof of the existence of dark matter" on cluster scales is the Bullet cluster, a cluster formed after the direct collision of two large clusters of galaxies [34]. The baryonic matter component remained in the center of the collision according to X-ray observations whereas most of the total mass seems to be located outside of the center based on gravitational lensing, clearly showing a spatial separation between baryonic and dark matter. This also indicates that dark matter is in very good approximation collisionless compared to the hydrogen gas.

On cosmological scales and overall the most convincing observation sustaining not only particle dark matter but also the hot big bang theory is the CMB, the last radiation emitted during the epoch of recombination when the temperature of the primordial plasma was small enough to form hydrogen out of electrons and protons. The temperature anisotropies in the CMB spectrum are expected to be due to small density fluctuations at the end of the inflationary epoch which allowed dark matter to accumulate within these overdense regions. The attraction of baryonic matter towards the gravitational well was counteracted by the electromagnetic pressure. The resulting oscillations are what is nowadays observed as temperature fluctuations in the CMB and allow the most precise measurements to date of the relic density of cold dark matter and the baryonic component. The fit of the ΛCDM model to the angular CMB power spectrum from Planck data [7] results in the densities:

$$\Omega_\Lambda h^2 = 0.3107 \pm 0.0082\,, \tag{3.2a}$$

$$\Omega_\mathrm{b} h^2 = 0.02237 \pm 0.00015\,, \tag{3.2b}$$

$$\Omega_\mathrm{CDM} h^2 = 0.120 \pm 0.0012 \tag{3.2c}$$

for dark energy, baryonic matter and dark matter, respectively. The indicated uncertainty corresponds to the 68 % confidence interval, and $h \sim 0.67$ is the reduced Hubble constant and stands for the present Hubble expansion rate H_0 in units of $100\,\mathrm{km\,s^{-1}\,Mpc^{-1}}$. Note that the measured DM relic density relies on the the six-parameter cosmological concordance model that besides the three-parameters in Eq. (3.2) includes the assumption that the initial perturbations are adiabatic and Gaussian with the power law spectrum

$$\mathcal{P}(k) = A_s \left(\frac{k}{k_0}\right)^{n_s - 1} \tag{3.3}$$

described by the spectral index n_s and the amplitude A_s of the primordial density fluctuations whose values are determined to be $n_s = 0.9649(42)$ and $\ln\!\left(10^{10} A_s\right) = 3.044(14)$. The last parameter is the optical depth τ that is related to damping of small scale fluctuations of the CMB due to Thomson scattering. It is important to realize this dependence of the DM relic density measurement to the underlying cosmological model as, e.g., the inclusion of five additional physical parameters in the model like non-zero neutrino masses can even enlarge the allowed range for the dark matter relic density by a factor of two [35].[1] Relaxing the assumption of a constant comoving DM density through the possibility that at any time dark matter can be transformed into a non-interacting form of radiation like gravitational waves may decrease Ω_CDM further by up to 10 % [36]. In contrast, adding data from galaxy surveys like the Sloan Digital Sky Survey (SDSS) [37] or BOSS [38] on the imprint of baryonic acoustic oscillations (BAOs) onto the local matter distribution merely changes the central value of Ω_CDM insignificantly. In addition, large N-body simulations with the density fluctuations from the CMB as initial conditions such as *The Millennium Simulation Project* [39] or *The Bolshoi Simulation* [40] show that cold dark matter is necessary to be consistent with hierarchical structure formation seen in such galaxy and redshift surveys. This means that small structures form first and build gradually up to larger ones. A predominately hot dark matter component would instead lead to the formation of larger structures first.

---

[1] This analysis was performed using WMAP and SDSS data.

3.2 Theories of Dark Matter

There are different approaches to the dark matter problem. One possibility originating in the desire to explain the anomalous rotation curves is to modify Newtonian gravity, $a = GM/r^2$, such that at small accelerations $a \ll a^* \approx H_0$, a test particle moves according to $a^2/a^* = GM/r^2$. This approach is called Modified Newtonian Dynamics (MOND) [41] and is able to explain the flat rotation curves but has the obvious problem of being non-relativistic and violating momentum conservation. However, MOND successfully predicts the empirical Tully-Fisher relation of astrophysics which relates the mass of a spiral galaxy to its asymptotic rotation velocity [42]. The best known modification of general relativity that promotes MOND to a fully relativistic theory is TeVeS [43] standing for Tensor-Vector-Scalar gravitational field theory. However, such theories predict different propagation speeds for gravitational and electromagnetic waves which are highly constrained through the simultaneous observation of the gravitational waves from the neutron star merger GW170817 and its electromagnetic counterpart [44]. In addition, alternative gravity theories are not capable so far to correctly predict the temperature and polarization spectrum of the CMB and the large-scale structure all at the same time [45]. This experimental incompatibility of modified theories of gravity points towards the particle nature of dark matter to explain all observations. Therefore, the discussion of dark matter candidates in the following focuses on particle dark matter.

3.2.1 Dark Matter in the Standard Model

The SM neutrinos are at first glance a good DM candidate due to their properties of being stable, electrically neutral, interacting only weakly and being, according to neutrino oscillations [46, 47], endowed with a non-vanishing mass. However, they 1) are too light to be consistent with structure formation and 2) being fermions they violate the Tremaine-Gunn bound [48] which is a lower bound on the DM mass based on the Pauli exclusion principle. Alternatively, one can also search for baryonic dark matter. One option are Massive Astrophysical Compact Halo Objects (MACHOs) [49] that emit very little or no light. Examples are brown dwarfs, neutron stars or black holes. However, these types of objects are clearly disfavored since in our current understanding star formation happened after BBN rendering MACHOs incompatible with CMB data. If on the other hand such astrophysical objects consisting of baryonic matter have been formed before BBN, the CMB constraints do not apply, as their energy density gets then subtracted from the baryonic budget. This is the case for primordial black holes (PBH) whose formation requires large primordial density fluctuations at small scales [50]. Therefore, PBHs belong in principle into the next section due to the dependence of their formation on the non-SM inflationary scenario. Another possibility falling also into the category of baryonic dark matter is that DM is a “sexaquark” (or “hexaquark”), a hypothetical spin-0 bound state S made up of two up quarks, two down quarks and two strange quarks $S \sim uuddss$ [51, 52]. Such a bound state is interesting because it is expected to have an unusually large binding energy indicating its stability. However, this state is so far lacking experimental evidence and its binding energy still needs be computed from lattice QCD. Besides, there is the question whether its coupling to other baryons like neutrons and protons is actually small enough to not cause an overabundance of S. Since the Standard Model seems to fail to provide a good dark matter candidate, some beyond the SM candidates for DM are discussed next.

3.2.2 Beyond the Standard Model Candidates

For a long time the most appealing particle dark matter candidate have been WIMPs, as they are consistent with structure formation due to their non-relativistic velocity and naturally lead via chemical freeze-out from the primordial Standard Model plasma to the observed relic density. This development to the most promising candidate was in particular driven by theories like supersymmetry and universal extra dimensions (UED) which were originally thought of and investigated as solutions to the hierarchy and other fine-tuning problems but then naturally gave rise to a suitable dark matter candidate at the electroweak scale in form of the lightest neutralino for supersymmetric theories [53] and the lightest Kaluza-Klein state for UED [54]. The simplest extension of the Standard Model that incorporates supersymmetry as a global symmetry is the R-parity conserving Minimal Supersymmetric Standard Model (MSSM) [55] which will be discussed in more depth in Ch. 4. If supersymmetry is promoted to a local symmetry instead, a theory of gravity—called supergravity [56]—naturally appears on top containing the gravitino, the partner particle of the graviton, as another dark matter candidate. Despite its theoretical elegance and potential solutions to outstanding problems in particle physics, supersymmetry has not yet been observed experimentally. Collider experiments, such as those conducted at the LHC, have placed stringent constraints on the masses of superpartners, pushing them to higher energy scales [57]. The absence of direct evidence for SUSY has led to various extensions of the MSSM, such as the Next-to-Minimal Supersymmetric Standard Model (NMSSM), which adds additional one singlet chiral superfield to the MSSM, namely the singlino in the neutralino sector. Note that the singlino is not only added to have another dark matter candidate but also to generate the μ term dynamically, thus curing the μ-problem of the MSSM as another naturalness issue [58]. On the complete opposite site of supersymmetric extensions in terms of free parameters is the idea of "minimal dark matter" where the DM is the lightest neutral component of an electroweak n-plet that is added to the SM and the only free parameter of the model is the DM mass which is entirely fixed through the relic density [59].

In opposition to WIMPs, dark matter candidates that have never been in equilibrium with the SM are called feebly interacting massive particles (FIMPs). Their relic density can be explained via the so-called freeze-in mechanism [60] where the DM is assumed to have a negligible abundance after reheating and is subsequently produced through annihilation or decay processes of SM particles. A natural realization of the freeze-in mechanism occurs, e.g., if a kinetically mixed dark photon [61] couples to a Dirac fermion that serves as dark matter [62]. Another simple FIMP model is a singlet scalar as dark matter that only interacts with the SM via the Higgs field [63].

Two other candidates that naturally emerge from theories that were initially proposed to solve other open questions of the Standard Model are axions and sterile neutrinos. Axions appear as the pseudo-Nambu-Goldstone bosons of the spontaneously broken Peccei–Quinn symmetry [64] to solve the strong CP-problem but can also constitute dark matter via the misalignment mechanism if they are sufficiently light and long-lived [65]. The need to solve the CP-problem imposes a certain relationship between the axion mass and its coupling to photons. If this requirement is lifted and both are independent parameters, one talks about axion-like particles (ALPs) [66]. Sterile neutrinos on the other hand are used to explain the observed non-zero neutrino masses but can at the same time make up the dark matter via the Dodelson-Widrow mechanism [67], the Shi–Fuller mechanism [68] or via radiative neutrino mass generation [69, 70].

Another angle that could provide insights into the nature of dark matter is the Higgs sector as there is no definitive guiding principle for its construction, although the Higgs sector has been validated as the source of electroweak symmetry breaking. Therefore, BSM theories commonly propose an expanded scalar sector with the MSSM as a prime example. Another possibility is, for example, the Inert Doublet Model [71, 72] that introduces a second $\mathrm{SU}(2)_L$ Higgs doublet and an unbroken $\mathbb{Z}_2$ symmetry to stabilize the new fields.

However, given the null results of dark matter searches so far and the plethora of dark matter candidates, the research focus of WIMP DM has shifted more towards simplified dark matter models which remain agnostic about their ultraviolet (UV) completion but allow to systematically study different dark matter types, i.e., scalar, fermionic or vector dark matter and different kinds of mediators responsible for the interaction with the Standard Model, see, e.g., Refs. [73, 74] for a test of simplified WIMP models against existing and future experimental limits. One simplified model where the DM candidate annihilates only into SM leptons via a scalar mediator is studied in Ch. 5.

Lastly, even in the "nightmare scenario" that dark matter has only gravitational interactions, the observed relic density can be explained through graviton mediated annihilations of Standard Model particles into dark matter, given that the DM mass is between a few TeV and 10^{16} GeV and assuming a negligible DM abundance after reheating [75].

3.3 The Relic Abundance of a Single Thermal Dark Matter Species

The standard starting point for the calculation of the DM relic density through production from the primordial plasma of SM particles is the semi-classical Boltzmann equation (2.2) which for a single DM species χ in a FLRW background reads

$$E\left(\frac{\partial f_\chi}{\partial t} - H|\mathbf{p}|\frac{\partial f_\chi}{\partial|\mathbf{p}|}\right) = \hat{C}[f_\chi] \tag{3.4}$$

with the energy $E = \sqrt{\mathbf{p}^2 + m_\chi^2}$ of the dark matter particle. Equation (3.4) describes the evolution of the DM phase space distribution function $f_\chi(p,t)$ in time t. The collision operator $\hat{C}[f_\chi]$ has already been defined in general in Eq. (2.12) and takes into account the loss and gain of DM particles at the momentum mode $|\mathbf{p}|$ through interactions with the Standard Model plasma.

The momentum derivative responsible for modeling the cosmological redshift can be absorbed into the phase space density by rewriting the Boltzmann equation in terms of a dimensionless comoving momentum $\mathbf{q} \sim a\mathbf{p}$ which correspond to the physical momentum defined in Eq. (2.8). This turns the partial differential equation into an infinite set of coupled ordinary differential equations

$$\frac{\mathrm{d}f_\chi(\mathbf{q},t)}{\mathrm{d}t} = \hat{C}[f_\chi]\,, \tag{3.5}$$

where one has to make the identification $f_\chi(\mathbf{p},t) = f_\chi(\mathbf{q},t)$. Thus, one gets one equation for every comoving momentum mode. Since the equilibrium distribution functions in Eq. (2.14) depend implicitly on time through the temperature, it is instructive to express the evolution of $f_\chi(\mathbf{q},t)$ not in terms of time but through the photon temperature T or alternatively through the dimensionless quantity $x = m_0/T$, where m_0 is in general some reference scale which is usually identified with the DM mass m_χ. This change of variable from t to T is achieved by using the scale factor as a time variable in the intermediate step $\frac{\mathrm{d}f_\chi}{\mathrm{d}a} = \frac{1}{Ha}\hat{C}[f_\chi]$ and replacing the derivative with respect to $a(t)$ afterwards by assuming entropy conservation $\frac{\mathrm{d}}{\mathrm{d}x}\left(sa^3\right) = 0$ giving

$$E\frac{\mathrm{d}f_\chi}{\mathrm{d}x} = -\frac{\mathrm{d}s}{\mathrm{d}x}\frac{1}{3sH}\hat{C}[f_\chi]\,. \tag{3.6}$$

During radiation domination, i.e., for $T \gtrsim 100\,\mathrm{eV}$, the entropy density $s = h_{\text{eff}}(T)\frac{2\pi^2}{45}T^3$ and the energy density $\rho = g_{\text{eff}}(T)\frac{\pi^2}{30}T^4$ can be safely expressed in terms of the SM effective number of relativistic degrees of freedom, $h_{\text{eff}}(T)$ and $g_{\text{eff}}(T)$, for which one can use, e.g., the tabulated values from the lattice QCD calculation [76]. Applying the Friedmann equation (2.4a) for a flat Universe $H^2 = \rho/(3M_{\text{Pl}}^2)$ gives the final equation

$$E\frac{\mathrm{d}f_\chi(\mathbf{q},x)}{\mathrm{d}x} = \sqrt{\frac{90}{\pi^2}}\frac{\tilde{g}(T)}{g_{\text{eff}}^{1/2}(T)}\frac{xM_{\text{Pl}}}{m_0^2}\hat{C}[f_\chi]\,, \tag{3.7}$$

where the function $\tilde{g}(T)$ containing the temperature derivative of the entropy degrees of freedom reads

$$\tilde{g}(T) = 1 + \frac{1}{3}\frac{\mathrm{d}\ln h_{\text{eff}}(T)}{\mathrm{d}\ln T}. \tag{3.8}$$

Lastly, it is necessary to pick a convention for the proportionality factor relating the comoving momentum $\mathbf{q}$ to the momentum $\mathbf{p}$. Since it is only possible to consider the ratio of the scale factor relative to its value at some other reference temperature T', a suitable definition of the comoving momentum is

$$\mathbf{q} = \left[h_{\text{eff}}(T')\right]^{-1/3}\frac{\mathbf{p}}{T'}\frac{a(T)}{a(T')} = \left[h_{\text{eff}}(T)\right]^{-1/3}\frac{\mathbf{p}}{T}. \tag{3.9}$$

3.3.1 The Collision Terms

To simplify the evaluation of the collision term, one generally assumes CP invariance as well as that two-body processes $a\,b \leftrightarrow 1\,2$ dominate dark matter production [77]. In this particular case of a two-particle reaction R, the collision term (2.12) reduces to

$$\hat{C}_R[f_a] = \frac{1}{2g_a}\int \mathrm{d}\Pi_b\,\mathrm{d}\Pi_1\,\mathrm{d}\Pi_2\,|\mathcal{M}_{ab\to12}|^2(2\pi)^4\delta^{(4)}(p_a+p_b-p_1-p_2)\,\mathcal{P}(f_a,f_b,f_1,f_2) \tag{3.10}$$

with particle a carrying g_a internal degrees of freedom. It should be highlighted again that in this convention $|\mathcal{M}_{ab\to12}|^2 = |\mathcal{M}_{12\to ab}|^2$ always represents the squared matrix element *summed* (not averaged) over both initial and final internal degrees of freedom like spin or color and includes a symmetry factor $1/2$ for identical particles in either the initial or final state. The phase space densities are contained in the population factor

$$\mathcal{P}(f_a,f_b,f_1,f_2) = f_1f_2(1\pm f_a)(1\pm f_b) - f_af_b(1\pm f_1)(1\pm f_2)\,, \tag{3.11}$$

with $+(-)$ accounting for Bose enhancement (Pauli blocking) of the final states. According to the number of appearances of the unknown DM distribution function f_χ in the loss and gain terms, the collision term can be split further into a number changing contribution, $\hat{C}_{\text{ann}}$, from DM-DM annihilation processes into SM final states, a number conserving part, $\hat{C}_{\text{el}}$, from elastic scattering processes of DM with SM particles responsible for maintaining kinetic equilibrium and a collision term $\hat{C}_{\rm self}$ describing self-scattering processes. In the next step, the relevant individual $2 \to 2$ contributions to $\hat{C}$ are worked out in more detail.

For non-relativistic DM, the Bose enhancement and Pauli blocking factors can be safely neglected, thus implying that in $\hat{C}_{\rm ann}$, SM particles are, due to energy conservation, in very good approximation described by a Boltzmann distribution and that consequently the statistical factors accompanying the SM densities can be dropped as well. These simplifications allow to express the annihilation collision term as

$$\hat{C}_{\rm ann}[f_\chi] = \frac{g_\chi E}{2\pi^2} \int_0^\infty {\rm d}|\tilde{\mathbf{p}}|\, |\tilde{\mathbf{p}}|^2 \langle v_{\rm Møl}\sigma_{\rm ann}\rangle_\theta \left[f_{\rm MB}(E) f_{\rm MB}(\tilde{E}) - f_\chi(E) f_\chi(\tilde{E}) \right] \tag{3.12}$$

with $\tilde{E} = \sqrt{\tilde{\mathbf{p}}^2 + m_\chi^2}$ and the azimuthally averaged annihilation cross section

$$\langle v_{\rm Møl}\sigma_{\rm ann}\rangle_\theta = \frac{1}{2}\int_{-1}^{1} {\rm d}\cos\theta\, v_{\rm Møl}\sigma_{\rm ann}\,. \tag{3.13}$$

Here, the Møller velocity is $v_{\rm Møl} = \sqrt{s(s-4m_\chi^2)}/(2E\tilde{E})$, with θ denoting the angle between the incoming momenta p_a and p_b. In contrast to the annihilation term, the elastic collision term

$$\begin{aligned}\hat{C}_{\rm el}[f_\chi] = \frac{1}{2g_\chi}\int & {\rm d}\Pi_b\, {\rm d}\Pi_1\, {\rm d}\Pi_2\, |\mathcal{M}_{\chi j\to\chi j}|^2 (2\pi)^4 \delta^{(4)}(p_a + p_b - p_1 - p_2) \\ & \times \left[f_\chi(p_1) f_\pm^{(j)}(p_2)(1 \mp f_\pm^{(j)}(p_b)) - f_\chi(p_a) f_\pm^{(j)}(p_b)(1 \mp f_\pm^{(j)}(p_2)\right]\end{aligned} \tag{3.14}$$

contains the unknown DM distribution function f_χ along with the equilibrium density $f_\pm^{(j)}$ of a SM particle j in both the loss and gain terms, significantly increasing the evaluation complexity of $\hat{C}_{\rm el}$ since there remain in general four integrals after imposing four-momentum conservation and using the rotational symmetry around the axis defined by the incoming momentum.

For this reason, the DM code DRAKE implements by default the scattering term through the Fokker-Planck type operator [78]

$$\hat{C}_{\rm FP}[f_\chi] = \frac{E}{2}\gamma(T)\left[TE\partial_{|\mathbf{p}|}^2 + \left(|\mathbf{p}| + 2T\frac{E}{|\mathbf{p}|} + T\frac{|\mathbf{p}|}{E}\right)\partial_{|\mathbf{p}|} + 3\right] f_\chi \tag{3.15}$$

in contrast to the full expression for $\hat{C}_{\rm el}$. This approximation is valid under the assumption of non-relativistic DM and if the momentum transfer is small compared to the DM mass. The elastic scattering matrix element enters through the momentum exchange rate

$$\gamma(T) = \frac{1}{48\pi^3 g_\chi m_\chi^3 T}\sum_j \int_{m_j}^\infty {\rm d}\omega\, f_\pm(\omega)[1 \mp f_\pm(\omega)]\left(|\mathbf{k}|^4 \langle |\mathcal{M}_{\chi j\to\chi j}|^2\rangle_t\right) \tag{3.16}$$

and is an integral over the energy $\omega = \sqrt{\mathbf{k}^2 + m_j^2}$ of the bath particle j. The averaged matrix element entering in Eq. (3.16) is given by

$$\langle |\mathcal{M}_{\chi j\to\chi j}|^2\rangle_t = \frac{1}{8|\mathbf{k}|^4}\int_{-4k_{\rm cm}^2}^0 {\rm d}t\,(-t)|\mathcal{M}_{\chi j\to\chi j}|^2, \tag{3.17}$$

where the lower integration limit is defined through the center-of-mass (c.m) momentum

$$k_{\text{cm}}^2 = \left(s - (m_\chi - m_j)^2\right)\left(s - (m_\chi + m_j)^2\right)/4s \tag{3.18}$$

evaluated at $s = m_\chi^2 + 2\omega m_\chi + m_j^2$. These are in principle the equations one has to solve but there are further assumptions that significantly simplify the evaluation. These are explained in the next sections.

3.3.2 The Standard Number Density Treatment

The standard procedure [79–81] of calculating the freeze-out abundance of a single relic particle is to reformulate the Boltzmann equation (3.4) as an equation for the dark matter number density n_χ. This achieved by integrating Eq. (3.4) over $g_\chi \, \mathrm{d}^3\mathbf{p}\,/(2\pi)^3$ such that only number-changing annihilation processes survive

$$\dot{n}_\chi + 3Hn_\chi = g_\chi \int \frac{\mathrm{d}^3\mathbf{p}}{(2\pi)^3} \hat{C}_{\text{ann}}[f_\chi]\,. \tag{3.19}$$

In order to evaluate the right hand side, the usual assumption is that the dark matter phase space density obeys a Maxwell-Boltzmann distribution function (2.17) with a temperature equal to the photon temperature, i.e., one makes the ansatz

$$f_\chi(E) = \frac{n_\chi}{\bar{n}_\chi^{\text{nr}}} f_{\text{MB}}(E, T, \mu = 0)\,, \tag{3.20}$$

where the bar on n_χ sets $\mu = 0$ in Eq. (2.18a). This ansatz is motivated by the fact that scattering processes between DM and SM particles happen at a rate much faster than DM annihilation processes since the relativistic SM number densities are not Boltzmann suppressed like n_χ. Under these assumptions, five out of the six integrals in Eq. (3.19) can be performed analytically, meaning that the evolution of the DM number density is described through the single Boltzmann equation

$$\dot{n}_\chi + 3Hn_\chi \;=\; \langle\sigma_{\text{ann}} v\rangle_T \left((\bar{n}_\chi^{\text{nr}})^2 - n_\chi^2\right), \tag{3.21}$$

which is effectively an evolution equation for the chemical potential $\mu_\chi = T \ln\!\left(n_\chi/\bar{n}_\chi^{\text{nr}}\right)$. The thermally averaged DM annihilation cross section into SM particles $\langle\sigma_{\text{ann}} v\rangle_T$ can be simply stated in terms of a single integral over the collision energy

$$\langle\sigma_{\text{ann}} v\rangle_T = \frac{1}{8 m_\chi^4 T K_2^2(m_\chi/T)} \int_{4m_\chi^2}^{\infty} \mathrm{d}s\, \sigma_{\chi\chi\to\text{SM}}(s) \sqrt{s}(s - 4m_\chi^2) K_1(\sqrt{s}/T)\,. \tag{3.22}$$

Today's DM relic density is then determined from the DM number density $n_\chi(T_\infty)$ long after freeze-out through

$$\Omega_\chi h^2 = \kappa \frac{n_\chi(T_\infty) m_\chi}{\rho_c/h^2} \frac{h_{\text{eff}}(T_0)}{h_{\text{eff}}(T_\infty)} \left(\frac{T_0}{T_\infty}\right)^3, \tag{3.23}$$

with $\kappa = 1(2)$ if χ is self-conjugate (non-self-conjugate), today's photon temperature T_0 and the photon temperature T_∞ long after freeze-out. More precisely, $T_\infty > T_0$ just denotes the end of the numerical integration routine.

3.3.3 The Fluid Dynamics Approach

The main assumption that enters in the standard number density treatment described above is that kinetic equilibrium is maintained until the end of chemical freeze-out, i.e., until DM number changing processes are no longer active. If this assumption is not met or one wants to test whether elastic scattering processes between the dark sector and the SM are efficient enough to keep both sectors in kinetic equilibrium, it is in principle necessary to solve the full Boltzmann equation (3.4) on the level of the phase space distribution function. However, as first pointed out in Ref. [82] an alternative to the computationally expensive momentum-dependent Boltzmann equation is to take a hydrodynamic approach and consider next to the zeroth momentum, which is nothing but the number density n_χ, additionally the second moment of Eq. (3.4) defined as

$$T_\chi = \left\langle \frac{|\mathbf{p}|^2}{3E} \right\rangle = \frac{g_\chi}{n_\chi} \int \frac{\mathrm{d}^3\mathbf{p}}{(2\pi^3)} \frac{|\mathbf{p}|^2}{3E} f_\chi(E). \tag{3.24}$$

This quantity can be thought of as a definition for the DM "temperature" T_χ. However, in order to close the Boltzmann hierarchy, this approach requires further assumptions on the DM phase space distribution function. The simplest approach it to assume that DM still has a Maxwellian shape $f_\chi \sim e^{-E/T_\chi}$ but with the photon temperature replaced with T_χ which also has the advantage that Eq. (3.24) becomes an identity. This leads to two coupled differential equations, one for n_χ and one for T_χ. These are

$$\frac{1}{Y_\chi}\frac{\mathrm{d}Y_\chi}{\mathrm{d}x} = \frac{sY_\chi}{x\tilde{H}} \left[\frac{(Y_\chi^{\mathrm{eq}})^2}{Y_\chi^2} \langle \sigma_{\mathrm{ann}} v \rangle_T - \langle \sigma_{\mathrm{ann}} v \rangle_{T_\chi} \right], \tag{3.25a}$$

$$\begin{aligned} \frac{1}{y}\frac{\mathrm{d}y}{\mathrm{d}x} = \frac{\langle \hat{C}_{\mathrm{el}} \rangle_2}{x\tilde{H}} &+ \frac{sY_\chi}{x\tilde{H}} \left[\langle \sigma_{\mathrm{ann}} v \rangle_{T_\chi} - \langle \sigma_{\mathrm{ann}} v \rangle_{2,T_\chi} \right] \\ &+ \frac{sY_\chi}{x\tilde{H}} \frac{(Y_\chi^{\mathrm{eq}})^2}{Y_\chi^2} \left[\frac{y_{\mathrm{eq}}}{y} \langle \sigma_{\mathrm{ann}} v \rangle_{2,T} - \langle \sigma_{\mathrm{ann}} v \rangle_T \right] + \frac{\tilde{g}}{x} \frac{\langle p^4/E^3 \rangle_{T_\chi}}{3T_\chi}, \end{aligned} \tag{3.25b}$$

where the number density is expressed through the yield $Y_\chi = n_\chi/s$ and the temperature through the dimensionless version $y = T_\chi m_\chi s^{-2/3}$ of the second momentum moment with $y_{\mathrm{eq}} = m_\chi T s^{-2/3}$ and $\tilde{H} = H/\tilde{g}$. The temperature subscript on the (thermal) averages indicates whether the SM or DM distribution is used to perform the average while a '2' as subscript refers to the additional appearance of $|\mathbf{p}|^2/3E$ in the averaging process. A more detailed discussion of the cBE approach as well as the precise definition of $\langle \sigma_{\mathrm{ann}} v \rangle_2$ and $\langle |\mathbf{p}|^4/E^3 \rangle_{T_\chi}$ is available in Refs. [83, 84]. Note that the elastic collision term does not drop out in the second moment in contrast to the zeroth moment but enters through the average

$$\langle \hat{C}_{\mathrm{el}} \rangle_2 = \frac{g_\chi}{n_\chi T_\chi} \int \frac{\mathrm{d}^3\mathbf{p}}{(2\pi)^3} \frac{|\mathbf{p}|^2}{3E} \hat{C}_{\mathrm{el}} \tag{3.26}$$

which simplifies to $\langle \hat{C}_{\mathrm{el}} \rangle_2 \to \gamma(T)(y_{\mathrm{eq}}/y - 1)$ for the Fokker-Planck approximation in Eq. (3.15), if the additional relativistic $\langle p^4/E^3 \rangle_{T_\chi}$ correction in $\hat{C}_{\mathrm{FP}}$ is neglected.

3.3.4 Uncertainties in the Estimation of the Freeze-Out Abundance

The calculation of the freeze-out abundance as presented in the previous sections and in particular the number density equation (3.21) come with different kinds of theoretical uncertainties or "missing pieces" that one should be aware of. These are briefly collected in the following:

- Uncertainties of the **SM effective number of degrees of freedom** g_{eff} and h_{eff} enter the estimation of the relic density through the Hubble rate. These uncertainties are relatively large in the region of the electroweak and the QCD crossover transition as these have to treated non-perturbatively using lattice methods. Building up on the previous calculations [76,85–88] of the SM equation of state (EoS), the authors of Ref. [89] compared different EoS estimates, finding that the EoS error induces an uncertainty of the dark matter abundance of almost 10 % for DM masses in the 1 to 1000 GeV region.

- Additionally, the **Hubble rate in the pre-BBN era** is in principle unknown since there could, e.g., be additional relativistic states that increase the expansion rate but are currently undetectable. To quantify the sensitivity of the DM abundance to a modified expansion rate, a temperature-dependent dark energy density of the form

$$\rho_D(T) = \rho_D(T_0)\left(\frac{T}{T_0}\right)^{n_D} \tag{3.27}$$

  was added as a new contribution to the Hubble rate in Ref. [90]. Depending on whether this energy density is supposed to mimic matter, radiation or a quintessence field, n_D takes one of the three values $\{3, 4, 6\}$. For two different exemplary SUSY models, it was found that even a small change in the expansion rate that otherwise leaves BBN in tact can increase the DM abundance by a factor of up to 10^6. Therefore, it is suggested to only use the measured relic density as an upper bound as it is already done in multi-component dark matter models. One possible way to probe the Hubble rate in the pre-BBN era and to remove this "uncertainty" is through gravitational waves from cosmic strings [91].

- **Multi-body final states** with more than two particles are usually neglected as these are in principle of higher-order and propagator suppressed. However, final states with a real and a virtual massive particle that subsequently decays like $WW^* \to Wf\bar{f}$ or $t\bar{t}^* \to tWb$ can become important at threshold. In the context of the MSSM, Ref. [92] found that the inclusion of such three-body final states can decrease the neutralino relic density by up to 10 %. Moreover, the addition of a third final-state particle can lift the helicity suppression of the anihilation of two Majorana dark matter particles into two SM fermions and therefore increase the annihilation rate by orders of magnitude [93].

- Into the same category fall **higher-order corrections** to the averaged annihilation cross section that also include a third massless gauge boson in the final state within the real emission contribution. The effect on the neutralino relic density of such corrections in the strong coupling will be discussed in more detail in Ch. 4 and lies generally also in the 10 % region. **Bound-state formation** can alter the relic density significantly as well [94,95].

- Moreover, already the usage of the number density Boltzmann equation (3.21) at NLO is problematic for two reasons. First, the additional Bose distribution function entering in the collision term for the real emission contribution is simply ignored since energy conservation for $2 \to 3$ processes no longer strictly enforces Maxwellian distribution functions. The same holds true for the Bose enhancement and Fermi blocking factors. Secondly, additional **finite-temperature effects** from the interaction of internal and external particles with the surrounding plasma are not accounted for as the collision term is derived from S-matrix elements. The second issue can be addressed by starting systematically from the framework of non-equilibrium QFT which will be introduced in Ch. 6 and such finite-temperature corrections will be computed explictly for neutrino scattering in the subsequent Ch. 7. However, Refs. [96–98] found that such finite-temperature corrections are for freeze-out additionally suppressed by several powers of T/m_χ compared to the vacuum corrections. To interpret this statement correctly, recall that freeze-out usually happens at temperatures $T \sim m_\chi/25$.

- The **early kinetic decoupling (eKD) effect** [83,99] describes the failure of the assumption of kinetic equilibrium leading to the number density Boltzmann equation (3.21) and can lead to an increase of the final DM relic density by more than an order of magnitude. The eKD effect for a forbidden DM model will be discussed in detail in Ch. 5.

3.4 Experimental Dark Matter Searches

Numerous experiments are carried out today to specifically search for (WIMP) dark matter. These searches can be generally classified into the three detection strategies: indirect and direct detection as well as production in accelerators. These will be briefly outlined in the following.

3.4.1 Indirect Detection

The detection of signatures from dark matter annihilation or decay into SM particles from distant locations is the central idea behind indirect searches. This means that earth- and satellite-based experiments look for fluxes of stable SM particles like photons, neutrinos, $e^\pm$, (anti)protons and (anti)deuterons that are either directly from the primary annihilation channel or result from the processes of decay, showering and hadronization of all intermediate unstable particles which is, e.g., the case for a quark-antiquark pair or weak gauge bosons in the final state. Even though a monochromatic γ-ray spectrum from the primary process $\mathrm{DM}\,\mathrm{DM} \to \gamma\,\gamma$, i.e., a γ-ray line, would be a “smoking gun” signal for dark matter, annihilations into photons are typically subdominant. Therefore, indirect searches most of the time focus on secondary particles with continuous energy spectra. Typical target regions of indirect detection experiments are those with a local dark matter overdensity as a result of gravitational accumulation or those with low astrophysical backgrounds compared to the expected signal. Example targets are the galactic center (GC), dwarf spheroidal galaxies (dSph), that are expected to be particularly rich in dark matter, celestial bodies like our sun or the center of the earth, or even the entire Universe by measuring a cosmological flux of γ-rays or neutrinos. An alternative to looking for signals from present-day dark matter annihilation or decay is to look at the imprint onto the CMB and BBN that dark matter annihilations would have.

Due to the non-observation of a conclusive positive dark matter signal, results of indirect searches are usually presented as limits on the thermally averaged annihilation cross section (or decay rate) into a particular SM final state, however, usually under the important assumptions of

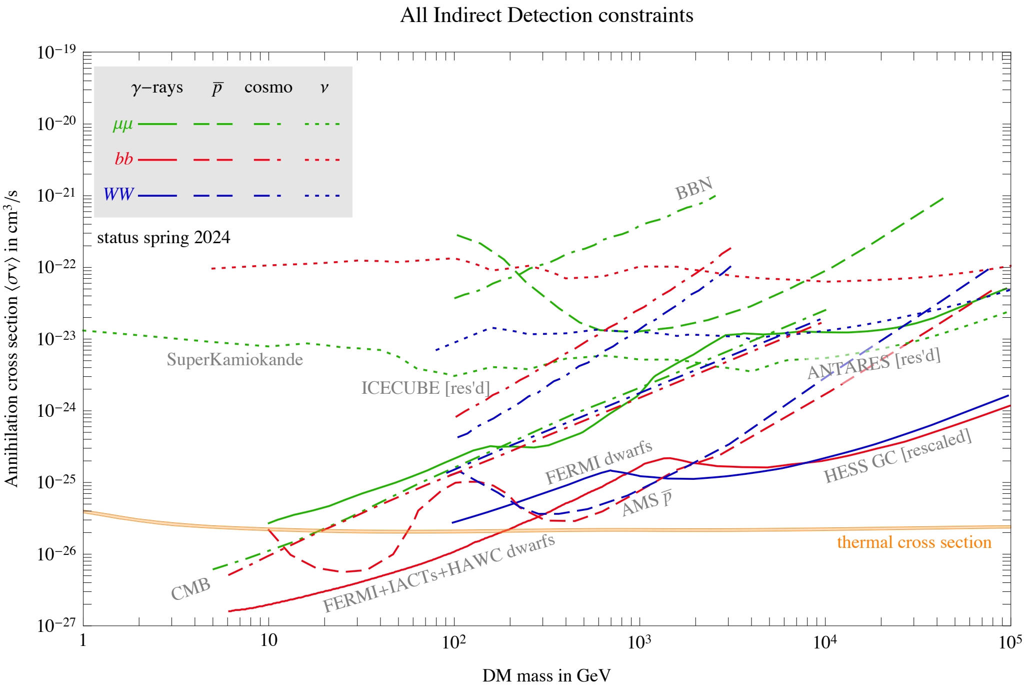

Figure 3.2: Summary of the latest most stringent limits on WIMP annihilations into $\mu^+\mu^-$ (green), $b\bar{b}$ (red) or W^+W^- (blue), from different searches. Some limits are rescaled with respect to the original publications to match a NFW profile. Also plotted is the thermal cross section $\langle\sigma v\rangle \approx 2.2 \times 10^{-26}\,\mathrm{cm}^3/\mathrm{s}$ that reproduces roughly the correct relic abundance. Figure taken from Ref. [27].

an s-wave dominated and therefore constant annihilation cross section and that DM annihilates 100 % of the time into the respective channel. Figure 3.2 summarizes the current most stringent bounds on weak-scale DM annihilations into $\mu^+\mu^-$, $b\bar{b}$ and W^+W^- from different observatories and search strategies. In more detail, the limits come form the ground-based γ-ray telescopes H.E.S.S. [100], VERITAS [101] and MAGIC [102] that are collectively referred to as imaging atmospheric Cherenkov telescopes (IACTs) in the plot and that work with mirror telescopes to directly detect the Cherenkov light that is produced when an energetic cosmic ray enters the atmosphere. The future CTA experiment, for example, also belongs into this category and aims to improve existing limits by an order of magnitude [103]. These limits are supplemented by observations with the satellite-based gamma-ray telescope Fermi-LAT [104] and the HAWC [105] experiment which in contrast to the IACTs works with water tanks and photomultiplier tubes to detect the Cherenkov radiation. The combined limit in Fig. 3.2 was published in Ref. [106]. For completeness, one should mention that the IACTs perform of course line searches from dark matter annihilation as well, see, e.g., Refs. [107, 108]. Limits from charged cosmic rays are also obtained with the AMS-02 [109] experiment which is mounted to the International Space Station (ISS). Here, in particular antiprotons and antideuterons are excellent probes of dark matter as the observable Universe consists of only very little antimatter compared to matter. Lastly, the current best constrains from the neutrino observatories IceCube [110] at the south pole, Super-Kamiokande [111] in the Kamioka mine in Japan and ANTARES [112] in the Mediterranean Sea are shown as well. These limits are comparably by one to two orders of magnitude weaker due to the elusive nature of the neutrino. However, neutrinos have therefore the advantage that the origin of the signal can

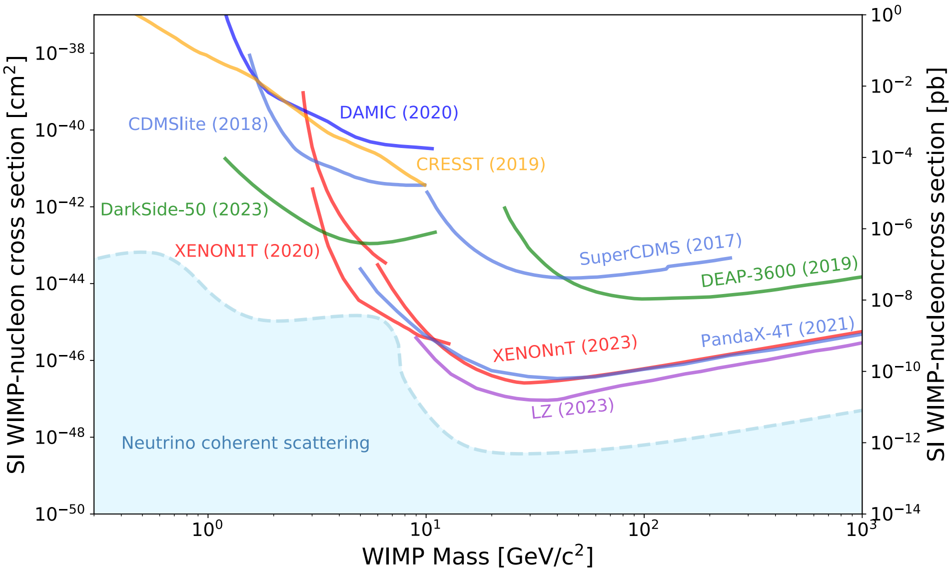

Figure 3.3: Current upper limits on the spin-independent DM-nucleon cross section as a function of the dark matter mass from different direct detection experiments. Figure taken from Ref. [116].

be easily reconstructed while charged cosmic rays are deflected in intergalactic magnetic fields. Planned successor experiments are KM3NeT [113] for ANTARES, Hyper-Kamiokande [114] for Super-Kamiokande and PINGU [115] for IceCube.

3.4.2 Direct Detection

The basic idea of direct detection is to search for electron or nuclear recoil events in terrestrial detectors from the (in)elastic scattering of dark matter with atoms in a at best background free target material, of course under the assumption of a non-negligible local dark matter density which is usually taken to be $\rho_0 = 0.3\,\mathrm{GeV/cm^3}$ [118]. Typical target materials are on the one hand nobel gases like xenon or argon and on the other hand semiconductors like germanium or silicon. In most direct detection experiments, information about the recoil and the energy deposited in the detector is obtained via two of the following three remnants of the recoil which are scintillation light, phonons (heat) or electrons from the ionization of the detector material. As these different probes of dark matter scattering inside the detector are sensitive in different energy regions and to distinguish best between background and an actual signal, two signal channels are usually employed while using all three has been technically challenging so far. An exception is, e.g., the PICO experiment which makes use of a bubble chamber filled with halocarbons.

Due to the lack of a discovery so far, direct detection experiments usually present their results as limits on the spin-independent (SI) and spin-dependent (SD) dark matter nucleon scattering cross section. As an example, the latest results on the SI cross section from the xenon based experiments PandaX-4T [119], XENON1T [120], XENONnT [121], LUX-ZEPLIN (LZ) [122] and the argon based experiments DarkSide-50 [123] and DEAP-3600 [124] are displayed in Fig. 3.3. Additionally shown are the limits from the detectors SuperCDMS [125], CDMSlite [126], DAMIC [127] and CRESST [128] that use semiconductors as targets. Also displayed is the “neutrino floor” which is the parameter region where direct detection experiments become sensitive to coherent elastic

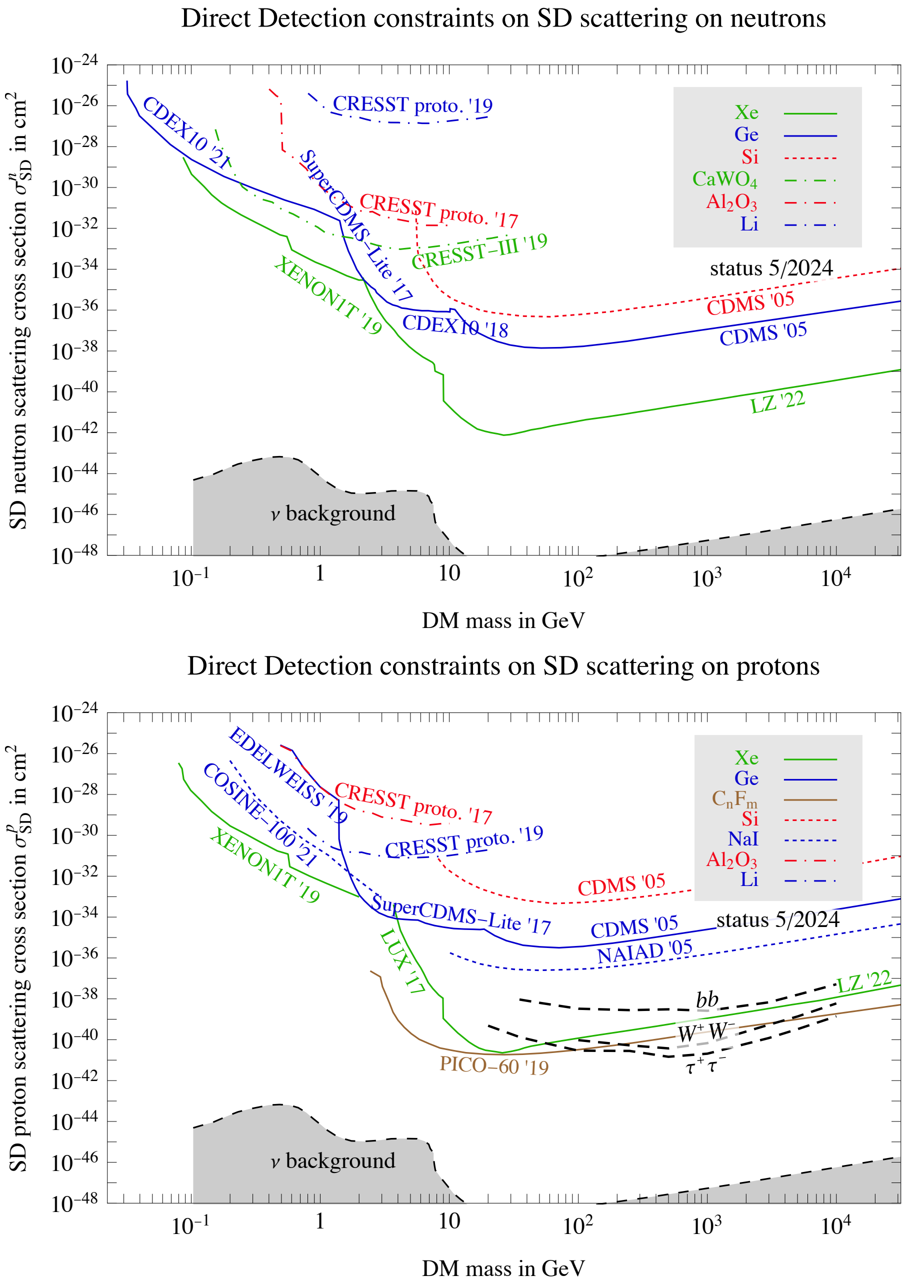

Figure 3.4: As in Fig. 3.3, but for the spin-dependent cross section on neutrons (top) and on protons (bottom). Also shown are the indirect detection limits from IceCube [117] as black dashed lines along with the DM annihilation channels that produce the neutrinos in the Sun. Figures taken from Ref. [27].

neutrino-nucleus scattering (CEνNS). This means that neutrinos with an astrophysical origin like those from the fusion processes inside the sun become an irreducible background in direct dark matter searches. This is also the sensitivity that future direct detection experiments like DARWIN [129] want to achieve. One possibility to circumvent this so-called "neutrino fog" is to try to gather additionally information on the direction of the dark matter flux. One proposal for such a directional dark matter detector is the CYGNUS-1000 [130] experiment.

The current best limits on the spin-dependent direct detection cross section for scattering on protons and neutrons are shown in Fig. 3.4. These come from the experiments LZ [122], Xenon1T [131], CRESST [132, 133], EDELWEISS [134], CRESST-III [128], CDEX10 [135, 136], CDMS [137], SuperCDMS-Lite [138], NAIAD [139], COSINE-100 [140] and PICO-60 [141]. Interestingly, the most stringent limit on the SD cross section still comes from indirect detection, namely from the non-observation of neutrinos produced within dark matter annihilation processes in the sun with the IceCube detector [117].

In addition, one can search for an annual modulation of the recoil signal caused by the change of the earth's relative velocity with respect to the galactic dark matter halo due to its orbit around the sun. The DAMA/LIBRA [142] collaboration claims to have observed such an annual modulation. However, the dark matter interpretation of the observed signal is not compatible with other dark matter search experiments like COSINE-100 as the region in the σ^{SI} versus WIMP mass plane that can accommodate such a signal has already been excluded [143].

3.4.3 Accelerator Searches

The production of dark matter at collider and fixed-target experiments represents the third possible method to search for DM and examine its properties. Compared to direct and indirect detection, accelerator searches have the main advantage of being free from astrophysical uncertainties like the (local) DM number density but are on the downside most of the time severely model-dependent. One important exception is the model-independent limit from LEP on long-lived scalars and fermions carrying an electric charge $|Q/e| = 1$ whose masses are constrained to be heavier than 100 GeV [144]. This limit applies indirectly do dark matter through, e.g., the coannihilation partner of the DM particle. One possibility to still keep collider analyses as model independent as possible is to work on the level of effective field theories or simplified models that include the "mediator" as additional degree of freedom of the theory [145].

There are now generally multiple search strategies in accelerator settings but the most common ones feature missing energy, resonances in the invariant mass spectrum, displaced vertices or involve the Higgs sector. All of these signatures are, e.g., an integral part of the dark matter searches conducted with the general-purpose detectors ATLAS [146] and CMS [147] at the LHC.

- **Mono-X searches** in colliders look for large missing transverse energy $\not{E}_T$ (MET) along with a SM particle X from either the initial or final state that recoils against the undetected system, where X could be a photon, W- or Z-boson, a SM-Higgs h or a jet. The idea is that DM particles just escape the detector due to their small interaction strength and therefore carry away some transverse momentum p_T but since the initial particles collide collinearly this missing energy must be precisely contained in the sum of the momenta of the detected final states like X. However, SM neutrinos lead to the same signature of missing p_T and therefore any excess in $\not{E}_T$ has to be carefully disentangled from the SM background.

- **Resonant searches** look for a peak above the expected SM background in the invariant mass spectrum of two visible SM final states. Di-jets and dileptons are here particularly sensitive search channels.
- **Higgs sector searches** look for dark matter that is produced in the decay of a Higgs boson and therefore enhances the Higgs to invisible decay width. ATLAS and CMS reported then the important model-independent limit

$$\mathrm{Br}(h \to \mathrm{inv}) \leq \begin{cases} 0.145, & \text{ATLAS [148]} \\ 0.18, & \text{CMS [149]} \end{cases} . \tag{3.28}$$

While hadron colliders like Tevatron and the LHC are good at providing limits on weak-scale DM, important limits on light dark matter (LDM) with masses ranging from a few hundred MeV to 10 GeV come from the e^+e^- machines BaBar and Belle II as well as experiments like E137 [150] or NA62 [151] that can run in a beam-dump mode. Such limits on LDM are discussed in more detail in Ch. 5 in the context of a forbidden DM model. Future electron-positron colliders like FCC-ee [152], ILC [153], CEPC [154] would allow to further scrutinize dark matter indirectly through, e.g., more precise measurements of the Higgs potential or the Z-decay width, while a future hadron collider like FCC-hh [155] or a 10 TeV muon collider [156] could directly produce dark matter pairs.

Chapter 4

SUSY-QCD Corrections to Neutralino Dark Matter in the MSSM

The sub-percent accuracy of the dark matter relic density measurement by Planck in Eq. (3.2c), clearly calls for the evaluation of the dark matter annihilation cross sections beyond the tree-level approximation to match the experimental and theoretical uncertainty. The impact of higher-order corrections to DM annihilation in the context of the relic density, both strong and electroweak, has already been discussed within many well-motivated and intensely studied extensions of the SM such as the MSSM [157–171], the NMSSM [172,173], or the Inert Doublet Model [174,175]. In addition, it has been shown that the relic density can potentially receive large corrections from non-perturbative effects like the Sommerfeld enhancement coming from the exchange of light mediators between the annihilating particles [176–178] or the formation of bound-states [94, 95, 179–181]. Besides the increased precision, a further advantage of full loop calculations is that they allow for a systematical evaluation of the theoretical uncertainties from missing higher-order corrections through variations of the renormalization scheme as well as the renormalization scale [170, 182].

The need for an increased theoretical precision extends to the calculation of indirect detection signals from present-day DM annihilation processes [168, 183–186] as well as to DM-nucleon interactions in the context of direct DM detection. Calculations of higher-order corrections to the corresponding scattering cross sections have been computed in many UV-complete models like the MSSM [187–193], the Inert Doublet Model [194, 195], simple Higgs-portal models [196–199], the Next-to-Minimal Two Higgs Doublet Model [200], a vector DM model [201], the Singlet-Extended Two Higgs Doublet Model [202], but also in simplified fermionic DM models [203–205], or frameworks described through effective operators [206, 207].

In contrast, public tools for the (automated) calculation of the DM relic density such as DarkSUSY [208,209], SuperIso Relic [210–212], MicrOMEGAs [213–216] or MadDM [217,218] only take into account tree-level cross sections which, however, are in some cases improved through effective couplings to capture at least some higher-order effects. Therefore, the main objective of this chapter is to present the necessary theoretical background and techniques for calculating higher-order corrections to DM annihilation, all in the context of the high-energy code DM@NLO, a package designed for the precision calculation of dark matter (co)annihilation cross-sections and elastic dark matter-nucleon scattering amplitudes in the MSSM at next-to-leading order in the strong coupling α_s. After a brief review of the MSSM and established technical details related to NLO calculations in Secs. 4.1 and 4.2, a generalization of the Catani-Seymour dipole subtraction method for massive initial-particles is worked out in Sec. 4.3 which has been one bottleneck in the automation of NLO corrections so far besides the automated inclusion of a stable renormalization scheme. As an example, the calculation of the $\mathcal{O}(\alpha_s)$ corrections to the processes

$$\tilde{t}_1\tilde{t}_1^* \longrightarrow gg\,, \tag{4.1a}$$

$$\tilde{t}_1\tilde{t}_1^* \longrightarrow q\bar{q}\,, \tag{4.1b}$$

including the Sommerfeld enhancement effect are presented in Sec. 4.4 as the most recent addition to DM@NLO, where $q \in \{u, d, c, s\}$ denote effectively massless quark flavors at the energy scale of neutralino annihilation. These two processes are treated simultaneously since they are separate at tree level but have to be merged into one at NLO accuracy in order to obtain an infrared safe cross section. The user interface to DM@NLO is presented in Sec. 4.5 while Sec. 4.6 provides a brief summary.

4.1 Supersymmetry, the MSSM and Neutralino Dark Matter

At this point, it is instructive to briefly introduce the main idea behind supersymmetry [219, 220] along with the particle content of the MSSM. For more detailed and comprehensive discussions, in particular a list of other motivations for SUSY besides dark matter like the hierarchy problem [221], i.e., the stabilization of the Higgs mass against radiative corrections, or the natural unification of the strong and the electroweak force at an energy scale $\Lambda_{\mathrm{GUT}} \sim 10^{16}\,\mathrm{GeV}$ in the MSSM, the standard textbooks [222, 223] and review articles [55, 224, 225] should be consulted.

4.1.1 The Supersymmetry Algebra

With the success of relativistic (gauge) quantum field theories to describe elementary particles, the idea of supersymmetry grew out of the pursuit to combine in a non-trivial way the external spacetime symmetries given by the Poincaré group with internal symmetries like, e.g., the global SU(3) flavor symmetry. Mathematically, the combination proceeds through the introduction of a "Lie superalgebra" which, in the simplest case, is based on two anticommuting generators Q_α and $\bar{Q}_{\dot{\alpha}}$ that obey the anticommutation relations

$$\{Q_\alpha, Q_\beta\} = \{\bar{Q}_\alpha, \bar{Q}_\beta\} = 0\,, \tag{4.2a}$$

$$\{Q_\alpha, \bar{Q}_{\dot{\alpha}}\} = 2(\sigma^\mu)_{\alpha\dot{\alpha}}P_\mu \tag{4.2b}$$

involving the generator P_μ of spacetime translations and the Pauli four-vector σ^μ. This is in contrast to the ordinary commuting generators of a Lie algebra. As already suggested through the van der Waerden notation, the two supersymmetry generators transform as two-component Weyl spinors under the Lorentz group and obey the commutation rules

$$[M^{\mu\nu}, Q_\alpha] = (\sigma^{\mu\nu})_\alpha{}^\beta Q_\beta\,, \tag{4.3a}$$

$$\left[M^{\mu\nu}, \bar{Q}^{\dot{\alpha}}\right] = (\bar{\sigma}^{\mu\nu})^{\dot{\alpha}}{}_{\dot{\beta}} Q_{\dot{\beta}} \,, \tag{4.3b}$$

with the generators $M_{\mu\nu}$ of the Lorentz group. Due to the fermionic nature of the SUSY generators, one must, at least schematically, have

$$Q\,|\text{fermion}\rangle = |\text{boson}\rangle \ , \tag{4.4a}$$

$$Q\,|\text{boson}\rangle = |\text{fermion}\rangle \ , \tag{4.4b}$$

to preserve the right anticommutation relations as required by the spin-statistics theorem. This means that, under SUSY, fermions transform into bosons and vice versa. Particles that emerge from each other through SUSY operators are called "superpartners" and are therefore considered to be part of the same "supermultiplet". The remaining commutation relations

$$[Q_\alpha, P_\mu] = \left[\bar{Q}_{\dot{\alpha}}, P_\mu\right] = 0 \,, \tag{4.5}$$

have the important consequence the all particles within the same supermultiplet must possess the same mass, meaning that, if SUSY should be realized in nature, it must be broken, since for instance a scalar superpartner of the electron would have already been experimentally verified if it existed.

4.1.2 Particle Content of the MSSM

The R-parity conserving MSSM is the minimal supersymmtric extension of the Standard Model, incorporating one set, $\mathcal{N} = 1$, of SUSY generators as well as an additional discrete $\mathbb{Z}_2$ symmetry called R-parity that was originally introduced to avoid lepton or baryon number violating processes that are subject to stringent experimental constraints but are allowed by the principles of supersymmetry, gauge invariance, and renormalizability. The corresponding conserved multiplicative quantum number is defined as

$$P_R = (-1)^{3(B-L)+2s} \ , \tag{4.6}$$

where B is the baryon number, L the lepton number and s the spin. R-parity has the significant phenomenological consequence that each Standard Model particle has R-parity $+1$, while each supersymmetric particle (sparticle) has R-parity -1. This prevents sparticles from decaying solely into Standard Model particles, thus allowing for a stable dark matter candidate.

In the MSSM, each helicity state of a fermion receives a scalar superpartner, which differs from its Standard Model counterpart only in spin, meaning that the SM quarks q have as superparners the spin-0 and color charged squarks $\tilde{q}$ and that the superpartners of the charged SM leptons l are the spin-0 sleptons $\tilde{l}$ without any color charge. Correspondingly, SM neutrinos ν have the sneutrinos $\tilde{\nu}$ as superpartners. Similarly, all the SM gauge bosons have a Majorana fermion as superpartner, the gauginos: the bino $\tilde{B}$, winos $\tilde{W}^{\pm}$, $\tilde{W}^0$, and gluinos $\tilde{g}$.

Unlike the Standard Model, the MSSM includes two Higgs doublets, H_u and H_d, instead of one, leading to five physical Higgs bosons: two neutral CP-even h^0 and H^0, one neutral CP-odd A^0, and two charged $H^{\pm}$ Higgs bosons. This Two-Higgs-Doublet structure is necessary to avoid quantum-level inconsistencies due to gauge anomalies in the electroweak sector. The doublet H_u, with hypercharge $Y = +1/2$, gives mass to the up-type quarks, while the other one H_d, with

$Y = -1/2$, gives mass to down-type quarks and charged leptons. The fermionic superpartners of the Higgs bosons are called Higgsinos. The four neutralinos $\tilde{\chi}_i^0$, $i = 1, \ldots, 4$, are finally the admixtures of the neutral gauginos $\tilde{B}$, $\tilde{W}^0$, $\tilde{H}_u^0$ and $\tilde{H}_d^0$, connected through the mixing matrix Z, and the charginos $\tilde{\chi}_{1,2}^{\pm}$ are their charged analogue.

As already mentioned, the commutation relation (4.5) implies that particles within the same supermultiplet must have identical masses. However, since no superpartners have been observed experimentally, it suggests that SUSY must be broken. There is no consensus on the specific mechanism of SUSY breaking, but the general idea is that it occurs in a hidden sector and is transmitted to the visible sector via a messenger, which could be gravity or a gauge force. Practically, the simplest way to break SUSY is by adding extra terms to the effective MSSM Lagrangian that explicitly break SUSY. These terms must be "soft" in the sense that they should still allow the cancellation of fermionic and bosonic loop corrections to the Higgs mass.

According to the Supersymmetry Parameter Analysis (SPA) convention [226], the agreed form of the soft SUSY breaking Lagrangian is:

$$\begin{aligned}
-\mathcal{L}_{\text{soft}} =& \frac{1}{2}\left(M_1 \tilde{B}\tilde{B} + M_2 \tilde{W}\tilde{W} + M_3 \tilde{g}\tilde{g} + \text{h.c.}\right) + \tilde{Q}_{iL}^* \left(m_{\tilde{Q}}^2\right)_{ij} \tilde{Q}_{jL} + \tilde{L}_{iL}^* \left(m_{\tilde{L}}^2\right)_{ij} \tilde{L}_{jL} \\
&+ \tilde{u}_{iR}^* \left(m_{\tilde{u}}^2\right)_{ij} \tilde{u}_{jR} + \tilde{d}_{iR}^* \left(m_{\tilde{d}}^2\right)_{ij} \tilde{d}_{jR} + \tilde{e}_{iR}^* \left(m_{\tilde{e}}^2\right)_{ij} \tilde{e}_{jR} \\
&+ m_{H_d}^2 \left|H_d\right|^2 + m_{H_u}^2 \left|H_u\right|^2 - \left(B\mu H_d \cdot H_u + \text{h.c.}\right) \\
&+ \left[\left(T_u\right)_{ij} H_u \cdot \tilde{Q}_{iL} \tilde{u}_{jR}^* + \left(T_d\right)_{ij} H_d \cdot \tilde{Q}_{iL} \tilde{d}_{jR}^* + \left(T_e\right)_{ij} H_d \cdot \tilde{L}_{iL} \tilde{e}_{jR}^* + \text{h.c.}\right] ,
\end{aligned} \tag{4.7}$$

where the T matrices are defined as the product of Yukawa couplings Y and the soft SUSY breaking trilinear couplings A, i.e., $T_{ij} = A_{ij} Y_{ij}$ without any summation. In Eq. (4.7), only generational indices are explicitly shown, while all others are implicitly summed over. Unlike unbroken SUSY, where only the supersymmetric higgsino mass term μ is an additional parameter, the soft SUSY breaking introduces a total of 105 new free parameters in addition to the 19 free parameters already present in the Standard Model Lagrangian such that it is almost impossible to explore the MSSM parameter space in full generality. For this reason, more constrained versions of the MSSM parameter space based on strong experimental evidence are used. The most general one is the phenomenological MSSM (pMSSM) with 19 free parameters, the so-called pMSSM-19, which is based on the assumptions [227] of (1) no additional flavor changing neutral currents, (2) no new sources of CP-violation and (3) identical soft-SUSY breaking scalar mass terms for the first two generations known as first and second generation universality. These assumptions leave the following 19 free parameters:

- The ratio of the two vevs of the two Higgs doublets: $\tan(\beta)$
- The bino, wino and gluino mass parameters: M_1, M_2, M_3
- The trilinear couplings of the third generation: A_t, A_b, A_τ
- The higgsino mass parameter: μ
- The pole mass of the pseudoscalar Higgs boson: m_{A^0}
- The soft slepton masses: $M_{\tilde{l}_L}$, $M_{\tilde{\tau}_L}$, $M_{\tilde{l}_R}$, $M_{\tilde{\tau}_R}$
- The soft squark masses: $M_{\tilde{q}_L}$, $M_{\tilde{u}_R}$, $M_{\tilde{d}_R}$, $M_{\tilde{q}_{3L}}$, $M_{\tilde{t}_R}$, $M_{\tilde{b}_R}$

4.1.3 Standard Computation of the Neutralino Relic Density

The standard procedure [81] of calculating the abundance of neutralino dark matter in the MSSM is based on the assumptions that all sparticles (i) eventually decay to the lightest neutralino (ii) are in kinetic equilibrium with the SM thermal bath due to sufficiently large elastic scattering rates, (iii) share the same chemical potential and (iv) are highly non-relativistic so that in-medium as well as finite-temperature effects are negligible. The latter means in particular that even for the annihilation of two SUSY particles into n SM particles, all bath particles are assumed to obey a Maxwell-Boltzmann distribution. Under these assumptions, the evolution of the neutralino number density is also described through the single Boltzmann equation (3.21) but where the thermally averaged annihilation cross section is now composed out of all all possible $2 \to n$ (co)annihilation channels of sparticles into a set X of n SM particles,

$$\langle \sigma_{\text{ann}} v \rangle \;=\; \sum_{a,b} \langle \sigma_{ab\to X} v \rangle \frac{\bar{n}_a^{\text{nr}}}{\bar{n}_\chi^{\text{nr}}} \frac{\bar{n}_b^{\text{nr}}}{\bar{n}_\chi^{\text{nr}}} \,. \tag{4.8}$$

For two different initial particles, the thermal average (3.22) can also be cast into a single integral over the energy $\sqrt{s} = \sqrt{m_a^2 + p_{\text{cm}}^2} + \sqrt{m_b^2 + p_{\text{cm}}^2}$ with p_{cm} being the relative center of mass momentum,

$$\langle \sigma_{ab\to X} v \rangle = \frac{1}{2\,T\, m_a^2 m_b^2\, K_2(m_a/T)\, K_2(m_b/T)} \int \mathrm{d}s\, \sqrt{s}\, p_{\text{cm}}^2 \sigma_{ab\to X}(p_{\text{cm}}) K_1(\sqrt{s}/T)\,. \tag{4.9}$$

Here, it is important to recall Eq. (2.19) showing that non-relativistic equilibrium number densities are exponentially suppressed

$$\frac{n_a^{\text{nr}}}{n_\chi^{\text{nr}}} \sim \exp\biggl(-\frac{m_a - m_\chi}{T}\biggr) \tag{4.10}$$

with the direct consequence that besides pure neutralino annihilation only those processes contribute significantly to $\langle \sigma_{\text{ann}} v \rangle$ with a small mass difference between the neutralino and the co-annihilation partner.

4.2 Dark Matter Annihilation Beyond Tree Level

At NLO, the tree-level DM (co)annihilation cross-section σ^{Tree} is extended by the contribution

$$\Delta\sigma^{\text{NLO}} \;=\; \int_m \mathrm{d}\sigma^{\text{V}} + \int_{m+1} \mathrm{d}\sigma^{\text{R}} \;, \tag{4.11}$$

which contains virtual ($\mathrm{d}\sigma^{\text{V}}$) and real ($\mathrm{d}\sigma^{\text{R}}$) corrections, contributing at the same order in the coupling constant, which, in the context of DM@NLO, are one-loop corrections in SUSY-QCD at order α_s, including the emission of a real gluon. The integration domain of the integrals refers to the number of final-state particles.

4.2.1 Regularization

The virtual corrections are plagued by ultraviolet divergences whose removal requires a (numerically well behaved) renormalization scheme, coming along with a suitable regularization prescription. Besides schemes like Pauli-Villars regularization [228], lattice regularization [229] or the obvious solution of introducing a cutoff in the UV [230], the most favored regularization methods for non-Abelian gauge theories are dimensional schemes [231] due to their advantage of preserving not only Lorentz invariance but also gauge invariance as well as unitarity. Here, the underlying idea is to use the dimension as regularization parameter by analytically continuing loop integrals to a complex number of dimensions $D = 4 - 2\varepsilon$ through the replacement

$$\int \frac{\mathrm{d}^4 q}{(2\pi)^4} \to \mu^{2\varepsilon} \int \frac{\mathrm{d}^D q}{(2\pi)^D} \tag{4.12}$$

of the integration measure. The renormalization scale μ with mass dimension $[\mu] = 1$ is introduced to ensure that the mass dimension of the integrals remains unchanged. As a consequence of Eq. (4.12) divergences manifest themselves as poles in ε in the complex plane. In more detail, at NLO, UV, soft and collinear divergences take the form of simple $1/\varepsilon$ poles, whereas soft-collinear divergences appear as double poles.

In D dimensions, the Dirac γ-matrices are kept four-dimensional by definition $\mathrm{Tr}\left(\gamma^\mu \gamma^\nu\right) = 4\eta^{\mu\nu}$ but Lorentz indices take values from zero to $D-1$ such that the components of a momentum vector become

$$q^\mu = (q^0, q^1, \ldots, q^{D-1}) \,. \tag{4.13}$$

However, mapping a vector boson with $D-2$ degrees of freedom under supersymmetry transformations (4.4) to a Majorana spinor with two degrees of freedom is obviously not consistent [232]. For this reason, there exist by now two main dimensional schemes for the calculation of matrix elements at one-loop order, which are dimensional regularization and dimensional reduction, where the latter was designed to avoid the aforementioned mismatch between fermionic and bosonic degrees of freedom in supersymmetric theories. Both have in common that the number of dimensions of all momenta and spacetime coordinates is analytically continued to $D \neq 4$ dimensions as in Eq. (4.12) but differ in the precise definition of the dimensionality of "internal" and "external" vector bosons. Internal gauge bosons are defined as those that appear in one-particle irreducible (1PI) diagrams of the virtual corrections or that become soft or collinear in a phase space integrals related to the real corrections. External gauge bosons are then defined as all other gauge bosons. In order to formulate the different treatments of internal and external gauge fields without mathematical inconsistencies [233], three different spaces are introduced: the original four-dimensional space (4S), the quasi-four-dimensional space (Q4S), the quasi-D-dimensional space (QDS) as a subspace of Q4S and the remainder QεS through Q4S = QDS $\oplus$ QεS [234, 235]. Following the definitions in Ref. [236], each of the two main schemes has two subvariants. For dimensional regularization these are:

- **Conventional dimensional regularization (CDR)**: Internal and external gauge bosons are treated as D-dimensional.
- **'t Hooft-Veltman scheme (HV)**: External gauge bosons liven in 4S whereas internal ones are D-dimensional.

The two variants of dimensional reduction on the other hand are:

- **Original dimensional reduction (DRED or DR)**: Internal and external gauge bosons are elements of Q4S.

- **Four-dimensional helicity scheme (FDH)**: External gauge bosons are strictly four-dimensional whereas internal ones are quasi-four-dimensional.

For explicit calculations, it is convenient to capture the scheme-dependent terms through the number of helicity states of internal gauge bosons as $h_g^{\mathrm{RS}} = 2(1 - \varepsilon + r\varepsilon)$. The parameter r is defined as

$$r = \begin{cases} 0, \text{ CDR, HV} \\ 1, \text{ DRED, FDH} \end{cases} \tag{4.14}$$

and allows to distinguish between the different schemes. Practically, the r-dependence enters through traces of the metric tensors which evaluate either to four or D. As DM@NLO was initially designed with only supersymmetric theories in mind, it employs the SUSY-preserving dimensional reduction schemes. In dimensional schemes, however, the treatment of γ^5 is quite peculiar. The problem is that the two γ^5-relations

$$\mathrm{Tr}\left(\gamma^\mu\gamma^\nu\gamma^\rho\gamma^\sigma\gamma^5\right) = 4i\varepsilon^{\mu\nu\rho\sigma}\,, \tag{4.15a}$$

$$\left\{\gamma^5, \gamma^\mu\right\} = 0 \tag{4.15b}$$

valid in four-dimensional spacetimes are incompatible with each other in $D \neq 4$ dimensions [237]. The following two approaches have been developed to circumvent this issue:

- The **t'Hooft-Veltman-Breitenlohner-Maison (HVBM) scheme** [238] defines γ^5 as an element of 4S and, as a result, retains the trace (4.15a).
- In the **naive scheme (NS)**, the anti-commutation relation (4.15b) of γ^5 with all other γ-matrices is kept causing, however, a vanishing trace of γ^5 with any number of γ-matrices.

The HVBM scheme has for supersymmetric theories like the MSSM the disadvantage that SUSY is already broken at the one-loop level [235]. Therefore, the naive scheme is the preferred scheme in the context of regularization via dimensional reduction.

4.2.2 Scalar n-Point Functions and Passarino-Veltman Reduction

A central method for the calculation of one-loop integrals within dimensional schemes is the Passarino-Veltman reduction [239, 240]. The starting point is that a general one-loop integral

$$T^N_{\mu_1,\dots,\mu_M}\left(p_1,\dots,p_{N-1},m_0,\dots,m_{N-1}\right) = \frac{(2\pi\mu)^{2\varepsilon}}{i\pi^2}\int \mathrm{d}^D q \frac{q_{\mu_1}\cdots q_{\mu_M}}{\mathcal{D}_0\mathcal{D}_1\cdots\mathcal{D}_{N-1}} \tag{4.16}$$

with $N \leq 4$ propagators

$$\mathcal{D}_0 = q^2 - m_0^2 + i\epsilon \tag{4.17a}$$

$$\mathcal{D}_1 = (q + p_1)^2 - m_1^2 + i\epsilon \tag{4.17b}$$

$$\dots \tag{4.17c}$$

$$\mathcal{D}_{N-1} = (q + p_{N-1})^2 - m_{N-1}^2 + i\epsilon \tag{4.17d}$$

in the denominator and M loop momenta $q_{\mu_1},\dots,q_{\mu_M}$ in the numerator can be systematically reduced to four scalar ($M = 0$) integrals which are commonly relabelled via $T^1 \to A_0$, $T^2 \to B_0$,

$T^3 \to C_0$ and $T^4 \to D_0$. Their argument sets are defined as

$$A_0(m_0^2) = \int_q \frac{1}{\mathcal{D}_0} \,, \tag{4.18a}$$

$$B_0(p_1^2, m_0^2, m_1^2) = \int_q \frac{1}{\mathcal{D}_0 \mathcal{D}_1} \,, \tag{4.18b}$$

$$C_0(p_1^2, (p_1 - p_2)^2, p_2^2, m_0^2, m_1^2, m_2^2) = \int_q \frac{1}{\mathcal{D}_0 \mathcal{D}_1 \mathcal{D}_2} \,, \tag{4.18c}$$

$$D_0(p_1^2, (p_2 - p_1)^2, (p_3 - p_2)^2, p_3^2, p_2^2, (p_3 - p_1)^2, m_0^2, m_1^2, m_2^2, m_3^2) = \int_q \frac{1}{\mathcal{D}_0 \mathcal{D}_1 \mathcal{D}_2 \mathcal{D}_3} \tag{4.18d}$$

with the shorthand notation

$$\int_q = \frac{(2\pi\mu)^{2\varepsilon}}{i\pi^2} \int \mathrm{d}^D q \,. \tag{4.19}$$

As an example, the evaluation of the simplest scalar integral with only one propagator proceeds through a Wick rotation and reads

$$A_0(m^2) = m^2 \left(\Delta - \ln\left(\frac{m^2}{\mu^2}\right) + 1 + \mathcal{O}(\varepsilon) \right) \,, \tag{4.20}$$

where the UV pole is contained in the abbreviation $\Delta = \frac{1}{\varepsilon} - \gamma_E + \ln 4\pi$ with the Euler–Mascheroni constant $\gamma_E \approx 0.577\,21$. The computation of a tensor integral is then performed by considering all symmetric and covariant tensor structures of rank M that can be built out of the momenta $p_1, \ldots, p_{N-1}$ and metric tensors, i.e., one performs the decomposition

$$B^\mu = p_1^\mu B_1 \tag{4.21a}$$

$$B^{\mu\nu} = \eta^{\mu\nu} B_{00} + p_1^\mu p_1^\nu B_{11} \tag{4.21b}$$

$$C^\mu = p_1^\mu C_1 + p_2^\mu C_2 \tag{4.21c}$$

$$C^{\mu\nu} = \eta^{\mu\nu} C_{00} + \sum_{i,j=1}^{2} p_i^\mu p_j^\nu C_{ij} \tag{4.21d}$$

$$C^{\mu\nu\rho} = \sum_{i=1}^{2} \left(\eta^{\mu\nu} p_i^\rho + g^{\mu\rho} p_i^\nu + g^{\nu\rho} p_i^\mu\right) C_{00i} + \sum_{i,j,k=1}^{2} p_i^\mu p_j^\nu p_l^\rho C_{ijk} \tag{4.21e}$$

$$\ldots$$

The coefficients B_1, B_{00}, B_{11} and so on are called Passarino-Veltman coefficient functions and are computed by solving a linear system of equations obtained from the contraction of the decomposition (4.21) with their external momenta and metric tensors.

Even though analytical expressions for the four scalar integrals in Eq. (4.18) are, e.g., available in Refs. [241–243], from a practical point of view, these integrals as well as the corresponding coefficient functions in Eq. (4.21) can conveniently be computed numerically for many argument sets with purpose-built loop libraries like LoopTools [244], OneLOop [245], Collier [246], QCDLoop [247] or the loop library contained in DM@NLO [248] which can also handle for some argument sets the case of a vanishing Gram determinant, see Ref. [191], which is, e.g., relevant for the computation of dark matter signals in direct and indirect detection experiments.

4.2.3 $\overline{\text{DR}}$ and On-Shell Renormalization

The final removal of the UV divergences requires the renormalization of masses, couplings and fields. Two different approaches within loop calculations are [230]:

- **Bare perturbation theory** where the calculation is performed in terms of unrenormalized parameters and only in the end the UV divergent terms are absorbed into the corresponding physical parameters.
- In contrast, **renormalized perturbation theory** starts directly with the physical parameters, however, at the cost of introducing a set of counterterms that contain the UV divergent parts and come with separate Feynman rules.

The latter is the more common approach and is also adopted within DM@NLO. As an example, the scalar ϕ^4-theory with the renormalizable Lagrangian density $\mathcal{L} = \mathcal{L}_0 - \mathcal{V}$ is considered, where

$$\mathcal{L}_0 = \frac{1}{2}\partial_\mu\phi\partial^\mu\phi - \frac{1}{2}m^2\phi^2 \tag{4.22}$$

is the free field Lagrangian and $\mathcal{V} = \frac{\lambda}{4!}\phi^4$ the potential containing the self-interaction term. One option is then to introduce a set of multiplicative renormalization constants, multiply them with the renormalized quantities to yield the divergence and expand them up to the desired order. In the one-loop case, i.e., at $\mathcal{O}(\lambda)$, one has

$$\phi_0 = \sqrt{Z_\phi}\phi \simeq \left(1 + \frac{1}{2}\delta Z_\phi\right)\phi\,, \tag{4.23a}$$

$$\lambda_0 = Z_\lambda\lambda \simeq \lambda + \delta\lambda\,, \tag{4.23b}$$

$$m_0^2 = Z_m m^2 \simeq m^2 + \delta m^2\,. \tag{4.23c}$$

As a result, the Lagrangian is extended through a part containing the counterterms,

$$\mathcal{L}_{\text{count}} = \frac{1}{2}\partial_\mu\phi\partial^\mu\phi - (\delta m^2 + m^2\delta Z_\phi)\frac{\phi^2}{2} - (\delta\lambda + 2\delta Z_\phi)\frac{\phi^4}{4!}\,. \tag{4.24}$$

Next comes the selection of a renormalization scheme determining the finite parts of the renormalization constants. To illustrate to popular choices, the renormalized self-energy

$$\Pi(p^2) = \Pi_0 - (p^2 - m^2)\delta Z_\phi + \delta m^2 \tag{4.25}$$

with $\Pi_0 = \frac{\lambda}{32\pi^2}A_0(m^2)$ is needed. Again, there are two common schemes:

- Within the **modified minimal subtraction ($\overline{\text{MS}}$) renormalization scheme** the divergence is regularized in the CDR or HV variant of dimensional regularization and only the UV divergence Δ is subtracted, i.e., the $1/\varepsilon$ pole including the finite $\ln(4\pi)$ and γ_E parts. As Π_0 is independent of the external momentum, this choice amounts to $\delta Z_\phi = 0$ and $\delta m^2 = -\frac{m^2\lambda}{32\pi^2}\Delta$. The analogue of the $\overline{\text{MS}}$ scheme in dimensional reduction is called the $\overline{\text{DR}}$ scheme.
- In the **on-shell (OS) renormalization scheme**, the finite parts are chosen such that the renormalized mass appearing in Green's functions can be identified with the observed mass m_P. This scheme is therefore particularly suited for particles whose mass can be directly

measured like the electron or the top quark. Since the full ϕ-propagator must be of the form $1/(p^2 - m^2 + \Pi(p^2))$, the requirement $m = m_P$ is equivalent to the renormalization conditions,

$$\operatorname{Re}\Pi(p^2)\Big|_{p^2=m_P^2} = 0\,, \tag{4.26}$$

$$\frac{\partial}{\partial p^2}\Pi(p^2)\Big|_{p^2=m_P^2} = 0\,. \tag{4.27}$$

In more detail, the first condition defines the renormalized mass to be the observed mass which is defined as the pole of the full propagator and the second one ensures a unit residue of the full propagator. As before, this yields $\delta Z_\phi = 0$, but $\delta m^2 = -\Pi_0$.

4.2.4 Renormalization of the MSSM

When it comes to the renormalization of the MSSM, the squark masses have to be renormalized carefully since the stop and sbottom sectors have to be treated simultaneously due to the fact that the up- and down-type squarks share the common soft breaking parameter $M_{\tilde{q}}$ as a result of the $\mathrm{SU}(2)_L$ gauge symmetry. The squark mass matrix can be diagonalized,

$$U^{\tilde{q}} \begin{pmatrix} m_{LL}^2 & m_{LR}^2 \\ m_{RL}^2 & m_{RR}^2 \end{pmatrix} (U^{\tilde{q}})^\dagger = \begin{pmatrix} m_{\tilde{q}_1}^2 & 0 \\ 0 & m_{\tilde{q}_2}^2 \end{pmatrix} \tag{4.28}$$

with the two physical masses $m_{\tilde{q}_1}^2$ and $m_{\tilde{q}_2}^2$ being the eigenvalues of the non-diagonal mass matrix with the entries

$$m_{LL}^2 = M_{\tilde{Q}}^2 + (I_q^{3L} - e_q s_W^2)\cos 2\beta m_Z^2 + m_q^2\,, \tag{4.29a}$$

$$m_{RR}^2 = M_{\tilde{U},\tilde{D}}^2 + e_q s_W^2 \cos 2\beta m_Z^2 + m_q^2\,, \tag{4.29b}$$

$$m_{LR}^2 = m_{RL}^2 = m_q(A_q - \mu(\tan\beta)^{-2I_q^{3L}})\,. \tag{4.29c}$$

Here, I_q^{3L} denotes the third component of the weak isopsin and e_q the electric charge carried by the quark q. Out of the eleven parameters given by the soft-breaking terms $M_{\tilde{Q}}$, $M_{\tilde{U}}$, $M_{\tilde{D}}$, A_t, A_b, the physical masses $m_{\tilde{t}_1}$, $m_{\tilde{t}_2}$, $m_{\tilde{b}_1}$, $m_{\tilde{b}_2}$ and the mixing angles $\theta_{\tilde{t}}$ and $\theta_{\tilde{b}}$ only five are completely independent. As the renormalization scheme in DM@NLO should be applicable to all (co)annihilation channels with squarks in a leading role, the soft SUSY-breaking masses $M_{\tilde{Q}}$, $M_{\tilde{U}}$, $M_{\tilde{D}}$ are replaced as input parameters by the physical on-shell masses $m_{\tilde{b}_1}$, $m_{\tilde{b}_2}$ and $m_{\tilde{t}_1}$. The three aforementioned soft parameters are then fixed through the requirement that Eq. (4.28) holds even at the one-loop order which, by inverting the corresponding eigenvalue equations, results in two possible solutions,

$$m_{LL}^2 = \frac{m_{\tilde{q}_1}^2 + m_{\tilde{q}_2}^2}{2} \pm \frac{1}{2}\sqrt{(m_{\tilde{q}_1} - m_{\tilde{q}_2})^2 - 4m_{LR}^4}\,, \tag{4.30a}$$

$$m_{RR}^2 = \frac{m_{\tilde{q}_1}^2 + m_{\tilde{q}_2}^2}{2} \mp \frac{1}{2}\sqrt{(m_{\tilde{q}_1} - m_{\tilde{q}_2})^2 - 4m_{LR}^4}\,, \tag{4.30b}$$

for the diagonal entries of the mass matrix. Consequently, there are two possible values for $M_{\tilde{Q}}$, $M_{\tilde{U}}$, and $M_{\tilde{D}}$. However, not both of them may yield a numerically stable renormalization scheme, the reason being that the diagonalization may not correctly reproduce the mass of the lighter stop used as an input value, and, more importantly, the counterterm belonging to the heavier stop mass $\delta m_{\tilde{t}_2} \sim (U^{\tilde{t}}_{21} U^{\tilde{t}}_{12})^{-1}$ may become singular for vanishing off-diagonal elements of the squark mixing matrix. The same problem might occur in the counterterm related to the squark mixing angle $\delta\theta_{\tilde{q}} \sim (U^{\tilde{q}}_{11} U^{\tilde{q}}_{22} + U^{\tilde{q}}_{12} U^{\tilde{q}}_{21})^{-1}$. To avoid these issues, a scheme is defined as numerically stable if the following three conditions are fulfilled:

- $|m^{\text{out}}_{\tilde{t}_1} - m^{\text{in}}_{\tilde{t}_1}|/m^{\text{in}}_{\tilde{t}_1} < 10^{-5}$,
- $|\text{Re}\, U^{\tilde{q}}_{11} U^{\tilde{q}}_{21}| > 10^{-4}$ for $q \in \{t, b\}$,
- $|\text{Re}\, (U^{\tilde{t}}_{11} U^{\tilde{t}}_{22} + U^{\tilde{t}}_{12} U^{\tilde{t}}_{21})| > 10^{-4}$.

Otherwise a scheme is declared as invalid (unstable). Given that both solutions are compatible, by default the solution is chosen where the dependent stop mass $m_{\tilde{t}_2}$ is closer to the corresponding physical value.

In a series of analyses [164–166, 169, 171], the following three renormalization schemes, adapted to the situation of DM (co)annihilation, have been included in DM@NLO:

0: m_b, m_t, $m_{\tilde{f}}$, $\theta_{\tilde{f}}$, A_f are all $\overline{\text{DR}}$ parameters.

1: m_b, A_b and A_t are $\overline{\text{DR}}$ input parameters whereas m_t, $m_{\tilde{t}_1}$ $m_{\tilde{b}_1}$ and $m_{\tilde{b}_2}$ are OS masses. $\theta_{\tilde{t}}$, $\theta_{\tilde{b}}$ and $m_{\tilde{t}_2}$ are then dependent quantities.

2: m_t, m_b, A_b and A_t are $\overline{\text{DR}}$ input parameters and $m_{\tilde{t}_1}$, $m_{\tilde{b}_1}$ and $m_{\tilde{b}_2}$ are OS masses. $\theta_{\tilde{t}}$, $\theta_{\tilde{b}}$ and $m_{\tilde{t}_2}$ are then dependent quantities.

The hybrid on-shell/$\overline{\text{DR}}$ scheme 1, which resembles the RS2 scheme presented in Ref. [249], is the recommended choice since it was found to be robust over large regions of the parameter space for (co)annihilations involving stops [164, 165], whereas the other two schemes are well suited for the estimation of theoretical uncertainties from scheme variations. The integration of an automated selection of the best renormalization scheme as, e.g., discussed in Ref. [250] would be a useful future addition.

4.2.5 Three-Particle Phase Space

While the virtual corrections come from loop diagrams, the real corrections arise from the radiation of another massless gauge boson which in the case of DM@NLO is a gluon. As the evaluation of the associated three-particle phase space with the final-state momenta k_1, k_2 and k_3 given by

$$\int \mathrm{d}\phi_3 = \int \frac{\mathrm{d}^4 k_1}{(2\pi)^4} \frac{\mathrm{d}^4 k_2}{(2\pi)^4} \frac{\mathrm{d}^4 k_3}{(2\pi)^4} (2\pi)\delta(k_1^2 - m_1^2)\Theta(k_1^0)(2\pi)\delta(k_2^2 - m_2^2)\Theta(k_2^0) \\ \times (2\pi)\delta(k_3^2 - m_3^2)\Theta(k_3^0)\delta^{(4)}(k_1 + k_2 + k_3 - p_a - p_b) \quad (4.31)$$

is a non-trivial task, the parametrization adopted in DM@NLO from Ref. [251] is provided here. The final integration variables are the angles η, θ, ϕ and the two energies k_1^0, k_3^0 which can be re-expressed through the dimensionless quantities

$$x_i = \frac{2k_i^0}{\sqrt{s}},\ i = 1, 2, 3\,, \qquad \mu_i = \frac{m_i}{\sqrt{s}},\ i = 1, 2, 3, a, b\,. \quad (4.32)$$

Then, energy conservation takes the from $x_1+x_2+x_3=2$ and integrating out the Dirac distributions yields the final phase space

$$\int \mathrm{d}\phi_3 = \frac{s}{32}\frac{1}{(2\pi)^5}\int \mathrm{d}x_1\,\mathrm{d}\eta\,\mathrm{d}x_3\,\mathrm{d}\!\cos\theta\,\mathrm{d}\phi \tag{4.33}$$

with the integration limits

$$\eta \in (0,2\pi), \qquad \phi \in (0,2\pi), \qquad \theta \in (0,\pi), \tag{4.34a}$$

$$x_3^{\min} = 2\mu_3, \qquad x_3^{\max} = 1-\mu_+^2+\mu_3^2, \tag{4.34b}$$

$$(x_1)^{\max}_{\min} = \frac{1}{2\tau}\left[\sigma(\tau+\mu_+\mu_-) \pm \sqrt{x_3^2-4\mu_3^2}\sqrt{\left(\tau-\mu_+^2\right)\left(\tau-\mu_-^2\right)}\right] \tag{4.34c}$$

that contain the abbreviations

$$\sigma = 2-x_3\,, \qquad \tau = 1-x_3+\mu_3^2\,, \qquad \mu_\pm = \mu_1\pm\mu_2\,. \tag{4.35}$$

The energies are defined in the the c.m. frame of the initial momenta p_a and p_b that are chosen to be aligned with the z-axis, i.e.,

$$p_a^\mu = \frac{\sqrt{s}}{2}\left(1+\mu_a^2-\mu_b^2, 0, 0, \sqrt{(1-\mu_a^2-\mu_b^2)^2-4\mu_a^2\mu_b^2}\right)\,, \tag{4.36a}$$

$$p_b^\mu = \frac{\sqrt{s}}{2}\left(1-\mu_a^2+\mu_b^2, 0, 0, -\sqrt{(1-\mu_a^2-\mu_b^2)^2-4\mu_a^2\mu_b^2}\right)\,, \tag{4.36b}$$

where s is the squared c.m. energy. The final-state momenta must then take the form

$$\mathbf{k}_1 = \frac{\sqrt{s}}{2}\sqrt{x_1^2-4\mu_1^2}\begin{pmatrix}\cos(\eta)\cos(\theta)\sin(\xi)+\sin(\theta)\cos(\xi)\\ \sin(\eta)\sin(\xi)\\ \cos(\theta)\cos(\xi)-\cos(\eta)\sin(\theta)\sin(\xi)\end{pmatrix}\,, \tag{4.37a}$$

$$\mathbf{k}_3 = \frac{\sqrt{s}}{2}\sqrt{x_3^2-4\mu_3^2}\begin{pmatrix}\sin(\theta)\\ 0\\ \cos(\theta)\end{pmatrix}\,. \tag{4.37b}$$

The remaining three-momentum $\mathbf{k}_2$ follows from momentum conservation $\mathbf{k}_2 = -\mathbf{k}_1-\mathbf{k}_3$ and the auxiliary angle ξ between $\mathbf{k}_1$ and $\mathbf{k}_3$ is fixed to the value

$$\cos\xi = \frac{(2-x_1-x_3)^2+4\mu_1^2+4\mu_3^2-4\mu_2^2-x_1^2-x_3^2}{2\sqrt{x_1^2-\mu_1^2}\sqrt{x_3^2-\mu_3^2}}\,. \tag{4.38}$$

The main technical complication in the evaluation of the real emission contribution comes from infrared singularities originating, without loss of generality, in propagators of the from

$$\frac{1}{(k_1+k_3)^2-m_1^2} = \frac{1}{2k_3^0(k_1^0-|\mathbf{k}_1|\cos\xi)}\,, \tag{4.39}$$

where k_3 is used to denote the momentum of the radiated (massless) gluon since this expression diverges if the energy k_3^0 approaches zero, known as a soft divergence. If the other particle labeled by k_1 is massless as well, a collinear singularity can appear in addition for $\cos\xi \to 1$.

4.2.6 Intermediate On-Shell Resonance Subtraction

Besides the infrared divergences in the real emission contribution there can occur another subtlety, namely that an internal propagator can go on-shell. In DM@NLO, this is the case for the process $\tilde{\chi}^0_n \tilde{t}_i \to bW^+$, where the internal top propagator can become on-shell if the collisional energy $\sqrt{s}$ exceeds the top mass m_t. To cure the singularity, the "Prospino scheme" defined in Refs. [252, 253] is adopted. It entails substituting the top propagator with the Breit-Wigner form, according to

$$\frac{1}{p^2 - m_t^2} \;\to\; \frac{1}{p^2 - m_t^2 + i m_t \Gamma_t}\,, \tag{4.40}$$

in the resonant part $\mathcal{M}_\mathrm{r}$ of the total real emission amplitude $\mathcal{M}_\mathrm{tot} = \mathcal{M}_\mathrm{r} + \mathcal{M}_\mathrm{nr}$ belonging to the bW^+ final state, whereas the non-resonant piece $\mathcal{M}_\mathrm{nr}$ remains unchanged. Since the process $\tilde{\chi}^0_n \tilde{t}_i \to tg$ corresponding to an on-shell top is already accounted for in the calculation of the neutralino relic density, the contribution from the leading order on-shell production of a top with the subsequent decay into a bottom quark and a W-boson is removed locally through the replacement

$$\left|\mathcal{M}_\mathrm{r}\right|^2 \;\to\; \left|\mathcal{M}_\mathrm{r}\right|^2 - \frac{m_t^2 \Gamma_t^2}{(p^2 - m_t^2)^2 + m_t^2 \Gamma_t^2} \left|\mathcal{M}_\mathrm{r}\right|^2_{p_t^2 = m_t^2} \tag{4.41}$$

with the physical top width Γ_t. This procedure has the advantage that it is not necessary to modify the interference $\mathrm{Re}(\mathcal{M}_\mathrm{r}^* \mathcal{M}_\mathrm{nr})$ containing only one on-shell propagator and thus finite principal-value integrals. However, to stabilize the numerical integration, a small artificial top width $\Gamma_t = 10^{-3} \cdot m_t$ is used in DM@NLO in the interference part instead of the physical width.

4.2.7 Non-Perturbative Effects

Having discussed perturbative corrections, there are also important non-perturbative effects relevant for dark matter annihilation. One is the Sommerfeld [254] or Sakharov enhancement [255] which is an elementary quantum mechanical effect that increases (decreases) annihilation cross sections for small relative velocities in the presence of an attractive (repulsive) long-range potential affecting the incoming particles. From a field theory point of view, this effect is described by ladder diagrams involving the exchange of light mediators with some coupling λ to the initial particles. More quantitatively, the Sommerfeld factor

$$S_0^{[\mathbf{R}]} \;=\; \left|\phi^{[\mathbf{R}]}(0)\right|^2 \tag{4.42}$$

is obtained as a solution $\phi(\mathbf{r})$ evaluated at the origin $\mathbf{r} = 0$ of the stationary Schrödinger equation for the potential describing the interaction of the annihilating particles transforming under the representation $\mathbf{R}$ of the corresponding force carriers. For an s-wave dominated annihilation process, the Sommerfeld factor simply multiplies the perturbative tree-level cross section giving the Sommerfeld corrected cross section

$$\sigma^\mathrm{Som} = \sum_{\mathbf{R}} S_0^{[\mathbf{R}]} \sigma_{\mathbf{R}}^\mathrm{Tree}\,, \tag{4.43}$$

where the sum runs over all irreducible representations contained in the decomposition of the initial particle pair. In a collider context, the exchange takes place between the final-state particles as these kinds of higher-order effects are important close to production threshold and are reffered to as Coulomb corrections instead. In this convention for the Sommerfeld factor, the free wave-function is normalised to one $|\phi_0^{[\mathbf{R}]}(0)|^2 = 1$ to ensure that $\sigma^{\mathrm{Som}} \to \sigma^{\mathrm{Tree}}$ is fulfilled if the interaction governing the enhancement effect is turned off ($\lambda \to 0$). When combining the Sommerfeld effect with the full $\mathcal{O}(\lambda^2)$ correction, one has to be careful to not overcount the single mediator exchange contained in both calculations. In DM@NLO both are matched by removing the $\mathcal{O}(\lambda^2)$ contribution from the Sommerfeld factor. A detailed example with gluons playing the role of the aforementioned light mediators is given in Sec. 4.4.3 in the context of the higher-order corrections to stop-antistop annihilation. When the Sommerfeld enhancement is relevant, also the formation of bound states is important [94]. For a phenomenological study taking into account both of these effects in the context of simplified t-channel dark matter models [256] that are essentially the stop-neutralino sector of the MSSM, see, e.g., Ref. [257].

4.3 The Dipole Formalism for Massive Initial-State Particles

It remains the precise treatment of the real emission processes as their numerical evaluation is problematic in phase space regions where the squared matrix element becomes soft or collinear. Only the sum of the real and virtual corrections is infrared finite in a unitary QFT such as the Standard Model or the MSSM according to the Kinoshita-Lee-Nauenberg (KLN) theorem [258]. The two main general approaches which allow the analytic cancellation of infrared singularities between both contributions are subtraction methods [259–261] and phase space slicing (PSS) methods [262–265]. A general treatment of massive initial particles, e.g., in supersymmetric QCD, as required for dark matter (co)annihilation processes is available for the slicing approach, but not for the subtraction methods. In Ref. [266], photon radiation off heavy fermions in QED was considered, but a small photon mass was used as a regulator. Consequently, the results cannot be simply transferred to non-Abelian theories, where divergences are commonly regularized via a dimensional scheme. In Refs. [267, 268] a fully massive dipole formalism for initial-final dipoles in conventional dimensional regularization was considered, however, leaving out, e.g., the emission off a massless final-state quark with a massive spectator and in a different convention of parameters compared to the one used in the original work [260], complicating the computation of necessary integration limits. Ref. [269] focuses primarily on the case of the initial-initial dipole configuration corresponding to the emission of a gluon into the final state off a massive initial quark and pays particular attention to the necessary modifications of the standard treatment of parton distribution functions in the final dipole formulae required by the inclusion of mass effects. The phase space slicing method has been successfully applied to dark matter calculations in the past [164, 165, 169], but this approach has the practical disadvantages that the squared real emission matrix element has to be subdivided into finite, soft, collinear and soft-collinear contributions and that the final result depends on the chosen cutoffs. In addition, the slicing method is found to be less accurate and efficient compared to the dipole approach [270].

For these reasons, it is the objective of this section to extend the Catani-Seymour dipole subtraction method to massive initial states for initial-final as well as initial-initial dipoles in a *unified* notation similar to the one used in Ref. [261] and provide all formulae for squark and gluino (co)annihilation as required by dark matter calculations as in [271]. All formulae are provided for different dimensional schemes, as conventional dimensional regularization breaks supersymmetry already at the one-loop level. By a simple change of the color factor, the results can also be applied to heavy scalar and fermionic dark matter in general. The provided formulae also allow for one massive and one massless particle in the initial state. The results do not apply to splitting processes where the mass of the parent particle is unequal to the mass of one of its decay products such as the splitting $g \to q\bar{q}$ into massive quarks.

4.3.1 Review of the Dipole Subtraction Method

Due to the large number of terms that enter during the standard Feynman-diagrammatic calculation of (SUSY)-QCD matrix elements, it is often impossible to perform the integration over the $m+1$ particle phase space in Eq. (4.11) analytically in D dimensions except for the very simplest processes. In order to make a numerical evaluation of the real emission matrix elements over the whole phase space possible, i.e., without relying on cuts and approximations as in the phase space slicing approach, Catani and Seymour developed the dipole subtraction method [260]. The basic idea is to construct an auxiliary cross section $\mathrm{d}\sigma^{\mathrm{A}}$ which converges pointwise to $\mathrm{d}\sigma^{\mathrm{R}}$ in the singular region in D dimensions, so that $\mathrm{d}\sigma^{\mathrm{R}} - \mathrm{d}\sigma^{\mathrm{A}}$ is finite over the whole region of phase space and can be integrated in four dimensions. At the same time it must be possible to integrate $\mathrm{d}\sigma^{\mathrm{A}}$ analytically in D dimensions over the one-particle phase space of the radiated massless particle giving rise to the divergence. This allows to add back the subtraction term and to cancel those divergences appearing in the virtual contribution which are present in the form of simple or double poles in ε. The computation of the NLO correction can then be summarized as

$$\Delta\sigma^{\mathrm{NLO}} = \int_{m+1} \left[\mathrm{d}\sigma^{\mathrm{R}}_{\varepsilon=0} - \mathrm{d}\sigma^{\mathrm{A}}_{\varepsilon=0}\right] + \int_{m} \left[\mathrm{d}\sigma^{\mathrm{V}} + \int_{1} \mathrm{d}\sigma^{\mathrm{A}}\right]_{\varepsilon=0} . \tag{4.44}$$

The counterterm $\mathrm{d}\sigma^{\mathrm{A}}$ is constructed from the knowledge that QCD amplitudes factorize in the soft and collinear limit in the process-dependent Born level cross section $\mathrm{d}\sigma^{\mathrm{B}}$ convolved with a universal splitting kernel $\mathrm{d}\mathbf{V}_{\mathrm{dipole}}$, which reflects the singular behavior. From another point of view, the factorization can be thought of as a two-step process. In the first step, m final state particles are produced through the Born level cross section $\mathrm{d}\sigma^{\mathrm{B}}$. In the second step, the final $(m+1)$-particle configuration is reached through the decay of one of the m particles - *the emitter* - into two particles. This last step is described by the splitting function $\mathrm{d}\mathbf{V}_{\mathrm{dipole}}$. The information about color and spin correlations is accounted for by referencing an additional particle - *the spectator*. The final expression for $\mathrm{d}\sigma^{\mathrm{A}}$ is obtained by summing over all possible emitter-spectator pairs

$$\int_{m+1} \mathrm{d}\sigma^{\mathrm{A}} = \sum_{\mathrm{dipoles}} \int_{m} \mathrm{d}\sigma^{\mathrm{B}} \otimes \int_{1} \mathrm{d}\mathbf{V}_{\mathrm{dipole}} = \sum_{\mathrm{dipoles}} \int_{m} \left[\mathrm{d}\sigma^{\mathrm{B}} \otimes \mathbf{I}\right] , \tag{4.45}$$

where the universal factor $\mathbf{I}$ corresponds to the integral of the dipole splitting function over the one particle phase space, and thus cancels the infrared divergences in the virtual part. The fact that the underlying structure of this factorization is formed by these pairs led to the name “dipole formalism”. However, as this factorization holds only in the strict soft and collinear limit and it is desirable that $\mathrm{d}\sigma^{\mathrm{A}}$ approximates $\mathrm{d}\sigma^{\mathrm{R}}$ also in a small region around the singularity to render the subtraction procedure numerically stable, one has to introduce the so-called *dipole momenta* to ensure that the factorization does not violate momentum conservation. These obey momentum conservation in the whole $m+1$-particle phase space and are defined through a smooth map from the $m+3$ real emission momenta to the $m+2$ dipole momenta. Their precise definition depends on the kinematical situation and therefore their concrete expressions will be given in the sections dedicated to the different emitter-spectator pairs.

In order to allow for a general construction of the auxiliary cross section, the aforementioned color and spin correlations are implemented into the factorization formula by realizing the splitting functions $\mathbf{V}_{\text{dipole}}$ as operators that act on matrix elements which are defined as abstract objects in color and spin space. For this purpose, the conventions and the notation established in Refs. [260,261] is used which is introduced again for completeness in the following. That is, colored particles in the initial state are labeled by $a, b, \ldots$ and those in the final state by $i, j, k, \ldots$. Since non-colored particles are irrelevant for the subtraction procedure, they are suppressed in the notation. Scattering amplitudes are considered as objects in an abstract vector space spanned by the spins s_a, s_i and colors c_a, c_i of all colored particles involved in the process

$$|\{i,a\}\rangle_m = \frac{1}{\prod_b \sqrt{n_c(b)}} \mathcal{M}_m^{\{c_i,s_i;c_a,s_a\}}\left(\{p_i;p_a\}\right)\left(|\{c_i;c_a\}\rangle \otimes |\{s_i;s_a\}\rangle\right), \tag{4.46}$$

where $\prod_b \sqrt{n_c(b)}$ fixes the normalization by averaging over the $n_c(b)$ color degrees of freedom for each initial particle b. The kets $|\{c_i;c_a\}\rangle$ and $|\{s_i;s_a\}\rangle$ constitute formally an orthogonal basis of the color and spin space, respectively. The color charge operators $\mathbf{T}_i$ or $\mathbf{T}_a$ reflect the emission of a gluon (or another massless colored particle) from a particle i or a. Their action on color space is defined as

$$\begin{aligned} {}_m\langle\{i,a\}|\, \mathbf{T}_j \cdot \mathbf{T}_k \,|\{i,a\}\rangle_m = \frac{1}{\prod_b n_c(b)} &\left[\mathcal{M}_m^{c_1,\ldots,c_j,\ldots,c_k,\ldots,c_m;\{a\}}\left(\{p_i;p_a\}\right)\right]^* \\ &\times \mathcal{T}^e_{c_j d_j}\mathcal{T}^e_{c_k d_k}\mathcal{M}_m^{d_1,\ldots,d_j,\ldots,d_k,\ldots,d_m;\{a\}}\left(\{p_i;p_a\}\right) \end{aligned} \tag{4.47}$$

and analogously if j or k are initial-state particles. For a final-state particle j, the color charge matrix $\mathcal{T}^e_{cd}$ is defined as

$$\mathcal{T}^e_{c_j d_j} = \begin{cases} -if_{c_j d_j e} & \\ T^e_{c_j d_j} & \text{if } j \text{ is in the} \\ -T^e_{d_j c_j} & \end{cases} \begin{matrix} \text{adjoint} \\ \text{fundamental} \\ \text{anti-fundamental} \end{matrix} \quad \text{representation of } \mathfrak{su}(3)_c, \tag{4.48}$$

with $T^a = \frac{\lambda^a}{2}$ being half of the Gell-Mann matrices λ^a and f_{abc} the structure constants of $\mathfrak{su}(3)_c$. The color charge operator $\mathbf{T}_a$ of an initial particle a obeys the same action defined in Eq. (4.47). However, by crossing symmetry the color charge matrix in this case is defined as

$$\mathcal{T}^e_{c_a d_a} = \begin{cases} -if_{c_a d_a e} & \\ -T^e_{d_a c_a} & \text{if } a \text{ is in the} \\ T^e_{c_a d_a} & \end{cases} \begin{matrix} \text{adjoint} \\ \text{fundamental} \\ \text{anti-fundamental} \end{matrix} \quad \text{representation of } \mathfrak{su}(3)_c. \tag{4.49}$$

Since each ket $|\{i,a\}\rangle_m$ must be a color singlet, color conservation can be written as

$$\left(\sum_j \mathbf{T}_j + \sum_b \mathbf{T}_b\right)|\{i,a\}\rangle_m = \sum_I \mathbf{T}_I\,|\{i,a\}\rangle_m = 0\,, \tag{4.50}$$

where the index I runs over both initial and final state particles. Furthermore, the commutation relation

$$[\mathbf{T}_i, \mathbf{T}_j] = 0 \text{ if } i \neq j, \quad \mathbf{T}_i^2 = C_i = \begin{cases} C_A, & i \text{ adjoint} \\ C_F, & i \text{ (anti)-fundamental} \end{cases} \tag{4.51}$$

with the quadratic Casimir operators C_i follows directly from the definition of the color charge operators.

With these definitions and conventions at hand, the dipole splitting functions which approximate the real emission matrix element in the soft and collinear limit can be constructed. *In the soft limit*, where the momentum of a gluon i tends to zero, the real emission matrix element can be written in terms of an eikonal current of the gluon

$$\mathbf{J}^\mu = \sum_a \frac{p_a^\mu}{p_a \cdot p_i} \mathbf{T}_a + \sum_j \frac{p_j^\mu}{p_j \cdot p_i} \mathbf{T}_j = \sum_I \frac{p_I^\mu}{p_I \cdot p_i} \mathbf{T}_I \tag{4.52}$$

and behaves as

$$\begin{aligned} {}_{m+1,a\ldots}\langle \ldots, i, \ldots, j, \ldots; a, \ldots | \ldots, i, \ldots, j, \ldots; a, \ldots \rangle_{m+1,a\ldots} &\xrightarrow{p_i \to 0} \\ - 4\pi \mu^{2\varepsilon} \alpha_s \; {}_{m,a\ldots}\langle \ldots, j, \ldots; a, \ldots | \, \mathbf{J}_\mu^\dagger \mathbf{J}^\mu \, | \ldots, j, \ldots; a, \ldots \rangle_{m,a\ldots} \, . \end{aligned} \tag{4.53}$$

Again, the renormalization scale μ comes from the transition from four to D spacetime dimensions. By using partial fractioning

$$\frac{p_I \cdot p_K}{(p_I \cdot p_i)(p_K \cdot p_i)} = \frac{p_I \cdot p_K}{(p_I \cdot p_i)(p_I + p_K) \cdot p_i} + \frac{p_I \cdot p_K}{(p_K \cdot p_i)(p_I + p_K) \cdot p_i} \tag{4.54}$$

and color conservation, the squared eikonal current can be recast into a sum over emitter (I) and spectator (K) pairs

$$\mathbf{J}_\mu^\dagger \mathbf{J}^\mu = \sum_{I,K} \frac{p_I \cdot p_K}{(p_I \cdot p_i)(p_K \cdot p_i)} \mathbf{T}_I \cdot \mathbf{T}_K \sum_{\substack{I,K \\ I \neq K}} \frac{1}{p_I \cdot p_i} \left(\frac{2 p_I \cdot p_K}{(p_I + p_K) \cdot p_i} - \frac{m_I^2}{p_I \cdot p_i} \right) \mathbf{T}_I \cdot \mathbf{T}_K . \tag{4.55}$$

For two final-state particles i and j that are produced through a splitting $\widetilde{ij} \to i + j$ of a parent

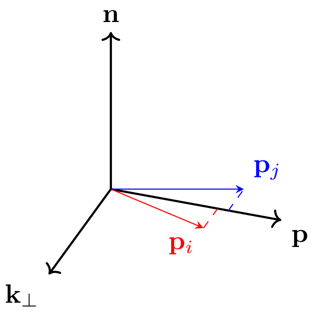

Figure 4.1: Sudakov vector parametrization.

particle $\widetilde{ij}$, there is also a *collinear divergence* if i and j are massless or a *quasi-collinear* divergence if i and j are massive but their mass is small compared to the energy scale of the calculation so that the true collinear divergence is screened by the non-zero mass. In order to make the divergence visible, their momenta p_i and p_j can be expressed through the Sudakov parametrization

$$p_i^\mu = zp^\mu + k_\perp^\mu - \frac{k_\perp^2 + z^2 m_{ij}^2 - m_i^2}{z}\frac{n^\mu}{2p\cdot n}, \tag{4.56a}$$

$$p_j^\mu = (1-z)p^\mu - k_\perp^\mu - \frac{k_\perp^2 + (1-z)^2 m_{ij}^2 - m_j^2}{1-z}\frac{n^\mu}{2p\cdot n}, \tag{4.56b}$$

where the timelike momentum p with $p = m_{ij}^2$ gives the collinear direction and an auxiliary light-like four-vector n is needed to specify the transverse component $k_\perp$ which is perpendicular to n and p ($k_\perp \cdot n = k_\perp \cdot p = 0$), cf. Fig. 4.1. The variable z corresponds to the momentum fraction involved in the splitting. With the help of this parametrization, the squared real emission matrix element reduces in the (quasi)-collinear limit to

$$\begin{aligned} &{}_{m+1,a\ldots}\langle \ldots, i, j, \ldots; a, \ldots | \ldots, i, j, \ldots; a, \ldots \rangle_{m+1,a\ldots} \xrightarrow{p_i \| p_j} \\ &\qquad \frac{4\pi\mu^{2\varepsilon}\alpha_s}{p_i\cdot p_j}\;{}_{m,a\ldots}\left\langle \ldots, \widetilde{ij}, \ldots; a, \ldots \middle| \hat{P}_{\widetilde{ij},i}(z, k_\perp; \varepsilon) \middle| \ldots, \widetilde{ij}, \ldots; a, \ldots \right\rangle_{m,a\ldots} \end{aligned} \tag{4.57}$$

with the (generalized) Altarelli-Parisi [272] splitting function $\hat{P}_{\widetilde{ij},i}(z, k_\perp; \varepsilon)$. As the process $q \to q+g$ is required for massless as well as massive quarks, the quasi-collinear limit is included which corresponds to the collinear one in the zero-mass limit. Only the pure collinear limit on the hand is considered for the splittings $g \to q + \bar{q}$ and $g \to gg$. The associated splitting functions are given by [261, 272, 273]:

$$\langle s| \hat{P}_{qg}(z, k_\perp; \varepsilon) |s'\rangle = \delta_{ss'} C_F \left[\frac{2(1-z)}{z} + \frac{1}{2}h_g^{\mathrm{RS}} z - \frac{m_q^2}{p_g\cdot p_q}\right], \tag{4.58a}$$

$$\langle \mu| \hat{P}_{gq}(z, k_\perp; \varepsilon) |\nu\rangle = T_F \left[-\eta^{\mu\nu} + 4z(1-z)\frac{k_\perp^\mu k_\perp^\nu}{k_\perp^2}\right], \tag{4.58b}$$

$$\langle \mu| \hat{P}_{gg}(z, k_\perp; \varepsilon) |\nu\rangle = 2C_A \left[-\eta^{\mu\nu}\left(\frac{z}{1-z} + \frac{1-z}{z}\right) - h_g^{\mathrm{RS}} z(1-z)\frac{k_\perp^\mu k_\perp^\nu}{k_\perp^2}\right]. \tag{4.58c}$$

Recall that the number of internal helicity states of the gluon h_g^{RS} allows to distinguish between different dimensional schemes. For the construction of the dipole splitting function $\mathbf{V}_{\mathrm{dipole}}$, both, the soft and the collinear limit, need to be taken into account. However, it is not simply possible to naively add both limits as this will lead to an "over-counting" of the soft divergence, as the Altarelli-Parisi splitting functions also diverge in the soft limit. Therefore, it is necessary to construct the dipole splitting functions such that both limits are fulfilled separately, i.e., the overlapping region is only taken into account once.

The final *dipole factorization formula* that defines the auxiliary squared matrix element related to $\mathrm{d}\sigma^{\mathrm{A}}$ is

$$\left|\mathcal{M}_{m+1}^{\mathrm{A}}\right|^2 = \sum_{i,j}\sum_{k\neq i,j}\mathcal{D}_{ij,k} + \sum_{i,j}\sum_{a}\mathcal{D}_{ij}^{a} + \sum_{a,i}\sum_{j\neq i}\mathcal{D}_{j}^{ai} + \sum_{a,i}\sum_{b\neq a}\mathcal{D}^{ai,b}, \tag{4.59}$$

where one has to distinguish between four different dipoles for the four different initial/final-state combinations of emitter and spectator. The precise definition of the dipoles $\mathcal{D}_{ij}^{a}$, $\mathcal{D}_{j}^{ai}$ and $\mathcal{D}^{ai,b}$

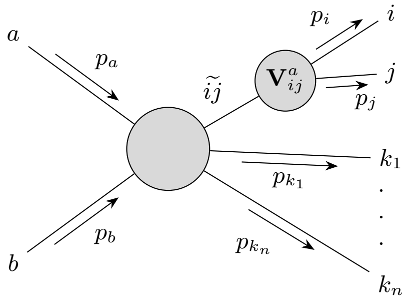

Figure 4.2: Diagrammatic interpretation of the dipole $\mathcal{D}^a_{ij}$ and the associated splitting function $\mathbf{V}^a_{ij}$.

related to the splitting kernels $\mathbf{V}_{\text{dipole}}$ as well as the process dependent kernels themselves will be given in the following sections. A definition for the dipole $\mathcal{D}_{ij,k}$ where emitter and spectator are both from the final state is not provided as this case is already fully covered for the massive and the massless case in Refs. [260, 261].

4.3.2 Final-State Emitter and Initial-State Spectator

The dipole contribution $\mathcal{D}^a_{ij}$ in Eq. (4.59) is defined as

$$\mathcal{D}^a_{ij} = \frac{1}{-2p_i \cdot p_j} \frac{1}{x_{ij,a}} {}_{m,a}\Big\langle \ldots, \widetilde{ij}, \ldots; \tilde{a}, \ldots \Big| \frac{\mathbf{T}_a \cdot \mathbf{T}_{ij}}{\mathbf{T}^2_{ij}} \mathbf{V}^a_{ij} \Big| \ldots, \widetilde{ij}, \ldots; \tilde{a}, \ldots \Big\rangle_{m,a}, \tag{4.60}$$

where the function $\mathbf{V}^a_{ij}$ describes the splitting process $\widetilde{ij} \to i + j$ and the variable $x_{ij,a}$ will be defined in the section on the kinematical quantities used for the formulation of the splitting kernels. The tree matrix element with m final-state particles is obtained from the original one with $(m+1)$ particles by replacing i and j with the emitter $\widetilde{ij}$ of momentum $\tilde{p}_{ij}$ and by exchanging the initial particle a with $\tilde{a}$ of momentum $\tilde{p}_a$. In the following, only the specific case $m_{ij} = m_j$ is considered where the mass of the emitter $\widetilde{ij}$ is identical to the one of j as the more general case $m_{ij} \neq m_j$ case is not needed for the example processes.

Since a treatment of massless initial particles is already available in the literature [260, 261], the initial particle a will be treated as massive throughout, whereas the final-state particle with momentum p_j can have an arbitrary mass. The mass of i is allows zero, i.e., in summary,

$$p_a^2 = m_a^2 > 0, \qquad p_j^2 = m_j^2, \qquad p_i^2 = 0. \tag{4.61}$$

Kinematics

For the construction of the dipole $\mathcal{D}^a_{ij}$, the kinematic quantities introduced in Ref. [266] for photon emission off massive fermions are adopted. However, as a small photon mass is used in Ref. [266] as infrared regulator, the crucial part lies in the generalization of the phase space parametrization from four to D dimensions.

The two main quantities are the total outgoing momentum of the dipole phase space $P = p_i + p_j$ and the total transferred momentum

$$Q = P - p_a = p_b - \sum_k p_k = \tilde{p}_{ij} - \tilde{p}_a\,, \tag{4.62}$$

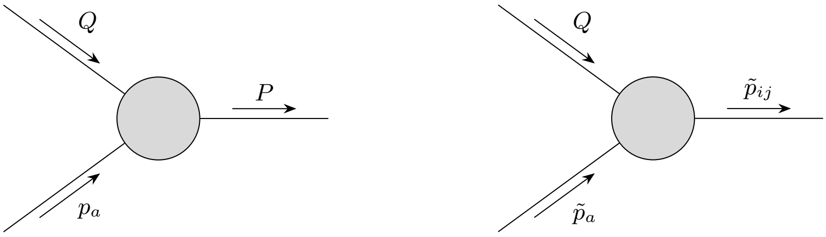

Figure 4.3: Kinematics for a final-state emitter and an initial-state spectator in the original momenta (left) and the dipole momenta (right).

where k runs over the momenta of all other $(m-1)$ final-state particles besides p_i and p_j, cf. Figs. 4.2 and 4.3. At this point, one should highlight the difference between P and $\widetilde{p}_{ij}$. That is, P is the true momentum of the parent particle $\widetilde{ij}$ in the real emission matrix element whereas $\tilde{p}_{ij}$ is the dipole momentum which is inserted into the tree matrix element as momentum of $\widetilde{ij}$ within the auxiliary matrix element. For the explicit definition of the dipole splitting functions and the dipole momenta some auxiliary variables are used. These are first of all the momentum fractions

$$z_j = \frac{p_a \cdot p_j}{P \cdot p_a} = 1 - z_i \,, \qquad x_{ij,a} = \frac{P \cdot p_a - p_i \cdot p_j}{P \cdot p_a} \,, \tag{4.63}$$

which take by definition only values between zero and one and behave in the soft ($p_i^\mu \to 0$) and collinear limit ($p_i \cdot p_j \to 0$) as $z_i \to 0$, $z_j \to 1$ and $x_{ij,a} \to 1$. The different quantities are related through

$$P^2 = \frac{-\bar{Q}^2}{x_{ij,a}} + Q^2 - m_a^2 \,, \qquad P \cdot p_a = \frac{-\bar{Q}^2}{2x_{ij,a}} \tag{4.64}$$

with the abbreviation $\bar{Q}^2 = Q^2 - m_a^2 - m_j^2$. It is worth noting that since the product $P \cdot p_a$ is always positive and $x_{ij,a}$ can only take values between zero and one, $\bar{Q}^2$ is always negative such that $\sqrt{\bar{Q}^4} = -\bar{Q}^2$ with $\bar{Q}^4 = \left(\bar{Q}^2\right)^2$. In addition, there will appear the auxiliary variables

$$\lambda_{aj} = \lambda\left(Q^2, m_j^2, m_a^2\right) = \bar{Q}^4 - 4m_a^2 m_j^2 \,, \tag{4.65a}$$

$$R(x) = \frac{\sqrt{\left(\bar{Q}^2 + 2m_a^2 x\right)^2 - 4m_a^2 Q^2 x^2}}{\sqrt{\lambda_{aj}}} \tag{4.65b}$$

with the Källén function $\lambda(x,y,z) = x^2 + y^2 + z^2 - 2xy - 2yz - 2zx$ as well as the reduced masses η_n and the relative velocity v between $\tilde{p}_{ij}$ and $\tilde{p}_a$,

$$\eta_n = \frac{m_n^2}{-\bar{Q}^2} \quad (n = a, j), \qquad v = \frac{\sqrt{\lambda_{aj}}}{-\bar{Q}^2}. \tag{4.66}$$

It is straightforward to check that $P^2 \to m_j^2$ and $R(x_{ij,a}) \to 1$ in the soft and collinear limit. The dipole momenta of emitter and spectator

$$\tilde{p}_{ij}^\mu = \frac{x_{ij,a}}{R(x_{ij,a})} p_a^\mu + \left(\frac{1}{R(x_{ij,a})} \frac{\bar{Q}^2 + 2m_a^2 x_{ij,a}}{2Q^2} - \frac{Q^2 + m_a^2 - m_j^2}{2Q^2} + 1 \right) Q^\mu \tag{4.67a}$$

$$\tilde{p}_a^\mu = \tilde{p}_{ij}^\mu - Q^\mu \tag{4.67b}$$

are constructed from the requirement to fulfill the on-shell conditions $\tilde{p}_a^2 = m_a^2$, $\tilde{p}_{ij}^2 = m_{ij}^2$ and momentum conservation $\tilde{p}_a + p_b = \tilde{p}_{ij} + p_k$.

Phase Space Factorization

The factorization of the $(m+1)$-particle phase space $\mathrm{d}\phi_{m+1}\left(p_i, p_j, p_k; p_a + p_b\right)$ into the m-particle phase space $\mathrm{d}\phi_m\left(P(x), p_k; p_a + p_b\right)$ and the dipole phase space $\left[\mathrm{d}p_i\left(Q^2, x, z_i\right)\right]$ is derived in App. A.1.1 and corresponds to a convolution over the parameter x

$$\int \mathrm{d}\phi_{m+1}\left(p_i, p_j, p_k; p_a + p_b\right)\theta(x_{ij,a} - x_0) = \int_{x_0}^{1} \mathrm{d}x \int \mathrm{d}\phi_m\left(P(x), p_k; p_a + p_b\right) \int \left[\mathrm{d}p_i\left(Q^2, x, z_i\right)\right], \tag{4.68}$$

where x plays the role of $x_{ij,a}$. In Eq. (4.68) an additional auxiliary parameter x_0 with $0 \leq x_0 < 1$ is introduced as a lower limit on x which is provided by the constraint that the argument of the square root in Eq. (4.65b) remains positive for all possible values of Q^2. This translates into the condition

$$\frac{-\bar{Q}^2}{2m_a\left(m_a - \sqrt{Q^2}\right)} < x_0 < 1, \tag{4.69}$$

if $0 < \sqrt{Q^2} < m_a - m_j$. If the latter condition is not met, any value for x_0 between zero and one can be used. Since the singular behavior occurs for $x \to 1$, applying the splitting function $\mathbf{V}_{ij}^a$ only for $x_0 \leq x \leq 1$ still cancels the divergences. In addition, the independence of $\Delta\sigma^{\mathrm{NLO}}$ on the choice of x_0 serves as a non-trivial check for the correct implementation of the subtraction procedure. The integration of the dipole splitting function over the one-particle phase space

$$\int \left[\mathrm{d}p_i\left(Q^2, x, z_i\right)\right] = \frac{1}{(4\pi)^{2-\varepsilon}} \frac{\left(P^2\right)^{-\varepsilon}}{\Gamma(1-\varepsilon)} \frac{-\bar{Q}^2}{x^2} \left(\frac{R(x)\sqrt{\lambda_{aj}}}{-\bar{Q}^2}\right)^{2\varepsilon-1} \int_{z_-}^{z_+} \mathrm{d}z_i \left[\left(z_i - z_-\right)\left(z_+ - z_i\right)\right]^{-\varepsilon} \tag{4.70}$$

with the integration limits

$$z_\pm = \frac{1-x}{2} \frac{-\bar{Q}^2 \pm \sqrt{\lambda_{aj}}R(x)}{xm_j^2 - \bar{Q}^2(1-x)} \tag{4.71}$$

yields the singular behavior parameterized by $D = 4 - 2\varepsilon$ dimensions. In the massless case $m_j = 0$ the integration limits related to z_i simplify to $z_\pm = \frac{1}{2}\left(1 \pm R(x)\right)$.

The Dipole Splitting Functions

The functions $\mathbf{V}_{ij}^a$ in Eq. (4.60) are provided for the four (SUSY)-QCD splitting processes:

- $q \to g(p_i) + q(p_j)$: $m_i = 0$ and $m_{ij} = m_j = m_q$
- $\tilde{q} \to g(p_i) + \tilde{q}(p_j)$: $m_i = 0$ and $m_{ij} = m_j = m_{\tilde{q}}$
- $g \to g(p_i) + g(p_j)$: $m_{ij} = m_i = m_j = 0$
- $g \to q(p_i) + \bar{q}(p_j)$: $m_i = m_j = m_{ij} = m_q = 0$.

The processes where the particles are exchanged through their corresponding antiparticles are formally identical to those given here and are therefore not listed separately. The dipole splitting functions read explicitly

$$\langle s|\mathbf{V}^a_{gq}|s'\rangle = 8\pi\alpha_s\mu^{2\varepsilon}C_F\left(\frac{2}{2-x_{ij,a}-z_j}-2+\frac{1}{2}h_g^{\mathrm{RS}}z_i-\frac{m_j^2}{p_i\cdot p_j}\right)\delta_{ss'}=\langle\mathbf{V}^a_{gq}\rangle\delta_{ss'}\,, \tag{4.72a}$$

$$\langle s|\mathbf{V}^a_{g\tilde{q}}|s'\rangle = 8\pi\alpha_s\mu^{2\varepsilon}C_F\left(\frac{2}{2-x_{ij,a}-z_j}-2-\frac{m_j^2}{p_i\cdot p_j}\right)\delta_{ss'}=\langle\mathbf{V}^a_{g\tilde{q}}\rangle\delta_{ss'}\,, \tag{4.72b}$$

$$\langle \mu|\mathbf{V}^a_{gg}|\nu\rangle = 16\pi\alpha_s\mu^{2\varepsilon}C_A\left[-\eta^{\mu\nu}\left(\frac{1}{1+z_i-x_{ij,a}}+\frac{1}{2-z_i-x_{ij,a}}-2\right)+\frac{h_g^{\mathrm{RS}}}{2p_i\cdot p_j}\mathcal{C}^{\mu\nu}\right]\,, \tag{4.72c}$$

$$\langle \mu|\mathbf{V}^a_{q\bar{q}}|\nu\rangle = 8\pi\alpha_s\mu^{2\varepsilon}T_F\left(-\eta^{\mu\nu}-\frac{2}{p_i\cdot p_j}\mathcal{C}^{\mu\nu}\right)\,. \tag{4.72d}$$

In contrast to the work done in Refs. [261, 267], the dipole splitting functions for processes involving quarks and gluons in Eqs. (4.72a) and (4.72c) also include the number of helicity states of the gluon h_g^{RS} in order to distinguish directly between the different variants of dimensional regularization schemes. The dipole splitting function for the squarks in Eq. (4.72b) was derived by using the Eikonal approximation for a process involving the emission of a gluon off a squark. The function in Eq. (4.72a) for the splitting $q \to g + q$ is valid for a massive as well as a massless quark and the one in Eq. (4.72b) for the splitting $\tilde{q} \to g\tilde{q}$ can also be applied to the process $\tilde{g} \to g\tilde{g}$ since Eq. (4.72b) only contains the soft limit. The spin correlation tensor

$$\mathcal{C}^{\mu\nu} = \left(z_i^{(m)}p_i^\mu - z_j^{(m)}p_j^\mu\right)\left(z_i^{(m)}p_i^\nu - z_j^{(m)}p_j^\nu\right) \tag{4.73}$$

depending on the new variables

$$z_i^{(m)} = z_i - z_- = z_i - \frac{1}{2}\left(1-R(x)\right),\quad z_j^{(m)} = z_j - z_- = z_j - \frac{1}{2}\left(1-R(x)\right) \tag{4.74}$$

is constructed such that it reduces to $k_\perp^\mu k_\perp^\nu$ in the collinear limit as dictated by Eq. (4.58) and is at the same time orthogonal to the direction of the emitter

$$\tilde{p}_{ij}^\mu\mathcal{C}_{\mu\nu} = \tilde{p}_{ij}^\nu\mathcal{C}_{\mu\nu} = 0. \tag{4.75}$$

The orthogonality allows to simplify the integration of the non-diagonal dipole functions in helicity space over the one-particle phase space in Eq. (4.70) which is complicated due to the additional azimuthal correlations. However, the integral over the spin correlation tensor takes by Lorentz invariance (it can only depend on $\tilde{p}_{ij}$ and $\tilde{p}_a$) the form

$$\int\left[\mathrm{d}p_i\left(Q^2,P^2,z_i\right)\right]\mathcal{C}^{\mu\nu} = -A_1\eta^{\mu\nu}+A_2\frac{\tilde{p}_{ij}^\mu\tilde{p}_a^\nu+\tilde{p}_{ij}^\nu\tilde{p}_a^\mu}{\tilde{p}_{ij}\cdot\tilde{p}_a}-A_3\frac{m_a^2\tilde{p}_{ij}^\mu\tilde{p}_{ij}^\nu}{\left(\tilde{p}_{ij}\cdot\tilde{p}_a\right)^2}+A_4\frac{\tilde{p}_a^\mu\tilde{p}_a^\nu}{m_a^2}. \tag{4.76}$$

At this point, note that the metric tensor multiplying A_1 is quasi-D-dimensional as momenta are kept in D dimensions in all dimensional schemes. Due to the transversality condition on $\mathcal{C}_{\mu\nu}$ in Eq. (4.75) the term A_4 is zero and one finds additionally $A_1 = A_2$ such that the right hand side reduces to

$$-A_1\left(\eta^{\mu\nu}-\frac{\tilde{p}_{ij}^\mu\tilde{p}_a^\nu+\tilde{p}_{ij}^\nu\tilde{p}_a^\mu}{\tilde{p}_{ij}\cdot\tilde{p}_a}\right)-A_3\frac{m_a^2\tilde{p}_{ij}^\mu\tilde{p}_{ij}^\nu}{\left(\tilde{p}_{ij}\cdot\tilde{p}_a\right)^2}. \tag{4.77}$$

Therefore, A_1 can be disentangled by performing the azimuthal average over the transverse polarizations of the emitter

$$A_1 = \int \left[\mathrm{d}p_i \left(Q^2, P^2, z_i\right)\right] \frac{1}{D-2} d_{\mu\nu} \left(\tilde{p}_{ij}, \tilde{p}_a\right) \mathcal{C}^{\mu\nu} \tag{4.78}$$

with the help of the polarization tensor

$$d^{\mu\nu} \left(\tilde{p}_{ij}, \tilde{p}_a\right) = -\eta^{\mu\nu} + \frac{\tilde{p}^{\mu}_{ij}\tilde{p}^{\nu}_{a} + \tilde{p}^{\nu}_{ij}\tilde{p}^{\mu}_{a}}{\tilde{p}_{ij} \cdot \tilde{p}_a} - m_a^2 \frac{\tilde{p}^{\mu}_{ij}\tilde{p}^{\nu}_{ij}}{(\tilde{p}_{ij} \cdot \tilde{p}_a)^2} \tag{4.79}$$

which fulfills in D dimensions $d^{\mu\nu} d_{\mu\nu} = D-2$. The coefficient A_3 drops out in this computation since $d_{\mu\nu}\left(\tilde{p}_{ij}, \tilde{p}_a\right) \tilde{p}^{\mu}_{ij}\tilde{p}^{\nu}_{ij} = 0$. Furthermore, A_3 is irrelevant because of the Slavnov-Taylor identity $\tilde{p}^{\mu}_{ij}\mathcal{M}_{\mu} = 0$ which holds for any matrix element $\mathcal{M}_{\mu}$ in a Becchi-Rouet-Stora-Tyutin (BRST)-invariant theory where the polarization vector $\epsilon^{\mu}(\lambda, \tilde{p}_{ij})$ has been amputated if all other polarization vectors in $\mathcal{M}_{\mu}$ are transverse. This means in particular that the spin-averaged splitting functions $\langle \mathbf{V}^a_{ij} \rangle$ emerging from Eq. (4.78) are diagonal in helicity space, i.e., proportional to $-\eta^{\mu\nu}$. Concretely, they are

$$\langle \mathbf{V}^a_{gg} \rangle = 16\pi\alpha_s \mu^{2\varepsilon} C_A \left[\frac{1}{1+z_i - x_{ij,a}} + \frac{1}{2-z_i-x_{ij,a}} - 2 + \frac{h_g^{\mathrm{RS}}}{2(1-\varepsilon)} \left(z_+ - z_i\right)\left(z_i - z_-\right)\right], \tag{4.80a}$$

$$\langle \mathbf{V}^a_{q\bar{q}} \rangle = 8\pi\alpha_s \mu^{2\varepsilon} T_F \left(1 - \frac{2}{1-\varepsilon}(z_+ - z_i)(z_i - z_-)\right), \tag{4.80b}$$

where $z_{\pm}$ correspond to the integration limits in Eq. (4.71).

The Integrated Dipole Functions

The integral of the spin-averaged dipole function $\langle \mathbf{V}^a_{ij} \rangle$ over the dipole phase space is defined as

$$\frac{\alpha_s}{2\pi} \frac{1}{\Gamma(1-\varepsilon)} \left(\frac{4\pi\mu^2}{-\bar{Q}^2}\right)^{\varepsilon} I^a_{ij}\left(x; \varepsilon\right) = \int \left[\mathrm{d}p_i \left(Q^2, x, z_i\right)\right] \frac{1}{2p_i \cdot p_j} \frac{1}{x} \langle \mathbf{V}^a_{ij} \rangle, \tag{4.81}$$

where I^a_{ij} depends on the auxiliary variable x (and Q^2). As the cases $m_j \neq 0$ and $m_j = 0$ for the process $q \to gq$ have to be treated separately due to the presence of an additional collinear divergence in the massless case, the associated integrated dipole is marked with a hat $\hat{I}$ for $m_j = 0$ to distinguish it from the massive case. The integration generally proceeds through the integral representation of the Gauss hypergeometric function

$${}_2F_1(a, b; c; z) = \frac{\Gamma(c)}{\Gamma(b)\Gamma(c-b)} \int_0^1 \mathrm{d}t \, \frac{t^{b-1}(1-t)^{c-b-1}}{(1-zt)^a} \tag{4.82}$$

after applying the substitution $t = (z_i - z_-)/(z_+ - z_-)$ to bring the dipole phase space (4.70) into the form

$$\int_{z_-}^{z_+} \mathrm{d}z_i \left[\left(z_i - z_-\right)\left(z_+ - z_i\right)\right]^{-\varepsilon} = \left(z_+ - z_-\right)^{1-2\varepsilon} \int_0^1 \mathrm{d}t \left[(1-t)t\right]^{-\varepsilon}. \tag{4.83}$$

In particular, the function

$$\begin{aligned}I_1(z;\varepsilon) =& z\int_0^1 \mathrm{d}t\,\frac{((1-t)t)^{-\varepsilon}}{1-zt} = z\beta(1-\varepsilon,1-\varepsilon)\,{}_2F_1(1,1-\varepsilon;2-2\varepsilon;z)\\ =& -\ln(1-z)+\varepsilon\left(2\,\mathrm{Li}_2(z)+\frac{1}{2}\ln^2(1-z)\right)+\mathcal{O}(\varepsilon^2)\end{aligned} \tag{4.84}$$

with $A(x)=(z_+-z_-)/(1-x+z_-)$ and $\tilde{A}(x)=(z_+-z_-)/(2-x-z_-)$ as arguments appears several times. Its series expansion in ε is sketched in App. A.2 while the explicit expressions for the integrated counterparts $I^a_{ij}\,(x;\varepsilon)$ are collected in App. A.3.1.

Importantly, the functions I^a_{ij} feature an $1/(1-x)^\varepsilon$ behavior such that the infrared divergence appears at the endpoint $x\to 1$. The numerical integration over x becomes then feasible through the application of the $[...]^+$-distribution

$$g(x)=[g(x)]^+_{[a,b]}+\delta(x-b)\int_a^b \mathrm{d}y\,g(y) \tag{4.85}$$

which serves as an artificially inserted zero to render the endpoint contribution finite. In detail, this means that the integrated counterparts are decomposed into an infrared finite piece $\left[J^a_{ij}\,(x)\right]_+$ containing all the "plus"-distributions and the endpoint part which is further decomposed a finite $J^{a;\mathrm{NS}}_{ij}$ and singular $J^{a;\mathrm{S}}_{ij}$ piece containing the $1/\varepsilon$ and $1/\varepsilon^2$ poles:

$$I^a_{gq}\,(x;\varepsilon)=C_F\left\{\left[J^a_{gq}\,(x)\right]_+ +\delta(1-x)\left(J^{a;\mathrm{S}}_{gq}\,(\varepsilon)+J^{a;\mathrm{NS}}_{gq}\right)\right\}+\mathcal{O}(\varepsilon)\,, \tag{4.86a}$$

$$I^a_{g\tilde{q}}\,(x;\varepsilon)=C_F\left\{\left[J^a_{g\tilde{q}}\,(x)\right]_+ +\delta(1-x)\left(J^{a;\mathrm{S}}_{g\tilde{q}}\,(\varepsilon)+J^{a;\mathrm{NS}}_{g\tilde{q}}\right)\right\}+\mathcal{O}(\varepsilon)\,, \tag{4.86b}$$

$$I^a_{gg}\,(x;\varepsilon)=2C_A\left\{\left[J^a_{gg}\,(x)\right]_+ +\delta(1-x)\left(J^{a;\mathrm{S}}_{gg}\,(\varepsilon)+J^{a;\mathrm{NS}}_{gg}\right)\right\}+\mathcal{O}(\varepsilon)\,, \tag{4.86c}$$

$$I^a_{q\bar{q}}\,(x;\varepsilon)=T_F\left\{\left[J^a_{q\bar{q}}\,(x)\right]_+ +\delta(1-x)\left(J^{a;\mathrm{S}}_{q\bar{q}}\,(\varepsilon)+J^{a;\mathrm{NS}}_{q\bar{q}}\right)\right\}+\mathcal{O}(\varepsilon). \tag{4.86d}$$

For the two cases involving either a soft or a collinear divergence this decomposition proceeds practically through the identity

$$\int_{x_0}^1 \mathrm{d}x\,\frac{1}{(1-x)^{1+\varepsilon}}f(x)=\left(-\frac{1}{\varepsilon}+\ln(1-x_0)\right)f(1)+\int_{x_0}^1\mathrm{d}x\,\frac{1}{1-x}\left(f(x)-f(1)\right)+\mathcal{O}(\varepsilon)\,. \tag{4.87}$$

For gluon emission off massive (s)quarks the final results are

$$\left[J^a_{gq}\,(x)\right]_+ =\frac{2}{x^2}\left[\frac{1}{1-x}\right]^+_{[x_0,1]}\left(\frac{(x-1)^2}{4(x(\eta_j-1)+1)^2}-1+\frac{1}{vR(x)}\ln(1+A(x))\right)\,, \tag{4.88a}$$

$$\left[J^a_{g\tilde{q}}\,(x)\right]_+ =\frac{2}{x^2}\left[\frac{1}{1-x}\right]^+_{[x_0,1]}\left(\frac{1}{vR(x)}\ln(1+A(x))-1\right)\,, \tag{4.88b}$$

$$J^{a;\mathrm{S}}_{gq}\,(\varepsilon)=J^{a;\mathrm{S}}_{g\tilde{q}}\,(\varepsilon)=\frac{1}{\varepsilon}\left(1-\frac{1}{v}\ln(A+1)\right)\,, \tag{4.88c}$$

$$J^{a;\mathrm{NS}}_{gq}=J^{a;\mathrm{NS}}_{g\tilde{q}}=\frac{2}{v}\left(\frac{1}{2}(v-\ln(A+1))\ln\left(\frac{\eta_j}{(1-x_0)^2}\right)+v+\frac{1}{4}\ln^2(1+A)+\mathrm{Li}_2\,(-A)\right)\,. \tag{4.88d}$$

Recall that A is evaluated at $x=1$ in Eqs. (4.88c) and (4.88d). For the case of the splitting process

$g \to q\bar{q}$ the continuum and endpoint contributions are

$$\left[J^a_{q\bar{q}}\left(x\right)\right]_+ = \left[\frac{1}{1-x}\right]^+_{[x_0,1]} \frac{1}{x^2}\left(1-\frac{1}{3}R(x)^2\right) , \tag{4.89a}$$

$$J^{a;\mathrm{S}}_{q\bar{q}}\left(\varepsilon\right) = -\frac{2}{3\varepsilon} , \tag{4.89b}$$

$$J^{a;\mathrm{NS}}_{q\bar{q}} = -\frac{10}{9} + \frac{2}{3}\ln\left(1-x_0\right) . \tag{4.89c}$$

Obtaining the explicit form of the infrared poles for massless quarks in the splittings $q \to gq$ and $g \to gg$ is more involved due to the fact that besides the factor $1/\left(1-x\right)^{1+\varepsilon}$, the function $I_1(-A;\varepsilon)$ also diverges for $x \to 1$ corresponding to the soft-collinear divergence. As the expansion in ε of $I_1(-A;\varepsilon)$ is not analytic for $x = 1$, the hypergeometric function itself has to be placed in this case inside the $[...]^+$-distribution. This is achieved by introducing the argument of the hypergeometric function as the new integration variable $y_A(x) = 1/A(x) = (1-x)\mathcal{A}\left(x\right)$ with

$$\mathcal{A}\left(x\right) = \frac{2((1-\eta_a)x-2)}{\rho(2x-3-\rho)} \tag{4.90}$$

and $\rho = \sqrt{1+4\eta_a(x-1)x}$. In this new variable y_A only the integral

$$\mathcal{I}_1\left(y_0;\varepsilon\right) = \int_0^{y_0} \mathrm{d}y\, \frac{1}{y^{1+\varepsilon}} I_1\left(-\frac{1}{y},\varepsilon\right) = -\frac{1}{2\varepsilon^2} + \frac{\pi^2}{12} - \mathrm{Li}_2\left(-\frac{1}{y_0}\right) + \mathcal{O}(\varepsilon) \tag{4.91}$$

has to be computed analytically which is outlined in App. A.2. As the numerical integration of the $[...]^+$-distribution is still performed in terms of x, the derivative $y'_A(x) = \partial y_A(x)/\partial x = \left((3-4x)\eta_a - 1\right)/\rho^3$ has to be included inside the "plus"-distribution. The final results read then

$$\left[\hat{J}^a_{gq}\left(x\right)\right]_+ = \frac{2}{x^2}\left(-\frac{3}{4}\left[\frac{1}{1-x}\right]^+_{[x_0,1]} + \left[y'_A(x)A(x)\ln\left(1+A(x)\right)\right]^+_{[x_0,1]} \frac{\mathcal{A}(x)}{y'_A(x)R(x)}\right) , \tag{4.92a}$$

$$\hat{J}^{a;\mathrm{S}}_{gq}\left(\varepsilon\right) = \frac{1}{\varepsilon^2} + \frac{1}{\varepsilon}\left(\ln\left(1+\eta_a\right) + \frac{3}{2}\right) , \tag{4.92b}$$

$$\hat{J}^{a;\mathrm{NS}}_{gq} = \frac{1}{2}\ln^2\left(1+\eta_a\right) - \frac{3}{2}\ln\left(1-x_0\right) + 2\,\mathrm{Li}_2\left(-A(x_0)\right) + \frac{7-r}{2} - \frac{\pi^2}{6} , \tag{4.92c}$$

$$\left[J^a_{gg}\left(x\right)\right]_+ = \frac{1}{x^2}\left(\left[y'_A(x)A(x)\ln\left(1+A(x)\right)\right]^+_{[x_0,1]} \frac{2\mathcal{A}(x)}{y'_A(x)R(x)} + \left[\frac{1}{1-x}\right]^+_{[x_0,1]}\left(\frac{R(x)^2}{6} - 2\right)\right) , \tag{4.92d}$$

$$J^{a;\mathrm{S}}_{gg}\left(\varepsilon\right) = \frac{1}{\varepsilon^2} + \frac{1}{\varepsilon}\left(\ln\left(1+\eta_a\right) + \frac{11}{6}\right) , \tag{4.92e}$$

$$J^{a;\mathrm{NS}}_{gg} = \frac{1}{2}\ln^2\left(1+\eta_a\right) - \frac{11}{6}\ln\left(1-x_0\right) + 2\,\mathrm{Li}_2\left(-A(x_0)\right) + \frac{67}{18} - \frac{\pi^2}{6} - \frac{r}{6} . \tag{4.92f}$$

4.3.3 Initial-State Emitter and Final-State Spectator

The dipole $\mathcal{D}^{ai}_j$ in Eq. (4.59) is defined as

$$\mathcal{D}^{ai}_j = -\frac{1}{2p_a\cdot p_i}\frac{1}{x_{ij,a}}\; {}_{m,\widetilde{ai}}\Big\langle \ldots,\tilde{j},\ldots;\widetilde{ai},\ldots\Big|\, \frac{\mathbf{T}_j\cdot\mathbf{T}_{ai}}{\mathbf{T}^2_{ai}}\mathbf{V}^{ai}_j \,\Big|\ldots,\tilde{j},\ldots;\widetilde{ai},\ldots\Big\rangle_{m,\widetilde{ai}} , \tag{4.93}$$

where $\mathbf{V}_j^{ai}$ describes the splitting process $a \to i + \widetilde{ai}$. The tree-level matrix element is obtained from the original matrix element with $(m+1)$-particles in the final state by replacing the momentum p_a of the particle a in the tree-level matrix element by the dipole momentum $\tilde{p}_{ai}$, the momentum p_j of j by $\tilde{p}_j$ and discarding the final-state particle i. Similar to the previous section, only the case where the masses of a and $\widetilde{ai}$ are identical is treated.

Kinematics and Phase Space Factorization

The case of an initial-state emitter and final-state spectator is kinematically identical to the case of a final-state emitter and an initial-state spectator after switching the roles played by $\widetilde{ij}$ and a. Particle j takes over the role of the spectator and the associated dipole momenta are relabelled accordingly as $\tilde{p}_{ij} \to \tilde{p}_j$ and $\tilde{p}_a \to \tilde{p}_{ai}$. Therefore, the kinematics from Sec. 4.3.2 can be adopted completely.

The Dipole Splitting Functions

The function $\mathbf{V}_j^{ai}$ in Eq. (4.93) for the SUSY-QCD splitting process

- $\tilde{q}(p_a) \to g(p_i) + \tilde{q}$: $m_i = 0$ and $m_a = m_{\tilde{q}}$

in presence of a massive emitter $\widetilde{ai}$ reads

$$\langle \mathbf{V}_j^{\tilde{q}g} \rangle = 8\pi\alpha_s C_F \mu^{2\varepsilon} \left(\frac{2}{2 - x_{ij,a} - z_j} - 2 - \frac{m_a^2 x_{ij,a}}{p_a \cdot p_i} \right). \tag{4.94}$$

The same function holds for the gluino splitting process $\tilde{g} \to g\tilde{g}$ as well as for $q \to gq$ involving a massive quark as Eq. (4.94) only accounts for the soft limit. For the gluino, only the color factor C_F has to be replaced by C_A.

The Integrated Dipole Functions

Similar to before, the integral of the spin-averaged dipole function $\langle \mathbf{V}_j^{ai} \rangle$ over the dipole phase space is defined as

$$\frac{\alpha_s}{2\pi} \frac{1}{\Gamma(1-\varepsilon)} \left(\frac{4\pi\mu^2}{-\bar{Q}^2} \right)^{\varepsilon} I_j^{a,\widetilde{ai}}(x;\varepsilon) = \int \left[\mathrm{d}p_i \left(Q^2, x, z_i \right) \right] \frac{1}{2p_a \cdot p_i} \frac{1}{x} \langle \mathbf{V}_j^{ai} \rangle \tag{4.95}$$

and the intermediate results for the integrated dipoles are collected in App. A.3.2. As in the previous section, the integral over the dipole phase space can be performed again by using the Gauss hypergeometric function, however, besides $I_1(z;\epsilon)$ also the function

$$\begin{aligned} I_2(z;\varepsilon) &= z \int_0^1 \mathrm{d}t \, \frac{((1-t)t)^{-\varepsilon}}{(1-zt)^2} = z\beta(1-\varepsilon, 1-\varepsilon) \, {}_2F_1(2, 1-\varepsilon; 2-2\varepsilon; z) \\ &= \frac{z}{1-z} + \varepsilon \frac{2-z}{z-1} \ln(1-z) + \mathcal{O}(\varepsilon^2) \end{aligned} \tag{4.96}$$

is needed accompanied by the additional argument $B(x) = (z_+ - z_-)/z_-$ next to $A(x)$. The extraction of the divergences proceeds then again through a decomposition of the form

$$I_j^{\tilde{q}\tilde{q}}(x;\varepsilon) = C_F \left\{ \left[J_j^{\tilde{q}\tilde{q}}(x) \right]_+ + \delta(1-x) \left(J_j^{\tilde{q}\tilde{q};\mathrm{S}}(\varepsilon) + J_j^{\tilde{q}\tilde{q};\mathrm{NS}} \right) \right\} + \mathcal{O}(\varepsilon) \tag{4.97}$$

involving the "plus"-distribution. For the massive case, using Eq. (4.87), the decomposition is straightforward and results in

$$\begin{aligned}
\left[J_j^{\tilde{q}\tilde{q}}(x)\right]_+ &= \left[\frac{1}{1-x}\right]^+_{[x_0,1]} \\
&\qquad \times \frac{2}{vR(x)x^2}\left(x\ln(1+B(x)) - \ln(1+A(x)) - 4\eta_a x^2 \frac{(\eta_j-1)x+1}{1-v^2R(x)^2} vR(x)\right) , && (4.98\text{a}) \\
J_j^{\tilde{q}\tilde{q};\mathrm{S}}(\varepsilon) &= \frac{1}{\varepsilon}\left(1 - \frac{1}{v}\ln\left(\frac{1+B}{1+A}\right)\right) , && (4.98\text{b}) \\
J_j^{\tilde{q}\tilde{q};\mathrm{NS}} &= \frac{1}{v}\left(\left(v + \ln\left(\frac{1+A}{1+B}\right)\right)\ln\left(\frac{\eta_j}{(1-x_0)^2}\right) + \ln(1+B)\right. \\
&\qquad \left. + \frac{1}{2}\left[\ln^2(1+B) - \ln^2(1+A)\right] + 2\,\mathrm{Li}_2\left(-B\right) - 2\,\mathrm{Li}_2\left(-A\right)\right) . && (4.98\text{c})
\end{aligned}$$

Performing this decomposition on the other hand in the massless case $m_j = 0$ is again more involved due to the presence of a soft-collinear divergence but it is possible to proceed as before by introducing the variable $y_B(x) = 1/B(x) = (1-x)\mathcal{B}(x)$ as the new integration variable with $\mathcal{B}(x) = 2\eta_a x/(\rho^2+\rho)$ and by then employing the integral

$$\mathcal{I}_2(y_0;\varepsilon) = \int_0^{y_0} \mathrm{d}y\, \frac{1}{y^{1+\varepsilon}} I_2\left(-\frac{1}{y};\varepsilon\right) = \frac{1}{2\varepsilon} + \ln\left(1 + \frac{1}{y_0}\right) + \mathcal{O}(\varepsilon) . \tag{4.99}$$

For its derivation see App. A.2. Due to the change of variables from x to y_B the derivative $y'_B(x) = \partial y_B(x)/\partial x = \eta_a(1-2x)/\rho^3$ has to be placed inside the $[\ldots]^+$-distribution. The different contributions to Eq. (4.97) in the massless case are then

$$\begin{aligned}
\left[\hat{J}_j^{\tilde{q}\tilde{q}}(x)\right]_+ &= \frac{2}{R(x)x}\left(\left[y'_B(x)B(x)\ln\left(1+B(x)\right)\right]^+_{[x_0,1]} \frac{\mathcal{B}(x)}{y'_B(x)}\right. \\
&\left. - \left[y'_A(x)A(x)\ln\left(1+A(x)\right)\right]^+_{[x_0,1]} \frac{\mathcal{A}(x)}{x y'_A(x)} - \left[y'_B(x)\frac{B^2(x)}{1+B(x)}\right]^+_{[x_0,1]} \frac{\mathcal{B}(x)}{2y'_B(x)}\left(1+R(x)\right)\right) ,
\end{aligned} \tag{4.100}$$

$$\hat{J}_j^{\tilde{q}\tilde{q};\mathrm{S}}(\varepsilon) = \frac{1}{\varepsilon}\left(1 - \ln\left(\frac{1+\eta_a}{\eta_a}\right)\right) , \tag{4.101}$$

$$\hat{J}_j^{\tilde{q}\tilde{q};\mathrm{NS}} = \frac{1}{2}\ln^2\left(\eta_a\right) + \ln\left(\eta_a\right) - \frac{1}{2}\ln^2\left(1+\eta_a\right) - 2\,\mathrm{Li}_2\left(-A(x_0)\right) + 2\,\mathrm{Li}_2\left(-B(x_0)\right) + 2\ln\left(1+B(x_0)\right) . \tag{4.102}$$

4.3.4 Initial-State Emitter and Initial-State Spectator

The dipole for emitter and spectator both from the initial state is defined as

$$\mathcal{D}^{ai,b} = \frac{1}{-2p_a\cdot p_i}\frac{1}{x_{i,ab}}\, {}_{m,ab}\!\left\langle \tilde{1}, ..., \widetilde{m+1}; \widetilde{ai}, b\right| \frac{\mathbf{T}_b\cdot\mathbf{T}_{ai}}{\mathbf{T}^2_{ai}} \mathbf{V}^{ai,b} \left|\tilde{1}, ..., \widetilde{m+1}; \widetilde{ai}, b\right\rangle_{m,ab} , \tag{4.103}$$

where the m-particle matrix element is obtained by discarding the particle i in the $(m+1)$-particle matrix element and rescaling the momenta p_k of all other final state particles to their dipole analogues $\tilde{p}_k$ as well as p_a to $\tilde{p}_{ai}$ while the momentum of the spectator p_b remains unchanged. The operator $\mathbf{V}^{ai,b}$ in Eq. (4.103) describes the splitting $a \to \widetilde{ai} + i$.

Kinematics and Phase Space Factorization

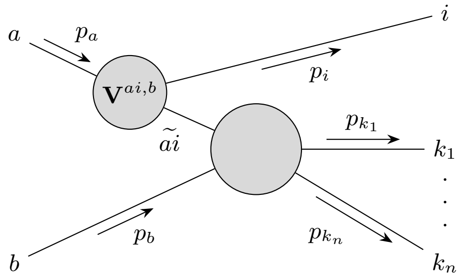

Figure 4.4: Diagrammatic interpretation of the dipole $\mathcal{D}^{ai,b}$ and the associated splitting function $\mathbf{V}^{ai,b}$.

For the parametrization of the divergences, the auxiliary variables

$$x_{i,ab} = \frac{p_a \cdot p_b - p_i \cdot p_a - p_i \cdot p_b}{p_a \cdot p_b}\,, \qquad y = \frac{p_a \cdot p_i}{p_a \cdot p_b} \tag{4.104}$$

are used which behave in the soft limit $p_i^\mu \to 0$ as $x_{i,ab} \to 1$ and $y \to 0$. The sum of all outgoing momenta p_k except for the soft gluon is denoted by

$$P = p_a + p_b - p_i = \sum_k p_k\,, \tag{4.105}$$

cf. Figs. 4.4 and 4.5. Furthermore, it is convenient to define the abbreviations

$$\lambda_{ab} = \lambda\left(s, m_a^2, m_b^2\right) = \overline{s}^2 - 4m_a^2 m_b^2\,, \tag{4.106a}$$

$$\overline{s} = s - m_a^2 - m_b^2\,. \tag{4.106b}$$

The construction of the dipole momenta is different from the previous two cases. Instead of modifying only the momenta of emitter and spectator, the momentum of the spectator p_b remains unchanged whereas all other momenta are modified. The new momenta

$$\tilde{p}_{ai}^\mu = \sqrt{\frac{\lambda\left(P^2, m_a^2, m_b^2\right)}{\lambda_{ab}}}\, p_a^\mu + \left(\frac{P^2 - m_a^2 - m_b^2}{2m_b^2} - \frac{p_a \cdot p_b}{m_b^2}\sqrt{\frac{\lambda\left(P^2, m_a^2, m_b^2\right)}{\lambda_{ab}}}\right) p_b^\mu\,, \tag{4.107a}$$

$$\tilde{P}^\mu = \tilde{p}_{ai}^\mu + p_b^\mu \tag{4.107b}$$

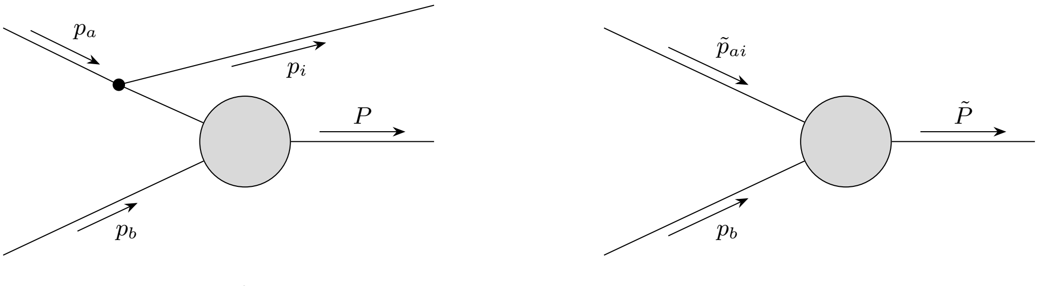

Figure 4.5: Kinematics for an initial-state emitter and an initial-state spectator in the original momenta (left) and the dipole momenta (right).

are then built from the requirement to retain the mass-shell relations $\tilde{p}_{ai}^2 = m_{ai}^2$ and $\tilde{P}^2 = P^2$. The outgoing momenta p_k except for p_i are modified by a Lorentz transformation $\tilde{p}_k^\mu = \Lambda^\mu{}_\nu p_k^\nu$ with

$$\Lambda^\mu{}_\nu = \eta^\mu{}_\nu - \frac{\left(P+\tilde{P}\right)^\mu \left(P+\tilde{P}\right)_\nu}{P^2 + P\cdot\tilde{P}} + \frac{2\tilde{P}^\mu P_\nu}{P^2}. \tag{4.108}$$

If follows from direct calculation that $\Lambda^\mu{}_\nu$ indeed leaves the Minkowski metric invariant $\Lambda_\rho{}^\mu \Lambda^{\rho\nu} = \eta^{\mu\nu}$ such that it can be verified easily that the new momenta $\tilde{p}_k$ obey the on-shell condition $\tilde{p}_k^2 = m_k^2$. The definition of these momenta coincides with [266]. In order to ensure that $\lambda\left(P^2, m_a^2, m_b^2\right)$ remains positive, so that the dipole momenta take only real values, the kinematical lower bound

$$x_{i,ab} > x_0 \geq \hat{x} = \frac{2m_a m_b}{\bar{s}} \tag{4.109}$$

on $x_{i,ab}$ has to be enforced. For values of $x_{i,ab}$ below x_0 the splitting functions $\mathbf{V}^{ai,b}$ are set to zero. The dependence on the lower bound x_0 must cancel out and can therefore be chosen arbitrarily which offers the possibility to check whether the implementation of the subtraction procedure is correct. The factorization of the single-particle phase space $[\mathrm{d}p_i\,(s,x,y)]$ from the $(m+1)$-particle phase space $\mathrm{d}\phi_{m+1}\,(p_i, P; p_a + p_b)$ is derived in App. A.1.2. It corresponds to a convolution over x which plays the role of $x_{i,ab}$

$$\int \mathrm{d}\phi_{m+1}\,(p_i, P; p_a + p_b)\,\theta(x_{i,ab} - x_0) = \int_{x_0}^1 \mathrm{d}x \int \mathrm{d}\phi_m\,(\tilde{p}_k(x); \tilde{p}_{ai}(x) + p_b) \int [\mathrm{d}p_i\,(s,x,y)]\,. \tag{4.110}$$

In $D = 4 - 2\varepsilon$ dimensions the dipole phase space becomes

$$\int [\mathrm{d}p_i\,(s,x,y)] = \frac{\bar{s}^{2-2\varepsilon}}{(4\pi)^{2-\varepsilon}\Gamma(1-\varepsilon)} \frac{s^{-\varepsilon}}{\sqrt{\lambda_{ab}}^{1-2\varepsilon}} \int_{y_-}^{y_+} \mathrm{d}y\,[(y-y_-)(y_+-y)]^{-\varepsilon} \tag{4.111}$$

where the integration boundaries read

$$y_\pm = \frac{1-x}{2s}\left(\bar{s} + 2m_a^2 \pm \sqrt{\lambda_{ab}}\right). \tag{4.112}$$

From Eq. (4.107b) it can be deduced that the squared c.m. energy

$$\tilde{s} = P^2 = \bar{s}x + m_a^2 + m_b^2 \tag{4.113}$$

of the reduced phase space $\mathrm{d}\phi_m\,(\tilde{p}_k(x); \tilde{p}_{ai}(x) + p_b)$ is already determined through x and the original c.m. energy $\sqrt{s}$.

The Dipole Splitting Function

The dipole function $\mathbf{V}^{ai,b}$ in Eq. (4.103) for the SUSY-QCD process

- $\tilde{q}(p_a) \to g(p_i) + \tilde{q}$: $m_i = 0$ and $m_{ai} = m_a = m_{\tilde{q}}$

reads

$$\langle \mathbf{V}^{\tilde{q}g,b} \rangle = 8\pi\alpha_s\mu^{2\varepsilon} C_F \left(\frac{2}{1-x_{i,ab}} - 2 - \frac{x_{i,ab} m_a^2}{p_a \cdot p_i}\right). \tag{4.114}$$

The dipole splitting functions for the processes involving a gluino $\tilde{g} \to g\tilde{g}$ and a massive quark

$q \to gq$ are for the pure soft limit identical to Eq. (4.114) where only the color factor C_F has to be replaced by C_A for the gluino. For this reason, only the squark splitting function is treated in the following without losing generality. The same splitting function holds if the squark is replaced by an antisquark.

The Integrated Dipole Functions

In complete analogy to previous cases, the integrated dipole for the case of emitter and spectator both from the initial state is defined as

$$\frac{\alpha_s}{2\pi} \frac{1}{\Gamma(1-\varepsilon)} \left(\frac{4\pi\mu^2}{\bar{s}}\right)^{\varepsilon} I^{a,\widetilde{ai},b}(x;\varepsilon) = \int \left[\mathrm{d}p_i\left(s,x,y\right)\right] \frac{1}{2p_a \cdot p_i} \frac{1}{x_{i,ab}} \langle \mathbf{V}^{ai,b} \rangle \tag{4.115}$$

and the integration can be performed again with the help of the already known integrals $I_1(z;\varepsilon)$ and $I_2(z;\varepsilon)$ after rewriting the denominator in the dipole as $2p_a \cdot p_i = y\bar{s}$ and applying the substitution $t = (y - y_-)/(y_+ - y_-)$ in the dipole phase space (4.110):

$$\int_{y_-}^{y_+} \mathrm{d}y \left[\left(y - y_-\right)\left(y_+ - y\right)\right]^{-\varepsilon} = \left(y_+ - y_-\right)^{1-2\varepsilon} \int_0^1 \mathrm{d}t \left[(1-t)t\right]^{-\varepsilon} \, . \tag{4.116}$$

The integrated counterpart of the splitting function (4.114) then reads

$$I^{\tilde{q}\tilde{q},b}(x;\varepsilon) = \frac{C_F}{\sqrt{\lambda_{ab}}} \frac{2}{(1-x)^{1+2\varepsilon}} \left(\frac{s}{\bar{s}}\right)^{\varepsilon} \left(\frac{2m_a^2 s}{d_1} I_2(-C;\varepsilon) - \bar{s} I_1(-C;\varepsilon)\right) \, , \tag{4.117}$$

where the new auxiliary variables C and d_1 are defined as

$$C = \frac{y_+ - y_-}{y_-} = \frac{2\sqrt{\lambda_{ab}}}{d_1}, \quad d_1 = \bar{s} + 2m_a^2 - \sqrt{\lambda_{ab}} \, . \tag{4.118}$$

Since only massive initial states are considered here, it is safe to use the series expansions of I_1 and I_2. As before, the soft divergence is disentangled with the help of the $[\dots]^+$-prescription according to

$$I^{\tilde{q}\tilde{q},b}(x;\varepsilon) = C_F \left\{ \left[J^{\tilde{q}\tilde{q},b}(x)\right]_+ + \delta(1-x) \left[J^{\tilde{q}\tilde{q},b;\mathrm{S}}(\varepsilon) + J^{\tilde{q}\tilde{q},b;\mathrm{NS}}\right] \right\} + \mathcal{O}(\varepsilon) \, , \tag{4.119}$$

where the continuum part containing the “plus”-distribution and the endpoint parts are given by

$$\left[J^{\tilde{q}\tilde{q},b}(x)\right]_+ = 2 \left[\frac{1}{1-x}\right]^+_{[x_0,1]} \left(d_2 \ln(1+C) - 1\right) , \tag{4.120a}$$

$$J^{\tilde{q}\tilde{q},b;\mathrm{S}}(\varepsilon) = \frac{1}{\varepsilon} \left(1 - d_2 \ln(1+C)\right) \, , \tag{4.120b}$$

$$\begin{aligned} J^{\tilde{q}\tilde{q},b;\mathrm{NS}} = \frac{1}{C} \ln(1+C)\,(C+2) + \frac{d_2}{2} \left(4\,\mathrm{Li}_2(-C) + \ln^2(1+C)\right) \\ + \left(1 - d_2 \ln(1+C)\right) \ln\left(\frac{s}{\bar{s}(1-x_0)^2}\right) \end{aligned} \tag{4.120c}$$

with $d_2 = \bar{s}/\sqrt{\lambda_{ab}}$.

4.3.5 Examples and Comparison with the Phase Space Slicing Method

To exemplify the usage of the generalized dipole method, it is applied to the processes $\tilde{\chi}_1^0\tilde{t}_1 \to tg$ and $\tilde{t}_1\tilde{t}_1 \to tt$ which are already part of DM@NLO. The correct implementation is then verified by comparing the resulting full $\mathcal{O}(\alpha_s)$ corrections numerically with the ones obtained with the phase space slicing method that was originally used for these two processes. In more detail, for the first process with a top quark and a gluon in the final state the two-cutoff phase space slicing method was used. Within this approach the three particle phase space is split into a hard and a soft part by imposing a soft cutoff δ_s on the energy of the radiated gluon. The hard phase space region is split further into a hard and collinear as well as a hard and non-collinear part through a collinear cutoff δ_c:

$$\sigma^{\mathrm{R}} = \sigma^{\mathrm{hard}}_{\mathrm{coll}}(\delta_s, \delta_c) + \sigma^{\mathrm{hard}}_{\text{non-coll}}(\delta_s, \delta_c) + \sigma^{\mathrm{soft}}(\delta_s). \tag{4.121}$$

If there occurs no collinear divergence, as in the second process under consideration with two top quarks in the final state, the soft cutoff is already sufficient. In this way the real emission cross section σ^{R} is split into a finite part $\sigma^{\mathrm{hard}}_{\text{non-coll}}(\delta_s, \delta_c)$, which is safe for numerical evaluation in four dimensions, whereas the two other parts have to be integrated analytically in D dimensions to isolate the infrared poles. For the numerical comparison the "Scenario I" in the pMSSM-19 from Ref. [169] is used along with the hybrid on-shell/$\overline{\mathrm{DR}}$ renormalization scheme 1 introduced in Sec. 4.2.4. The corresponding soft-breaking parameters are reproduced for convenience in Tab. 4.1 with all input parameters defined at the SUSY-scale $Q^2_{\mathrm{SUSY}} = m^{\mathrm{Tree}}_{\tilde{t}_1} m^{\mathrm{Tree}}_{\tilde{t}_2}$, which is also taken to be the renormalization scale $\mu_R = Q_{\mathrm{SUSY}}$. The associated physical mass spectrum is computed with the public spectrum generator SPheno 3.3.3 [274,275]. The most relevant masses for the two given processes such as the mass of the lightest neutralino, the lightest stop and the gluino are shown in Tab. 4.1 as well. For all considered processes the integration of the three particle phase space and of the "plus"-distribution within the dipole subtraction method is performed by employing the VEGAS adaptive Monte Carlo integration algorithm [276] from the CUBA-1.1 library [277], whereas the two particle phase space is integrated with the non-adaptive Gauss-Kronrod-Patterson integration routine from FormCalc [278]. Both algorithms also provide an estimate on the numerical error. These are combined to the total numerical error of the NLO correction

M_1	M_2	M_3	$M_{\tilde{l}_L}$	$M_{\tilde{\tau}_L}$	$M_{\tilde{l}_R}$	$M_{\tilde{\tau}_R}$	$M_{\tilde{q}_L}$	$M_{\tilde{q}_{3L}}$	$M_{\tilde{u}_R}$
1278.5	2093.5	1267.2	3134.1	1503.9	2102.5	1780.4	3796.6	2535.1	3995.0
$M_{\tilde{t}_R}$	$M_{\tilde{d}_R}$	$M_{\tilde{b}_R}$	A_t	A_b	A_τ	μ	m_{A^0}	$\tan\beta$	Q_{SUSY}
1258.7	3133.2	3303.8	2755.3	2320.9	-1440.3	-3952.6	3624.8	15.5	1784.6

$m_{\tilde{\chi}_1^0}$	$m_{\tilde{\chi}_2^0}$	$m_{\tilde{\chi}_1^\pm}$	$m_{\tilde{t}_1}$	$m_{\tilde{b}_1}$	$m_{\tilde{g}}$	m_{h^0}	m_{H^0}
1279.7	2153.6	2153.5	1301.9	2554.2	1495.5	125.8	3625.6

Table 4.1: Reference scenario within the pMSSM-19 and the corresponding physical mass spectrum for the numerical comparison. All dimensionful quantities are given in GeV.

$$\varepsilon_{\mathrm{NLO}} = \sqrt{\varepsilon^2_{\mathrm{plus}} + \varepsilon^2_{\mathrm{V}} + \varepsilon^2_{\mathrm{R}}}, \tag{4.122}$$

computed as the geometric mean of the respective numerical errors of the “plus”-distribution ($\varepsilon_{\text{plus}}$), the virtual ($\varepsilon_{\text{V}}$) and the real ($\varepsilon_{\text{R}}$) contribution. For the PSS approach, $\varepsilon_{\text{plus}}$ is set to zero.

The Process $\tilde{\chi}_1^0\tilde{t}_1 \to tg$

The $\mathcal{O}(\alpha_s)$ SUSY-QCD corrections to neutralino-stop coannihilation into a gluon and a top quark have been discussed in Ref. [165] including a detailed account on the application of the phase space slicing method with two cutoffs.

At NLO, the process $\tilde{\chi}_1^0\tilde{t}_1 \to tg$ receives contributions from the two real emission processes

$$\tilde{t}_1(p_a) + \tilde{\chi}_1^0(p_b) \longrightarrow t(p_1) + g(p_2) + g(p_3) \tag{4.123}$$

and

$$\tilde{t}_1(p_a) + \tilde{\chi}_1^0(p_b) \longrightarrow t(p_1) + q(p_2) + \bar{q}(p_3). \tag{4.124}$$

The splitting of a gluon into a massless quark-antiquark pair has to be included, since the first four quark flavors $N_f = 4$ are treated as effectively massless in DM@NLO. For a process involving only three colored particles, the different color projections fully factorize in terms of the associated quadratic Casimirs. Therefore, it is not necessary to calculate any color-correlated tree amplitudes thanks to the relation

$$2\mathbf{T}_2 \cdot \mathbf{T}_3 \left|1,2,3\right\rangle = \left(\mathbf{T}_1^2 - \mathbf{T}_2^2 - \mathbf{T}_3^2\right) \left|1,2,3\right\rangle , \tag{4.125}$$

which holds analogously for $\mathbf{T}_1 \cdot \mathbf{T}_3$ and $\mathbf{T}_1 \cdot \mathbf{T}_2$. The dipole factorization formula in Eq. (4.59) yields a total of ten dipoles to compensate all infrared divergences in the three-particle phase space for the process with two final-state gluons,

$$\mathcal{D}_{31,2} = \frac{1}{2p_1 \cdot p_3} \frac{C_A}{2C_F} \langle \mathbf{V}_{g_3 t_1,2} \rangle |\mathcal{M}_2\left(p_a, \tilde{p}_{31}, \tilde{p}_2\right)|^2 , \tag{4.126a}$$

$$\mathcal{D}_{21,3} = \frac{1}{2p_1 \cdot p_2} \frac{C_A}{2C_F} \langle \mathbf{V}_{g_2 t_1,3} \rangle |\mathcal{M}_2\left(p_a, \tilde{p}_{21}, \tilde{p}_3\right)|^2 , \tag{4.126b}$$

$$\mathcal{D}_{23,1} = \frac{1}{2p_2 \cdot p_3} \frac{1}{2} \langle \mu | \mathbf{V}_{g_2 g_3,1} | \nu \rangle \mathcal{T}_{\mu\nu}\left(p_a, \tilde{p}_1, \tilde{p}_{23}\right) , \tag{4.126c}$$

$$\mathcal{D}_{23}^{a} = \frac{1}{2p_2 \cdot p_3} \frac{1}{x_{23,a}} \frac{1}{2} \langle \mu | \mathbf{V}_{g_2 g_3}^{a} | \nu \rangle \mathcal{T}_{\mu\nu}\left(\tilde{p}_a, p_1, \tilde{p}_{23}\right) , \tag{4.126d}$$

$$\mathcal{D}_{31}^{a} = \frac{1}{2p_1 \cdot p_3} \frac{1}{x_{31,a}} \left(1 - \frac{C_A}{2C_F}\right) \langle \mathbf{V}_{g_3 t_1}^{a} \rangle |\mathcal{M}_2\left(\tilde{p}_a, \tilde{p}_{31}, p_2\right)|^2 , \tag{4.126e}$$

$$\mathcal{D}_{21}^{a} = \frac{1}{2p_1 \cdot p_2} \frac{1}{x_{21,a}} \left(1 - \frac{C_A}{2C_F}\right) \langle \mathbf{V}_{g_2 t_1}^{a} \rangle |\mathcal{M}_2\left(\tilde{p}_a, \tilde{p}_{21}, p_3\right)|^2 , \tag{4.126f}$$

$$\mathcal{D}_{2}^{a3} = \frac{1}{2p_a \cdot p_3} \frac{1}{x_{32,a}} \frac{C_A}{2C_F} \langle \mathbf{V}_{2}^{\tilde{t}_{1,a} g_3} \rangle |\mathcal{M}_2\left(\tilde{p}_{a3}, p_1, \tilde{p}_2\right)|^2 , \tag{4.126g}$$

$$\mathcal{D}_{3}^{a2} = \frac{1}{2p_a \cdot p_2} \frac{1}{x_{23,a}} \frac{C_A}{2C_F} \langle \mathbf{V}_{3}^{\tilde{t}_{1,a} g_2} \rangle |\mathcal{M}_2\left(\tilde{p}_{a2}, p_1, \tilde{p}_3\right)|^2 , \tag{4.126h}$$

$$\mathcal{D}_{1}^{a3} = \frac{1}{2p_a \cdot p_3} \frac{1}{x_{31,a}} \left(1 - \frac{C_A}{2C_F}\right) \langle \mathbf{V}_{1}^{\tilde{t}_{1,a} g_3} \rangle |\mathcal{M}_2\left(\tilde{p}_{a3}, \tilde{p}_1, p_2\right)|^2 , \tag{4.126i}$$

$$\mathcal{D}_{1}^{a2} = \frac{1}{2p_a \cdot p_2} \frac{1}{x_{21,a}} \left(1 - \frac{C_A}{2C_F}\right) \langle \mathbf{V}_{1}^{\tilde{t}_{1,a} g_2} \rangle |\mathcal{M}_2\left(\tilde{p}_{a2}, \tilde{p}_1, p_3\right)|^2 \tag{4.126j}$$

with the squared tree-level matrix element $|\mathcal{M}_2\left(p_{\tilde{t}_1}, p_t, p_g\right)|^2$. The tensor $\mathcal{T}_{\mu\nu}$ corresponds to the squared leading-order amplitude where the polarization vector $\epsilon^\mu\left(\lambda, \tilde{p}_{ij}\right)$ of the emitter gluon has been amputated. Since both gluons can become soft in the splittings $\tilde{t}_1 \to \tilde{t}_1 g$ and $t \to tg$, one dipole is introduced for each individual gluon in the final state. To cancel the collinear divergences from the production of the N_f massless quark-antiquark pairs, the two dipoles

$$\mathcal{D}_{23,1} = \frac{1}{2p_2 \cdot p_3} \frac{1}{2} \langle \mu | \mathbf{V}_{q_2\bar{q}_3,1} | \nu \rangle \mathcal{T}_{\mu\nu}\left(p_a, \tilde{p}_{23}, \tilde{p}_1\right), \tag{4.127a}$$

$$\mathcal{D}_{23}^a = \frac{1}{2p_2 \cdot p_3} \frac{1}{x_{23,a}} \frac{1}{2} \langle \mu | \mathbf{V}^a_{q_2\bar{q}_3} | \nu \rangle \mathcal{T}_{\mu\nu}\left(\tilde{p}_a, p_1, \tilde{p}_{23}\right) \tag{4.127b}$$

are needed as well. Then, the auxiliary cross section that cancels the infrared divergences of the virtual one-loop corrections is constructed from the three insertion operators

$$\begin{aligned}\langle 1,2,3 | \, \mathbf{I}_2(\varepsilon, \mu^2, \{p_i, m_i\}) \, | 1,2,3 \rangle &= \frac{\alpha_s}{4\pi} \frac{(4\pi)^\varepsilon}{\Gamma(1-\varepsilon)} |\mathcal{M}_2|^2 \\ \times \Bigg[C_A \left(\frac{\mu^2}{s_{12}}\right)^\varepsilon & \left(2\mathcal{V}^{(\mathrm{S})}\left(s_{12}, m_t, 0; \varepsilon\right) + \mathcal{V}_g^{(\mathrm{NS})}\left(s_{12}, 0, m_t; \kappa\right) + \mathcal{V}_t^{(\mathrm{NS})}\left(s_{12}, m_t, 0\right) - \frac{2\pi^2}{3} \right) \\ + \Gamma_g^{\mathrm{FDH}}(\varepsilon) + \gamma_g \ln\left(\frac{\mu^2}{s_{12}}\right) + \gamma_g + K_g &+ \frac{C_A}{C_F} \left(\Gamma_t\left(\mu, m_t; \varepsilon\right) + \gamma_t \ln\left(\frac{\mu^2}{s_{12}}\right) + \gamma_t + K_t \right) \Bigg], \end{aligned} \tag{4.128}$$

$$\begin{aligned}\langle 1,2,3 | \, \mathbf{I}_{2,\tilde{t}_1}\left(x; \varepsilon, \mu^2; \{p_i, m_i\}, p_a\right) | 1,2,3 \rangle &= \frac{\alpha_s}{4\pi} \frac{(4\pi)^\varepsilon}{\Gamma(1-\varepsilon)} |\mathcal{M}_2|^2 \\ \times \left(\left(\frac{\mu^2}{-\bar{\tilde{t}}}\right)^\varepsilon \mathcal{V}_g(x, \tilde{t}, 0; \varepsilon) \right. &+ \left. \left(2 - \frac{C_A}{C_F}\right) \left(\frac{\mu^2}{-\bar{\tilde{u}}}\right)^\varepsilon \mathcal{V}_t(x, \tilde{u}, m_t; \varepsilon) \right), \end{aligned} \tag{4.129}$$

$$\begin{aligned}\langle 1,2,3 | \, \mathbf{I}_{2,\tilde{q}\tilde{q}}\left(x; \varepsilon, \mu^2; \{p_i, m_i\}, p_a\right) | 1,2,3 \rangle &= \frac{\alpha_s}{4\pi} \frac{(4\pi)^\varepsilon}{\Gamma(1-\varepsilon)} |\mathcal{M}_2|^2 \\ \times \left(\frac{C_A}{C_F} \left(\frac{\mu^2}{-\bar{\tilde{t}}}\right)^\varepsilon \mathcal{V}^{\tilde{q},\tilde{q}}(x, \tilde{t}, 0; \varepsilon) \right. &+ \left. \left(2 - \frac{C_A}{C_F}\right) \left(\frac{\mu^2}{-\bar{\tilde{u}}}\right)^\varepsilon \mathcal{V}^{\tilde{q},\tilde{q}}(x, \tilde{u}, m_t; \varepsilon) \right) \end{aligned} \tag{4.130}$$

with $s_{12} = s - m_t^2$ where the first one in Eq. (4.128) corresponds to emitter and spectator both from the final state, the second one in Eq. (4.129) to final-state emitters with the spectator from the initial state and the last one in Eq. (4.130) to an initial-state emitter with final-state spectators. The dipole invariants $\tilde{t} = (\tilde{p}_{\tilde{t}_1} - \tilde{p}_g)^2$ and $\tilde{u} = (\tilde{p}_{\tilde{t}_1} - \tilde{p}_t)^2$ correspond to the Mandelstam variables $t = (p_{\tilde{t}_1} - p_g)^2$ and $u = (p_t - p_{\tilde{t}_1})^2$ in the squared Born amplitude and they play the role of Q^2. With that, the "barred variables" $\bar{\tilde{t}}$ and $\bar{\tilde{u}}$ are given by

$$\bar{\tilde{t}} = \tilde{t} - m_{\tilde{t}_1}^2, \qquad \bar{\tilde{u}} = \tilde{u} - m_{\tilde{t}_1}^2 - m_t^2. \tag{4.131}$$

The insertion operator in Eq. (4.128) for emitter and spectator both from the final state as well as the related flavor functions given by

$$\mathcal{V}^{(\mathrm{S})}\left(s_{12}, m_t, 0; \varepsilon\right) = \frac{1}{2\varepsilon^2} + \frac{1}{2\varepsilon} \ln\left(\frac{m_t^2}{s_{12}}\right) - \frac{1}{4} \ln^2\left(\frac{m_t^2}{s_{12}}\right) - \frac{\pi^2}{12} - \frac{1}{2} \ln\left(\frac{s_{12}}{s}\right) \left[\ln\left(\frac{m_t^2}{s_{12}}\right) + \ln\left(\frac{m_t^2}{s}\right) \right] \tag{4.132}$$

$$\mathcal{V}_g^{(\mathrm{NS})}(s_{12},0,m_t;\kappa) = \frac{\gamma_g}{C_A}\left(\ln\left(\frac{s_{12}}{s}\right) - 2\ln\left(\frac{\sqrt{s}-m_t}{\sqrt{s}}\right) - \frac{2m_t}{\sqrt{s}+m_t}\right) + \frac{\pi^2}{6} - \mathrm{Li}_2\left(\frac{s_{12}}{s}\right) + \left(\kappa - \frac{2}{3}\right)\frac{m_t^2}{s_{12}}\left(\left(2N_f\frac{T_F}{C_A} - 1\right)\ln\left(\frac{2m_t}{\sqrt{s}+m_t}\right)\right) \tag{4.133}$$

$$\mathcal{V}_t^{(\mathrm{NS})}(s_{12},m_t,0) = \frac{3}{2}\ln\left(\frac{s_{12}}{s}\right) + \frac{\pi^2}{6} - \mathrm{Li}_2\left(\frac{s_{12}}{s}\right) - 2\ln\left(\frac{s_{12}}{s}\right) - \frac{m_t^2}{s_{12}}\ln\left(\frac{m_t^2}{s}\right) \tag{4.134}$$

are provided in Ref. [261] where the function Γ_j reads for massive quarks

$$\Gamma_t(\mu,m_t;\varepsilon) = C_F\left(\frac{1}{\varepsilon} + \frac{1}{2}\ln\left(\frac{m_t^2}{\mu^2}\right) - 2\right), \tag{4.135}$$

while the definitions of the flavor functions in Eqs. (4.129) and (4.130) are available in Ref. [271]. The value of the variable κ in Eq. (4.133) can be chosen arbitrarily as its dependence must cancel out between the virtual and real part. Within the numerical comparison it is set to $\kappa = 0$. Note that due to Bose symmetry the dipoles which are related through the interchange of an emitted gluon result in the same integrated dipole. Therefore, it is sufficient to incorporate one of the integrated counterparts and weight it with a factor of two which gets canceled by the Bose symmetry factor $S_3 = \frac{1}{2}$ of the associated real emission cross section. This counting of symmetry factors is already incorporated into the definition of the flavor functions $\mathcal{V}_j$.[1] In order to perform the convolution in Eq. (4.68), the well-known parametrization of the two-particle phase

$$\int \mathrm{d}\phi\,(P(x),p_k;p_a+p_b) = \frac{1}{(4\pi)^2}\frac{1}{\sqrt{\lambda\left(s,m_a^2,m_b^2\right)}}\int_{Q_-^2(x)}^{Q_+^2(x)}\mathrm{d}Q^2\int_0^{2\pi}\mathrm{d}\varphi_k \tag{4.136}$$

is inserted, where φ_k denotes the azimuthal angle of p_k in the center-of-mass system of p_a+p_b. Since the integrand is rotationally invariant, the integration over φ_k yields a factor of 2π. It remains the determination of the integration limits of Q^2 as a function of x. This is achieved by expressing Q^2 in the c.m. frame of p_b and p_k

$$\begin{aligned} Q^2 &= m_b^2 + m_k^2 - 2E_bE_k + 2|\mathbf{p}_b||\mathbf{p}_k|\cos\vartheta \\ &= m_b^2 + m_k^2 - \frac{\left(s+m_b^2-m_a^2\right)\left(s+m_k^2-P^2\right)}{2s} + \cos\vartheta\frac{\sqrt{\lambda\left(s,m_a^2,m_b^2\right)}\sqrt{\lambda\left(s,m_k^2,P^2\right)}}{2s}, \end{aligned} \tag{4.137}$$

where ϑ corresponds to the angle between $\mathbf{p}_b$ and $\mathbf{p}_k$. The x dependence enters by expressing P^2 through x and Q^2 as given in Eq. (4.64) which results in an equation that can be solved for Q^2. The integration limits

$$Q_\pm^2(x) = \frac{1}{2}\frac{\alpha(x) \pm \beta(x)}{xs + (1-x)(m_b^2 - xm_a^2)} \tag{4.138}$$

with the abbreviations

$$\begin{aligned} \alpha(x) = x^2&\left(m_a^4 + 2m_a^2(m_b^2+m_k^2) - (m_b^2-s)^2\right) + 2m_b^2(m_a^2+m_j^2) \\ &- x\left(m_a^4 + m_a^2(4m_b^2+m_j^2+m_k^2-s) - (m_b^2-s)(m_b^2-m_j^2-m_k^2)\right), \end{aligned} \tag{4.139}$$

---

[1] The counting of symmetry factors for the general case of going from $m+1$ to m particles for a gluon and quark as emitter is discussed extensively in Ref. [260].

$$\beta(x) = x\sqrt{\lambda\left(m_a^2, m_b^2, s\right)}\sqrt{\left(m_a^2 - m_b^2\right)^2 (1-x)^2 + (1-x)\left(2m_a^2\left(m_j^2 + m_k^2(2x-1) - sx\right)\right. \\ \left.\left. - 2m_b^2\left(m_j^2 + m_k^2 - sx\right)\right) + \lambda(xs, m_k^2, m_j^2)} \tag{4.140}$$

are then obtained by setting $\cos\vartheta$ to its extreme values -1 and 1. Within the integration over Q^2 two different kinematical configurations have to be distinguished. The variable $\tilde{t}$ in Eqs. (4.129) and (4.130) equals Q^2 for the cases $m_j = 0$, $m_k = m_t$, whereas $\tilde{u}$ equals Q^2 for $m_j = m_t$, $m_k = 0$. After having fixed the values of x and Q^2 ($\tilde{u}$ and $\tilde{t}$) in the phase space integration, the squared c.m. energy $\tilde{s}$ of the new initial state with momenta $\tilde{p}_a$ and p_b can be determined as

$$\tilde{s} = (\tilde{p}_a + p_b)^2 = m_a^2 + m_b^2 + \frac{1}{R(x)}\left[x(s - m_a^2 - m_b^2)\right. \\ \left. + \frac{\bar{Q}^2 + 2m_a^2 x}{2Q^2}\left(m_b^2 - m_k^2 + Q^2\right)\right] - \frac{Q^2 + m_a^2 - m_j^2}{2Q^2}\left(m_b^2 - m_k^2 + Q^2\right). \tag{4.141}$$

The remaining "dipole Mandelstam variable" $\tilde{u}$ for $Q^2 = \tilde{t}$ and vice versa can then be deduced from $\tilde{s} + \tilde{u} + \tilde{t} = m_a^2 + m_b^2 + m_j^2 + m_k^2$. As the squared tree-level matrix element is a function of the usual Mandelstam variables s, t and u, these only need to be substituted through the dipole invariants $\tilde{s}$, $\tilde{t}$ and $\tilde{u}$, respectively, in order to formulate the tree-level matrix element in terms of the dipole momenta.

The independence of the final result on the lower integration limit x_0 is shown in Fig. 4.6. For the numerical comparison the value $x_0 = 0.9$ was chosen as it fulfills the condition in Eq. (4.69) for all probed c.m. momenta. For the determination of appropriate values for the soft and collinear cutoff, the behavior of the NLO correction is examined in dependence of both, which is shown in Fig. 4.6. In the end, the cutoffs are chosen to be $p_2^0, p_3^0 \geq \delta_s = 3.0 \cdot 10^{-4}\sqrt{s}$ and $2p_2 \cdot p_3 \geq \delta_c = 3.0 \cdot 10^{-6} s$ such that they are located in the broad plateau region in the lower right half of the plot.

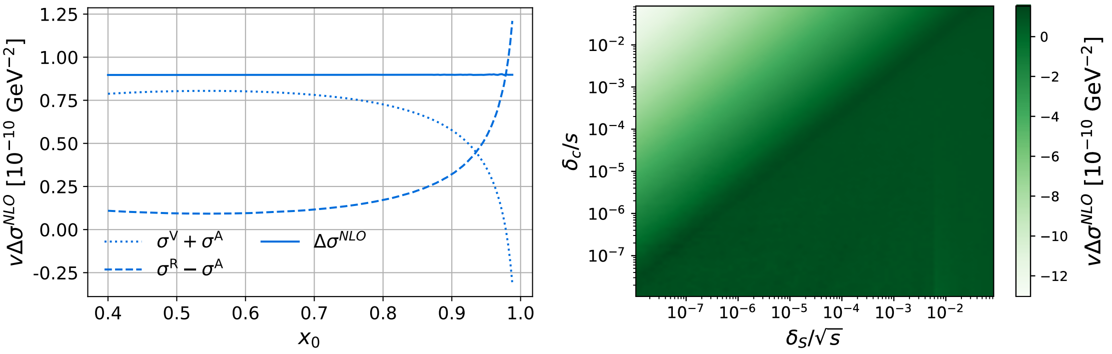

Figure 4.6: The NLO correction times velocity $v\Delta\sigma^{\mathrm{NLO}}$ subdivided into the virtual part plus the auxiliary cross section $\sigma^{\mathrm{V}} + \sigma^{\mathrm{A}}$ and the real part minus the auxiliary cross section $\sigma^{\mathrm{R}} - \sigma^{\mathrm{A}}$ for the process $\tilde{\chi}_1^0 \tilde{t}_1 \to tg$ for different values of the lower integration limit x_0 (left) as well as the dependence of the NLO correction obtained with the slicing method on the soft δ_s as well as the collinear cutoff δ_c (right). Both plots are created for the c.m. momentum $p_{\mathrm{cm}} = 100\,\mathrm{GeV}$.

In Tab. 4.2 and Fig. 4.7 the total cross section obtained with the two different methods is given for two different c.m. momenta p_{cm}, that are typical for dark matter annihilation. Even though all chosen cutoffs for a momentum of 100 GeV lie in the plateau region shown in the right plot of Fig. 4.6, the central values of the correction for the smallest and largest cutoff differ by 13 %, while the dependence on the artificially introduced lower integration limit x_0 of the dipole method is completely compensated between the virtual and real part. Furthermore, the total numerical error of the result obtained with the phase space slicing method for the NLO correction increases with decreasing cutoff values which is expected as the real cross section increases like $\ln(\delta_s/s)$ in the soft region and like $\ln(\delta_c/s)$ in the collinear one. In addition, the numerical integration error of the dipole method is at least one order of magnitude lower than the one of the slicing method so that the error of the dipole result is smaller than the linewidth in the plot. Both of these findings, the cutoff dependence as well as the integration error, show the superiority of the dipole subtraction method with respect to precision.

p_{cm} [GeV]	$v\sigma^{\text{Tree}}$	Method	$\delta_s/\sqrt{s}$	δ_c/s	$v\Delta\sigma^{\text{NLO}}$
100	4.604596	PSS	10^{-2}	10^{-3}	0.915 ± 0.036
			10^{-4}	10^{-6}	0.974 ± 0.152
			10^{-6}	10^{-7}	1.033 ± 0.241
		Dipole			0.891 ± 0.002
1200	2.501535	PSS	10^{-2}	10^{-3}	0.408 ± 0.021
			10^{-4}	10^{-6}	0.429 ± 0.083
			10^{-6}	10^{-7}	0.458 ± 0.135
		Dipole			0.385 ± 0.001

Table 4.2: Results on the correction $v\Delta\sigma^{\text{NLO}}$ of the process $\tilde{\chi}_1^0\tilde{t}_1 \to tg$ for two different c.m. momenta p_{cm}. All cross sections times velocity are given in 10^{-10} GeV^{-2}.

The Process $\tilde{t}_1\tilde{t}_1 \to tt$

As another example, the process

$$\tilde{t}_1(p_a, s) + \tilde{t}_1(p_b, t) \longrightarrow t(p_1, i) + t(p_2, j) + g(p_3, a) \tag{4.142}$$

is considered where the parentheses contain the particle momenta p_a, p_b, p_1, p_2, p_3 and the corresponding color indices s, t, i, j, a. This process is chosen as it allows to demonstrate and compare the dipole formalism for situations with two massive and color charged particles in the initial state. The NLO corrections for this process, originally performed with the slicing method, are discussed in Ref. [169]. The auxiliary squared matrix element receives contributions from in total twelve dipoles and reads

$$\left|\mathcal{M}_3^{\text{A}}\right|^2 = \mathcal{D}_{13,2} + \mathcal{D}_{23,1} + \mathcal{D}_{13}^a + \mathcal{D}_{13}^b + \mathcal{D}_{23}^a + \mathcal{D}_{23}^b + \mathcal{D}_1^{a3} + \mathcal{D}_1^{b3} + \mathcal{D}_2^{a3} + \mathcal{D}_2^{b3} + \mathcal{D}^{a3,b} + \mathcal{D}^{b3,a}, \tag{4.143}$$

where the subtraction functions are consistently set to zero for values of x below $x_0 = \frac{2m_t^2}{\bar{s}}$ in conjunction with Eq. (4.109).

For a process involving four colored particles it is no longer possible to factorize the color charge algebra. However, it follows from color conservation, that four of the six color charge operators $\mathbf{T}_i\mathbf{T}_j$ with $i \neq j$ can be expressed through the quadratic Casimir invariants and $\mathbf{T}_1\mathbf{T}_2$, $\mathbf{T}_1\mathbf{T}_3$

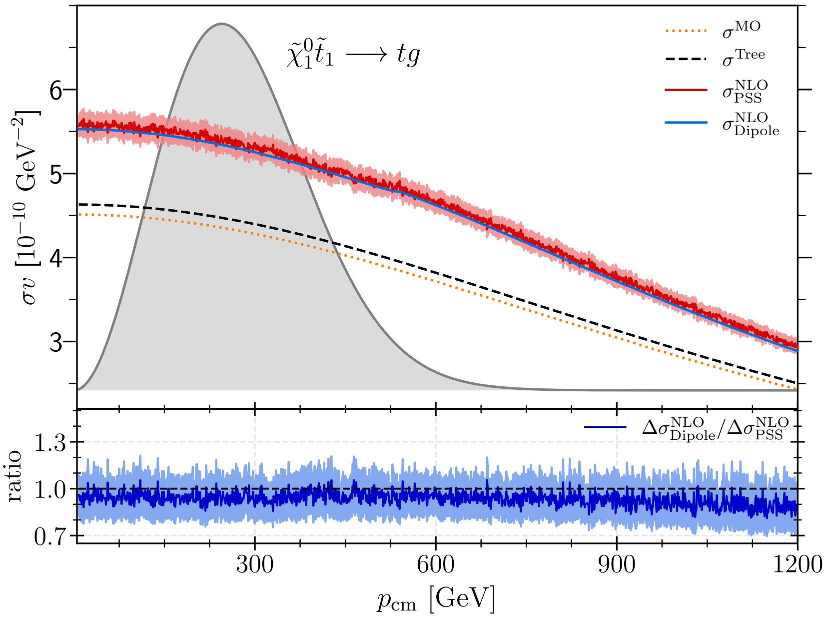

Figure 4.7: Neutralino-stop coannihilation cross section σv with a top and a gluon in the final state for the example scenario defined in Tab. 4.1. The leading order result is computed with MicrOMEAGs 2.4.1 (MO) and DM@NLO (Tree). The NLO results are calculated with the phase space slicing method (PSS) and the dipole method (Dipole). The lower panel shows the ratio of the NLO corrections obtained with the two different approaches. The uncertainty band in the upper panel corresponds to the total numerical error ε_{NLO} defined in Eq. (4.122). The gray shaded area shows the thermal velocity distribution of the neutralino at the freeze-out temperature in arbitrary units.

giving [260]:

$$\mathbf{T}_3\mathbf{T}_4 \left|1,2,3,4\right\rangle = \left[\frac{1}{2}\left(C_1 + C_2 - C_3 - C_4\right) + \mathbf{T}_1\mathbf{T}_2\right] \left|1,2,3,4\right\rangle \ , \tag{4.144a}$$

$$\mathbf{T}_2\mathbf{T}_4 \left|1,2,3,4\right\rangle = \left[\frac{1}{2}\left(C_1 + C_3 - C_2 - C_4\right) + \mathbf{T}_1\mathbf{T}_3\right] \left|1,2,3,4\right\rangle \ , \tag{4.144b}$$

$$\mathbf{T}_2\mathbf{T}_3 \left|1,2,3,4\right\rangle = \left[\frac{1}{2}\left(C_4 - C_1 - C_2 - C_3\right) - \mathbf{T}_1\mathbf{T}_2 - \mathbf{T}_1\mathbf{T}_3\right] \left|1,2,3,4\right\rangle \ , \tag{4.144c}$$

$$\mathbf{T}_1\mathbf{T}_4 \left|1,2,3,4\right\rangle = -\left(C_1 + \mathbf{T}_1\mathbf{T}_2 + \mathbf{T}_1\mathbf{T}_3\right) \left|1,2,3,4\right\rangle \ . \tag{4.144d}$$

The four color charge operators are associated with the particles in our process as follows:

$$\mathbf{T}_1 = \mathbf{T}_{\tilde{q}_s},\ \mathbf{T}_2 = \mathbf{T}_{\tilde{q}_t},\ \mathbf{T}_3 = \mathbf{T}_{t_i},\ \mathbf{T}_4 = \mathbf{T}_{t_j}. \tag{4.145}$$

For the remaining two operators the color correlations have to be evaluated explicitly:

$$\left\langle 1,2,3,4\right| \mathbf{T}_1\mathbf{T}_2 \left|1,2,3,4\right\rangle = \left[\mathcal{M}_2^{ij;lt}\right]^* T^c_{sl}T^c_{kt}\mathcal{M}_2^{ij;sk}, \tag{4.146a}$$

$$\left\langle 1,2,3,4\right| \mathbf{T}_1\mathbf{T}_3 \left|1,2,3,4\right\rangle = \left[\mathcal{M}_2^{ij;kt}\right]^* \left(-T^c_{sk}T^c_{il}\right)\mathcal{M}_2^{lj;st} \tag{4.146b}$$

with the tree level matrix element $\mathcal{M}_2^{ij;st}$. As the application of the dipole formulas has already been exemplified in the previous section for all emitter-spectator pairs besides the configuration where both are from the initial state, only the two particle phase space integration in the convolution in Eq. (4.110) needs still to be covered. In order to provide a general expression for the parametrization of the phase space, the masses related to the momenta p_1 and p_2 are labelled as m_1 and m_2 and the masses m_a and m_b of the initial particles are distigiushed even though they are identical in this case. Since the variable x enters the phase space integration only through the reduced squared c.m. energy $\tilde{s}$ given in Eq. (4.113) the well-known parametrization

$$\int \mathrm{d}\phi\left(\tilde{p}_k(x);\tilde{p}_{ai}(x)+p_b\right)=\frac{1}{(4\pi)^2\sqrt{\lambda_{\tilde{s}}}}\int_{q_-^2(\tilde{s})}^{q_+^2(\tilde{s})}\mathrm{d}q^2\int_0^{2\pi}\mathrm{d}\varphi' \tag{4.147}$$

with the integration limits

$$q_\pm^2\left(\tilde{s}\right)=m_a^2+m_1^2-\frac{\left(\tilde{s}+m_a^2-m_b^2\right)\left(\tilde{s}+m_1^2-m_2^2\right)}{2\tilde{s}}\pm\frac{\sqrt{\lambda_{\tilde{s}}}}{2\tilde{s}}\sqrt{\lambda\left(\tilde{s},m_1^2,m_2^2\right)} \tag{4.148}$$

can be employed, where $q^2=(\tilde{p}_{a3}-\tilde{p}_1)^2$ plays the role of a Mandelstam variable and the abbreviation $\lambda_{\tilde{s}}$ is given by $\lambda_{\tilde{s}}=\lambda(\tilde{s},m_a^2,m_b^2)$. The remaining dipole Mandelstam variable that enters the squared Born amplitude is determined through $m_a^2+m_b^2+m_1^2+m_2^2-\tilde{s}-q^2$. For the numerical comparison in Fig. 4.8, the cutoff for the slicing method is chosen as $p_3^0\geq\delta_s=10^{-5}\sqrt{s}$. In Tab. 4.3, results for the $\mathcal{O}(\alpha_s)$ corrections for different cutoff values δ_s and c.m. momenta are shown in comparison with the corresponding results obtained with the dipole approach. Similar to the previous example, the integration error of the slicing method increases with decreasing cutoff values while the errors of dipole method are at least one order of magnitude lower than the ones for small cutoff values indicating again that the dipole method is ahead of the slicing approach.

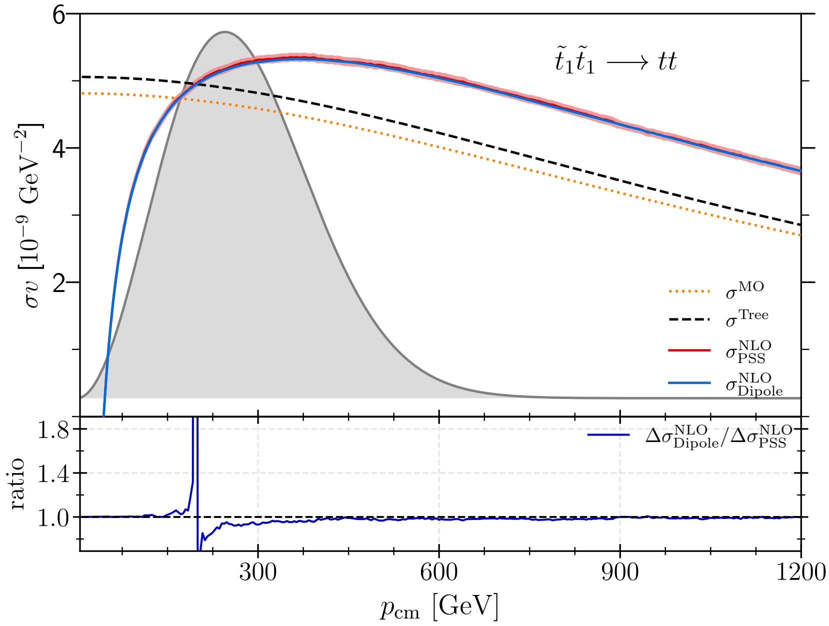

Figure 4.8: Same as Fig. 4.7 but for the annihilation process $\tilde{t}_1\tilde{t}_1\to tt$.

p_{cm} [GeV]	$v\sigma^{\text{Tree}}$	Method	$\delta_s/\sqrt{s}$	$v\Delta\sigma^{\text{NLO}}$
100	5.030288	PSS	10^{-2}	-1.392 ± 0.018
			10^{-4}	-1.407 ± 0.032
			10^{-6}	-1.399 ± 0.053
		Dipole		-1.410 ± 0.007
1200	2.853008	PSS	10^{-2}	0.821 ± 0.016
			10^{-4}	0.810 ± 0.036
			10^{-6}	0.787 ± 0.062
		Dipole		0.802 ± 0.007

Table 4.3: Results on the correction $v\Delta\sigma^{\text{NLO}}$ of the process $\tilde{t}_1\tilde{t}_1 \to tt$ for two different p_{cm}. All cross sections times velocity are given in 10^{-9} GeV^{-2}.

4.4 Stop Annihilation into Gluons and Light Quarks

The small annihilation cross section of a neutralino with a mass in the $\mathcal{O}(100\,\text{GeV})$ region that can be probed at the LHC [57, 279] is difficult to reconcile with the measured relic DM abundance [280]. One interesting possibility to address this conundrum is to choose the lighter stop to be almost mass degenerate with the lightest neutralino such that according to Eq. (4.10) stop coannihilation processes in the early Universe allow to reproduce the right amount of dark matter [281–285]. Other possibilities to enhance the effective annihilation cross section are, e.g., gluino coannihilation [286] or direct-channel resonances at $2m_{\tilde{\chi}_1^0}$ [287].

A stop as next-to-lightest supersymmetric particle (NLSP) is not an unnatural assumption since the tree-level mass of the lightest Higgs boson in the MSSM is bounded from above by $m_{Z^0}|\cos 2\beta|$ which requires large quantum corrections to be consistent with the observation of a SM-like 125 GeV Higgs boson [288, 289]. The dominant contribution to the Higgs mass comes from the stop sector where a large trilinear coupling A_t is needed in order for these corrections to be large enough, indicating a large mass splitting in the stop sector [290]. The mass splitting is enhanced further through the fact that the off-diagonal entries in the sfermion mixing matrix are proportional to the associated masses of the SM partners, indicating a rather light $\tilde{t}_1$. While the Sommerfeld enhancement effect of stop-antistop annihilation is already taken into account in some analyses [284, 285] of the MSSM parameters space, the calculation of the full NLO corrections in α_s is long overdue, and subject of the following sections.

4.4.1 The Leading-Order Cross Section and the DM Scenario

To prepare for the subsequent discussion of the higher-order corrections and to clarify the notation, it is instructive to start with the analytic computation of the tree-level cross sections of the processes in Eq. (4.1) and discuss the importance of stop annihilation in the context of the neutralino relic density.

Leading order cross section

The Feynman diagrams for the leading order processes are displayed in Fig. 4.9 along with the naming convention for momenta and other relevant indices. Using Feynman gauge ($\xi = 1$) for

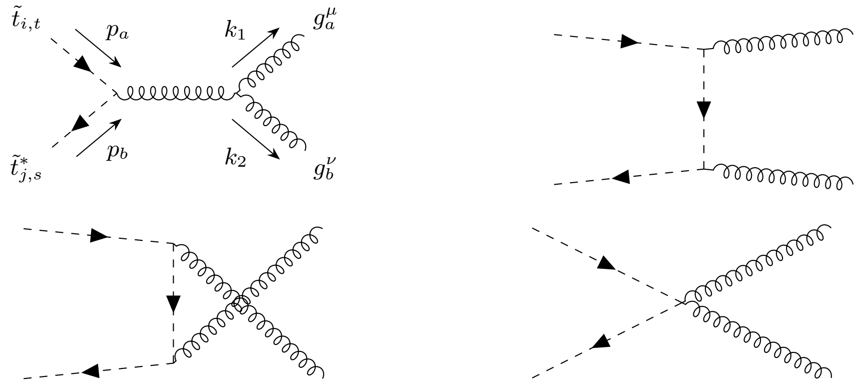

(a) Graphs for the annihilation into two gluons given by the amplitude $\mathcal{M}_{gg}^{\text{Tree}}$.

(b) Graph for the annihilation into a massless quark-antiquark pair given by the amplitude $\mathcal{M}_{q\bar{q}}^{\text{Tree}}$.

(c) Graph for the annihilation into a ghost-antighost pair given by the amplitude $\mathcal{S}_1^{\text{Tree}}$. The amplitude for $\mathcal{S}_2^{\text{Tree}}$ is obtained by reversing the ghost flow.

Figure 4.9: Tree-level Feynman diagrams associated with the annihilation of a stop-antistop pair into gluons and quarks. Four-momenta (p_a, p_b, k_1, k_2), sfermion indices (i, j), colors (s,t,a,b,r,u) and Lorentz indices (μ, ν) are explicitly labeled in the respective first diagrams.

internal lines and following the MSSM Feynman rules [291], the corresponding amplitudes with amputated polarization vectors $\epsilon^*_\mu(\lambda_1, k_1)$ and $\epsilon^*_\nu(\lambda_2, k_2)$ for the annihilation into two gluons are

$$\mathcal{M}_s^{\mu\nu} = f_{abc}T^c_{st}\frac{g_s^2}{s}\left(p_b - p_a\right)_\rho\left(\eta^{\rho\nu}\left(k_1 + 2k_2\right)^\mu - \eta^{\rho\mu}\left(2k_1 + k_2\right)^\nu + \eta^{\mu\nu}\left(k_1 - k_2\right)^\rho\right) , \tag{4.149a}$$

$$\mathcal{M}_t^{\mu\nu} = (T^bT^a)_{st}\frac{ig_s^2}{t - m_i^2}\left(2p_a - k_1\right)^\mu\left(2p_b - k_2\right)^\nu , \tag{4.149b}$$

$$\mathcal{M}_u^{\mu\nu} = (T^aT^b)_{st}\frac{ig_s^2}{u - m_i^2}\left(2p_b - k_1\right)^\mu\left(2p_a - k_2\right)^\nu , \tag{4.149c}$$

$$\mathcal{M}_v^{\mu\nu} = i\left\{T^a, T^b\right\}_{st}g_s^2\eta^{\mu\nu} \tag{4.149d}$$

with $g_s = \sqrt{4\pi\alpha_s}$. These are labeled according to which of the Mandelstam variables

$$s = \left(p_a + p_b\right)^2 = \left(k_1 + k_2\right)^2 , \tag{4.150a}$$

$$t = \left(k_1 - p_a\right)^2 = \left(k_2 - p_b\right)^2 , \tag{4.150b}$$

$$u = \left(k_2 - p_a\right)^2 = \left(k_1 - p_b\right)^2 \tag{4.150c}$$

appears in the propagator apart from the last topology which is commonly referred to as v-channel. The total transition amplitude is then given by $\mathcal{M}_{gg}^{\text{Tree}} = \mathcal{M}_s + \mathcal{M}_t + \mathcal{M}_u + \mathcal{M}_v$. The amplitude for the annihilation into a massless quark-antiquark pair on the other hand reads

$$\mathcal{M}_{q\bar{q}}^{\text{Tree}} = T_{st}^a T_{ru}^a \frac{ig_s^2}{s} \left(p_a - p_b\right)_\sigma \bar{u}^{(s)}(k_1)\gamma^\sigma v^{(s)}(k_2) \,. \tag{4.151}$$

An important aspect of the investigated processes is that both initial- and final-state particles are charged under $\mathrm{SU}(3)_c$. In order to be able to distinguish between attractive and repulsive color potentials in the context of non-perturbative corrections to the annihilation cross section in the non-relativistic regime like the Sommerfeld enhancement or bound-state formation, it is necessary to decompose the tensor product representations under which the two incoming and outgoing particles transform into their respective irreducible representations. The (s)quark-anti(s)quark system can be decomposed into a color octet and a color singlet

$$\mathbf{3} \otimes \overline{\mathbf{3}} = \mathbf{8} \oplus \mathbf{1} \,, \tag{4.152}$$

whereas the decomposition of the two-gluon system involves higher multiplet representations and reads

$$\mathbf{8} \otimes \mathbf{8} = \mathbf{1} \oplus \mathbf{8}_S \oplus \mathbf{8}_A \oplus \overline{\mathbf{10}} \oplus \mathbf{10} \oplus \mathbf{27}. \tag{4.153}$$

For the decomposition of the tree-level scattering amplitudes

$$\mathcal{M}_{gg}^{\text{Tree}} = \sum_{\mathbf{R}} c_{gg}^{[\mathbf{R}]} \mathcal{M}_{gg,[\mathbf{R}]}^{\text{Tree}} \,, \tag{4.154a}$$

$$\mathcal{M}_{q\bar{q}}^{\text{Tree}} = \sum_{\mathbf{R}} c_{q\bar{q}}^{[\mathbf{R}]} \mathcal{M}_{q\bar{q},[\mathbf{R}]}^{\text{Tree}} \tag{4.154b}$$

into equivalent irreducible representations $\mathbf{R}$ that appear simultaneously in the initial as well as final state, the orthogonal and normalized multiplet basis elements $c^{[\mathbf{R}]}$ spanning the invariant subspaces $\mathbf{R}$ from Ref. [292] can be used. For the gluonic system these are

$$c_{gg}^{[\mathbf{1}]} = \frac{1}{\sqrt{N_c(N_c^2-1)}} \delta_{st}\delta_{ab} \,, \tag{4.155a}$$

$$c_{gg}^{[\mathbf{8_S}]} = \sqrt{\frac{2N_c}{C_F(N_c^2-4)}} d_{abc} T_{st}^c \,, \tag{4.155b}$$

$$c_{gg}^{[\mathbf{8_A}]} = i\sqrt{\frac{1}{N_c^2 C_F}} f_{abc} T_{st}^c \,, \tag{4.155c}$$

while for the quark-antiquark final state one has

$$c_{q\bar{q}}^{[\mathbf{1}]} = \frac{1}{N_c} \delta_{st}\delta_{ur} \,, \tag{4.156a}$$

$$c_{q\bar{q}}^{[\mathbf{8}]} = \frac{1}{\sqrt{N_c^2-1}} \left(\delta_{su}\delta_{tr} - \frac{1}{N_c}\delta_{st}\delta_{ur}\right) \tag{4.156b}$$

with $C_F = {}^{(N_c^2-1)}\!/_{2N_c}$ and $N_c = 3$. Practically, the decomposition into the orthogonal basis elements proceeds through the relations

$$T_{ij}^a T_{kl}^a = \frac{1}{2} \left(\delta_{il}\delta_{jk} - \frac{1}{N_c}\delta_{ij}\delta_{kl}\right) \,, \tag{4.157a}$$

$$T^a T^b = \frac{1}{2}\left[\frac{1}{N_c}\delta_{ab}\mathbb{1} + (d_{abc} + i f_{abc})\, T^c\right] \tag{4.157b}$$

for the fundamental $\mathrm{SU}(N_c)$ generators [293].

Another important aspect in a non-Abelian theory is the treatment of internal and external polarization states. In order to include only the physical external gluon states in the transition probability, two different computational approaches are compared with each other. This serves also as an internal consistency check of the calculation. The first one is to explicitly sum only the transverse polarizations λ_T with the help of the completeness relation

$$\sum_T \epsilon^\mu(\lambda_T, k)^* \epsilon^\nu(\lambda_T, k) = -\eta^{\mu\nu} + \frac{k^\mu n^\nu + k^\nu n^\mu}{n \cdot k} - n^2 \frac{k^\mu k^\nu}{(n \cdot k)^2} \tag{4.158}$$

which holds as an algebraic relation independently of the gauge fixing condition used for the gluon propagators and where n is an arbitrary direction in momentum space that fulfills $n \cdot k \neq 0$ and $\epsilon(\lambda_T, k) \cdot n = 0$. For some lightlike n with $n^2 = 0$ this is also referred to as the light-cone gauge. As there appear only two external gluons in the tree-level process, it is instructive to choose n as the momentum of the respective other gluon. The second possibility is to use only $-\eta^{\mu\nu}$ as polarization sum but subtract the longitudinal polarizations through ghosts. To show how the two ghost amplitudes

$$\mathcal{S}_1^{\text{Tree}} = \mathcal{S}_2^{\text{Tree}} = -f_{abc} T^c_{st} \frac{g_s^2}{2s}(u - t) \tag{4.159}$$

corresponding to the graph in Fig. 4.9c cancel precisely the longitudinal polarizations, one can use the invariance of general n-point functions in SUSY-QCD under BRST-transformations [294, 295] to derive the two Slavnov-Taylor identities

$$k_1^\mu \mathcal{M}^{\text{Tree}}_{gg,\mu\nu} = -k_{2,\nu} \mathcal{S}_1^{\text{Tree}}\,, \tag{4.160a}$$

$$k_2^\nu \mathcal{M}^{\text{Tree}}_{gg,\mu\nu} = -k_{1,\mu} \mathcal{S}_2^{\text{Tree}} \tag{4.160b}$$

involving the two ghost amplitudes. In more detail, Eq. (4.160a) follows from the application of the BRST-transformations

$$\delta_B \tilde{q}_i = i c_a T^a_{ij} \tilde{q}_j \tag{4.161a}$$

$$\delta_B g^\mu_a = \frac{1}{g_s}\partial^\mu c_a + f_{abc} g^\mu_b c_c \tag{4.161b}$$

$$\delta_B \bar{c}_a = -\frac{1}{g_s}\partial_\mu g^\mu_a \tag{4.161c}$$

to the correlation function $\langle \Omega | \, T\{\tilde{q}\, \tilde{q}^* \, \bar{c}_a \, g^\nu_b\} \, |\Omega\rangle = 0$ with $|\Omega\rangle$ denoting the ground state. Equation (4.160b) is obtained in the same way but by using $\langle \Omega | \, T\{\tilde{q}\, \tilde{q}^* \, g^\mu_a \, \bar{c}_b\} \, |\Omega\rangle = 0$ as the starting expression. Consequently, Eq. (4.160) allows to replace the longitudinal polarizations corresponding to all the terms proportional to k_1 and k_2 in Eq. (4.158) with ghost amplitudes. This gives for the squared matrix element summed over final-state polarizations the final expression

$$\mathcal{M}^{\text{Tree}}_{gg,\mu\nu} (\mathcal{M}^{\text{Tree}*}_{gg})^{\mu\nu} - |\mathcal{S}_1^{\text{Tree}}|^2 - |\mathcal{S}_2^{\text{Tree}}|^2. \tag{4.162}$$

The fermion spin sum for the quark-antiquark final state is performed in the usual way. After averaging (summing) over initial(final)-state colors and performing the remaining phase-space integration, the color-decomposed tree-level cross sections describing the annihilation into two gluons read

$$(\sigma v)^{\mathrm{Tree}}_{gg,[\mathbf{1}]} = \frac{16\pi\alpha_s^2}{27s\beta}\left[\beta(1+\rho)+\rho(\rho-2)\,\mathrm{atanh}(\beta)\right] , \tag{4.163a}$$

$$(\sigma v)^{\mathrm{Tree}}_{gg,[\mathbf{8}_S]} = \frac{5}{2}(\sigma v)^{\mathrm{Tree}}_{gg,[\mathbf{1}]} , \tag{4.163b}$$

$$(\sigma v)^{\mathrm{Tree}}_{gg,[\mathbf{8}_A]} = \frac{8\pi\alpha_s^2}{9s\beta}\left[\beta(1+8\rho)-3\rho(\rho+2)\,\mathrm{atanh}(\beta)\right] \tag{4.163c}$$

with $\rho = {}^{4m_{\tilde{i}}^2}\!/_{s}$ and $\beta = \sqrt{1-\rho}$ where $v = 2\beta$ corresponds to the relative velocity of the incoming squark-antisquark pair in the c.m. system. Only one color channel contributes to the annihilation into a massless quark-antiquark pair giving the cross section

$$(\sigma v)^{\mathrm{Tree}}_{q\bar{q},[\mathbf{8}]} = \frac{16\pi\alpha_s^2\beta^2}{27s} . \tag{4.164}$$

As both processes have to be combined at NLO, it makes sense to define already at tree-level

$$(\sigma v)^{\mathrm{Tree}} = (\sigma v)^{\mathrm{Tree}}_{gg} + N_f(\sigma v)^{\mathrm{Tree}}_{q\bar{q}} , \tag{4.165}$$

where, again, $N_f = 4$ corresponds to the number of effectively massless quark flavors.

Illustrative Example Scenario

To illustrate the importance of stop annihilation into gluons for the neutralino abundance and to showcase the capabilities of DM@NLO, we work in the constrained minimal supersymmetric extension of the Standard Model (cMSSM) which contains the simplifying assumption that the soft supersymmetry-breaking parameters unify at the gauge coupling unification scale of about 10^{16} GeV. This setup is entirely characterized through the universal scalar mass parameter m_0, the universal gaugino mass parameter $m_{1/2}$, the ratio of the vacuum expectation values of the neutral components of the two Higgs doublets $\tan\beta$, the universal trilinear coupling A_0, and the sign of the Higgs mixing parameter μ. Inspired by the search for non-excluded regions in the cMSSM parameter space [296], the reference scenario displayed in Tab. 4.4 is used in the following and MicrOMEGAs 5.3.41 with the standard CalcHEP implementation of the MSSM is used for the computation of the relic density and the contributions of different (co)annihilation channels.[2] As visible from Tab. 4.5 showing the most important (co)annihilation channels contributing to $\langle\sigma_{\mathrm{ann}}v\rangle$, the largest contribution comes with 36 % from stop-antistop annihilation into gluons followed by neutralino-stop coannihilation and stop pair-annihilation into top quarks which have been previously analyzed in Refs. [169] and [165], respectively. In total, DM@NLO provides the full one-loop SUSY-QCD corrections to 87 % of the effective annihilation cross section. Given that $Z_{11} \sim 1$, this scenario features a bino-like neutralino which is not surprising as large wino and higgsino components would lead to other gauginos being the NLSP. The gluino and slepton

---

[2] Note that numerical differences in the physical mass spectrum occur with respect to Ref. [296] since SPheno 4.0.5 is used as spectrum generator here, whereas Ref. [296] makes use of a private code. This is also the reason why $A_0 = 4m_0$ is chosen in the example scenario in Tab. 4.4 versus $A_0 = 3m_0$ in Ref. [296].

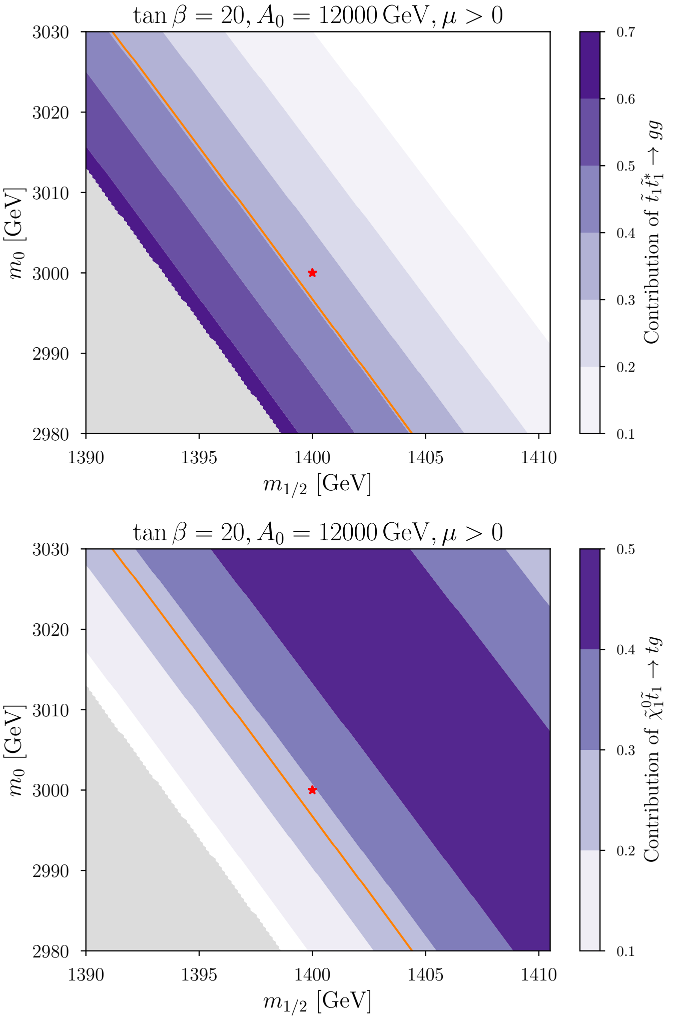

Figure 4.10: Contribution of the two most relevant processes to the neutralino relic density that can be corrected with DM@NLO in the $m_{1/2}$-m_0 plane around the chosen reference scenario which is highlighted with a red star. The region where the neutralino is not the LSP is marked in gray. The orange band indicates the parameter region that is consistent with the Planck measurement (3.2c) at the 2σ level based on the tree-level cross sections provided by CalcHEP.

m_0	$m_{1/2}$	$\tan\beta$	A_0	$m_{\tilde{\chi}_1^0}$	$m_{\tilde{t}_1}$	Z_{11}
3000	1400	20	12000	606.3	648.3	~ 1

Table 4.4: Example scenario in the cMSSM with a positive Higgs supersymmetric mixing parameter μ where stop (co)annihliation is the dominant dark matter mechanism. All dimensionful quantities are in GeV.

Channel	Contribution
$\tilde{t}_1\ \tilde{t}_1^* \to g\ g$	36 %
$\tilde{\chi}_1^0\ \tilde{t}_1 \to t\ g$	29 %
$\tilde{\chi}_1^0\ \tilde{t}_1 \to W^+\ b$	8 %
$\tilde{t}_1\ \tilde{t}_1 \to t\ t$	6 %
$\tilde{t}_1\ \tilde{t}_1^* \to \gamma\ g$	4 %
$\tilde{\chi}_1^0\ \tilde{t}_1 \to Z^0\ t$	4 %
$\tilde{\chi}_1^0\ \tilde{t}_1 \to h^0\ t$	4 %
`DM@NLO` total	87 %

Table 4.5: Dominant annihilation channels contributing to $\langle\sigma_{\text{ann}}v\rangle$ for the cMSSM scenario in Tab. 4.4. Further contributions below 2% are omitted.

sectors are much heavier ($> 2\,\text{TeV}$) than the stop sector such that they do not influence the dark matter phenomenology. In Fig. 4.10, the relative contributions to the relic density of the two most important channels are displayed in the $m_{1/2}$-m_0 plane in different shades of purple. As $m_{1/2}$ tunes the neutralino masses while m_0 mainly determines the stop mass, it becomes clear that for larger mass splittings between the lightest neutralino and the stop, neutralino-stop coannihilation becomes the dominant channel whereas for smaller mass splittings annihilation of stops into gluons are the dominant contribution. In addition, the region where the neutralino accounts for the whole dark matter content in the Universe and lies within the 2σ range of the experimental value is marked in orange. This region follows an almost straight line parallel to the boundary where the neutralino is no longer the LSP.

With the knowledge that stop annihilation into gluons is important for large regions around the reference scenario, the analytically calculated leading order cross sections for the two processes in Eq. (4.1) can be compared numerically to the ones generated with MicrOMEGAs which are all shown in Fig. 4.11. As a reminder that the values of the cross section impacts the relic density only in a limited energy range, the Boltzmann distribution which is involved in the computation of the thermally averaged cross section is shown at the freeze-out temperature in gray in arbitrary units. One observes that the DM@NLO result is about 30 % smaller for both processes. This is mainly due to the choice of the renormalization scale which enters at tree-level only through the strong coupling. For the DM@NLO result, μ_R is set to the SUSY-scale which takes for the particular scenario in Tab. 4.4 the value $Q_{\text{SUSY}} = 1368.2\,\text{GeV}$. In contrast, MicrOMEGAs 5.3.41 uses by default the scale $Q = 2m_{\tilde{\chi}_1^0}/3$[3] which is smaller than Q_{SUSY} for the investigated scenario and therefore corresponds to a larger strong coupling. The choice $\mu_R = Q_{\text{SUSY}}$ is motivated by the

---

[3] This scale choice is different from MicrOMEGAs 2.4.1, where $Q = 2m_{\tilde{\chi}_1^0}$ is used.

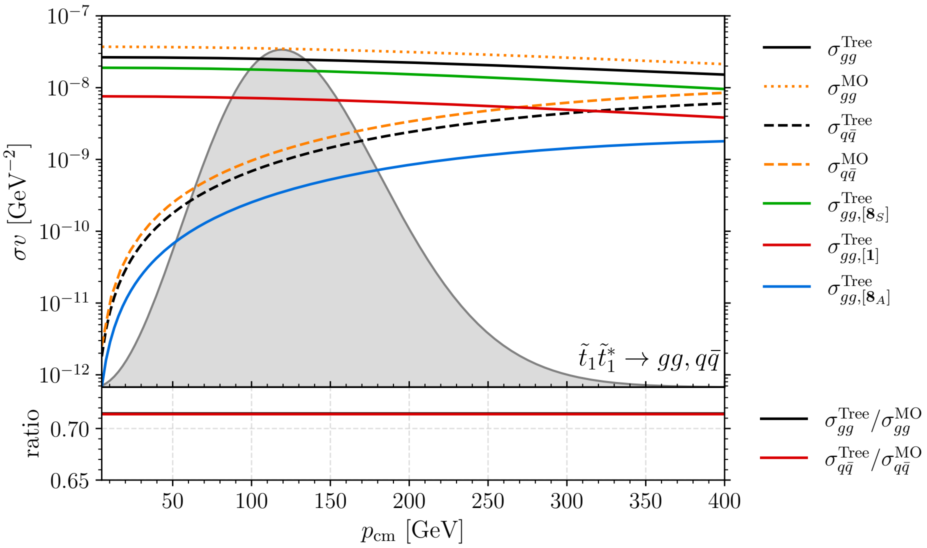

Figure 4.11: Leading order cross sections times velocity introduced in Sec. 4.4.1 as provided by DM@NLO as well the corresponding results from CalcHEP indicated with the superscript MO. All cross sections are displayed in dependence of the c.m. momentum p_{cm} for the reference scenario in Tab. 4.4.

fact that the besides the masses of the virtual particles in the loop, the process contains only two important scales: the mass of the lightest stop and the collisional energy s. Since most annihilations take place between $s = 4m_{\tilde{t}_1}^2$ and the peak of the velocity dis tribution at $s \sim (1.3\,\text{TeV})^2$, Q_{SUSY} is a suitable choice for the renormalization scale to avoid large logarithms.

Through comparison of the different color contributions to the combined leading order cross section depicted in Fig. 4.11 with the partial wave expansion

$$\sigma v = s_0 + v^2 s_1 + \mathcal{O}(v^4) \tag{4.166}$$

of a general velocity-weighted annihilation cross section σv, it becomes apparent that the singlet and symmetric octet contributions to the cross section with two external gluons are dominated by the s-wave component s_0 since they remain almost constant in v, whereas the antisymmetric octet part and the octet contribution to the quark-antiquark process take an inferior role and are suppressed at threshold corresponding to the s-wave and p-wave component s_1.

4.4.2 Computational Details of the Full NLO Corrections

Next, the technicalities of the full $\mathcal{O}(\alpha_s)$ corrections as well as the Sommerfeld enhancement are discussed. These have been calculated and verified with the publicly available tools FeynArts 3 [297], FeynCalc 9 [298], Tracer [299] and FormCalc 9 [300].

Virtual corrections and renormalization

The virtual amplitudes consist of propagator (self-energy), vertex and box corrections. Naively one might assume that the box corrections for the process with two final-state gluons are independent and UV finite on their own. However, they turn out to be UV divergent and fall under the

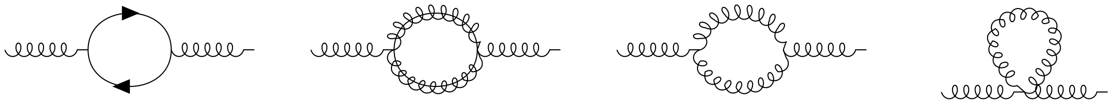

Figure 4.12: Example one-loop contributions to the gluon self-energy.

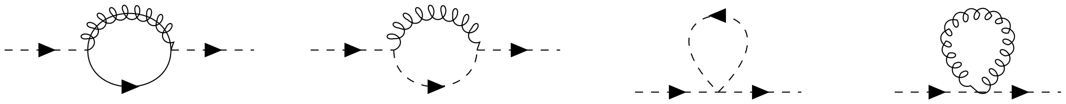

Figure 4.13: Contributions to the squark self-energy at one-loop.

renormalization of the four-squark-gluon vertex. Example Feynman diagrams for the different subgroups making up the virtual corrections are shown in Figs. (4.12) to (4.20). The whole set of diagrams is available in Ref. [171]. The longitudinal gluon polarizations are again subtracted by using ghosts. The resulting interference term of the tree-level matrix element with the virtual amplitudes for the process with two gluons in the final state summed over the final-state polarizations can then be written as

$$2\,\mathrm{Re}\left[(\mathcal{M}_{gg}^{\mathrm{Tree}*})^{\mu\nu}\mathcal{M}_{gg,\mu\nu}^{\mathrm{NLO}} - \mathcal{S}_1^{\mathrm{Tree}*}\mathcal{S}_1^{\mathrm{NLO}} - \mathcal{S}_2^{\mathrm{Tree}*}\mathcal{S}_2^{\mathrm{NLO}}\right] , \tag{4.167}$$

where some of the ghost corrections making up the ghost amplitudes $\mathcal{S}_i^{\mathrm{NLO}}$ $(i = 1, 2)$ are shown in Figs. 4.17 and 4.18. The virtual corrections are regularized by working in $D = 4 - 2\varepsilon$ dimensions within the SUSY preserving FDH scheme so that UV and IR divergences appear as poles of the form $1/\varepsilon$ and $1/\varepsilon^2$. The standard Passarino-Veltman reduction is used to express the one-loop amplitudes in terms of the scalar integrals A_0, B_0, C_0, D_0. The γ^5-matrix which enters through the squark-quark-gluino coupling is treated in the naive scheme. The Levi-Civita symbols that occur then through traces of γ^5 with four or more γ-matrices during the evaluation of diagrams with top quarks as virtual particles are directly set to zero since they vanish anyway when being contracted with the external momenta. The UV divergences that appear in the virtual corrections are removed through the renormalization of fields, masses and the strong coupling. Within this calculation, the hybrid on-shell/$\overline{\mathrm{DR}}$ renormalization scheme 1 according to the definition in Sec. 4.2.4 is employed. Since the renormalization of the gluon and the squark sector as well as the treatment of the bottom mass and the strong coupling have already been discussed in detail in the context of other processes [164–166], only aspects are covered in the following which are added newly to DM@NLO within this calculation such as the renormalization of ghosts and massless quarks.

Ghost Wave-function Renormalization

As ghost and antighost share the same self-energy they can be renormalized multiplicatively with the same wave function renormalization constant Z_c. The renormalized fields are then defined as

$$\bar{c}_a^0 = \sqrt{Z_c}\bar{c}_a^R , \tag{4.168a}$$

$$c_a^0 = \sqrt{Z_c}c_a^R . \tag{4.168b}$$

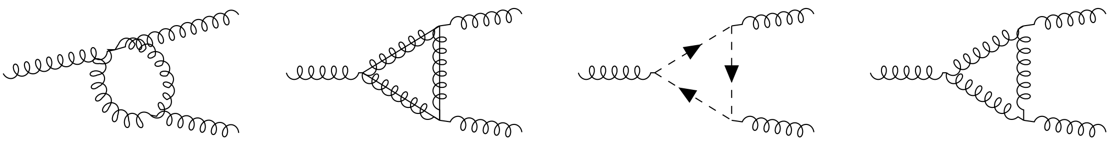

Figure 4.14: Example one-loop contributions to the triple-gluon vertex.

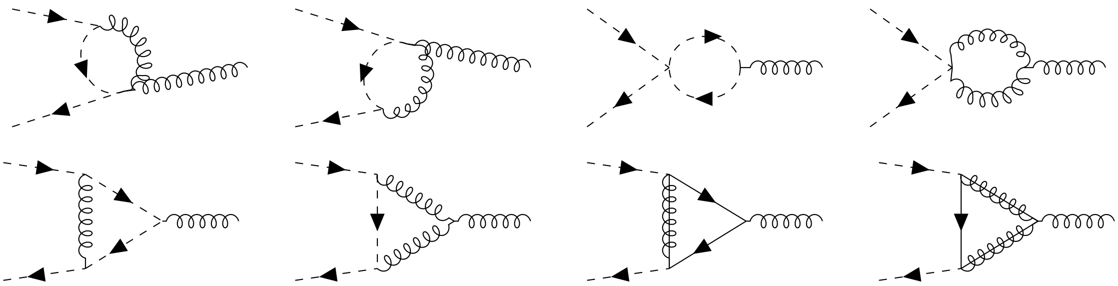

Figure 4.15: One-loop contributions to the squark-gluon vertex.

As Z_c is only needed up to $\mathcal{O}(\alpha_s)$, one can apply the perturbative expansion $Z_c = 1 + \delta Z_c$. Since the gluon is renormalized in the on-shell scheme, the same scheme is chosen for the ghost. That is, the ghost renormalization constant is obtained by requiring that the ghost propagator has a unit residue also at the one-loop level. This is enforced through

$$\delta Z_c = -\operatorname{Re} \dot{\Pi}_c \left(p^2\right)\Big|_{p^2=0} \,, \tag{4.169}$$

where $\dot{\Pi}_c\left(p^2\right) = \frac{\partial}{\partial p^2}\Pi_c(p^2)$ denotes the derivative of the ghost self-energy with respect to the external momentum p^2 and is given by

$$\dot{\Pi}_c(p^2) = -\frac{\alpha_s N_c}{8\pi}\left(B_0(p^2,0,0) - 1\right) \,. \tag{4.170}$$

The only diagram contributing to $\Pi_c(p^2)$ is depicted in Fig. 4.21. Due to the on-shell scheme the renormalization constant δZ_c contains not only UV but also IR divergent parts which both read explicitly

$$\delta Z_c^{\mathrm{UV}} = \frac{\alpha_s N_c}{8\pi\varepsilon_{\mathrm{UV}}} \,, \tag{4.171a}$$

$$\delta Z_c^{\mathrm{IR}} = -\frac{\alpha_s N_c}{8\pi\varepsilon_{\mathrm{IR}}} \,. \tag{4.171b}$$

Renormalization of the Massless Quarks

For the renormalization of massless quarks, the quark wave-function renormalization constants $Z_q^{L/R}$ are introduced for each quark chirality state separately such that

$$q_{L/R} = \sqrt{Z_q^{L/R}}q_{L/R} = (1 + \tfrac{1}{2}\delta Z_q^{L/R})q_{L/R}. \tag{4.172}$$

The renormalization constants are also determined in the on-shell scheme resulting in the condition

$$\delta Z_q^{L/R} = -\operatorname{Re}\Pi_q^{L/R}(0) \,, \tag{4.173}$$

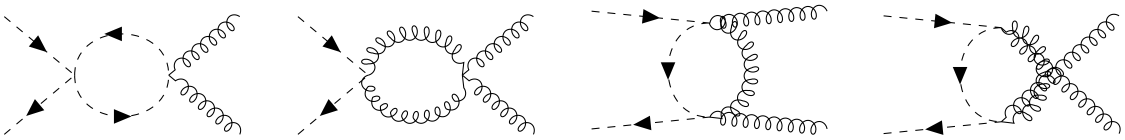

(a) Bubble contributions.

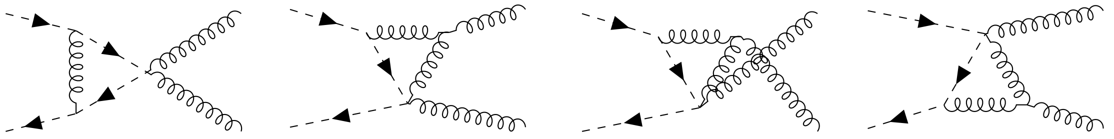

(b) Example triangle contributions.

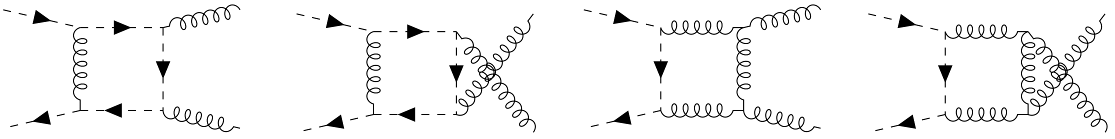

(c) Example box contributions.

Figure 4.16: Example one-loop corrections to the four-gluon-squark vertex.

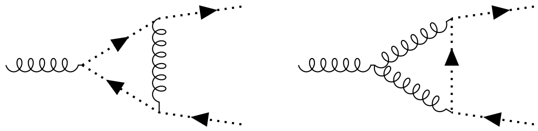

Figure 4.17: One-loop contributions to the ghost-gluon vertex.

where the scalar function $\Pi_q^{L/R}(p^2)$ follows from the decomposition of the quark self-energy $\Sigma_q(p)$ into its chiral parts through the projectors $P_{L/R} = \frac{1}{2}(1 \mp \gamma^5)$:

$$\Sigma_q(p) = \not{p}\left[P_L \Pi_q^L(p^2) + P_R \Pi_q^R(p^2)\right] + \Pi_q^{S,L}(p^2) P_L + \Pi_q^{S,R}(p^2) P_R \,. \tag{4.174}$$

The two contributing Feynman diagrams are shown in Fig. 4.22. The resulting renormalization constants contain the UV and IR divergent parts

$$\delta Z_q^{\mathrm{UV}} = -\frac{\alpha_s C_F}{2\pi\varepsilon_{\mathrm{UV}}} \,, \tag{4.175a}$$

$$\delta Z_q^{\mathrm{IR}} = \frac{\alpha_s C_F}{4\pi\varepsilon_{\mathrm{IR}}} \,, \tag{4.175b}$$

where the superscripts indicating the left/right-handed chirality states are dropped here for simplicity.

Real corrections

The infrared divergences in the virtual corrections are compensated by including the two real emission processes

$$\tilde{t}_1 \tilde{t}_1^* \longrightarrow g_a^\mu\,(k_1) + g_b^\nu\,(k_2) + g_c^\rho\,(k_3) \,, \tag{4.176a}$$

$$\tilde{t}_1 \tilde{t}_1^* \longrightarrow q_r\,(k_1) + \overline{q}_u\,(k_2) + g_a^\mu\,(k_3) \tag{4.176b}$$

with q denoting an effectively massless quark and where the initial squarks carry the same color and momentum labels as in Fig. 4.9. Some corresponding example Feynman diagrams are shown in

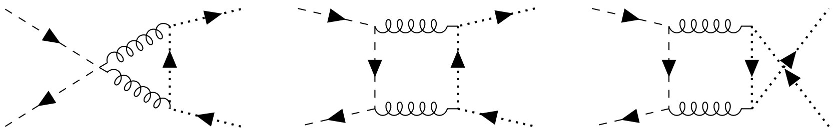

Figure 4.18: Triangle and box corrections to the ghost process $\mathcal{S}_1^{\mathrm{NLO}}$ which do not have a tree level analogue. The diagrams for $\mathcal{S}_2^{\mathrm{NLO}}$ can be obtained by reversing the ghost flow

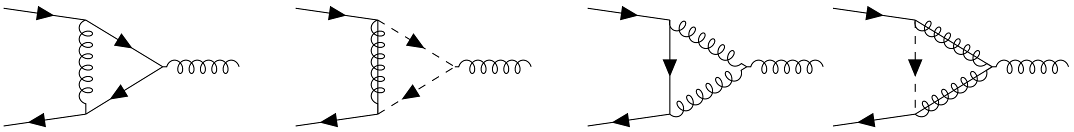

Figure 4.19: One-loop contributions to the quark-gluon vertex.

Figs. 4.23a and 4.23b where the momenta of the gluons in the first process have to be read from top to bottom starting with k_1. As in the tree-level calculation, $-\eta^{\mu\nu}$ is used here for the gluon polarization sum such that the longitudinal polarizations are subtracted using ghosts as asymptotic states. The result is cross checked against the result obtained with the full polarization sum (4.158). In order to arrive at the subtraction procedure involving ghosts, one can proceed as sketched in Sec. 4.4.1 by deriving the following two sets of Slavnov-Taylor identities from BRST-invariance. The first set relates the amputated three-gluon amplitude $\mathcal{M}_3^{\mu\nu\rho}$ to the six ghost amplitudes $\mathcal{S}_i^{\mu}$, $i = 1, \ldots, 6$ according to

$$k_{1,\mu}\mathcal{M}_3^{\mu\nu\rho} = -k_2^{\nu}\mathcal{S}_1^{\rho} - k_3^{\rho}\mathcal{S}_3^{\nu}\,, \tag{4.177a}$$

$$k_{2,\nu}\mathcal{M}_3^{\mu\nu\rho} = -k_1^{\mu}\mathcal{S}_2^{\rho} - k_3^{\rho}\mathcal{S}_6^{\mu}\,, \tag{4.177b}$$

$$k_{3,\rho}\mathcal{M}_3^{\mu\nu\rho} = -k_1^{\mu}\mathcal{S}_4^{\nu} - k_2^{\nu}\mathcal{S}_5^{\mu}\,, \tag{4.177c}$$

where, e.g., Eq. (4.177a) follows from the application of the BRST-transformations (4.161) to the correlation function $\langle\Omega|\, T\left\{\tilde{q}\, \tilde{q}^*\, \bar{c}_a\, g_b^{\nu}\, g_c^{\rho}\right\}|\Omega\rangle = 0$. The amputated ghost amplitudes are defined through the Feynman diagrams in Figs. (4.23c) to (4.23e) with the same color and momentum labels as in Eq. (4.176a). The second set equates the ghost amplitudes among themselves according to

$$k_{2,\nu}\mathcal{S}_4^{\nu} = k_{3,\rho}\mathcal{S}_2^{\rho}\,, \tag{4.178a}$$

$$k_{1,\mu}\mathcal{S}_5^{\mu} = k_{3,\rho}\mathcal{S}_1^{\rho}\,, \tag{4.178b}$$

$$k_{1,\mu}\mathcal{S}_6^{\mu} = k_{2,\nu}\mathcal{S}_3^{\nu} \tag{4.178c}$$

instead. Replacing all terms proportional to the momenta $k_1, \ldots, k_3$ in the polarization sum (4.158) through the identities (4.177) for each of the three gluons and exploiting additionally the identities in Eq. (4.178) as well as that

$$(\mathcal{S}_i - \mathcal{S}_{i+1})^* \cdot (\mathcal{S}_i - \mathcal{S}_{i+1}) = 0 \tag{4.179}$$

holds for $i = 1, 3, 5$ according to an explicit calculation with the help of Feynman rules, results in the following squared matrix element summed over the physical, i.e., transverse, final-state

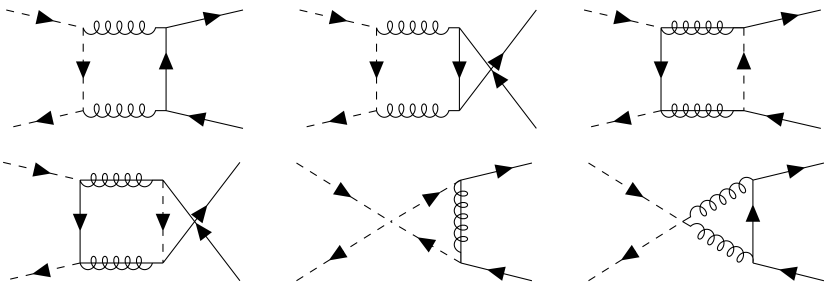

Figure 4.20: Box and triangle diagrams associated with stop-antistop annihilation into light quarks.

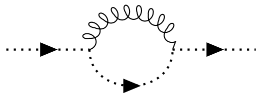

Figure 4.21: One-loop contribution to the ghost self-energy.

polarizations

$$-\mathcal{M}_3^{\mu\nu\rho}\mathcal{M}^*_{3,\mu\nu\rho} + \sum_{i=1}^{6} \mathcal{S}_i^{\mu}\mathcal{S}^*_{i,\mu}\,. \tag{4.180}$$

To make the integration over the three-particle phase space numerically feasible and to combine the real and virtual corrections to get an infrared safe cross section, the Catani-Seymour dipole subtraction method for massive initial states developed in Sec. 4.3 is used. According to the dipole factorization formula (4.59), the auxiliary squared matrix element related to $\mathrm{d}\sigma^{\mathrm{A}}$ for the process with three gluons in the final state consists of the 27 dipoles

$$\begin{aligned}|\mathcal{M}^{\mathrm{A}}_{\tilde{t}_1\tilde{t}_1^*\to ggg}|^2 = {}& \mathcal{D}_{12,3} + \mathcal{D}_{13,2} + \mathcal{D}_{23,1} + \mathcal{D}^{a1,b} + \mathcal{D}^{a2,b} + \mathcal{D}^{a3,b} + \mathcal{D}^{b1,a} + \mathcal{D}^{b2,a} + \mathcal{D}^{b3,a} \\ & + \mathcal{D}_1^{a2} + \mathcal{D}_1^{a3} + \mathcal{D}_2^{a1} + \mathcal{D}_2^{a3} + \mathcal{D}_3^{a2} + \mathcal{D}_3^{a1} + \mathcal{D}_1^{b2} + \mathcal{D}_1^{b3} + \mathcal{D}_2^{b1} + \mathcal{D}_2^{b3} + \mathcal{D}_3^{b2} \\ & + \mathcal{D}_3^{b1} + \mathcal{D}^a_{12} + \mathcal{D}^a_{23} + \mathcal{D}^a_{13} + \mathcal{D}^b_{12} + \mathcal{D}^b_{13} + \mathcal{D}^b_{23}\,,\end{aligned} \tag{4.181}$$

where the subscripts of the momenta in Eq. (4.176a) and Eq. (4.176b) are used to label the particles. For the process containing light quarks the 15 dipoles

$$\begin{aligned}|\mathcal{M}^{\mathrm{A}}_{\tilde{t}_1\tilde{t}_1^*\to \bar{q}qg}|^2 = {}& \mathcal{D}^{a3,b} + \mathcal{D}^{b3,a} + \mathcal{D}_1^{a3} + \mathcal{D}_2^{a3} + \mathcal{D}_1^{b3} + \mathcal{D}_2^{b3} \\ & + \mathcal{D}_{12,3} + \mathcal{D}_{13,2} + \mathcal{D}_{23,1} + \mathcal{D}^a_{12} + \mathcal{D}^b_{12} + \mathcal{D}^a_{31} + \mathcal{D}^a_{32} + \mathcal{D}^b_{31} + \mathcal{D}^b_{32}\end{aligned} \tag{4.182}$$

are needed. The explicit construction of the insertion operator which cancels the infrared divergences on the virtual side proceeds similarly to the examples provided in Sec. 4.3.

4.4.3 The Sommerfeld Enhancement

Besides the fixed-order NLO corrections, the stop-antistop annihilation cross section also receives important contributions from the exchange of n potential gluons, i.e., virtual gluons with momenta $q \sim \mathcal{O}(p_{\mathrm{cm}})$, between the incoming stop-antistop pair giving a correction factor proportional to $(\alpha_s/v)^n$. This is the well-known Sommerfeld enhancement introduced in Sec. 4.2.7 of higher-order terms that can spoil the perturbativity of the cross section in the non-relativistic regime where

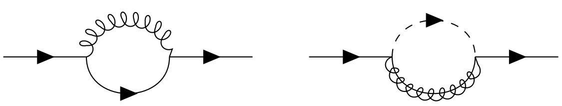

Figure 4.22: One-loop contributions to the quark self-energy.

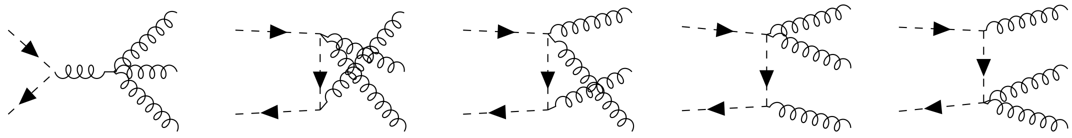

(a) Example graphs with three gluons in the final state that are associated with the amplitude $\mathcal{M}_3$.

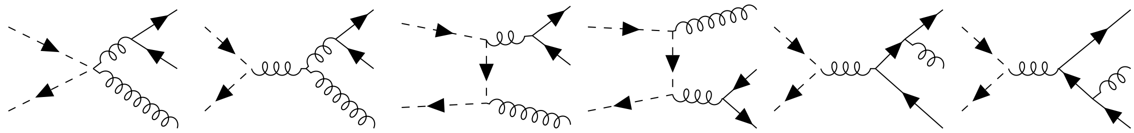

(b) Graphs with light quarks in the final state.

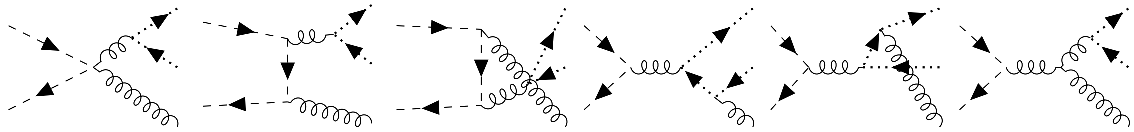

(c) Ghosts graphs associated with the amplitude $\mathcal{S}_1$. $\mathcal{S}_2$ is obtained by reversing the ghost flow.

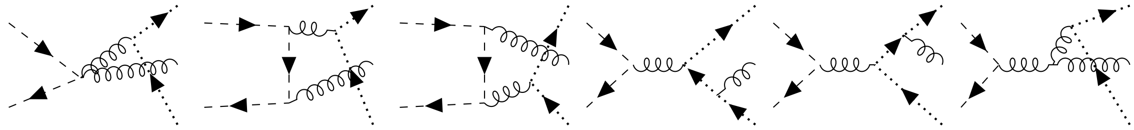

(d) Ghosts graphs associated associated with the amplitude $\mathcal{S}_3$. $\mathcal{S}_4$ is obtained by reversing the ghost flow.

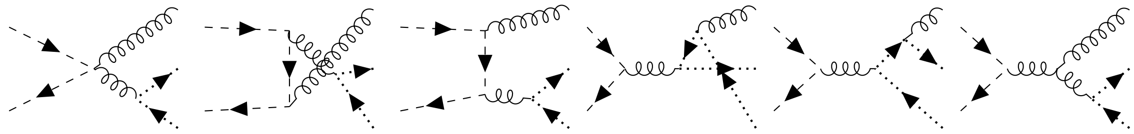

(e) Ghosts graphs associated with the amplitude $\mathcal{S}_5$. $\mathcal{S}_6$ is obtained by reversing the ghost flow.

Figure 4.23: Example real emission diagrams for stop annihilation into gluons and light quarks.

the relative velocity is of the order of or below the strong coupling, and therefore these terms need to be resummed to all orders in perturbation theory. The fact that the tree-level cross section is dominated by s-wave annihilations as discussed in Sec. 4.4.1 and visible in Fig. 4.11, allows to compute the Sommerfeld enhanced cross section

$$(\sigma v)^{\text{Som}} = S_{0,[\mathbf{8}]}\left((\sigma v)^{\text{Tree}}_{gg,[\mathbf{8_S}]} + (\sigma v)^{\text{Tree}}_{gg,[\mathbf{8_A}]} + N_f(\sigma v)^{\text{Tree}}_{q\bar{q},[\mathbf{8}]}\right) + S_{0,[\mathbf{1}]}\,(\sigma v)^{\text{Tree}}_{gg,[\mathbf{1}]} \tag{4.183}$$

by multiplying the leading order contribution with the Sommerfeld factor which is defined through

$$S_{0,[\mathbf{R}]} = \frac{\operatorname{Im}\mathcal{G}^{[\mathbf{R}]}(\mathbf{r}=0,\sqrt{s}+i\Gamma_{\tilde{t}_1})}{\operatorname{Im}\mathcal{G}_0(\mathbf{r}=0,\sqrt{s}+i\Gamma_{\tilde{t}_1})}\,, \tag{4.184}$$

and can be computed within the standard framework of non-relativstic QCD (NRQCD) described in Refs. [301,302]. The Green's function $\mathcal{G}^{[\mathbf{R}]}(\mathbf{r}=0,\sqrt{s}+i\Gamma_{\tilde{t}_1})$ is defined as solution of the Schrödinger equation

$$\Big[H^{[\mathbf{R}]} - \big(\sqrt{s} + i\Gamma_{\tilde{t}_1}\big)\Big]\mathcal{G}^{[\mathbf{R}]}\big(\mathbf{r}; \sqrt{s} + i\Gamma_{\tilde{t}_1}\big) = \delta^{(3)}(\mathbf{r}) \tag{4.185}$$

evaluated at the origin. The Hamiltonian is the one of quasi-stoponium and reads

$$H^{[\mathbf{R}]} = 2m_{\tilde{t}_1}^2 - \frac{1}{m_{\tilde{t}_1}}\nabla^2 + V^{[\mathbf{R}]}(\mathbf{r})\,. \tag{4.186}$$

The QCD Coulomb potential receives important contributions from gluon and fermion loops and reads at NLO in momentum space

$$\tilde{V}^{[\mathbf{R}]}(\mathbf{q}) = -C^{[\mathbf{R}]}\,\frac{4\pi\alpha_s(\mu_C)}{\mathbf{q}^2}\left\{1 + \frac{\alpha_s(\mu_C)}{4\pi}\left[\beta_0 \ln\left(\frac{\mu_C^2}{\mathbf{q}^2}\right) + a_1\right]\right\} \tag{4.187}$$

with the color factors $C^{[\mathbf{1}]} = C_F$ and $C^{[\mathbf{8}]} = C^{[\mathbf{8}_S]} = C^{[\mathbf{8}_A]} = -\frac{1}{2N_c}$ given by the Casimirs of the corresponding representation and the remaining constants

$$a_1 = \frac{31}{9}C_A - \frac{20}{9}T_F n_f\,, \tag{4.188a}$$

$$\beta_0 = \frac{11}{3}C_A - \frac{4}{3}T_f n_f \tag{4.188b}$$

with $n_f = 5$ for the Sommerfeld enhancement in contrast to $N_f = 4$ in the fixed-order calculation as the typical energy scale of the gluon in the Sommerfeld enhancement, $\mathcal{O}(100\,\text{GeV})$, is not large enough to take top quarks into account, or contributions from even heavier particles like squarks or gluinos. The analytic solution for the Green's function at the origin at NLO accuracy is

$$G^{[\mathbf{R}]}(\mathbf{r} = 0; \sqrt{s} + i\Gamma_{\tilde{t}_1}) = \frac{C^{[\mathbf{R}]}\alpha_s(\mu_C)m_{\tilde{t}_1}^2}{4\pi}\Big[g_{\text{LO}} + \frac{\alpha_s(\mu_C)}{4\pi}g_{\text{NLO}}\Big]\,, \tag{4.189}$$

where the LO and NLO contributions are given by the expressions

$$g_{\text{LO}} = -\frac{1}{2\kappa} + L - \psi^{(0)}, \tag{4.190a}$$

$$\begin{aligned} g_{\text{NLO}} = \beta_0\Big[&L^2 - 2L(\psi^{(0)} - \kappa\psi^{(1)}) + \kappa\psi^{(2)} + (\psi^{(0)})^2 - 3\psi^{(1)} - 2\kappa\psi^{(0)}\psi^{(1)} \\ &+ 4\,{}_4F_3(1,1,1,1;2,2,1-\kappa;1)\Big] + a_1\Big[L - \psi^{(0)} + \kappa\psi^{(1)}\Big]\,. \end{aligned} \tag{4.190b}$$

In Eq. (4.190), the function $\psi^{(n)} = \psi^{(n)}(1-\kappa)$ is the n-th derivative of $\psi(z) = \gamma_{\text{E}} + \mathrm{d}/\mathrm{d}z \ln\Gamma(z)$ with the argument $(1-\kappa)$. The remaining abbreviations are given by

$$\kappa = \frac{iC^{[\mathbf{R}]}\alpha_s(\mu_C)}{2v_s}\,, \qquad L = \ln\frac{i\mu_C}{2m_{\tilde{t}_1}v_s} \tag{4.191}$$

and depend on the non-relativistic velocity of the incoming particles

$$v_s = \sqrt{\frac{\sqrt{s} + i\Gamma_{\tilde{t}_1} - 2m_{\tilde{t}_1}}{m_{\tilde{t}_1}}}\,. \tag{4.192}$$

For the computation of the Sommerfeld factor, also the free Green's function $\mathcal{G}_0(0, \sqrt{s} + i\Gamma_{\tilde{t}_1}) = im_{\tilde{t}_1}^2 v_\mathrm{s}/(4\pi)$ is needed. The remaining aspect to address is the choice for the Coulomb scale μ_C at which the strong coupling in the QCD potential (4.187) is evaluated. Following Ref. [303], a suitable choice is

$$\mu_C = \max\left\{2m_{\tilde{t}_1} v_s, \mu_B\right\} . \tag{4.193}$$

The first value $2m_{\tilde{t}_1} v_s$ is motivated by the typical momentum transfer mediated by the potential gluons whereas the Bohr scale μ_B corresponds to twice the inverse Bohr radius r_B and is obtained by iteratively solving the equation

$$\mu_B \equiv 2/r_B = C_F m_{\tilde{t}_1} \alpha_s(\mu_B). \tag{4.194}$$

For the scenario in Tab. 4.4, the Bohr scale takes the value $\mu_B = 199\,\mathrm{GeV}$ and the associated value for the strong coupling in the $\overline{\mathrm{MS}}$-scheme with six active quark flavors is $\alpha_s(\mu_B) = 0.1061$.

As a single gluon exchange is already included in the NLO calculation (see Fig. 4.15 and Fig. 4.16), the fixed-order and the Sommerfeld enhanced cross section have to be matched in order to avoid double counting. This is achieved by taking only the terms starting at $\mathcal{O}(\alpha_s^2)$ in Eq. (4.184) into account defining the full cross section $(\sigma v)^\mathrm{Full}$. As described in the context of the NLO corrections to squark-pair annihilation into quarks [169], it is also possible to subtract the velocity-enhanced part from the fixed-order calculation in order to obtain the "pure" NLO cross section which can be written as

$$(\sigma v)_{v}^\mathrm{NLO} = (\sigma v)^\mathrm{NLO} + \frac{\alpha_s(\mu_R)\pi}{v_\mathrm{rel}} \left(\sum_{\mathbf{R}} C^{[\mathbf{R}]} (\sigma v)^\mathrm{Tree}_{gg,[\mathbf{R}]} + N_f C^{[\mathbf{8}]} (\sigma v)^\mathrm{Tree}_{q\bar{q}} \right) \tag{4.195}$$

with the relativistic relative velocity $v_\mathrm{rel} = v/(2-\rho)$.

4.4.4 Impact on the Cross Section and the Relic Density

Having calculated the virtual and real corrections as well as the Sommerfeld enhancement, the impact of these corrections on the annihilation cross section and on the neutralino relic density can be discussed in conjunction with the other important coannihilation channels from Tab. 4.5. However, the discussion is kept rather generic as the precise magnitude of the corrections depends on the specific realization of the MSSM.

Impact on the Annihilation Cross Section

For each channel shown in Tab. 4.5 that can be corrected with DM@NLO besides stop-antistop annihilation into gluons, the tree-level (black dashed line) as well as the one-loop cross section (blue solid line) are show in Fig. 4.24 as a function of the c.m. momentum p_cm. If the Sommerfeld enhancement is available, the corresponding cross section (green solid line) as well as the full cross-section (red solid line) are shown as well. For reference, the cross-section produced with the default MicrOMEGAs setup (orange solid line) is shown additionally. As before, the gray shaded area depicts (in arbitrary units) the thermal velocity distribution, in order to demonstrate for what p_cm the cross-section contributes to the total annihilation cross-section $\langle\sigma_\mathrm{ann} v\rangle$ the most. In the

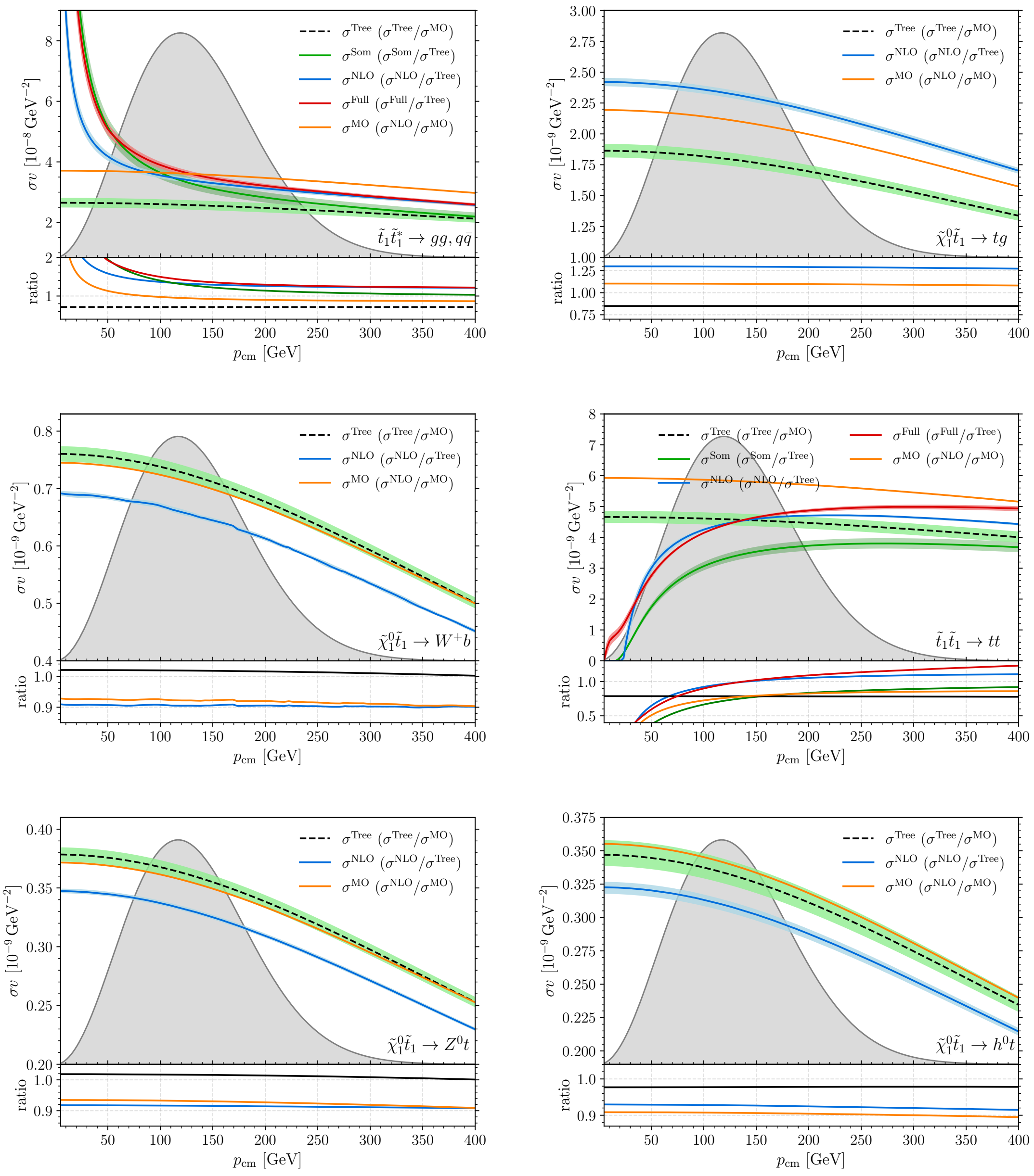

Figure 4.24: Tree-level (black dashed line), one-loop (blue solid line), full (red solid line) if present and MicrOMEGAs (orange solid line) cross sections for the dominant (co)annihilation channels shown in Tab. 4.5 that can be corrected with DM@NLO including the corresponding uncertainties from variations of the renormalisation scale μ_R by a factor of two around the central scale as shaded bands. The upper part of each plot shows the absolute value of σv together with the thermal velocity distribution (in arbitrary units), whereas the lower part shows the corresponding relative shift (second item in the legend).

lower part, the corresponding relative shifts of the different cross-section values (second item in the legend) are shown. Note again that the difference between the MicrOMEGAs prediction and the DM@NLO tree-level result is mainly due to the different choice of the renormalization scale. The uncertainties from variations of the renormalization scale μ_R by a factor of two around the central scale are displayed as shaded bands.

It becomes apparent that for stop-(anti)stop annihilation in the region of small relative velocities the Coulomb corrections from the exchange of multiple gluons between the incoming stops dominate the fully corrected annihilation cross section. For the gluonic final state, the singlet feels an attractive force whereas the squark and antisquark transforming under an eight dimensional representation are repelled from each other. In this case, the Sommerfeld corrections still lead to a total increase of the annihilation probability even though the LO cross section is dominated by the repulsive symmetric octet contribution. This is due the color suppression factor $1/(2N_c)$ in the Sommerfeld factor for the eight dimensional representations. For vanishing relative velocities, the enhanced cross section even diverges and approaches the well-known Coulomb singularity which could be cured by properly taking the formation of bound states into account. However, as the Boltzmann distribution almost vanishes for momenta around $p_{\text{cm}} = 0$, such effects are heavily suppressed. In contrast, the repulsive force dominates for stop pair-annihilation such that the corresponding corrected cross section decreases significantly compared to the tree-level value for small relative velocities whereas for larger p_{cm} the fixed-order NLO corrections cause a positive shift. In general, the NLO corrections drastically reduce in all cases the uncertainty from scale variations.

Impact on the relic density

It remains the investigation of the strong corrections on the final neutralino abundance. As before, for this purpose, a scan in the $m_{1/2}$-m_0 plane around the reference scenario of Tab. 4.4 is performed with the results shown in Fig. 4.25. There, the orange band (Ω_χ^{MO}) indicates the region consistent with the observed value $\Omega_{\text{CDM}}h^2$ from Eq. (3.2c) purely based on MicrOMEGAs, the blue band ($\Omega_\chi^{\text{Tree}}$) corresponds to the prediction where the DM@NLO tree-level cross sections replace the CalcHEP result, and the yellow band ($\Omega_\chi^{\text{Full}}$) is based on the full cross sections. In more detail, this means that the integration of the number density Boltzmann equation is still performed by MicrOMEGAs but that the cross sections are replaced by the ones implemented in DM@NLO if available and computed by CalcHEP otherwise. Again, the width of the three bands reflects the experimental 2σ uncertainty under the assumption that the lightest neutralino solely accounts for all of the measured DM relic density.

One can observe a clear separation between all three bands everywhere across the shown $m_{1/2}$-m_0 plane. The difference between the two tree-level results is again mainly due to the different scale choices. The black contour lines quantify the relative difference between the DM@NLO tree-level and the full calculation of the neutralino relic density. The increase amounts to roughly 16 % to 18 % in the regions consistent with the observed relic density, therefore exceeding the experimental uncertainty. This shift in Ω_{CDM} is mainly due to the corrections to the gluonic final state. As a consequence, the cosmologically favored parameter region is shifted towards larger stop masses for a fixed neutralino mass to compensate the increased effective annihilation cross section. It should again be stressed that DM@NLO allows to correct a large portion of the different contributions to the relic density which is larger than 80 % in the relevant region.

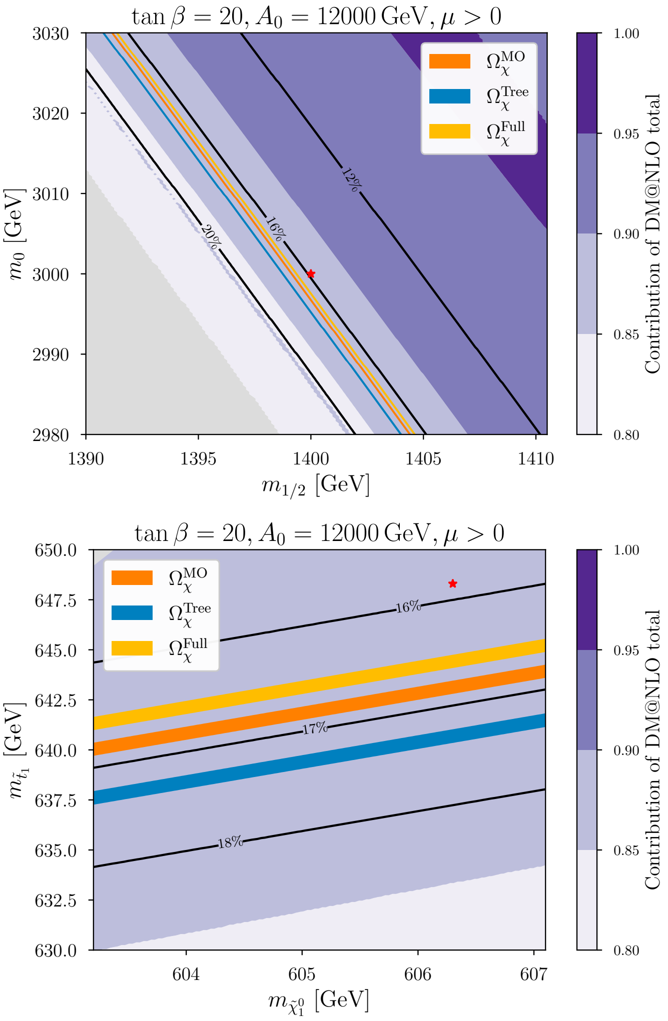

Figure 4.25: Bands compatible with the Planck measurement in Eq. (3.2c) in the $m_{1/2}$-m_0 plane (left) and the plane spanned by the associated physical masses of the lightest neutralino and the lightest stop (right) surrounding the example scenario from Tab. 4.4 shown in form of a red star. The three bands correspond to the MicrOMEGAs calculation (orange), our tree-level (blue) and our full corrections (yellow). The black solid lines indicate the relative change $(\Omega_\chi^{\text{Tree}} - \Omega_\chi^{\text{Full}})/\Omega_\chi^{\text{Tree}}$ in the relic density compared to our tree-level result.

4.5 The Precision Code DM@NLO

It remains the presentation of the user interface of the DM precision code DM@NLO based on Ref. [248]. As showcased in the previous sections, the code allows to numerically calculate the total DM (co)annihilation cross-sections at next-to-leading order in the strong coupling constant for most (co)annihilation channels within the MSSM including the Sommerfeld effect from the exchange of gluons or photons between the incoming particles. Even though not emphasized previously, besides providing also the $\mathcal{O}(\alpha_s)$ corrections to neutralino-nucleon scattering, the code also includes several resummed corrections, such as the SUSY-QCD Δm_b resummation. As the relevance of DM@NLO for direct detection has not yet been covered in this thesis before, the installation and running of the program is only presented after a brief review of the calculation of the spin-independent as well as spin-dependent elastic neutralino-nucleon scattering cross sections, since this is necessary to correctly interpret the DM@NLO output.

4.5.1 The Neutralino Direct Detection Rate

Results of direct dark matter detection experiments are usually presented as exclusion limits on the spin-dependent (SD) and spin-independent (SI) DM-nucleon scattering cross-sections, σ_N^{SD} and σ_N^{SI}, as a function of the DM mass (see Sec. 3.4.2). However, as the typical energies in a direct detection experiment are much smaller than the heavy particle masses of the microscopic theory mediating the interaction between DM and the constituents of a nucleon, it is customary to perform the calculation in the language of an effective field theory [304–307], i.e., by integrating out those heavy mediators. The spin-independent cross section

$$\sigma_N^{\mathrm{SI}} = \frac{\mu_N^2}{\pi}|g_N^{\mathrm{SI}}|^2 \tag{4.196}$$

is then expressed through the SI effective DM coupling to nucleons g_N^{SI} with $\mu_N = m_N m_\chi/(m_N+m_\chi)$ being the reduced mass of the DM-nucleon system. The effective coupling is computed as

$$g_N^{\mathrm{SI}} \;=\; \sum_q \langle N|\,\bar{q}q\,|N\rangle\, \alpha_q^{\mathrm{SI}}\,, \tag{4.197}$$

where the sum runs over all six quark flavors q and α_q^{SI} is the Wilson coefficient describing the SI interaction between quarks and the DM particle. The nuclear matrix element $\langle N|\,\bar{q}q\,|N\rangle$ can be qualitatively understood as the probability of finding the quark q inside the nucleon N and is commonly expressed through the scalar nuclear form factors f_{Tq}^N as

$$\langle N|\,m_q\bar{q}q\,|N\rangle \;=\; f_{Tq}^N\, m_N \tag{4.198}$$

with the quark mass m_q and the nucleon mass m_N. The scalar coefficients f_{Tq}^N are determined from experiment and lattice QCD and are another source of theoretical uncertainties. To highlight the latter point, in Tab. 4.6 the associated values that are hardcoded in DM@NLO and the two other DM packages DarkSUSY and MicrOMEGAs are shown. The heavy quark form factors f_{Tq}^N are

Scalar coefficient	DM@NLO	DarkSUSY	MicrOMEGAs
f^p_{Tu}	0.0208	0.023	0.0153
f^n_{Tu}	0.0189	0.019	0.0110
f^p_{Td}	0.0411	0.034	0.0191
f^n_{Td}	0.0451	0.041	0.0273
$f^p_{Ts} = f^n_{Ts}$	0.043	0.14	0.0447
$f^p_{Tc} = f^p_{Tb} = f^p_{Tt}$	0.0663	0.0595	0.0682
$f^n_{Tc} = f^n_{Tb} = f^n_{Tt}$	0.0661	0.0592	0.0679

Table 4.6: Scalar nuclear form factors f^N_{Tq} used in DM@NLO based on Ref. [309], DarkSUSY 6.4 based on Ref. [310] and MicrOMEGAs 5.3 [215].

obtained from those related to light quarks via the relation [308]

$$f^N_{Tc} \;=\; f^N_{Tb} \;=\; f^N_{Tt} \;=\; \frac{1}{27}\left(1 - \sum_{q=u,d,s} f^N_{Tq}\right). \tag{4.199}$$

The SD scattering cross section for DM on a single nucleon on the other hand is given by

$$\sigma^{\rm SD}_N \;=\; \frac{3\mu_N^2}{\pi}\left|g^{\rm SD}_N\right|^2, \tag{4.200}$$

where the effective SD coupling $g^{\rm SD}_N$ between DM and nucleons reads

$$g^{\rm SD}_N \;=\; \sum_{q=u,d,s} (\Delta q)_N\, \alpha^{\rm SD}_q \tag{4.201}$$

with the SD Wilson coefficient $\alpha^{\rm SD}_q$ describing the DM-quark interaction. In contrast to the SI case, the sum runs only over the light quarks u, d and s, as these carry the largest fraction of the nucleon spin which in turn is quantified through the axial-vector form factors $(\Delta q)_N$. The corresponding numerical values in DM@NLO are identified with those in MicrOMEGAs 5.3, given by

$$\begin{aligned}
(\Delta u)_p \;&=\; (\Delta d)_n \;=\; 0.842\,,\\
(\Delta d)_p \;&=\; (\Delta u)_n \;=\; -0.427\,,\\
(\Delta s)_p \;&=\; (\Delta s)_n \;=\; -0.085\,.
\end{aligned} \tag{4.202}$$

To provide a numerical example for the application of DM@NLO to direct detection, the neutralino-nucleon cross-sections for different values of $m_{1/2}$ around the example scenario from Tab. 4.4 is shown in Fig. 4.26, while a detailed discussion of direct detection in NLO SUSY-QCD is available in Ref. [191]. The upper panels show the SI proton (left) and neutron (right) cross sections, whereas the corresponding SD quantities are presented in the two lower panels. All quantities have been calculated with the DM@NLO code at tree level (black solid line), including the full $\mathcal{O}(\alpha_s)$ corrections to the dominant effective operators (blue solid line), MicrOMEGAs (orange solid line) and the corresponding analytic tree-level calculation.[4] Also shown are all three values of the

---

[4] More precisely, the orange solid line corresponds to the MicrOMEGAs function `nucleonAmplitudes`, which includes additionally the box corrections calculated in Ref. [188], while the green dotted line corresponds to the

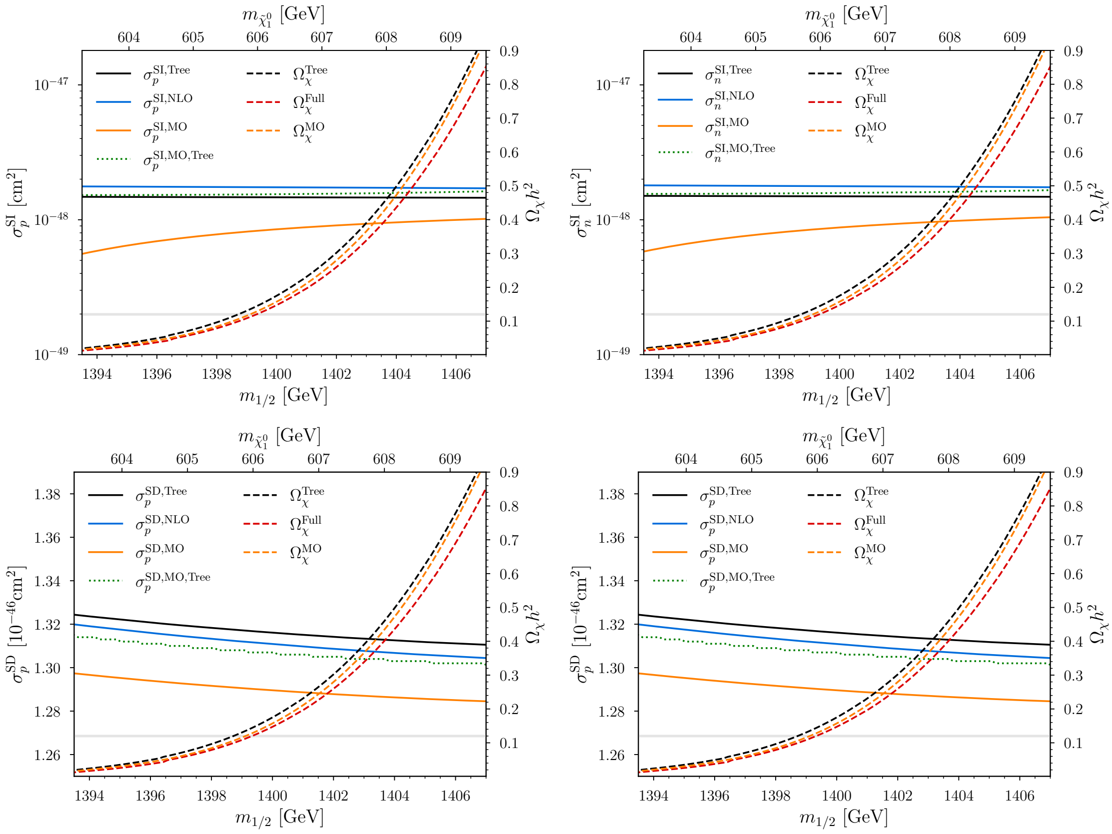

Figure 4.26: Spin-independent (top) and spin-dependent (bottom) neutralino-nucleon cross sections for protons (left) and neutrons (right) in the example scenario in Tab. 4.4 for different values of the universal gaugino mass parameter as well as the corresponding neutralino relic density obtained with MicrOMEGAs (MO), our tree-level calculation (Tree) and with our full calculation (Full). The upper and lower limits imposed by Eq. (3.2c) are indicated through the gray band.

resulting relic density ($\Omega_\chi^{\rm MO}$, $\Omega_\chi^{\rm Tree}$, $\Omega_\chi^{\rm Full}$) with the same color coding as in Fig. 4.25, as well as the Planck compatible value through a gray band. Note that the three curves increase as expected with the neutralino mass.

4.5.2 Installing and Running DM@NLO

The source code of the DM@NLO package is written in Fortran 77 and the corresponding C++ interface is designed similarly to the precision code Resummino [311, 312] for resummation predictions for gaugino and slepton pair production at hadron colliders. It is publicly available for download at the web page `https://dmnlo.hepforge.org` and is licensed under the European Union Public Licence v1.1.

The code can be compiled with the GNU compiler collection (GCC) and CMake version 3.0 or higher. As external dependencies, the libraries SLHALib-2.2 [313] and LoopTools-2.16 [244] are required for reading particle spectra following the Supersymmetry Les Houches Accord 2 (SLHA 2) convention [314, 315] and for evaluating one-loop integrals, respectively. The code ships directly with slightly modified versions of both libraries, as well as the CUBA-1.1 [277] library for performing multidimensional phase space integrals through the VEGAS Monte Carlo algorithm [276].

Installation

After the successful download, the code can easily be unpacked and installed by running the following commands in a Unix shell:

```
tar xvf DMNLO-X.Y.Z.tar
cd DMNLO-X.Y.Z
mkdir build
cd build
cmake .. [options]
make
make install
```

The last command is optional and places the DM@NLO binary `dmnlo` as well as the static library `libdmnlo.a` in the top-level source directory, which is the setup we assume in the following. Otherwise, the executable can be found in `build/bin` and the library in `build/src`. To install the code, e.g., system wide, the installation directory can be set with the `cmake` option

```
-DCMAKE_INSTALL_PREFIX=
```

Compilers different from the default C, C++ and Fortran compilers identified by CMake can be set with

```
-DCMAKE_<LANG>_COMPILER=
```

The path to an alternative LoopTools installation can be specified with `-DLOOPTOOLS=PATH` after setting `-DBUILD_LOOPTOOLS` (default: `ON`) to `OFF` if libraries and headers are installed in the same folder, or through `LOOPTOOLS_INCLUDE_DIR` and `LOOPTOOLS_LIB_DIR` if not.

After successful compilation, the local installation can be tested by running the commands

---

output of the function `MSSMDDtest(loop=0,...)` with the additional QCD corrections turned off `QCDcorrections=0`.

Process	Folder	References	Sommerfeld
$\tilde{\chi}^0_m\tilde{\chi}^0_n, \tilde{\chi}^\pm_i\tilde{\chi}^\mp_j, \tilde{\chi}^0_n\tilde{\chi}^\pm_i \to q\bar{q}, q\bar{q}'$	`ChiChi2QQ`	[158, 162, 163, 166]	✗
$\tilde{\chi}^0_n\tilde{q}_i \to q'\phi, q'\bar{V}, q'g$ with $q, q' \in \{t, b\}$	`NeuQ2qx`	[164, 165, 271]	✗
$\tilde{t}_1\tilde{t}_1^* \to VV, V\phi, \phi\phi, \ell\bar{\ell}$	`QQ2xx`	[167]	✓
$\tilde{q}_i\tilde{q}_j' \to qq'$ with $q, q' \in \{t, b\}$	`stst2QQ`	[169]	✓
$\tilde{\tau}_1\tilde{\tau}_1^* \to t\bar{t}$	`staustau2QQ`	[170]	✓
$\tilde{t}_i\tilde{t}_j^* \to gg, q\bar{q}$ with $q \in \{u, d, c, s\}$	`stsT2xx`	[171]	✓
$\tilde{\chi}^0_1 N \to \tilde{\chi}^0_1 N$	`DD`	[191]	–

Table 4.7: List of (co)annihilation and elastic DM-nucleon scattering processes included in DM@NLO, given together with the location of the corresponding source code in `run_dmnlo`, the references to the original publication and whether the Sommerfeld enhancement is included. Here, $\phi = \{h^0, H^0, A^0, H^\pm\}$, $V = \{Z^0, W^\pm, \gamma\}$, $\bar{V} = V \setminus \{\gamma\}$, and ℓ ($\bar{\ell}$) can be any (anti)lepton. The indices can take the values $\{m, n\} = \{1, 2, 3, 4\}$, $\{i, j\} = \{1, 2\}$.

```
./dmnlo --help
./dmnlo input/DMNLO.in
```

in a shell. The source files of the C++ interface to DM@NLO are located in `src`, whereas the processes themselves implemented in Fortran 77 are collected in the folder `run_dmnlo`. The name of each subfolder for every process supported by DM@NLO is summarized in Tab. 4.7, together with the key references documenting the corresponding calculational details. The directory `external` contains external dependencies like LoopTools or SLHALib. The folder `input/demo` provides for every process available in DM@NLO, sorted according the arXiv number of the corresponding publication, the associated example scenarios as SLHA 2 files as well as Python 3 plotting routines that partially use PySLHA [316] to read the particle spectra and allow to reproduce the most important cross section plots.

Running DM@NLO from the command line

As indicated above, DM@NLO can be executed in a shell through the command

```
./dmnlo <dmnlo-input-file>
```

where the mandatory argument `<dmnlo-input-file>` provides the path to a configuration file in plain text format specifying the process and corresponding input parameters. Details on all the available options in such an input configuration file are extensively documented in App. C.1. One example input file delivered with the code is `input/DMNLO.in`. Alternatively, the parameter values defined in the input file can also be passed through the command line interface (CLI), which then supersedes the value included in the text file. In the following, all possible command line options are described. A concise summary is also provided in App. C.2. The command line options follow the same naming convention as the variables in the configuration file, so that the transfer from the command line to the input file is straightforward. The general options that are valid for both the relic density as well as the direct detection module are going to be introduced first.

The path to the SLHA file containing the numerical values of masses, mixing angles and decay widths has to be defined with `--slha`. The value of the renormalization scale in GeV is fixed through the `--muR` option whereas the renormalization scheme must be set to one of the three schemes defined in Sec. 4.2.4 with the option `--renscheme`. Again, the mixed $\overline{\mathrm{DR}}$-OS scheme no. 1 is the recommended one.

The `--choosesol` option defines the solution in the heavy quark sector, with 0 being the recommended option, where the solution is chosen such that the dependent stop mass $m_{\tilde{t}_2}$ is closest to the corresponding on-shell value from the SLHA file (see the discussion in Sec. 4.2.4). The arguments 1 and 2 then correspond to the two solutions in Eq. (4.30a) and (4.30b), respectively. If DM@NLO is used from the command line and the renormalization scheme fails, the code simply stops after issuing a warning.

Also included is a legacy option which can only be turned on through the CLI by passing the flag `--legacy`. This mode defines the weak mixing angle θ_W and the W-mass as in the default MSSM model file in MicrOMEGAs 2.4.1, i.e., $\sin\theta_W = 0.481$ and $m_W = \cos\theta_W m_Z$ with m_Z being the on-shell Z-mass. This option is included since this definition was adopted in DM@NLO before the public release and allows to reproduce results from earlier publications. Starting with `v1.0.0`, however, the electroweak mixing angle is defined through the on-shell Z- and W-mass from the SLHA 2 file as

$$\sin^2\theta_W \;=\; 1 - \frac{m_W^2}{m_Z^2}\,. \tag{4.203}$$

Note that the legacy option should only be used for the reproduction of previously published results.

Lastly, the perturbative order of the calculation needs to be specified. This is only possible through the CLI. The argument `--lo` leads to LO-accurate predictions and `--nlo` to NLO accuracy. For the calculation of (co)annihilation cross sections there are two more accuracy options. The flag `--sommerfeld` returns the Sommerfeld enhancement alone, whereas `--full` returns the NLO result matched to the Sommerfeld enhancement. Otherwise the highest order available is assumed. If no Sommerfeld enhancement is available, the `--full` option returns just the NLO cross section.

The initial and final particles of the (co)annihilation process are fixed according to the PDG numbering scheme [317]. The two options `--particleA` and `--particleB` fix the initial state, whereas the two produced SM particles must be referred to by setting `--particle1` and `--particle2`. The collisional energy $\sqrt{s}$ has to be defined with `--pcm`, which is the center-of-mass momentum p_{cm} of the incoming particles. The option `--result` controls whether the output contains the total cross section σ or the cross section times velocity σv, both in units of GeV^{-2}, where the relative velocity is defined as $v = 2\lambda^{1/2}(s, m_a^2, m_b^2)/s$ with λ being the Källén function.

The direct detection module is enabled through the `--DD` option, which supersedes the specified (co)annihilation settings. The output contains then the SI and SD scattering cross sections of the lightest neutralino on protons and neutrons in cm^2, respectively. The scalar nuclear form factors from Tab. 4.6 can be found (and modified) in `DD/DD_Init.F`. The `--formfactor` option followed by an integer number (0 for DM@NLO, 1 for DarkSUSY and 2 for MicrOMEGAs) allows the user to select a set of values from Tab. 4.6.

The DM@NLO library

To facilitate the usage of DM@NLO from within other codes like MicrOMEGAs, the static library `libdmnlo.a` provides the two functions

```
double cs_dmnlo(order,na,nb,n1,n2,PcmIn,muR,&slha,rs,sol,&corrFlags)
void dd_dmnlo(order,muR,&slha,rs,sol,ff,&cs)
```

where the former returns the total (co)annihilation cross section and the latter writes the SI and SD DM-nucleon cross sections into the array `cs`. The renormalization scale is set with `muR`, the SLHA 2 input file with `slha`, the renormalization scheme through the flag `rs` and the associated solution for the three soft-breaking parameters with `rs`. The parameter `sol` corresponds to the `choosesol` option and `ff` in the argument set of the direct detection function to the `formfactor` option.

The integer `order` specifies the perturbative order of the calculation. Possible values are 0 for the LO result, 1 for the NLO result. For the computation of the (co)annihilation cross section, two additional options are available for the `order` parameter, namely 2 for the full result (including NLO calculation and Sommerfeld enhancement) and 3 for the Sommerfeld enhanced cross section alone (without including the NLO calculation).

The parameters `na` and `nb` are needed to fix the incoming particles through their respective PDG numbers, while `n1` and `n2` are meant to specify the two particles in the final state. The center-of-mass momentum is set through `PcmIn`. Finally, the integer array `corrFlags` allows to turn certain processes on and off, which may be useful if the corresponding contribution to the relic density is known to be negligible.

The static library `libdmnlo.a` also provides the two functions

```
int canImprove_dmnlo(na,nb,n1,n2)
int consistent_RS_dmnlo(rs,&slha,muR)
```

The former allows to check whether a given process can be corrected with DM@NLO, while the latter verifies whether the particle spectrum contained in `slha` yields a stable renormalization scheme. Alternative to the manual decision what annihilation channels to include, the file

```
minimal_example.cpp
```

located in `external/micromegas_5.3.41/MSSM` exemplifies the use of these functions with MicrOMEGAs in a way that only those channels contributing more than 2 % to the relic density are corrected. Before compiling the minimal example file through

```
make main=minimal_example.cpp
```

the file `micromegas_5.3.41/include/modelMakefile` has to be replaced with the associated modified version shipped with DM@NLO. This can be achieved by running

```
tar xvfk micromegas_5.3.41.tgz
```

in the `external/` directory where the `tar` option `-k` (or `--keep-old-files`) ensures that the modified version of `modelMakefile` containing the paths to the required libraries according to the default installation of DM@NLO is retained. For different paths or an alternative MicrOMEGAs version, `modelMakefile` has to be adjusted accordingly by the user. After successful compilation, the MicrOMEGAs interface can be tested by running

```
./minimal_example Scenario.spc
```

in a shell from the `MSSM` folder. For more details on the usage of the `corrFlags` argument, we refer to the explanation given in `minimal_example.cpp`.

4.6 Summary

In this chapter, higher-order corrections in the strong coupling constant to the neutralino relic density in the context of the DM@NLO program have been investigated. The latter is a numerical package designed for the precision calculation of dark matter (co)annihilation processes and direct detection in the MSSM. To better understand dark matter annihilation beyond leading order, many technical aspects entering a dark matter annihilation cross section at next-to-leading order have been introduced like a suitable regularization and renormalization prescription. In particular, an extension of the dipole subtraction method to massive initial states has been presented which now allows the cancellation of infrared divergent pieces between virtual and real corrections also beyond collider settings in a cosmological context. To illustrate the calculation of higher-order corrections, the NLO SUSY-QCD corrections to stop-antistop annihilation into gluons and light quarks have been presented in detail, finding that the two processes which are separate at leading order have to be combined at NLO in order to guarantee a well-defined and infrared safe cross section. From a physical point of view, these calculations were motivated by the fact that the increasing collider limits on the lightest neutralino mass are difficult to reconcile with the measured dark matter abundance as pure neutralino annihilation for $m_{\tilde{\chi}_1^0} \gtrsim 100\,\mathrm{GeV}$ often times leads to an overabundance. One possibility to circumvent this issue is colored coannihilation with the lightest stop as the NLSP. Then, the impact on the relic density has been investigated in a typical supersymmetric dark matter scenario using DM@NLO with the result that the inclusion of higher-order corrections to the relic density exceeds the experimental uncertainty of the dark matter content in the Universe. Apart from the benefit of having more precise predictions, it was shown that he inclusion of NLO corrections reduces the dependence of the cross section on the renormalization scale in the perturbative regime significantly. Thus, another major advantage of using NLO cross sections and beyond is the possibility to estimate theory errors. Lastly, it should be mentioned that the general structure of the code is well suited for the extension to non-supersymmetric models.

Chapter 5

Early Kinetic Decoupling of Forbidden Dark Matter

As already discussed, a theoretically appealing explanation of dark matter is that all of the corresponding energy density is made up of a single new elementary particle species with sufficiently strong interactions with the Standard Model to have established full thermal equilibrium at some point in the early Universe. Again, in this picture, today's DM relic abundance is set once the DM annihilation cross section falls below the Hubble expansion rate so that the dark sector drops out of chemical equilibrium and the DM number density becomes an effective comoving constant, a process referred to as freeze-out. Within the usual approach to determine the relic density, the classical Boltzmann equation describing the evolution of the DM phase space distribution function in a FLRW Universe is solved. To simplify the calculation, the majority of numerical DM codes, e.g., Refs. [209, 210, 214, 218], assume that kinetic equilibrium holds until long after chemical decoupling which then allows to trace only the integral over the DM phase space distribution function, i.e., the number density [80, 81]. However, kinetic decoupling might occur much earlier than chemical decoupling even in simple models given that the DM annihilation cross section exhibits a strong velocity dependence caused by, e.g., resonances, thresholds or the Sommerfeld enhancement effect [83, 84, 318, 319]. As a consequence, the final value of the relic abundance can be altered by more than an order of magnitude compared to the traditional number density approach [83, 84]. In order to adequately model the effect of early kinetic decoupling, extensions of this "standard" number density Boltzmann equation (nBE) approach have been developed. As discussed in Ch. 3, possibilities are for example (1) to solve a set of coupled Boltzmann equations (cBE) assuming that deviations from equilibrium are entirely described by the chemical potential and the temperature or (2) to obtain a numerical solution for the full Boltzmann equation (fBE) at the level of the phase space distribution function. Compared to the nBE treatment, the fluid approximation consists of two coupled Boltzmann equations, one for the number density and one for the velocity dispersion ("the DM temperature") by keeping the assumption of a thermal DM distribution, but at a temperature different from the photon temperature. It should be noted that the same kind of hydrodynamical formalism is also used to estimate the mass of the smallest dark matter subhalos [82] and to model the dynamics of domain walls within cosmological phase transitions [320]. Both of these two methods are available in the publicly available and WOLFRAM

Language based numerical precision code DRAKE [84]. However, the default implementation of the elastic collision term for both approaches relies on a Fokker-Planck (FP) type operator derived under the assumption of a small-momentum transfer between DM and SM particles in the thermal bath compared to the average DM momentum which is not necessarily the case if the DM particle and the scattering partner are close in mass. This, however, is a defining feature of forbidden or sub-threshold DM, which is a class of models where DM dominantly annihilates into heavier states [77, 321, 322]. These annihilations are made possible through the sufficiently large temperatures in the early Universe.

Going beyond the current state of research described above, based on Ref. [99], a C-based Boltzmann equation solver with full elastic collision terms for both approaches is presented in this chapter and, as an example, the forbidden DM model [323] is analyzed in which a singlet Dirac DM particle couples to SM leptons via a new scalar mediator. Again, the important part is that the analysis is carried out at the level of the phase space density without relying on simplifying approximations of the elastic collision term or on the Fokker-Planck version of the cBE approach alone as in Ref. [324]. For this purpose, all angular integrals of the full elastic collision term are performed analytically. This calculation and the associated methodology respond to the increasing interest in full solutions of the momentum-dependent Boltzmann equation not only in the context of the DM relic density [78, 84, 325–329], but also in many other areas, e.g., the precise computation of the effective number of neutrino species in the early Universe [330], leptogenesis [331], cosmic inflation [332] and gravitational waves from first order phase transitions [333]. As an alternative to the Boltzmann framework, Langevin simulations have been proposed to deal with nonequilibrium momentum distributions of non-relativistic DM in a FLRW background [334].

This chapter is composed as follows: the particle content of the forbidden DM model is introduced in Sec. 5.1. The parametrization of the collision term is shown in Sec. 5.2 followed by the outline of the numerical solution strategy for the momentum-dependent Boltzmann equation in Sec. 5.3. The detailed comparison of the relic density obtained with the different approaches including a discussion of the evolution of the phase space distribution function and the effect from DM self-scattering processes is performed in Sec. 5.4, followed by the presentation of the impact of current and projected limits besides the relic density from CMB observations, beam-dump and collider experiments on the parameter space. Conclusions are given in Sec. 5.5.

5.1 The Leptophilic Forbidden Dark Matter Model

The forbidden DM model under consideration consists of a Dirac fermion χ as DM with $g_\chi = 2$ degrees of freedom, which couples only to SM leptons through a real scalar ϕ as mediator. After electroweak symmetry breaking, the effective Lagrangian reads

$$\mathcal{L} = \mathcal{L}_{\mathrm{SM}} + \frac{1}{2}\phi(\Box - m_\phi^2)\phi + \bar{\chi}(i\not{\partial} - m_\chi)\chi - g^S_{ij}\phi\bar{l}_i l_j - i g^P_{ij}\phi\bar{l}_i\gamma_5 l_j - g^S_\chi\phi\bar{\chi}\chi - i g^P_\chi\phi\bar{\chi}\gamma_5\chi, \quad (5.1)$$

with the flavor indices $i, j = e, \mu, \tau$. In the absence of lepton flavor violation, the associated DM annihilation cross section into leptons reads

$$(\sigma v_{\mathrm{lab}})_{\chi\bar{\chi}\to l\bar{l}} = \frac{4\pi\sqrt{1-4m_l^2/s}}{s-2m_\chi^2}\,\frac{\alpha^P_\chi s + \alpha^S_\chi\left(s-4m_\chi^2\right)}{(s-m_\phi^2)^2+\Gamma_\phi^2 m_\phi^2}\left(\alpha^P_{ll}s + \alpha^S_{ll}\left(s-4m_l^2\right)\right), \quad (5.2)$$

with the laboratory velocity $v_{\text{lab}} = \left[s(s-4m_\chi^2)\right]^{1/2}/(s-2m_\chi^2)$, $\alpha_{i(i)}^{S,P} = (g_{i(i)}^{S,P})^2/(4\pi)$ and the decay width of the mediator

$$\Gamma_\phi = \frac{1}{2}\sum_{i=\chi,l}\sqrt{m_\phi^2 - 4m_i^2}\left[\alpha_{i(i)}^S\left(1-\frac{4m_i^2}{m_\phi^2}\right) + \alpha_{i(i)}^P\right], \tag{5.3}$$

where the sum runs over all kinematically accessible decay channels. The phenomenology of this model in the sub-threshold regime and its relic density within the standard kinetic equilibrium approach for a small mass difference $\delta = (m_l - m_\chi)/m_\chi$ have already been explored extensively in Ref. [323]. Given that Eq. (5.1) seems to contradict invariance under the electroweak gauge group, it is necessary to find an ultraviolet-complete alternative. This is, e.g., possible by extending the two-Higgs-doublet model by an SU$(2)_L$ scalar singlet which then couples to the new fermion acting as DM [335]. With a focus on the early kinetic decoupling effect, the study of the effective theory has been repeated in Ref. [324] where the relic density was computed with the cBE treatment based on the small momentum transfer approximation resulting in a reduction of the viable parameter space. However, as already pointed out by Refs. [84, 324], the FP approximation breaks down if the particles scattering off of each other are very close in mass, as it is the case in forbidden scenarios. For this reason, the main objective of this calculation is to include the full elastic collision term not only in the set of coupled Boltzmann equations but also to go beyond the cBE treatment and investigate the relic density as a solution of the full Boltzmann equation at the level of the phase space density (fBE).

5.2 Parametrization of the Elastic Collision Term

The inclusion of the full elastic collision term (3.14) requires a suitable parametrization of the associated momentum integrals. A general, yet numerically very expensive, parametrization of the collision term for generic two-particle interactions without any assumptions on the matrix element based on Ref. [336] is derived in App. B.1.1 and has been the method of choice in the literature so far to evaluate the full collision term in the context of predicting the DM relic abundance, see e.g., Refs. [327–329].

In contrast to this common method, the particular case is considered here where the matrix element depends only on one Mandelstam variable whose spatial component is labeled as $\mathbf{k}^2$ and that can be brought into the form

$$|\mathcal{M}_{ab\to 12}|^2 = c_0 + \frac{c_1}{\Delta_1 - \mathbf{k}^2} + \frac{c_2}{(\Delta_2 - \mathbf{k}^2)^2}, \tag{5.4}$$

with the $\mathbf{k}$-independent coefficients c_i and the two other free parameters Δ_1, Δ_2 since this the form of the elastic scattering matrix relevant for the investigated model. From the Lagrangian in Eq. (5.1) one obtains $\Delta_1 = \Delta_2 = (E_a - E_1)^2 - m_\phi^2$ and the coefficients

$$c_0 = 64\pi^2(\alpha_\chi^S + \alpha_\chi^P)(\alpha_{ll}^S + \alpha_{ll}^P), \tag{5.5a}$$

$$c_1 = 128\pi^2\Big\{\left(\alpha_{ll}^S + \alpha_{ll}^P\right)\left(\alpha_\chi^S(m_\phi^2 - 2m_\chi^2) + \alpha_\chi^P m_\phi^2\right) - 2\alpha_{ll}^S(\alpha_\chi^S + \alpha_\chi^P)m_l^2\Big\}, \tag{5.5b}$$

$$c_2 = 64\pi^2\left(\alpha_\chi^S(m_\phi^2 - 4m_\chi^2) + \alpha_\chi^P m_\phi^2\right)\left(\alpha_{ll}^S(m_\phi^2 - 4m_l^2) + \alpha_{ll}^P m_\phi^2\right). \tag{5.5c}$$

The advantage is that one can work out a more suited parametrization which allows to perform seven out of the nine momentum integrals analytically. As shown in App. B.2, the collision operator reads in the end

$$\hat{C}_{\mathrm{el}}[f_a] = \frac{1}{128\pi^3 |\mathbf{p}_a| g_a} \int_{m_1}^{\infty} \mathrm{d}E_1 \int_{\max(m_b, E_1 - E_a + m_2)}^{\infty} \mathrm{d}E_b \, \Pi(E_a, E_b, E_1)\, \mathcal{P}(f_a, f_b, f_1, f_2), \tag{5.6}$$

where the integration kernel defined through

$$\Pi(E_a, E_b, E_1) = \Theta(k_+ - k_-) \int_{k_-}^{k_+} \mathrm{d}|\mathbf{k}| \, |\mathcal{M}_{ab\to 12}|^2 \tag{5.7}$$

requires one more integration over $|\mathbf{k}|$ which, however, can be performed analytically for the matrix element in Eq. (5.4) with the help of the two integrals

$$I_1(\Delta, a, b) = \int_a^b \mathrm{d}x \, \frac{1}{\Delta - x^2} = \begin{cases} \frac{1}{2\sqrt{\Delta}} \left[\ln\left(\frac{\sqrt{\Delta} - a}{\sqrt{\Delta} - b} \right) + \ln\left(\frac{b + \sqrt{\Delta}}{a + \sqrt{\Delta}} \right) \right] & , \Delta > 0 \\ \frac{1}{b} - \frac{1}{a} & , \Delta = 0 \\ \frac{1}{\sqrt{-\Delta}} \left[\operatorname{atan}\left(a/\sqrt{-\Delta} \right) - \operatorname{atan}\left(b/\sqrt{-\Delta} \right) \right] & , \Delta < 0 \end{cases} , \tag{5.8a}$$

$$I_2(\Delta, a, b) = \int_a^b \mathrm{d}x \, \frac{1}{(\Delta - x^2)^2} = \frac{1}{2\Delta} \left(\frac{a}{a^2 - \Delta} - \frac{b}{b^2 - \Delta} + I_1(\Delta, a, b) \right) , \tag{5.8b}$$

thus, requiring the same, or even less, computational effort as the annihilation term in Eq. (3.12). It should be stressed that the application of this technique is not limited to elastic scatterings but can also be applied to, e.g., the annihilation operator if quantum statistical effects need to be included. Meanwhile, the parametrization presented here has been adopted in Ref. [337] to study the freeze-in of cannibal dark matter.

5.3 Discretization Technique and Solution Strategy

To solve Eq. (3.7) for the phase space distribution numerically, the comoving momenta are restricted to lie in the range $10^{-2} \leq q \leq 10^{2}$ and discretized into $N = 200$ points $q_1, \ldots, q_N$ since this range together with the number of momentum slices was found to allow to accurately solve the full Boltzmann equation for a wide range of DM masses. Inspired by CLASS [338] and FORTEPIANO [339], the comoving momentum space is discretized according to the Gauss–Laguerre (GL) quadrature formula, a method designed for integrals of the type

$$\int_0^{\infty} x^{\alpha} e^{-bx} f(x) \, \mathrm{d}x \approx \sum_{i=0}^{N-1} w_i^{(\alpha,b)} f(x_i) \, . \tag{5.9}$$

This quadrature rule is also valid for the two-dimensional energy or momentum integrals appearing in the collision term since the integrand is, through the phase space distribution functions, exponentially suppressed in both integration variables. A suitable, yet arbitrary, choice is to generate the weights $w_i^{(\alpha,b)}$ for the parameters $\alpha = 0$ and $b = 1/2$ which is, e.g., possible with the GNU Scientific Library [340]. As the distribution functions encountered here are not exactly proportional to e^{-bx}, the factor e^{bx} is defined into $f(x)$.

If, on the other hand, the scattering term is approximated by the Fokker-Planck type operator in Eq. (3.15), a logarithmic spacing is chosen instead of the GL prescription, as sixth order central difference formulas are used for the numerical evaluation of the first and second momentum derivatives to achieve a high accuracy, i.e., f_χ is taken as a function of $\log q$ with a uniform spacing $\Delta \ln q = \ln(q_{i+1}/q_i)$. For the in total six points outside the solution domain, the conditions $f_{-2} = f_{-1} = f_0 = f_1$ as well as $f_N = f_{N+1} = f_{N+2} = f_{N+3}$ with $f_l = f_\chi(q_l, t)$ are used. In addition, the momentum derivatives are computed in log-space, $\ln f_\chi(p,t)$, to obtain also a high accuracy for large momenta where the distribution function can differ by several orders of magnitude for neighboring points.

Even though the elastic collision term manifestly conserves the number of particles in the continuum limit, the discretized version can lead to a spurious change of the comoving number density in the initial high-temperature regime. Therefore the same prescription as in Ref. [84] is adopted and kinetic equilibrium is assumed if the ratio $\gamma(T)/H(T)$ is larger than 10^5. This means that the nBE is solved instead.

The set of N Boltzmann equations obtained after discretizing Eq. (3.7) are stiff differential equations which require special integration routines to overcome the stiffness difficulty. For this purpose, the CVODE solver based on the backward differentiation formula of the SUNDIALS library [341, 342] is used.

5.4 Numerical Analysis

Throughout the whole numerical analysis, similar to the original work [323], the DM couplings are identified with the values $\alpha_\chi^S = 0$ and $\alpha_\chi^P = 0.1$ defined at the energy scale corresponding to m_ϕ. This choice is motivated by two facts: First, expanding the squared c.m. energy in the laboratory velocity $s = 4m_\chi^2(1 + v_\mathrm{lab}^2/4) + \mathcal{O}\big(v_\mathrm{lab}^4\big)$ shows that only the coupling α_χ^P contributes (at tree-level) an s-wave component, suggesting that the scalar coupling is of minor importance for dark matter annihilation and can therefore be set to zero. Second, this choice ensures that both couplings remain perturbative $\alpha_\chi^S, \alpha_\chi^P < 1$ below $1\,\mathrm{TeV}$ for the investigated mediator mass range $0.1\,\mathrm{GeV} \leq m_\phi \leq 100\,\mathrm{GeV}$ as dictated by the one-loop renormalization group equation [343]

$$\mu \frac{\mathrm{d}\alpha_\chi^{S/P}}{\mathrm{d}\mu} = \frac{5}{2\pi} \alpha_\chi^{S/P} (\alpha_\chi^{S/P} + \alpha_\chi^{P/S}). \tag{5.10}$$

Coannihilations of the mediator ϕ are also not included in this calculation as the investigation is restricted to the mass region $\tilde{r} = m_\phi/m_l \geq 1.25$. Therefore, the cubic and quartic self-interaction terms involving the ϕ field are taken to be zero. Scatterings off the mediator are also neglected, as the same exponential suppression of the averaged coannihilation cross section due to this mass splitting appears in the associated momentum transfer rate $\gamma_\phi(x) \sim e^{-x\tilde{r}}$. However, as this line of reasoning only holds assuming (i) the mediator is in equilibrium with the SM and (ii) there are no large hierarchies present between the DM and lepton couplings as well as the mediator self-couplings which could compensate the suppression at early times, it would be interesting to drop these assumptions and include the mediator in the network of momentum-dependent Boltzmann equations.

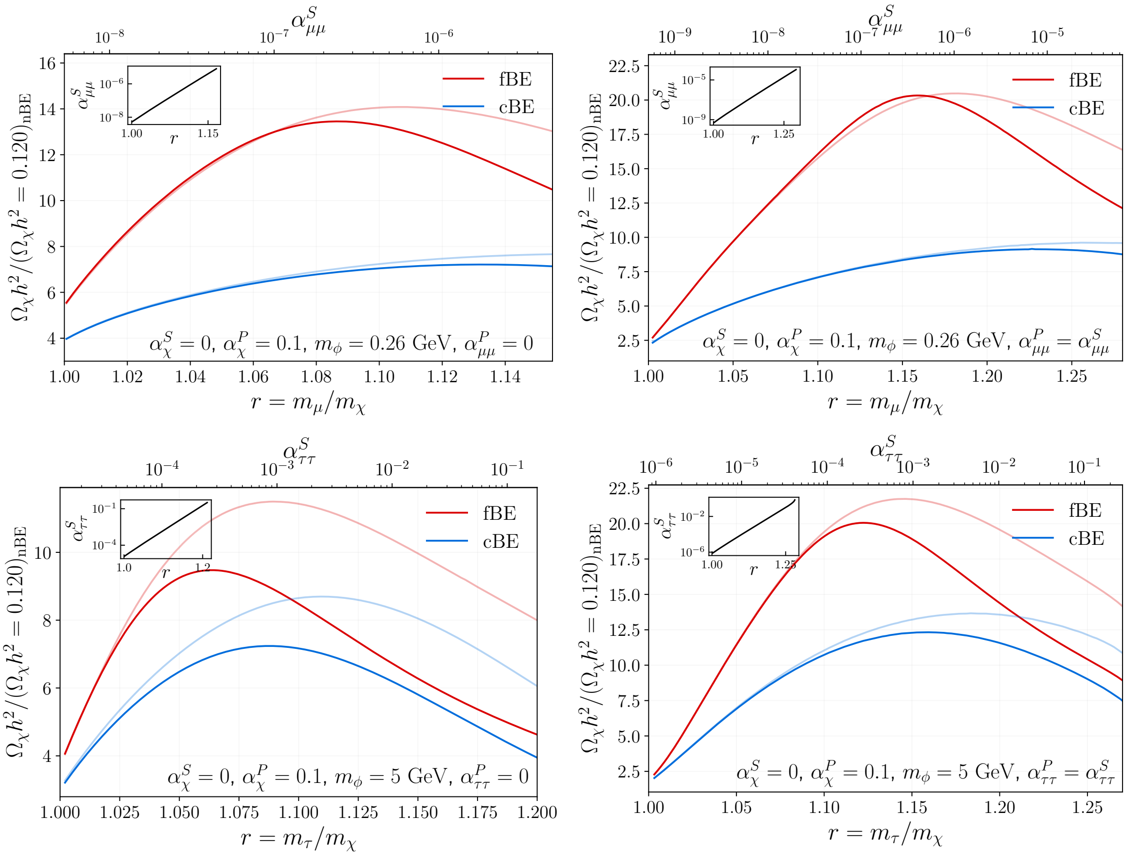

Figure 5.1: Ratio of the relic densities obtained with the cBE (blue) as well as the fBE (red) treatment and the number density approach as a function of the mass ratio $r = m_l/m_\chi$ for annihilations into muons (upper row) and tau leptons (lower row). In the left column, the pseudoscalar coupling is turned off whereas it is identical to the scalar coupling on the right. In all cases, the lepton coupling is chosen such that the result from the nBE method matches the experimentally observed relic abundance which imposes, to a very good approximation, an exponential relation between coupling and r (figure insets). The lines corresponding to the full elastic collision term are non-transparent, whereas the associated results obtained with the Fokker-Planck approximation are displayed with a lighter opacity.

5.4.1 The Relic Density Beyond Kinetic Equilibrium

As a start, it is useful to compare the DM relic density obtained from solving the Boltzmann equations (cBE and fBE) using the FP approximation on one hand and the full collision term on the other. In order to make a direct comparison with Ref. [324] possible, the results for the four benchmarks considered in Ref. [324] are displayed in Fig. 5.1. The relic density obtained with the cBE and fBE approaches for the two different implementations of the elastic collision term relative to the number density result are shown in Fig. 5.1 as a function of the inverse DM mass. For every m_χ, the lepton coupling α^S_{ll} is fixed by the requirement that the nBE result matches the experimentally observed relic density. Curves in bold colors correspond to the use of the full collision term, whereas curves with a lighter hue correspond to the use of the FP approximation. The upper panels deal with annihilation into muons, while the lower ones display the results for tau leptons in the final state. Furthermore, the left panel shows the results for $\alpha^P_{ll} = 0$, while the right panels are for $\alpha^S_{ll} = \alpha^P_{ll}$. One finds in this model that the early kinetic decoupling effect increases the

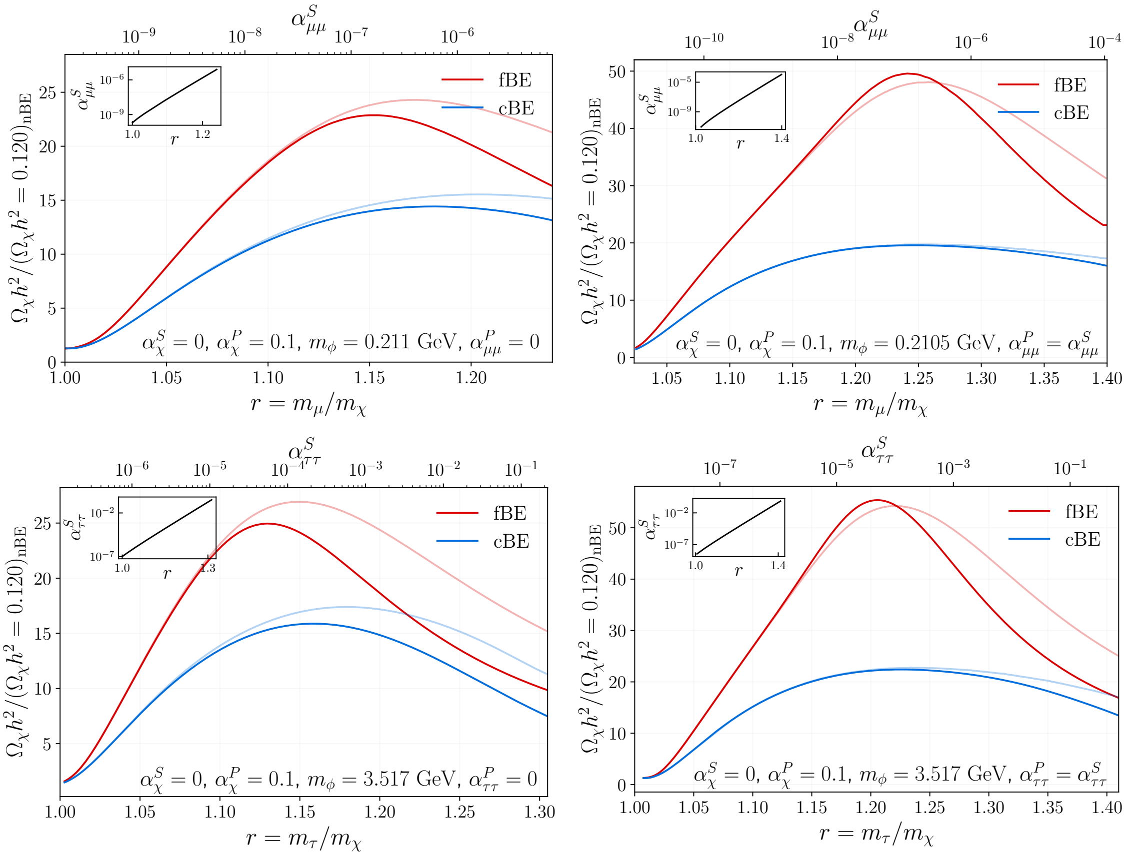

Figure 5.2: Same as Fig. 5.1, but for a m_ϕ that roughly corresponds to twice the muon (tau) mass in the upper (lower) panel.

relic density significantly and that the small-momentum approximation in general implies a smaller contribution from the elastic scattering collision term, which then leads to an overestimation of the relic density. Put differently, the full collision term keeps the DM distribution closer to equilibrium and, as a consequence, moves the associated relic density towards the number density result. This can be clearly seen in Fig. 5.1 by comparing darker and lighter hues of same-color curves. It is worth mentioning that the FP approximation tracks the full collision solution for a significant range of values of r in most of the cases. However, the two solutions significantly depart from each other for larger r values with the full collision solution in the fBE case approaching the nBE solution. For $r = 1$, DM still does not maintain kinetic equilibrium for this particular benchmark since for decreasing r, $2m_\chi$ moves towards the mediator mass and therefore the distribution function starts to be affected by the resonance.

In order to not only restrict the discussion to mediator masses far away from the di-muon or di-tau resonance, the same quantities are displayed in Fig. 5.2 but with a mediator corresponding to approximately twice the muon (upper panels) or tau mass (lower panels). As a result, the DM distribution function is in this case not only driven out of equilibrium through the forbidden nature of the model, but also significantly through the resonance. This enhancement can be clearly seen in the increased deviation from the nBE approach compared to the previous case where the mediator mass is much larger than the corresponding lepton mass. For example, the relic density from the fBE for the benchmark with a non-zero pseudoscalar coupling is more than 50 times that predicted

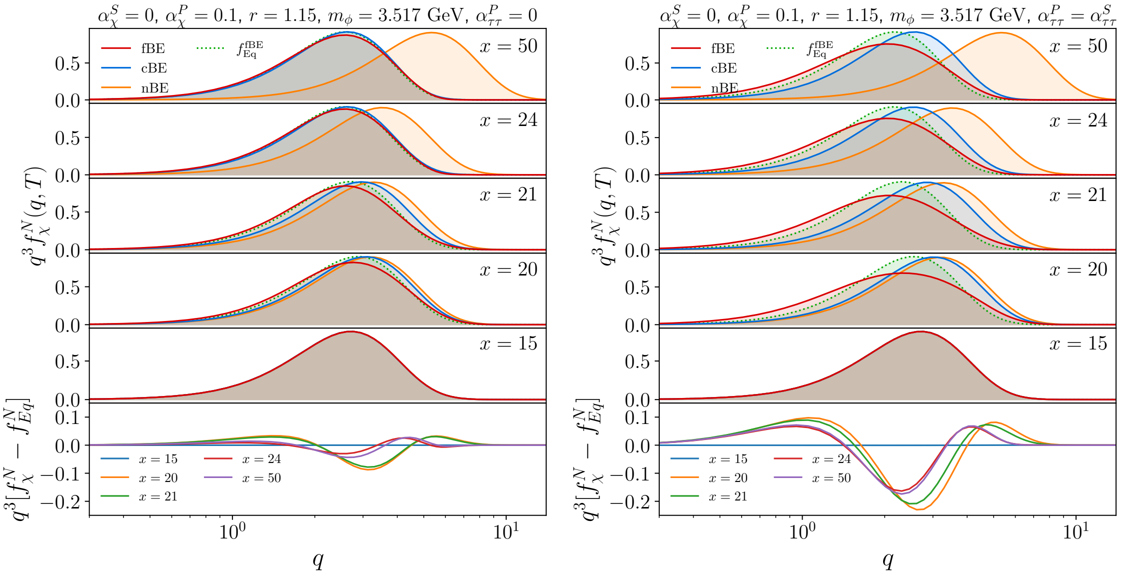

Figure 5.3: Upper panels: Snapshots of the normalized dark matter phase space distributions f^N_χ taken at different values of x plotted against the comoving momentum q for the case of annihilation into tau leptons with a mediator mass close to the di-tau resonance. The distributions from the cBE and fBE are both obtained with the full collision term. Lower panels: The difference of the phase space distribution function between the fBE and the corresponding equilibrium distribution evaluated at the DM temperature T_χ as defined in Eq. (3.24).

using the nBE and $\gtrsim 2.5$ times than the cBE result. It should be noted that the ratio of the relic densities in Figs. 5.1 and 5.2 is larger for the cases when $\alpha^S_{ll} = \alpha^P_{ll}$ than it is when $\alpha^P_{ll} = 0$. By examining Eq. (5.2), one can see that this is due to the fact that the s-wave component of the annihilation cross-section is suppressed for $\alpha^P_{ll} = 0$ through the small mass difference between leptons and DM which is not the case for $\alpha^S_{ll} = \alpha^P_{ll}$. On a qualitative level, this effect can also be understood through the difference between the phase space distribution functions obtained with the fBE and the corresponding equilibrium distribution functions $f^{\rm fBE}_{\rm Eq} \sim e^{-E/T_\chi}$ which is shown in the lowermost panels of Fig. 5.3 for five values of x for both choices of $\alpha^P_{\tau\tau}$ and $r = 1.15$. Here, the DM "temperature" T_χ is computed from f_χ itself as defined in Eq. (3.24). It becomes clear that the strong velocity dependence of the annihilation cross section leads to dips in the distribution function which cause the departure from equilibrium and are more pronounced for the $\alpha^S_{ll} = \alpha^P_{ll}$ case than for $\alpha^P_{ll} = 0$ and in particular near freeze-out at $x \sim 20$. The deeper the dip the more inefficient the DM annihilation becomes due to the smaller occupation number at the relevant momenta. This correlation then leads to a higher DM relic density as can be seen in Figs. 5.1 and 5.2. From the upper panels of Fig. 5.3 showing the evolution of the distribution function for five different values of x it becomes clear that the distributions obtained from the cBE and the fBE evolve in general to lower momenta compared to the equilibrium distribution evaluated at the photon temperature as the high momentum DM particles get depleted in order to overcome the annihilation threshold. It is also noticeable that the solution of the fBE departs away from $f^{\rm fBE}_{\rm Eq}$ at $x \sim 20$. While this deviation remains strong for the $\alpha^P_{\tau\tau} = \alpha^S_{\tau\tau}$ case shown in the right panel, the deviation almost vanishes at later times for the $\alpha^P_{\tau\tau} = 0$ case in the left panel. This difference can be understood by comparing the momentum transfer rate $\gamma(T)$ with the Hubble rate

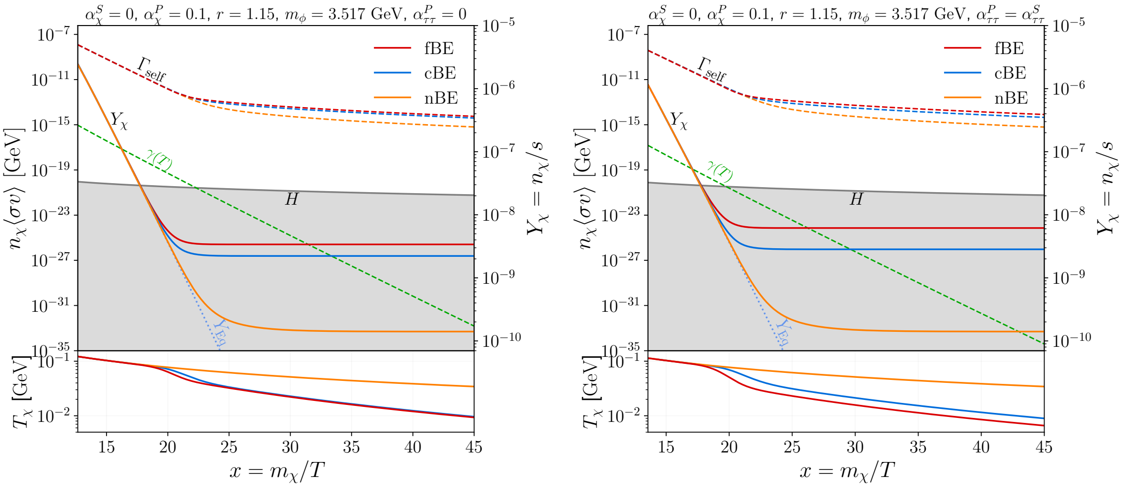

Figure 5.4: Evolution of the self-scattering rate $\Gamma_{\rm self}$, the yield parameter Y_χ, the momentum exchange rate $\gamma(T)$ and the DM temperature T_χ in x as obtained with the nBE, cBE and fBE approaches for annihilations into tau leptons with $m_\phi \approx 2m_\tau$. Note that the yield parameter Y_χ only accounts for the number of DM particles and not antiparticles and that $\Gamma_{\rm self}$ is obtained for the fBE case from the actual phase space distribution as defined in Eq. (5.11).

$H(T)$. Both are displayed in Fig. 5.4 as a function of x with the left panel corresponding to the case $\alpha_{\tau\tau}^P = 0$ while the right panel shows the case $\alpha_{\tau\tau}^P = \alpha_{\tau\tau}^S$. It is clear that for $\alpha_{\tau\tau}^P = 0$, $\gamma(T)$ is still comparable to $H(T)$ around $x \sim 24$ which means that elastic scattering is still effective enough to keep the phase space distributions from deviating too far away from equilibrium as visible in the left panel of Fig. 5.3. However, for $\alpha_{\tau\tau}^P = \alpha_{\tau\tau}^S$, $\gamma(T)$ is already much smaller than $H(T)$ at $x \sim 24$ which suggests that elastic scatterings are not strong enough leading to a larger deviation away from equilibrium. Figure 5.4 also shows the evolution of the DM yield in the nBE, cBE and fBE approaches. Notice how for cBE and fBE, DM freeze-out happens earlier than for the nBE case leading to a higher relic density. The effect of the phase space distribution shifting to lower momenta can also be seen in the lower panel of Fig. 5.4 where DM temperature T_χ is plotted. A clear drop away from the photon temperature is visible just before $x \sim 20$, where DM starts cooling faster than the SM bath. Note that the splitting between the cBE and fBE predictions can be attributed to the phase space distributions shown in Fig. 5.3.

Lastly, the question remains whether for this DM model with the particular choice $\alpha_\chi^S = 0$ and $\alpha_\chi^P = 0.1$ for the DM couplings, the cBE or fBE approach gives a more correct description of the freeze-out process. Since the cBE framework becomes exact under the assumption of maximally efficient DM self-interactions, the associated rate given by

$$\begin{aligned}\Gamma_{\rm self} = 2n_\chi \langle \sigma_{\rm self} v \rangle &= 2n_\chi \frac{\int {\rm d}^3\mathbf{p}_a \int {\rm d}^3\mathbf{p}_b \, \sigma_{\rm self} v_{\rm M\o l} f_\chi(E_a) f_\chi(E_b)}{\int {\rm d}^3\mathbf{p}_a \int {\rm d}^3\mathbf{p}_b \, f_\chi(E_a) f_\chi(E_b)} \\ &= \frac{g_\chi^2}{(2\pi)^4 n_\chi} \int_{m_\chi}^\infty {\rm d}E_a \, f_\chi(E_a) \int_{m_\chi}^\infty {\rm d}E_b \, f_\chi(E_b) \int_{s_-}^{s_+} {\rm d}s \, \sqrt{s(s-4m_\chi^2)} \sigma_{\rm self}(s), \end{aligned} \tag{5.11}$$

is shown in Fig. 5.4 for the same tau benchmarks used for the illustration of the evolution of the distribution functions. The integration limits in Eq. (5.11) are $s_\pm = (E_a + E_b)^2 - (p_a \mp p_b)^2$ and the self-scattering cross section $\sigma_{\rm self} = \sigma_{\chi\bar\chi \to \chi\bar\chi} + \sigma_{\chi\chi \to \chi\chi}$ is for the case $\alpha_\chi^S = 0$ necessary for this analysis

$$\sigma_{\chi\chi\to\chi\chi} = \frac{(\alpha_\chi^P)^2\pi}{2s}(3s-12m_\chi^2+5m_\phi^2)\left\{\frac{1}{s-4m_\chi^2+m_\phi^2}\right.$$
$$\left.+\frac{2m_\phi^2}{(s-4m_\chi^2)(s-4m_\chi^2+2m_\phi^2)}\ln\left(\frac{m_\phi^2}{s-4m_\chi^2+m_\phi^2}\right)\right\}, \quad (5.12)$$

for DM-DM scattering and by

$$\sigma_{\chi\bar{\chi}\to\chi\bar{\chi}} = \frac{(\alpha_\chi^P)^2\pi}{s}|D_\phi(s)|^2\left\{\frac{m_\phi^2}{s-4m_\chi^2}\left[2|D_\phi(s)|^{-2}+s(m_\phi^2-s)\right]\ln\left(\frac{m_\phi^2}{s-4m_\chi^2+m_\phi^2}\right)\right.$$
$$\left.+\frac{m_\phi^2}{s-4m_\chi^2+m_\phi^2}\left[s\left(\Gamma_\phi^2+4m_\chi^2-2m_\phi^2\right)+2\left(\Gamma_\phi^2+m_\phi^2\right)\left(m_\phi^2-2m_\chi^2\right)\right]+s^2\right\}, \quad (5.13)$$

for dark matter and anti-dark matter scattering with the propagator $|D_\phi(s)|^2 = 1/((s-m_\phi^2)^2 + m_\phi^2\Gamma_\phi^2)$. The factor two in front of the number density in Eq. (5.11) accounts for particles and antiparticles. For the nBE and cBE approaches, the average in the self-interaction rate reduces to the single integral over the collision energy defined in Eq. (3.22). It is clear from Fig. 5.4 that even long after freeze-out, the self-scattering rate remains more than five orders of magnitude above the Hubble rate meaning that the cBE treatment gives in this case a more correct depiction of the DM thermodynamics. In fact, the self-interactions are so strong, that the addition of the self-scattering collision term $\hat{C}_{\text{self}}$ to the right-hand side of the momentum-dependent Boltzmann equation makes a numerical solution of the fBE impossible while using the same number of momentum bins, not compromising on accuracy and ensuring that the implementation of $\hat{C}_{\text{self}}$ conserves the number of particles. Even though the self-interactions are so strong, they are not in conflict with astrophysical bounds [344].

5.4.2 Updated Exclusion Limits

In this section, the exclusion limits on forbidden DM annihilations into SM leptons based on the improved calculation of the relic density are updated. To compare the results with those of Ref. [323], the numerical analysis is performed in the plane spanned by the mediator mass and the scalar lepton coupling. The results for annihilations into $\mu^+\mu^-$ are shown in Fig. 5.5 while those for annihilations into $\tau^+\tau^-$ are presented in Fig. 5.6. For both channels, the pseudoscalar coupling is set to zero, $\alpha_{ll}^P = 0$, on the left panel and equal to the scalar coupling, $\alpha_{ll}^P = \alpha_{ll}^S$, on the right. As the analysis in the previous section shows that the small-momentum approximation still holds for significant ranges of DM masses in the forbidden regime, the calculation of the relic density in the following analysis is still based on the FP approximation with the advantage of a major reduction in run time. Even though the cBE treatement is assumed to give a more correct result, the results from the fBE approach in Figs. 5.5 and 5.6 are still shown for completeness to gauge the effect from DM self-scatterings on the exclusion limits.

For every given pair of parameters $(m_\phi,\, \alpha_{ll}^S)$, the DM mass in Figs. 5.5 and 5.6 is fixed through the requirement that the relic density corresponds to the experimentally observed value from Eq. (3.2c). This calculation can be carried out efficiently using, e.g., a logarithmically spaced bisection search. The thick gray, green and black curves corresponding to the nBE, cBE and fBE calculations, respectively, indicate the boundary $\delta = 0$ between the forbidden and non-forbidden regions. In the region above those curves the DM mass is smaller than the corresponding lepton mass and larger below. The boundary from the cBE and fBE approaches is almost identical and both approaches leave less parameter space with $\delta > 0$ compared to the nBE. The allowed white region is further constrained by terrestrial and space-based experiments as discussed next.

For both channels, the most important experimental constraint comes from DM annihilations into electromagnetically charged particles during the recombination epoch. The sensitivity of CMB anisotropies to such energy injection processes into the intergalactic medium (IGM) allows Planck to place the upper limit $f_{\text{eff}} \langle \sigma v \rangle / m_\chi \leq 3.5 \times 10^{-28}\,\text{cm}^3/\text{s}/\text{GeV}$ on the annihilation parameter where the efficiency factor f_{eff} describes the fraction of energy that is released in the annihilation and then transferred to the IGM [7]. It should be noted that this limit is only valid for an s-wave dominated and therefore almost constant annihilation cross section, i.e., $\langle \sigma v \rangle \simeq \sigma v_{\text{lab}} \simeq \text{const}$ [7]. For the numerical evaluation of the efficiency factor, the tabulated f_{eff} curves for DM masses below 5 GeV provided in Ref. [345] are applied. As a consequence of these robust energy injection constraints, the non-forbidden region where $\delta \leq 0$ and direct annihilations into leptons become possible is immediately ruled out. As already mentioned, the corresponding areas in Figs. 5.5 and 5.6 and are marked in gray for the nBE approach and in green for the cBE treatment. As the fBE result overlaps almost everywhere with the cBE one, only the boundary $\delta^{\text{fBE}} = 0$ is marked in black. In the forbidden region defined through $\delta > 0$, loop induced annihilations into photons can be sufficiently large to distort CMB anisotropies at a measurable level, even though being too small to have to be included in the relic density calculation. For the associated annihilation cross section one obtains the expression

$$(\sigma v_{\text{lab}})_{\chi\bar{\chi}\to\gamma\gamma} = \sum_{l=e,\mu,\tau} \frac{4\alpha_{\text{em}}^2 m_l^2}{\pi(s-2m_\chi^2)} \frac{\alpha_\chi^P s + \alpha_\chi^S \left(s - 4m_\chi^2\right)}{(s-m_\phi^2)^2 + m_\phi^2 \Gamma_\phi^2} \times \left\{ \alpha_{ll}^S \left|1 + (1-\tau_l^{-2}) \operatorname{asin}^2(\tau_l)\right|^2 + \alpha_{ll}^P \left|\operatorname{asin}^2(\tau_l)\right|^2 \right\}, \quad (5.14)$$

with $\tau_l = \sqrt{s}/2m_l$ and the fine-structure constant α_{em}. The forbidden region ruled out in this way based on the nBE calculation is shown in orange and in blue for the fBE treatment. Only the boundary of the cBE limit is marked in violet, as it is almost everywhere identical to the fBE result. Importantly and in contrast to this analysis, these energy injection limits have been determined in Refs. [323, 324] based on DM masses obtained with the nBE approach which is not sufficient as recalculating them based on the cBE and fBE approaches shows that the limits from annihilations into photons are actually more stringent and exclude a larger region of the parameter space. Included in red are also fBE projections from the CMB-S4 experiment [346], which is expected to improve the limit on DM annihilation by a factor of two (dotted) to three (dashed).

For the muon channel of Fig. 5.5, existing constraints from the electron beam-dump experiment E137 [150, 347] on the light dark scalar are displayed in gray. In addition, projected limits from the experiments BDX [347, 348], M^3 [349] and NA64-μ [350, 351] are shown. Here, included is, for the first time, the highest sensitivity limit from NA64-μ with 10^{13} muons on target (MOT) which is the goal the M^3-experiment plans on achieving in phase two after starting out with comparably less 10^{10} MOT in phase one. The exclusion limits from beam-dump experiments for the benchmark with

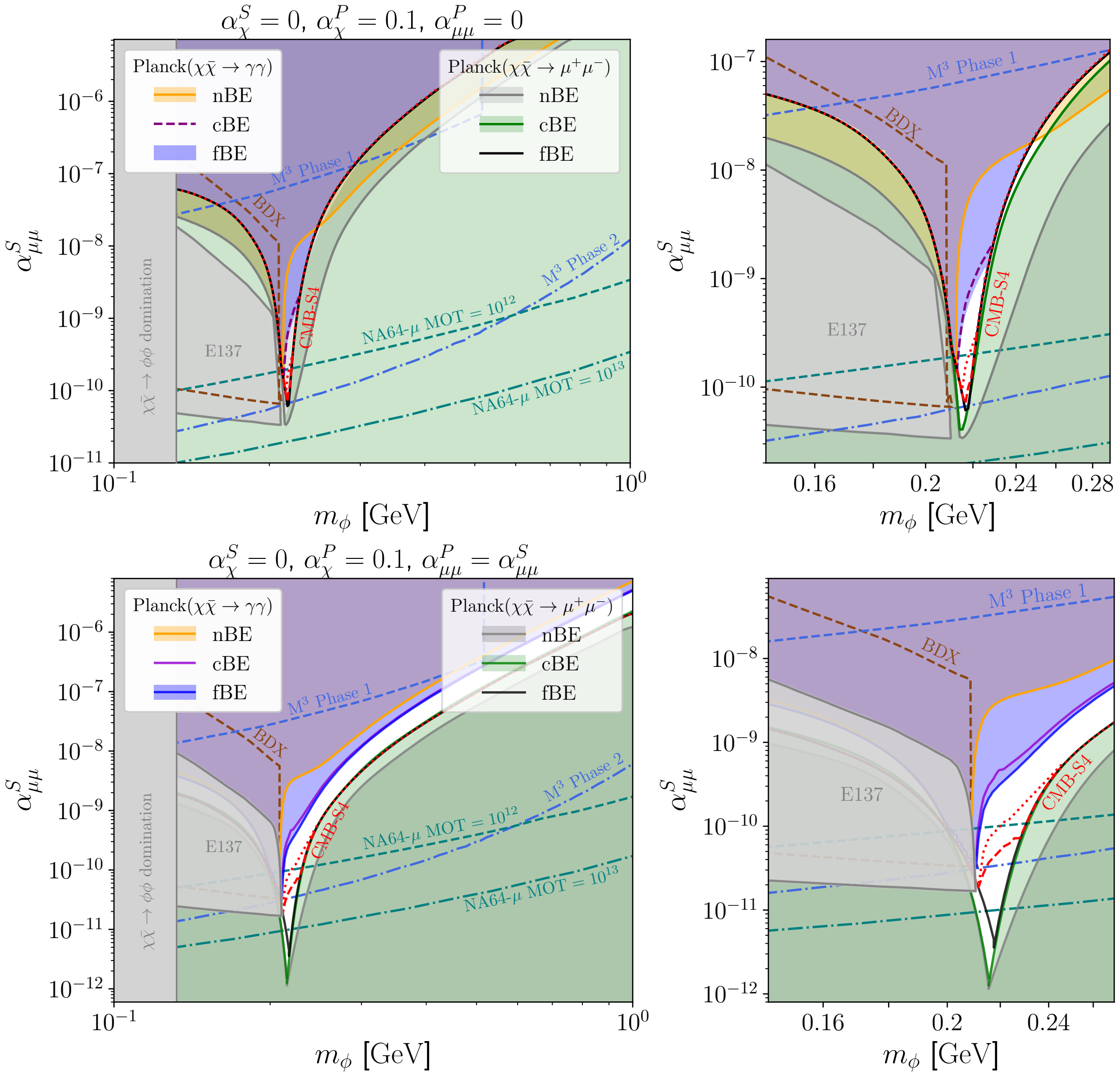

$\alpha_\chi^S = 0,\ \alpha_\chi^P = 0.1,\ \alpha_{\mu\mu}^P = 0$

$\alpha_\chi^S = 0,\ \alpha_\chi^P = 0.1,\ \alpha_{\mu\mu}^P = \alpha_{\mu\mu}^S$

Figure 5.5: Exclusion limits on forbidden DM annihilations into muons in the plane spanned by the mediator mass and the scalar lepton coupling for a vanishing pseudoscalar coupling $\alpha_{\mu\mu}^P = 0$ in the upper panel and for $\alpha_{\mu\mu}^P = \alpha_{\mu\mu}^S$ in the lower one. For both cases, the region around the resonance $m_\phi \approx 2m_\mu$ is shown enlarged on the right. The gray, green and black lines indicate the boundary where m_χ has to equal the muon mass in order to satisfy the relic density constraint based on the nBE, cBE and fBE calculations, respectively. The region below is then excluded by CMB limits on direct annihilations into muons. At every point in the plane above this boundary the DM mass is fixed through the requirement that the DM relic density lies within the observed range where the theory value is obtained using all three computational approaches. Every approach yields a different DM mass for the same parameter point, giving three different regions excluded by CMB constraints on annihilations into photons which are shown in orange, violet and blue for the nBE, cBE and fBE approach, respectively. Displayed are also existing and projected limits from CMB-S4 and the beam-dump experiments E137, BDX, M^3 and NA64-μ. The white space corresponds to the viable region. For more details, see the main text.

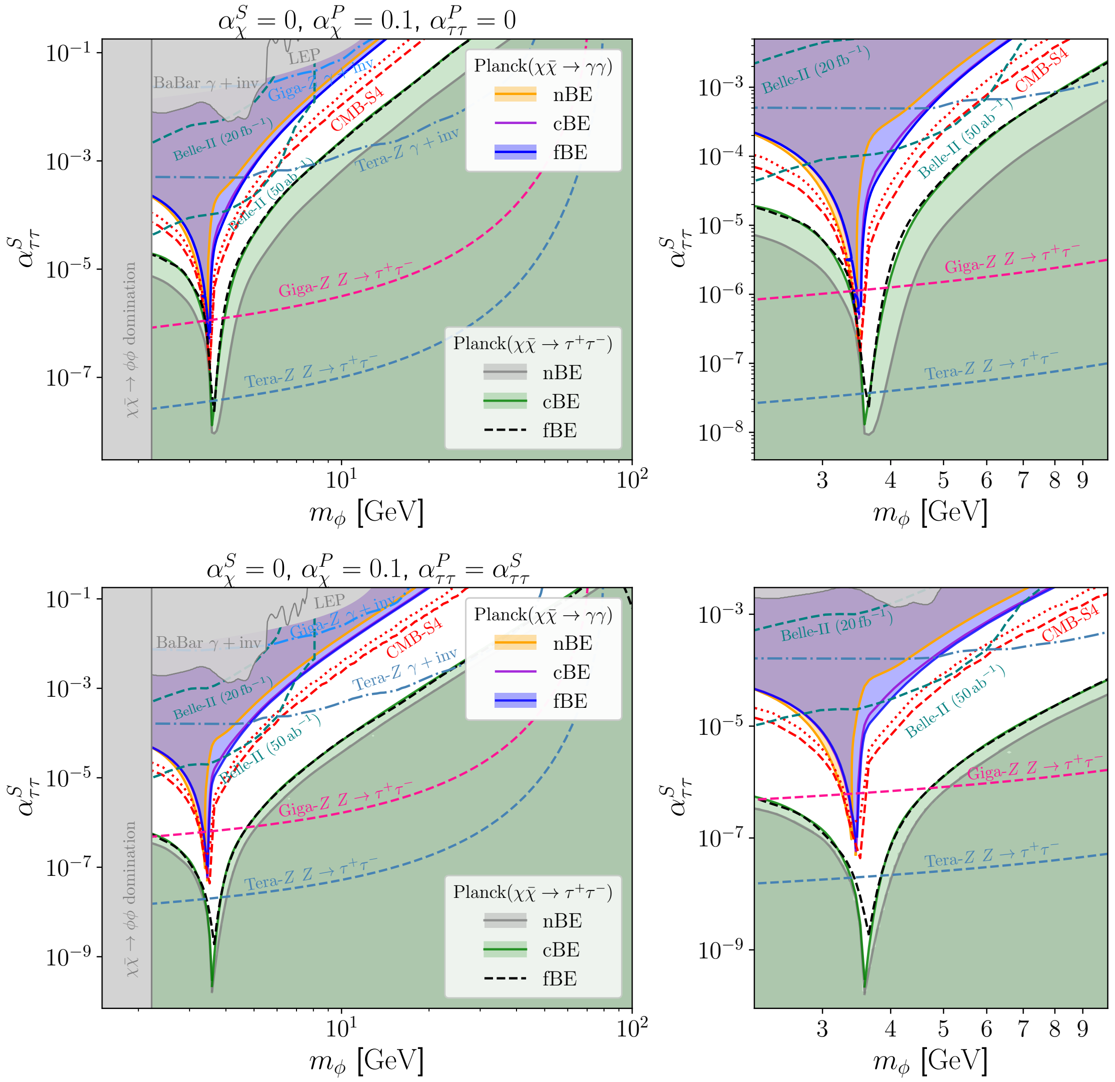

Figure 5.6: Exclusion limits on forbidden DM annihilations into tau leptons with the same structure as well as the same color coding regarding the CMB constraints on $\chi\bar{\chi} \to \tau\bar{\tau}$ and $\chi\bar{\chi} \to \gamma\gamma$ as in Fig. 5.5. In addition, existing and projected limits from LEP, BaBar, Belle-II, CMB-S4 and future e^+e^--colliders with Giga-Z and Tera-Z options are shown. For more details, see the main text.

a non-vanishing pseudoscalar coupling are recasted from the associated limit with $\alpha^P_{\mu\mu} = 0$ through the replacement $\alpha^S_{\mu\mu} \to \alpha^S_{\mu\mu}/2$ for every m_ϕ. This is motivated by the fact that according to the improved Weizsacker-Williams approximation [352] the dominant contribution of the radiative production cross section $N\mu \to N\mu\phi$ of the scalar in presence of a nucleon N in the target material is proportional to $\alpha^S_{\mu\mu}$.

For the tau channel of Fig. 5.6, one existing constraint comes from the LEP measurement of the partial Z decay width into tau leptons $\Gamma_{Z\to\tau^+\tau^-} = 84.08(22)\,\mathrm{MeV}$ [317] since it is sensitive to the process $Z \to \tau^+\tau^-\phi$ followed by a subsequent invisible decay of the new scalar into DM. To obtain a limit at the 2σ confidence level from this measurement, the new contribution to the Z decay width is required to be less than two times the uncertainty of the measured $Z \to \tau^+\tau^-$ width, i.e., the upper limit $\Gamma_{Z\to\tau^+\tau^-\phi}\mathrm{BR}(\phi \to \chi\bar{\chi}) < 0.44\,\mathrm{MeV}$ is applied. For the purpose of constraining annihilations into tau leptons, here and in the following the simplifying assumption is made that $m_\chi \approx m_\tau$ within the computation of the branching ratio $\mathrm{BR}(\phi \to \chi\bar{\chi})$. Decays of Z bosons can also be probed with a better sensitivity at future electron-positron colliders like FCC-ee [152] or CEPC [154] since these come with Giga-Z (Tera-Z) options which means adjusting the beam energy to the Z-pole and producing 10^9 (10^{12}) Z's. Assuming similar efficiencies and acceptances of the future experiments for tau leptons as for electrons and muons, these colliders can probe the exotic Z decay branching ratio $\mathrm{BR}(Z \to \tau^-\tau^+\not{E})$ down to approximately 10^{-8} ($10^{-9.5}$) for a Giga-Z factory (Tera-Z factory) [353]. Another relevant experimental constraint comes from mono-photon searches at BaBar [354], i.e., searches for a highly energetic monochromatic photon in association with missing energy. There are also projected limits for the same kind of search at BaBar's successor experiment Belle II [355] for integrated luminosities of $20\,\mathrm{fb}^{-1}$ and $50\,\mathrm{ab}^{-1}$. Present and future constraints are recasted both from mono-photon bounds on axion-like particles (ALPs) [356]. To do so, the production cross section of an ALP a in association with a photon is considered. It is given by

$$\sigma_{e^+e^-\to a\gamma} = \frac{\alpha_{\mathrm{em}} g^2_{a\gamma\gamma}}{24 s^{7/2}}(s - m_a^2)^3(s + 2m_e^2)(s - 4m_e^2)^{-\frac{1}{2}}\,, \tag{5.15}$$

as described by the Lagrangian density

$$\mathcal{L} = -\frac{g_{a\gamma\gamma}}{4} a F_{\mu\nu}\tilde{F}^{\mu\nu}\,, \tag{5.16}$$

where $g_{a\gamma\gamma}$ is the ALP-photon coupling, m_a the ALP mass and $\tilde{F}^{\mu\nu} = \epsilon^{\mu\nu\alpha\beta}F_{\alpha\beta}$ the dual field strength tensor. The same production cross section in the forbidden DM model, i.e., for the mediator ϕ instead of an ALP, is

$$\sigma_{e^+e^-\to\phi\gamma} = \sum_l \frac{2\alpha^3_{\mathrm{em}} m_l^2}{3\pi s^{7/2}} \frac{s + 2m_e^2}{s - m_\phi^2}(s - 4m_e^2)^{-\frac{1}{2}}\left(\alpha^S_{ll}|F^S_l(s)|^2 + \alpha^P_{ll}|F^P_l(s)|^2\right), \tag{5.17}$$

where the scalar and pseudoscalar form factors due to the lepton loop are defined through

$$F^S_l(q^2) = (q^2 - m_\phi^2)\left[2 + \left(q^2 + 4m_l^2 - m_\phi^2\right)C_0\right] + 2q^2\left[\Lambda\left(q^2, m_l, m_l\right) - \Lambda\left(m_\phi^2, m_l, m_l\right)\right]\,, \tag{5.18a}$$

$$F^P_l(q^2) = (q^2 - m_\phi^2)^2 C_0 \tag{5.18b}$$

with the Passarino-Veltman function $C_0(0, m_\phi^2, q^2; m_l, m_l, m_l)$ and the branch cut function

$$\Lambda(p^2; m, m) = \sqrt{1 - \frac{4m^2}{p^2}} \ln \left(\frac{\sqrt{p^2\,(p^2 - 4m^2)} + 2m^2 - p^2}{2m^2} \right) . \tag{5.19}$$

The limit is then recasted by solving the equation $\sigma_{e^+e^- \to a\gamma} = \sigma_{e^+e^- \to \phi\gamma} \mathrm{BR}(\phi \to \chi\bar{\chi})$ for every m_ϕ at the collision energy $\sqrt{s} = 10.58\,\mathrm{GeV}$ corresponding to the $\Upsilon(4S)$ resonance. Future Z-factories are able to perform the same mono-photon searches and can therefore put constraints on the branching ratio $\mathrm{BR}(Z \to \not{E}\gamma)$ [353] which in this model corresponds to an upper limit on the product $\mathrm{BR}(Z \to \phi\gamma)\mathrm{BR}(\phi \to \chi\bar{\chi})$. The associated decay width is given by

$$\Gamma_{Z \to \phi\gamma} = \sum_l \frac{3\alpha_{\mathrm{em}} G_F (g_{Z,l}^V)^2 m_l^2}{\sqrt{2}\pi^3 m_Z (m_Z^2 - m_\phi^2)} \left(\alpha_{ll}^S |F_l^S(m_Z^2)|^2 + \alpha_{ll}^P |F_l^P(m_Z^2)|^2 \right) \tag{5.20}$$

with the Fermi constant G_F and the vector part $g_{Z,l}^V = -\frac{1}{4} + \sin^2\theta_W$ of the Z-lepton coupling.

The implications of this updated calculation on the available parameter space can be seen by comparing the new results to the equilibrium results in Ref. [323]. A very interesting outcome is that forbidden annihilations into muons for the case of a vanishing pseudoscalar coupling can now be entirely probed with the future CMB-S4 experiment alone.[1] Furthermore, there is a significant reduction in the experimentally viable parameter space of the model. However, for the $\tau^+\tau^-$ final state more regions remain open compared to the muonic final state. Many future experiments will be able to probe the remaining parts of the parameter space, such as NA64-μ and M^3 for the di-muon and the Giga-Z and Tera-Z experiments for the di-tau final state. The inclusion of the latter sensitivity limits shows that almost the entire model parameter space can be probed in the near future. One should note in passing that the discussed limits are more stringent for the $\alpha_{ll}^P = 0$ case than they are for the $\alpha_{ll}^P = \alpha_{ll}^S$ case.

5.5 Conclusion

In this chapter, the early kinetic decoupling effect for forbidden DM annihilations into SM leptons has been studied by means of the momentum-dependent Boltzmann equation. The resulting DM relic density has been compared carefully with predictions obtained using the fluid approximation and the traditional number density approach for both, the full elastic collision term as well as the corresponding small-momentum transfer approximation, resulting in general in a significant increase of the DM relic abundance by more than an order of magnitude. From a technical side, particular emphasis was put on the analytical integration of all angular integrals appearing in the full elastic scattering collision term. Along this line, improvements in the numerical strategy have also been highlighted. With that, new experimental exclusion limits for the investigated model have been derived from the requirement that the fermionic dark matter candidate makes up all of the observed relic density, however, by using the Fokker-Planck approximation instead of the full operator, since we found both to be in very good agreement in the relevant regions of the model

---

[1] Note that Fig. 5.5 differs from the corresponding plot in Fig. 6 (left) of Ref. [324] due to a potential error in their calculation of the mediator's width as a similar result is recovered by keeping Γ_Φ constant for the whole scan with a value corresponding to one far away from the resonance. In addition, the calculation of the limits on DM annihilation into photons provided in Figs. 6 and 7 of Ref. [324], as already alluded to in the main text, seem to be still based on the masses obtained with the number density treatment.

parameter space. The resulting limits are especially strong for the muon channel compared to the tau channel. These results highlight again the necessity to take the early kinetic decoupling effect seriously and display the need to develop fast, reliable and general methods for the evaluation of full collision integrals in order to make the investigation of this effect in more complicated models with a richer particle content like the MSSM feasible.

Chapter 6

(Non)equilibrium Quantum Field Theory

Since Boltzmann equations are constructed from vacuum S-matrix elements relying on the assumption of free asymptotic states and formulated in terms of phase space densities for classical particles, they are by construction not well suited to provide a full quantum description of nonequilibrium systems consisting of interacting fields, in particular since there exists no well-defined notion of asymptotic sates in such systems. Instead, they can be described by means of real-time formalisms where the phase space densities are replaced by n-point correlation functions as the dynamical degrees of freedom. In the following, the derivation of this technique is briefly sketched with a particular emphasis on the Closed Time Path formalism for non-equilibrium [357, 358] as well as equilibrium [359, 360] situations.

The study of quantum field theories in equilibrium and non-equilibrium situations cumulated up to now into the following three well-defined formalisms:

- Imaginary-time (Matsubara) formalism [361]
- Real-time (Keldysh-Schwinger) formalism [362, 363]
- Thermo-field dynamics (Umezawa) formalism [364]

Historically, Matsubara was the first to construct a thermal field theory by exploiting the similarity of the statistical Boltzmann weight $e^{-\beta\hat{H}}$ with the time-evolution operator $e^{-it\hat{H}}$ by relating the inverse temperature $\beta = 1/T$ to time through a purely imaginary time variable $t = -i\beta$ in the evolution operator. Here, $\hat{H}$ is a, for illustrative purposes, time-independent Hamiltonian. However, through the intrinsic assumption of a Boltzmann distribution, the imaginary-time formalism only applies to equilibrium situations and is best suited for the calculation of static quantities. To circumvent this shortcoming and to construct a method that is additionally suited to treat the dynamics of a system, Schwinger and Keldysh allowed the time variable to lie on a general contour in the complex plane and therefore also includes real time values. For this reason the associated approach is called real-time formalism and has the advantage of being applicable to non-equilibrium system as well, however, at the prize of doubling the number of degrees of freedom. Independently, Umezawa et. al developed a different strategy within the framework of real-time formalism based on C^* algebras called thermo-field dynamics (TFD) which can essentially be thought of as an operator formalism and allows to answer questions on the structure of the thermal vacuum which are not accessible within the Keldysh-Schwinger approach. Also within TFD, one encounters the doubling of the degrees of freedom characteristic for real-time formalisms.

In the following, the focus will be on the Keldysh-Schwinger formalism which has already been extensively employed in the context of baryogenesis [365–377], inflation [378, 379], gravitational waves [380] and is also becoming more popular in the context of dark matter [97, 98, 381–387]. The fundamentals of the closed time path formalism are presented by using a real scalar field as an example and the Kadanoff-Baym equations are derived. After that the scalar and fermionic equilibrium propagators are derived and the Feynman rules at finite temperature are stated. Gauge fields and in particular their resummed propagators are briefly discussed in Sec. 6.3. In Sec. 6.4, often occurring integrals within closed time path calculations are evaluated and the results are then used in the subsequent Sec. 6.5 to calculate the one-loop photon self-energy in finite-temperature QED.

6.1 Scalar Fields

To develop the formalism, we first consider again a real scalar field ϕ with the Lagrangian density from Eq. (4.22). Compared to the calculation of S-matrix elements, the assumption of asymptotically-free states in the infinite past and future breaks down in medium. Here, the system can only be specified through a density matrix $\hat{\varrho}(t_i)$ at an initial time t_i such that one is left with the computation of expectation values of operators $\mathcal{O}$ at later times t by averaging over all possible states accessible to the system via the trace

$$\langle\hat{\mathcal{O}}\rangle_{\varrho}(t) = \mathrm{Tr}[\hat{\varrho}(t)\hat{\mathcal{O}}]\,. \tag{6.1}$$

It turns out that such ensemble averages can be computed by employing a generating functional where the time arguments of the field operators are not only restricted to lie on the real axis, but to consider time ordering along a general contour C in the complex time plane. The contour C we are working with is shown in Fig. 6.1 and starts at the initial time $t_i^+ = t_i + i\epsilon$ with an infinitesimal displacement parameter ϵ and runs parallel to the real t axis up to the time $t_f + i\epsilon$ where it performs a semicircle around t_f until it reaches $t_f - i\epsilon$, runs backwards to $t_i^- = t_i - i\epsilon$. The upper branch is called C_1 and the lower one C_2. Instead of using the labels 1 and 2 for the two branches, an alternative is to use the symbols ±, as originally suggested by Schwinger [362] and Keldysh [363]. However, within practical calculations it is more convenient to use numbers. For path ordering

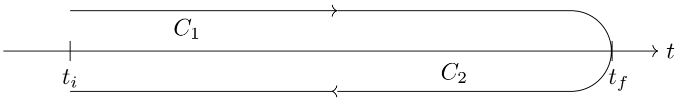

Figure 6.1: Finite-time Closed Time Path.

purposes it is also common to define the unit step function

$$\Theta_C(x^0,y^0) = \begin{cases} \Theta(x^0-y^0) & \text{if } x^0,y^0 \in C_1 \\ \Theta(y^0-x^0) & \text{if } x^0,y^0 \in C_2 \\ 1 & \text{if } x^0 \in C_2, y^0 \in C_1 \\ 0 & \text{if } x^0 \in C_1, y^0 \in C_2 \end{cases} \tag{6.2}$$

on the closed time path. The definition of the theta function on C leads in a natural way to the definition of the δ-function on the contour,

$$\delta_C(x^0,y^0) = \frac{\mathrm{d}\Theta_C(x^0,y^0)}{\mathrm{d}x^0} = \begin{cases} \delta(x^0-y^0) & \text{if } x^0,y^0 \in C_1 \\ -\delta(x^0-y^0) & \text{if } x^0,y^0 \in C_2 \\ 0 & \text{otherwise} \end{cases} . \tag{6.3}$$

For commuting functions $J(x)$ defined on the path C functional differentiation extends to

$$\frac{\delta J(x)}{\delta J(y)} = \delta_C^{(4)}(x,y) \tag{6.4}$$

with the contour-ordered δ-function for four-vectors $\delta_C^{(4)}(x,y) = \delta_C(x^0,y^0)\delta^{(3)}(\mathbf{x}-\mathbf{y})$.

6.1.1 The Generating Functional

In the end, one is interested in the computation of correlation functions of the form

$$i\Delta(x_1,\ldots,x_N) = \langle T_C\{\hat{\phi}(x_1)\ldots\hat{\phi}(x_N)\}\rangle_\varrho\,, \tag{6.5}$$

as these are directly connected to measurable physical quantities like the energy density or pressure of a system. Note that in contrast to vacuum field theory the time-ordering is here taken along the complex time path C. Therefore, it is instructive to define the generating functional

$$Z_C[J] = \mathrm{Tr}\left[\hat{\varrho}(t_i)\, T_C \exp\!\left(i\int_C \mathrm{d}^4x\, J(x)\hat{\phi}(x)\right)\right] \tag{6.6}$$

such that contour-ordered n-point functions can be simply obtained from functional differentiation with respect to the sources $J(x)$:

$$i\Delta(x_1,\ldots,x_N) = (-i)^N \frac{1}{Z_C[J]}\,\frac{\delta^N Z_C[J]}{\delta J(x_1)\ldots\delta J(x_N)}\bigg|_{J=0} . \tag{6.7}$$

Since it is desirable to not only restrict the time arguments of the correlation functions to the time interval $[t_i,t_f]$, it is common to take the limit $t_f\to\infty$ such that scalar field insertions can be obtained through functional differentiation for arbitrary times larger than t_i, leading to the infinite-time closed time path shown in Fig. 6.2. Since the density matrix is defined at the initial time, it is sensible to perform the trace in Eq. (6.6) by integrating over all possible initial-time field configurations $\phi(t_i^+,\mathbf{x})$ and insert another complete set of eigenstates of the field operator $\hat{\phi}(\mathbf{x})$ at

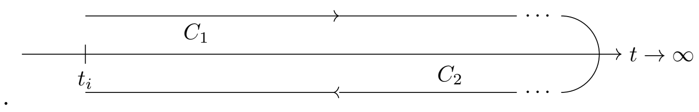

Figure 6.2: Infinite time Closed Time Path.

time t_i^- to re-express the generating functional in the form

$$Z_C[J] = \int [\mathrm{d}\phi_1][\mathrm{d}\phi_2] \left\langle \phi_1; t_i^+ \middle| \hat{\varrho}(t_i) \middle| \phi_2; t_i^- \right\rangle \left\langle \phi_2; t_i^- \middle| T_C \exp\Bigl(i \int_C \mathrm{d}^4x\, J(x)\hat{\phi}(x) \Bigr) \middle| \phi_1; t_i^+ \right\rangle . \tag{6.8}$$

To be precise, the measure $[\mathrm{d}\phi]$ it is defined via $[\mathrm{d}\phi] = \prod_{\mathbf{x}\in\mathbb{R}^3} \mathrm{d}\phi(\mathbf{x})$ and a ket $|\phi\rangle$ trough $|\phi\rangle = \otimes_{\mathbf{x}\in\mathbb{R}^3} |\phi(\mathbf{x})\rangle$. It is important to understand that Eq. (6.8) provides the motivation for choosing the closed time path C since this form of the generating functional allows to evaluate the matrix elements involving the density matrix without having to worry about time evolution. This is because the action of $\hat{\rho}(t_i)$ (in the limit $\epsilon \to 0$) on the field configurations $\left|\phi_1; t_i^+\right\rangle$ and $\left|\phi_2; t_i^-\right\rangle$ is known by definition while the transition amplitude can be reformulated conveniently for $\epsilon \to 0$ through the path integral

$$\begin{aligned} Z_C[J] = \int [\mathrm{d}\phi_1][\mathrm{d}\phi_2] \left\langle \phi_1; t_i^+ \middle| \hat{\varrho}(t_i) \middle| \phi_2; t_i^- \right\rangle & \\ \times \int_{\phi(\mathbf{x},t_i^+)=\phi_1(\mathbf{x})}^{\phi(\mathbf{x},t_i^-)=\phi_2(\mathbf{x})} \mathcal{D}\phi \exp\Bigl(i \int_C \mathrm{d}^4x (\mathcal{L}(x) + J(x)\phi(x)) \Bigr) . \end{aligned} \tag{6.9}$$

In other words, choosing the time path just from t_i to t_f along the real axis without the backward component would highly complicate the evaluation of the density matrix. It is also important to understand that the transition amplitude can only be rewritten using the path integral because the time path begins at the time t_i^+ where $\phi_1(\mathbf{x})$ is defined and ends at t_i^- where $\phi_2(\mathbf{x})$ is defined. It also becomes clear that one has to introduce the infinitesimally displaced initial times $t_i^{\pm}$ since the boundary conditions of the path integral would be ill-defined otherwise.

The most general density matrix can be parameterized as

$$\left\langle \phi_1; t_i^+ \middle| \hat{\varrho}(t_i) \middle| \phi_2; t_i^- \right\rangle = \mathfrak{N}\, e^{i f_C[\phi]} \tag{6.10}$$

with the the normalization constant $\mathfrak{N}$ and where the functional $f_C[\phi]$ can be written as the power expansion in the fields

$$f_C[\phi] = \alpha_0 + \sum_{n=1}^{\infty} \frac{1}{n!} \int_C \prod_{i=1}^{n} \mathrm{d}^4x_i\, \alpha_n(x_1, \ldots, x_n)\phi(x_1)\ldots\phi(x_n) \tag{6.11}$$

obeying the boundary conditions $\phi(t_i^+, \mathbf{x}) = \phi_1(\mathbf{x})$ and $\phi(t_i^-, \mathbf{x}) = \phi_2(\mathbf{x})$. The coefficients $\alpha_1(x_1)$, $\alpha_2(x_1, x_2)$, ... must further vanish identically for time arguments other than t_i since the density matrix is specified at the initial time t_i. With this generic parametrization of the density matrix the generating functional in Eq. (6.9) can be reduced to the single path integral

$$Z_C[J] = \mathfrak{N} \int \mathcal{D}\phi\, e^{i\left(S_C[\phi] + \int_C \mathrm{d}^4x J(x)\phi(x) + f_C[\phi]\right)} \tag{6.12}$$

without any boundary conditions on the field value $\phi(t_i^{\pm}, \mathbf{x})$. For many physically relevant scenarios, however, Gaussian or thermal initial conditions are sufficient. E.g., the reheating process in the early Universe at the end of the inflationary phase is described by an initially Gaussian density matrix to high accuracy. Both types can be absorbed in an elegant way into the existing terms for the action or the source term in the exponential of Eq. (6.12). Thermal initial conditions are ensured through a redefinition of the path which will be covered in Sec. 6.1.5 whereas for Gaussian initial conditions, α_0 is an irrelevant normalization constant, α_1 can be absorbed into the source term through $J(x) \to J(x) + \alpha_1(x)$ and the quadratic piece $\alpha_2(x, y)$ into the mass term, $\delta_C^{(4)}(x_1 - x_2)m^2 \to \delta_C^{(4)}(x_1 - x_2)m^2 - \alpha_2(x_1, x_2)$. In either case, in the absence of interactions, $\mathcal{V} = 0$, the path integral in Eq. (6.12) is Gaussian and can be evaluated analytically, as in vacuum theory (see, e.g., [388]), giving the form

$$Z_C^F[J] = \mathcal{N} \exp\biggl(-\frac{i}{2}\int_C \mathrm{d}^4x\, \mathrm{d}^4y\, J(x)\Delta_0(x-y)J(y)\biggr)\,, \tag{6.13}$$

for the free generating functional, where $\mathcal{N}$ is a normalization factor dropping out within the calculation of physical quantities and $i\Delta_0(x - y)$ the free propagator which must satisfy

$$(\Box_x + m^2)\Delta_0(x-y) = -\delta_C^{(4)}(x, y) \tag{6.14}$$

analogous to vacuum theory. In this convention, propagators are simply "i" times the Green's function $\Delta(x, y)$ which is also why propagator and Green's function may be used interchangeably. By replacing the fields in the potential through a functional derivative, it is easy to see that a perturbative expansion of the generating functional in Eq. (6.12) can be obtained from

$$Z_C[J] = \exp\biggl(-i\int_C \mathrm{d}^4x\, \mathcal{V}\left[\frac{\delta}{i\delta J(x)}\right]\biggr) Z_0[J]\,. \tag{6.15}$$

6.1.2 CTP Ordered Two-Point Functions

Given that the free propagator appears in the generating functional, two-point correlators are dissected in the following. The contour-ordered two-point function on the Keldysh-Schwinger contour for a scalar field $i\Delta(x, y)$ can be decomposed in terms of the linear independent greater and lesser Wightman functions

$$i\Delta^{>}(x, y) = \langle\hat{\phi}(x)\hat{\phi}(y)\rangle_{\varrho}\,, \tag{6.16a}$$

$$i\Delta^{<}(x, y) = \langle\hat{\phi}(y)\hat{\phi}(x)\rangle_{\varrho}\,. \tag{6.16b}$$

The superscripts $\gtrless$ are motivated through the fact that in the first case x^0 is assumed to appear "earlier" than y^0 on the time contour and vice versa. The Wightman functions decompose the propagator in the following way

$$i\Delta(x, y) = \langle T_C\{\hat{\phi}(x)\hat{\phi}(y)\}\rangle_{\varrho} = \Theta_C(x^0, y^0)i\Delta^{>}(x, y) + \Theta_C(y^0, x^0)i\Delta^{<}(x, y)\,. \tag{6.17}$$

Further, it is common to define the so-called statistical and spectral two-point functions $\Delta^{+}(x, y)$

and $\Delta^{-}(x,y)$, respectively, defined trough

$$i\Delta^{+}(x,y) = \frac{1}{2}\langle\{\hat{\phi}(x),\hat{\phi}(y)\}\rangle_{\varrho} = \frac{i}{2}\left[\Delta^{>}(x,y)+\Delta^{<}(x,y)\right] , \tag{6.18a}$$

$$\Delta^{-}(x,y) = \langle[\hat{\phi}(x),\hat{\phi}(y)]\rangle_{\varrho} = i\Delta^{>}(x,y) - i\Delta^{<}(x,y) , \tag{6.18b}$$

respectively, where in this convention the latter, i.e., Δ^{-}, is nothing but the spectral density $\wp = \Delta^{-}$, encoding all the information on the spectrum of single and multi-particle states in the theory.

As already visible from the definition of the contour-ordered Heaviside function in Eq. (6.2), the propagator $i\Delta(x,y)$ on the closed time path splits into four components depending on the position of the complex time arguments x^0 and y^0 on C. Therefore, one can also denote the branch on which the two time arguments lie by superscripts a, b corresponding to the position of the first and second time argument on C, respectively, such that $i\Delta^{ab}(x,y)$ takes as arguments ordinary, i.e., real, times. In the CTP formalism, this translates to the following four scalar Green's functions:

$$i\Delta^{11}(x,y) = \langle T\{\hat{\phi}(x)\hat{\phi}(y)\}\rangle_{\varrho} \qquad \text{if } x^0, y^0 \in C_1 \tag{6.19a}$$

$$i\Delta^{12}(x,y) = i\Delta^{<}(x,y) \qquad \text{if } x^0 \in C_1, y^0 \in C_2 \tag{6.19b}$$

$$i\Delta^{21}(x,y) = i\Delta^{>}(x,y) \qquad \text{if } x^0 \in C_2, y^0 \in C_1 \tag{6.19c}$$

$$i\Delta^{22}(x,y) = \langle \bar{T}\{\hat{\phi}(x)\hat{\phi}(y)\}\rangle_{\varrho} \qquad \text{if } x^0, y^0 \in C_2 \tag{6.19d}$$

where $\bar{T}$ denotes the anti-time ordering operator.[1] This structure of the propagators suggests that instead of keeping track of the position of the time-arguments on C, fields and sources can be split into two pieces instead, depending on whether they live on C_1 or C_2, thus, giving rise to the definition of the doublets

$$\phi = \begin{pmatrix} \phi_1 \\ \phi_2 \end{pmatrix} , \tag{6.20a}$$

$$J = \begin{pmatrix} J_1 & J_2 \end{pmatrix} , \tag{6.20b}$$

where, to be precise, $\phi_1, J_1 \in C_1$ and $\phi_2, J_2 \in C_2$. Defining the metric in this two dimensional space to be $(1,-1)$, rearranges the generating functional from Eq. (6.15) in the form

$$Z_C[J] = \mathcal{N}\exp\left(-i\int \mathrm{d}^4x \left(\mathcal{V}\left[\frac{\delta}{i\delta J_1(x)}\right] - \mathcal{V}\left[\frac{\delta}{i\delta J_2(x)}\right]\right)\right) \times \exp\left(-\frac{i}{2}\int \mathrm{d}^4x\,\mathrm{d}^4y\, J_a(x)\Delta_0^{ab}(x-y)J_b(y)\right) . \tag{6.21}$$

It should be stressed that the time integration in this case is over the C_1 branch, $t_i \leq x^0 \leq \infty$, as usual. Thus, the backward branch C_2 of the closed time path is effectively removed by doubling the number of degrees of freedom. In particular, this means that time arguments from now on lie only on the C_1 branch, thus replacing Θ_C with Θ.

---

[1] As common in the (non)equilibrium QFT literature, the superscripts $<$ and $>$ are also used here to denote the 12- and 21-components even though this overlaps with the notation for the Wightman functions.

As another consequence of introducing the doublets, the four propagators in Eq. (6.19) can be written as

$$i\Delta^{ab}(x,y) = \frac{1}{Z_C[J]} \left. \frac{\delta^2 Z_C[J]}{i\delta J_a(x) i\delta J_b(y)} \right|_{J=0} \tag{6.22}$$

highlighting that the Green's function in the space of twice the number of degrees of freedom can be written as a 2 × 2 matrix

$$\Delta = \begin{pmatrix} \Delta^{11} & \Delta^{12} \\ \Delta^{21} & \Delta^{22} \end{pmatrix} . \tag{6.23}$$

From the definitions in Eq. (6.19) one can recognize that not all four matrix components of the Green's function are independent but satisfy the constraint relation

$$\Delta^{11}(x,y) + \Delta^{22}(x,y) = \Delta^{12}(x,y) + \Delta^{21}(x,y) \tag{6.24}$$

as a consequence of the identity $\Theta(x) + \Theta(-x) = 1$. In statistical systems one is often not as interested in the causal Green's functions as in the physical Green's functions which are defined as

$$\Delta^R(x,y) = \theta(x^0 - y^0)\Delta^-(x,y)\,, \tag{6.25a}$$

$$\Delta^A(x,y) = -\theta(y^0 - x^0)\Delta^-(x,y)\,, \tag{6.25b}$$

$$\Delta^C(x,y) = 2\,\Delta^+(x,y)\,. \tag{6.25c}$$

These are the retarded, the advanced and the correlated propagators of the Keldysh representation and, interestingly, can be re-expressed through the definitions of the components of the causal Green's functions from Eq. (6.19) as

$$\Delta^R = \Delta^{11} - \Delta^{12} = \Delta^{21} - \Delta^{22}\,, \tag{6.26a}$$

$$\Delta^A = \Delta^{11} - \Delta^{21} = \Delta^{12} - \Delta^{22}\,, \tag{6.26b}$$

$$\Delta^C = \Delta^{11} + \Delta^{22} = \Delta^{12} + \Delta^{21}\,, \tag{6.26c}$$

where the spacetime arguments have been suppressed for brevity. The equations in (6.26) are inverted by

$$\Delta^{11} = \frac{1}{2}(\Delta^A + \Delta^R + \Delta^C)\,, \tag{6.27a}$$

$$\Delta^{22} = \frac{1}{2}(\Delta^C - \Delta^A - \Delta^R)\,, \tag{6.27b}$$

$$\Delta^{12} = \frac{1}{2}(\Delta^A + \Delta^C - \Delta^R)\,, \tag{6.27c}$$

$$\Delta^{21} = \frac{1}{2}(\Delta^C - \Delta^A + \Delta^R)\,. \tag{6.27d}$$

One can also extract the Hermitian and anti-Hermitian part of the retarded propagator via

$$\Delta^{\mathcal{H}} = \frac{1}{2}(\Delta^R + \Delta^A) = \frac{1}{2}(\Delta^{11} - \Delta^{22})\,, \tag{6.28a}$$

$$\Delta^{\mathcal{A}} = \frac{i}{2}(\Delta^R - \Delta^A) = \frac{\Delta^-}{2}\,, \tag{6.28b}$$

where the latter is closely related to the spectral density of states. The definition of the previously introduced bosonic CTP two-point functions and relations among those extend analogously to gauge fields.

6.1.3 The Dyson-Schwinger and Kadanoff-Baym Equations

While the n-point correlation functions discussed so far are free from bubbles, they still contain disconnected graphs. These are diagrams in which at least one external leg is not linked to all other external legs through some connected path. To exclude such disconnected diagrams one can, similar to vacuum theory, define the generating functional of the connected correlation functions

$$W_C[J] = -i \ln Z_C[J] \tag{6.29}$$

such that connected Green's functions $i\Delta_c$ can be generated through functional differentiation of $W_C[J]$:

$$i\Delta_c(x_1, \ldots, x_n) = \langle T_C\{\hat{\phi}(x_1)\ldots\hat{\phi}(x_N)\}\rangle_\varrho^{\mathrm{c}} = i \left.\frac{\delta^N W_C[J]}{i\delta J(x_1)\ldots i\delta J(x_N)}\right|_{J=0} . \tag{6.30}$$

Another important class of diagrams are 1PI graphs which remain connected if at most one internal line is cut. However, 1PI diagrams cannot be simply obtained from the generating functional by performing a normalization as before. The corresponding generating functional is defined through the classical field ϕ_{cl} which is the expectation value of the scalar field operator in the presence of a source:

$$\phi_{\mathrm{cl}}(x) = \langle\hat{\phi}(x)\rangle_\varrho^{\mathrm{c}} = \frac{\delta W_C[J]}{\delta J(x)} . \tag{6.31}$$

Note that $\phi_{\mathrm{cl}}(x)$ implicitly depends on the source term and can therefore be used to replace occurrences of $J(x)$ through to the classical field. This is achieved via the Legendre transform

$$\Gamma_C[\phi_{\mathrm{cl}}] = W_C[J] - \int_C \mathrm{d}^4x\, J(x)\phi_{\mathrm{cl}}(x) , \tag{6.32}$$

thus, defining the quantum effective action $\Gamma_C[\phi_{\mathrm{cl}}]$. By recalling that J and ϕ_{cl} are treated as independent variables, one finds the stationary condition

$$\frac{\delta\Gamma_C[\phi_{\mathrm{cl}}]}{\delta\phi_{\mathrm{cl}}(x)} = -J(x) . \tag{6.33}$$

The crucial advantage of the effective action is that it acts as the generating functional for 1PI correlation functions when the functional differentiation is performed with respect to the classical field,

$$i\Gamma_n(x_1, \ldots, x_N) = \langle T_C\{\hat{\phi}(x_1)\ldots\hat{\phi}(x_N)\}\rangle_\varrho^{\mathrm{1PI}} = i \left.\frac{\delta^N \Gamma_C[\phi_{\mathrm{cl}}]}{\delta\phi_{\mathrm{cl}}(x_1)\ldots\delta\phi_{\mathrm{cl}}(x_N)}\right|_{J=0} . \tag{6.34}$$

It follows the very important relation

$$\begin{aligned}\frac{\delta^2\Gamma_C[\phi_{\mathrm{cl}}]}{\delta J(y)\delta\phi_{\mathrm{cl}}(x)} &= -\frac{\delta J(x)}{\delta J(y)} = -\delta_C^{(4)}(x,y) \\ &= \int_C \mathrm{d}^4z\, \frac{\delta\phi_{\mathrm{cl}}(z)}{\delta J(y)}\frac{\delta^2\Gamma_C[\phi_{\mathrm{cl}}]}{\delta\phi_{\mathrm{cl}}(z)\delta\phi_{\mathrm{cl}}(x)} = -\int_C \mathrm{d}^4z\, \Delta_c(y,z)\Gamma_2(z,x) .\end{aligned} \tag{6.35}$$

Here, the functional derivatives of $W[J]$ give nothing but the exact propagator $i\Delta_c(x, y)$. The 1PI two-point function Γ_2 properly defines the self-energy $\Pi(x, y)$ (and $\Sigma(x, y)$ for fermionic fields) to all orders as the remainder

$$-\Pi(x, y) = \Gamma_2(x, y) - \Gamma_2^0(x, y)\,, \tag{6.36}$$

where $\Gamma_2^0(x, y)$ is the free contribution which, according to Eq. (6.35), is the inverse of the free propagator $i\Delta_0^c(x, y)$ and must therefore obey

$$\Gamma_2^0(x, y) = -(\Box_y + m^2)\delta_C^{(4)}(x, y)\,. \tag{6.37}$$

The decomposition of $\Gamma_2(x, y)$ into the free part and the self-energy yields the familiar form of the Dyson-Schwinger equation in position space

$$(\Box_x + m^2)\Delta_c(x, y) + \int_C \mathrm{d}^4z\, \Pi(x, z)\Delta_c(z, y) = -\delta_C^{(4)}(x, y) \tag{6.38}$$

which is essentially an evolution equation for the connected contour-ordered propagator. Similar to the two-point function in Eq. (6.17), one can decompose the self-energy along the contour via

$$\Pi(x, y) = \Theta_C(x, y)\Pi^>(x, y) + \Theta_C(y, x)\Pi^<(x, y)\,, \tag{6.39}$$

and introduce the same notation $\Pi^{ab}(x, y)$ as in Eq. (6.19) with the two superscripts a and b indicating the position on the time path of the first and second argument, respectively. It is also possible to define the retarded and advanced self-energies via

$$\begin{aligned}\Pi^R(x, y) &= \Theta(x^0 - y^0)(\Pi^>(x, y) - \Pi^<(x, y))\\ &= \Pi^{11}(x, y) - \Pi^{12}(x, y) = \Pi^{21}(x, y) - \Pi^{22}(x, y)\,, \qquad (6.40\text{a})\\ \Pi^A(x, y) &= \Theta(y^0 - x^0)(\Pi^<(x, y) - \Pi^>(x, y))\\ &= \Pi^{11}(x, y) - \Pi^{21}(x, y) = \Pi^{12}(x, y) - \Pi^{22}(x, y)\,. \qquad (6.40\text{b})\end{aligned}$$

Alternatively, in index notation, the Dyson-Schwinger equation (6.38) becomes

$$(\Box_x + m^2)\Delta_c^{ab}(x, y) - \sum_c (-1)^c \int_{C_1} \mathrm{d}^4z\, \Pi^{ac}(x, z)\Delta_c^{cb}(z, y) = (-1)^a\delta^{ab}\delta^{(4)}(x - y)\,. \tag{6.41}$$

These are four equations corresponding to the four CTP propagators (6.19) but as they are not linearly independent, Eq. (6.41) can be reformulated in terms of two separate sets: one set for the retarded and advanced propagators, and another set for the Wightman functions. Specifically, one finds

$$\begin{aligned}(-\Box_x - m^2)\Delta^{R/A}(x, y) &= (\Delta^{R/A} \odot \Pi^{R/A})(x, y) + \delta^{(4)}(x - y)\,, \qquad (6.42\text{a})\\ (-\Box_x - m^2)\Delta_c^{\gtrless}(x, y) &= (\Pi^{\gtrless} \odot \Delta_c^A)(x, y) + (\Pi^R \odot \Delta_c^{\gtrless})(x, y)\,, \qquad (6.42\text{b})\end{aligned}$$

where the product $(f \odot g)(x, y) = \int_{C_1} \mathrm{d}^4z\, f(x, z)g(z, y)$ stands for the integration over the intermediate variable. Within the usual abuse of the notation and to arrive at a compact notation, the superscripts of the off-diagonal components have been replaced with $\gtrless$. The retarded and advanced functions can be again replaced with the spectral and Hermitian ones through Eq. (6.28) yielding the Kadanoff-Baym equations of nonequilibrium quantum field theory [389, 390]

$$(-\Box_x - m^2)\Delta_c^{\gtrless} - \Pi^{\gtrless} \odot \Delta_c^{\mathcal{H}} - \Pi^{\mathcal{H}} \odot \Delta_c^{\gtrless} = \frac{1}{2}(\Pi^{>} \odot \Delta_c^{<} - \Pi^{<} \odot \Delta_c^{>})\,. \tag{6.43}$$

Because of their non-linear and non-local structure the Kadanoff-Baym equations are very difficult to solve but there are solutions in simplified setups, e.g., [366, 376, 391] in the context of baryogenesis through leptogenesis.

6.1.4 Wigner Representation and Gradient Expansion

In non-equilibrium situations, the Green's function $\Delta(x, y)$ does not only depend on the relative coordinate $r = x - y$ as in equilibrium but also on the average coordinate $(x + y)/2$. Therefore, a simple Fourier transform with respect to r is not sufficient to express the Green's function in momentum space as common in traditional S-matrix calculations. A more suited transformation is the Wigner transform, defined through

$$\Delta(p, z) = \int \mathrm{d}^4 r\, e^{ipr} \Delta\left(z + \frac{r}{2}, z - \frac{r}{2}\right) \tag{6.44}$$

with the mean coordinate z. As one can explictly check later in the equilibrium case, the phase space distribution function f_ϕ of the scalar field ϕ can be related in Wigner space to the Wightman functions via

$$f_\phi(\mathbf{p}, z) = \int_0^\infty \frac{\mathrm{d}p^0}{\pi} p^0 i\Delta^{<}(p, z)\,. \tag{6.45}$$

This means that in order to obtain a kinetic equation for the phase space distribution function that generalizes the Boltzmann equation (2.9) to a full quantum mechanical description, the Kadanoff-Baym equations (6.43) are needed in Wigner space. To actually perform the transformation, one can make use of the general relation

$$\int \mathrm{d}^4 r\, e^{ipr} \int \mathrm{d}^4 z\, f(x, z) g(z, y) = e^{-i\diamond}\{f(p, z)\}\{g(p, z)\}\,, \tag{6.46}$$

where the diamond operator is defined via

$$\diamond\{f(p, z)\}\{g(p, z)\} = \frac{1}{2}\left(\partial_z f \cdot \partial_p g - \partial_z f \cdot \partial_a g\right) \tag{6.47}$$

and the exponentiation of $\diamond$ has to be interpreted as a series expansion. Since the equation of motions (6.43) have the form of Eq. (6.46), they can simply be written in Wigner space as

$$(p^2 - \frac{1}{4}\partial_z^2 + ip \cdot \partial_z - m^2)\Delta_c^{\gtrless} - e^{-i\diamond}\{\Pi^{\gtrless}\}\{\Delta_c^{\mathcal{H}}\} - e^{-i\diamond}\{\Pi^{\mathcal{H}}\}\{\Delta_c^{\gtrless}\} = \mathcal{C} \tag{6.48}$$

with the collision term

$$\mathcal{C} = \frac{1}{2} e^{-i\diamond}(\{\Pi^{>}\}\{\Delta_c^{<}\} - \{\Pi^{<}\}\{\Delta_c^{>}\})\,. \tag{6.49}$$

These equations becomes much simpler in the gradient expansion which assumes that the average coordinate is small compared to the momentum p such that the series can be truncated to a certain order in the derivatives with respect to z. Formally, this assumption reads $\partial_z \ll p$. Assuming furthermore homogeneity and isotropy such that all spatial derivatives vanish yields from the real

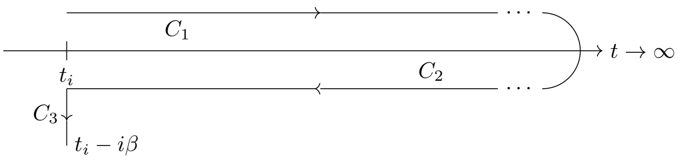

Figure 6.3: Finite temperature Closed Time Path.

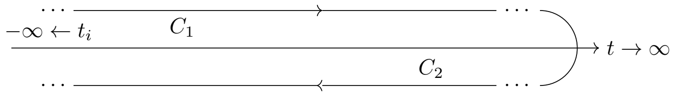

Figure 6.4: Keldysh-Schwinger closed time path.

part of Eq. (6.48) the kinetic equation

$$p^0 \partial_t (i\Delta^{\gtrless}) = -\frac{1}{2}(i\Pi^{>} i\Delta^{<} - i\Pi^{<} i\Delta^{>}) + \mathcal{O}\Big(\partial_t \Pi^{\gtrless;\mathcal{H}} \Delta^{\mathcal{H};\gtrless}\Big) . \tag{6.50}$$

6.1.5 Thermal Equilibrium

In thermal equilibrium, i.e., when a temperature $T = 1/\beta$ can be defined for all times, the density matrix coincides with the one in the canonical ensemble $\hat{\varrho}^{(\mathrm{eq})} = \frac{1}{\mathcal{Z}} e^{-\beta \hat{H}}$ where $\mathcal{Z} = \mathrm{Tr}\, e^{-\beta \hat{H}}$ is the corresponding partition function. The general treatment of quantum fields in equilibrium is based on the observation that $\hat{\varrho}^{(\mathrm{eq})}$ acts as an evolution operator in the imaginary time direction and can therefore be related to the time-evolution operator via

$$\hat{\varrho}^{(\mathrm{eq})} = \hat{U}(t_i^- - i\beta, t_i^-) . \tag{6.51}$$

Thus, for equilibrium systems, the initial density matrix can be eliminated from the generating functional in Eq. (6.9) by adding a third and imaginary branch C_3 to the complex contour C which runs from t_i^- to $t_i^- - i\beta$ parallel to the imaginary time axis resulting in the finite-temperature closed time path C_β shown in Fig. 6.3. The corresponding generating functional of C_β is then

$$Z_{C_\beta}[J] = \int \mathcal{D}\phi \exp\left(i \int_{C_\beta} \mathrm{d}^4 x (\mathcal{L}(x) + J(x)\phi(x)) \right) \tag{6.52}$$

with the periodic boundary conditions $\phi(\mathbf{x}, t_i) = \phi(\mathbf{x}, t_i - i\beta)$. It has been suggested [360] that in the limit $t_i \to -\infty$ the free generating functional $Z^F_{C_\beta}[J]$ factorizes as $Z^F_{C_\beta} = Z^F_{C_1 \cup C_2} Z^F_{C_3}$. Then correlation functions with real time arguments can be generated from $Z^F_{C_1 \cup C_2}$ alone since $Z^F_{C_3}$ contributes only to imaginary time arguments and therefore plays just the role of a multiplicative constant. However, this factorization or rather this limit comes at the prize of introducing some ambiguities, in particular when dealing with self-energy insertions [360, 392]. The associated path is shown in Fig. 6.4 and sometimes referred to as the Keldysh-Schwinger contour. It is remarkable that the path in Fig. 6.2 initially introduced for general non-equilibrium situations is in the limit $t_i \to \infty$ valid for equilibrium situations as well, as long as time arguments are restricted to be real.

Equation (6.51) futher implies that for any Heisenberg operator $\hat{\mathcal{O}}(t)$ one has

$$e^{-\beta \hat{H}} \hat{\mathcal{O}}(t) e^{\beta \hat{H}} = \hat{\mathcal{O}}(t + i\beta) . \tag{6.53}$$

From the cyclic property of the trace, useful relations between two-point functions can be constructed. E.g., consider the two Heisenberg operators $\hat{\mathcal{O}}_1(t)$ and $\hat{\mathcal{O}}_2(t)$ whose ensemble average in equilibrium is given by

$$\langle\hat{\mathcal{O}}_1(t)\hat{\mathcal{O}}_2(t')\rangle_\beta = \frac{1}{\mathcal{Z}}\,\mathrm{Tr}\left[e^{-\beta\hat{H}}\hat{\mathcal{O}}_1(t)\hat{\mathcal{O}}_2(t')\right] , \tag{6.54}$$

where the subscript ϱ on the average has been replaced by β to indicate the equilibrium initial conditions. Inserting the identity operator $\mathbb{1} = e^{\beta\hat{H}}e^{-\beta\hat{H}}$ between $\hat{\mathcal{O}}_1(t)$ and $\hat{\mathcal{O}}_2(t')$ and applying the time evolution in the imaginary direction as dictated by Eq. (6.53) yields after using the cyclicity of the trace operator

$$\langle\hat{\mathcal{O}}_1(t)\hat{\mathcal{O}}_2(t')\rangle_\beta = \langle\hat{\mathcal{O}}_2(t')\hat{\mathcal{O}}_1(t+i\beta)\rangle_\beta\,. \tag{6.55}$$

The identity in Eq. (6.55) is known as the Kubo-Martin-Schwinger (KMS) relation and can be regarded as the expression of detailed balance. For scalar field operators the KMS relation takes the form

$$\Delta^{>}(x,y) = \Delta^{<}((\mathbf{x},t+i\beta),y)\,. \tag{6.56}$$

As systems in thermal equilibrium are spacetime translation invariant such that equilibrium two-point correlators are only functions of the difference of their spacetime arguments $x-y$, i.e., $\Delta(x,y) = \Delta(r)$, the Wigner transform (6.44) reduces to the normal Fourier transform

$$\Delta^{\gtrless}(p) = \int \mathrm{d}^4 r\, \Delta^{\gtrless}(z) e^{ipr} \tag{6.57}$$

with respect to r where, within the usual abuse of notation, the functions in momentum and position space are only distinguished through the naming convention for their arguments, even though they are different. As known from zero temperature field theory, calculations in momentum space simplify considerably. This extends to the KMS relation which becomes in momentum space even more powerful and reads

$$\Delta^{>}(p) = e^{\beta p^0}\Delta^{<}(p) \tag{6.58}$$

Taking the Fourier transform of Eq. (6.14) with respect to the spatial coordinates $\mathbf{r} = \mathbf{x}-\mathbf{y}$ allows to rewrite the equation as

$$\left(\frac{\partial^2}{\partial x_0^2} + E^2\right)\Delta_0(x^0-y^0,E) = -\delta_C(x^0,y^0) \tag{6.59}$$

with $E = \sqrt{\mathbf{p}^2+m^2}$. The corresponding solution subject to the periodicity condition in Eq. (6.55) can be determined to be[2]

$$i\Delta_0(x^0-y^0,E) = \frac{f_B(E)}{2E}\Big[\Theta_C(x^0,y^0)\left(e^{\beta E - iE(x^0-y^0)} + e^{iE(x^0-y^0)}\right) \\ +\Theta_C(y^0,x^0)\left(e^{\beta E + iE(x^0-y^0)} + e^{-iE(x^0-y^0)}\right)\Big]\,. \tag{6.60}$$

Note that the expression for the propagator in Eq. (6.60) (i) reduces in the zero-temperature limit

---

[2] The Green's function $\Delta_0(x^0-y^0,E)$ can be found by starting from the one-dimensional harmonic oscillator $(\partial_t^2+\omega_0^2)G(t) = \delta(t)$ with the Green's function $G(t) = \Theta(t)\frac{\sin(t\omega_0)}{\omega_0}$ and applying additionally the periodicity condition $G(t) = G(t-i\beta)$ in the four distinct cases show in Eq. (6.2).

$\beta \to \infty$ to the conventional vacuum one on C_1, (ii) is an even function in r^0 and (iii) satisfies the KMS relation (6.56). Evaluating the Heaviside functions in the four distinct regions and taking the Fourier transform of the remaining temporal component yields the final form of the free thermal propagators for scalars:

$$i\Delta_0^{11}(p) = \frac{i}{p^2 - m^2 + i\epsilon} + 2\pi\delta(p^2 - m^2) f_B(|p^0|) = (i\Delta_0^{22})^*(p)\,, \tag{6.61a}$$

$$i\Delta_0^{12}(p) = 2\pi\delta(p^2 - m^2)\left[f_B(|p^0|) + \Theta(-p^0)\right]\,, \tag{6.61b}$$

$$i\Delta_0^{21}(p) = 2\pi\delta(p^2 - m^2)\left[f_B(|p^0|) + \Theta(p^0)\right]\,, \tag{6.61c}$$

where $f_B(E)$ is the Bose-Einstein distribution defined in Eq. (2.14a) for a vanishing chemical potential. With the propagator (6.61b) at hand, it is straightforward to check that the definition of ϕ's phase space density in Eq. (6.45) holds. For completeness, it is useful to write down the corresponding retarded and advanced propagators

$$i\Delta_0^{R/A}(p) = \frac{i}{p^2 - m^2 \pm i\mathrm{sgn}(p^0)\epsilon}\,, \tag{6.62}$$

as well as the correlated propagator

$$i\Delta_0^{C}(p) = 2\pi\left[1 + 2f_B(|p^0|)\right]\delta(p^2 - m^2) = \left[1 + 2f_B(p^0)\right]\Delta_0^-(p)\,, \tag{6.63}$$

where the relation to the spectral propagator Δ_0^- is another way of stating the KMS relation.

6.1.6 Feynman Rules at Finite Temperature

The finite-temperature Feynman rules follow from Eq. (6.21). They are as in vacuum with the only difference that there are two types of vertices, '1' and '2', accounting for the forward and the backward branch of the contour. Type-1 vertices remain unchanged compared to the zero-temperature field theory whereas type-2 vertices obtain an extra relative minus sign. A type-1 vertex and a type-2 vertex are then connected through $i\Delta_0^{12}(p)$ with the propagator momentum p flowing from '1' to '2'. Two type-1 vertices are connected through $i\Delta_0^{11}(p)$ and so on. This means that the nature of a field can only change through the off-diagonal propagators and a vertex can connect only to type-1 or solely to type-2 fields. In addition, one has to sum over all internal types of vertices. As in vacuum, energy-momentum conservation is imposed at each vertex through a δ-function and all undetermined loop momenta k are integrated over via $\int \mathrm{d}^4k\,/(2\pi)^4$.

6.2 Dirac Fermions

The extension of the Keldysh-Schwinger formalism to Dirac fermions with the free Lagrangian density $\mathcal{L}_0 = \bar{\psi}(i\partial\!\!\!/ - m)\psi$ is straightforward. Analogously to Eq. (6.17), the fermionic contour-ordered propagator

$$iS_{\alpha\beta}(x,y) = \langle T_C\{\hat{\psi}_\alpha(x)\hat{\bar{\psi}}_\beta(y)\}\rangle_\varrho = \Theta_C(x^0,y^0)iS^>_{\alpha\beta}(x,y) + \Theta_C(y^0,x^0)iS^<_{\alpha\beta}(x,y)\,. \tag{6.64}$$

can be decomposed into the two Wightman functions $S^{>}$ and $S^{<}$. These are defined trough

$$iS^{>}_{\alpha\beta}(x,y) = \langle \hat{\psi}_\alpha(x)\hat{\bar{\psi}}_\beta(y)\rangle_\varrho \,, \tag{6.65a}$$

$$iS^{<}_{\alpha\beta}(x,y) = -\langle \hat{\bar{\psi}}(y)_\beta\hat{\psi}_\alpha(x)\rangle_\varrho \,. \tag{6.65b}$$

The labels α and β denote spinor indices which are suppressed in the following. Also note the minus sign in Eq. (6.65b) due to the anti-commuting nature of fermions. Similar to the scalar case, the phase space distribution function f_ψ of ψ is obtained by tracing the lesser Wightman function,

$$f_\psi(\mathbf{p},z) = \int_0^\infty \frac{\mathrm{d}p^0}{4\pi}\,\mathrm{Tr}\left[-iS^{<}(p,z)\gamma^0\right] \,, \tag{6.66}$$

and the fermionic Kadanoff-Baym equations become

$$(i\not{\partial}_x - m)S_c^{\gtrless} - \Sigma^{\gtrless}\odot S_c^{\mathcal{H}} - \Sigma^{\mathcal{H}}\odot S_c^{\gtrless} = \frac{1}{2}(\Sigma^{>}\odot S_c^{<} - \Sigma^{<}\odot S_c^{>})\,, \tag{6.67}$$

where the fermionic analogue to the scalar self-energy Π is denoted by Σ. As before, these can be transformed to Wigner space giving

$$(\not{p} + \frac{i}{2}\not{\partial}_z - m)S_c^{\gtrless} - e^{-i\diamond}\{\Sigma^{\gtrless}\}\{S_c^{\mathcal{H}}\} - e^{-i\diamond}\{\Sigma^{\mathcal{H}}\}\{S_c^{\gtrless}\} = \frac{1}{2}e^{-i\diamond}(\{\Sigma^{>}\}\{S_c^{<}\} - \{\Sigma^{<}\}\{S_c^{>}\})\,. \tag{6.68}$$

In the gradient expansion, Eq. (6.68) shortens to

$$\gamma^0\partial_t(-iS^{\gtrless}) = i\Sigma^{>}iS^{<} - i\Sigma^{<}iS^{>} + \mathcal{O}\Big(\partial_t\Sigma^{\gtrless;\mathcal{H}}S^{\mathcal{H};\gtrless}\Big)\,. \tag{6.69}$$

Turning the discussion to the equilibrium situation, the fermionic KMS relation reads in position space $S^{>}(x,y) = -S^{<}((\mathbf{x},t+i\beta),y)$. Again, in momentum space it becomes more powerful:

$$S^{>}(p) = -e^{\beta p^0}S^{<}(p)\,. \tag{6.70}$$

Without going into the details of the path integral formulation for anti-commuting fields, just note that the free equilibrium propagators for Dirac fermions can be derived similarly to the bosonic ones with the result:

$$iS_0^{11}(p) = \frac{i(\not{p}+m)}{p^2-m^2+i\epsilon} - 2\pi(\not{p}+m)\delta(p^2-m^2)f_D(|p^0|) = \gamma^0(iS_0^{22})^\dagger\gamma^0\,, \tag{6.71a}$$

$$iS_0^{12}(p) = -2\pi(\not{p}+m)\delta(p^2-m^2)\left[f_D(|p^0|) - \Theta(-p^0)\right]\,, \tag{6.71b}$$

$$iS_0^{21}(p) = -2\pi(\not{p}+m)\delta(p^2-m^2)\left[f_D(|p^0|) - \Theta(p^0)\right]\,, \tag{6.71c}$$

where $f_D(E)$ is the Fermi-Dirac distribution function defined in Eq. (2.14b) for $\mu = 0$.

6.3 Gauge Fields at Finite Temperature

While the quantization of Dirac fields at finite temperature is a rather straightforward generalization of the scalar field, the quantization of gauge fields is technically more challenging, since, for instance, Faddeev–Popov ghosts are required even in Abelian gauge theories to cancel the unphysical degrees of freedom in covariant gauges. Otherwise one finds, e.g., in QED twice the free-energy due to twice the number of polarization states. However, as the ghost fields contribute only a multiplicative factor to the generating functional, this is only true for calculations of the partition function while the evaluation of Green's functions in linear gauges at $T \neq 0$ just requires a minor modification of the Feynman rules compared to vacuum. That is, the free gauge field propagator like the photon propagator in QED becomes a 2×2-matrix with an additional thermal component and can be written in terms of the scalar propagators as

$$iD^{ab}_{\mu\nu}(p) = d_{\mu\nu}(p) i\Delta^{ab}_0(p)|_{m=0} \,, \tag{6.72}$$

where the polarization tensor $d^{\mu\nu}(p)$ contains the Lorentz structure and takes for covariant R_ξ gauges the form

$$d^{\mu\nu}(p) = -\eta^{\mu\nu} + (1-\xi)\frac{p^\mu p^\nu}{p^2} \,. \tag{6.73}$$

The propagators for massive gauge bosons in the real-time formalism on the other hand have, e.g., been worked out in Ref. [393]. The dressed (or exact or resummed) gauge propagator $\bar{D}^{ab}_{\mu\nu}$ can be obtained from the self-energy function $\Pi^{\mu\nu}_{ab}$ which, in turn, can be calculated perturbatively, through the Dyson-Schwinger equation (6.42a) whose equilibrium version in momentum space becomes

$$\bar{D}^{R/A}_{\mu\nu} = D^{R/A}_{\mu\nu} + D^{R/A}_{\mu\alpha} \Pi^{\alpha\beta}_{R/A} \bar{D}^{R/A}_{\beta\nu} \tag{6.74}$$

with a suppressed dependence of the momentum p flowing through the propagator. By gauge invariance the full propagator can be decomposed into a longitudinal and a transverse part using the corresponding projectors [392, 394]

$$P^{00}_T = P^{0i}_T = P^{i0}_T = 0, \quad P^{ij}_T = -\delta^{ij} + \frac{p^i p^j}{|\mathbf{p}|^2} \,, \tag{6.75a}$$

$$P^{\mu\nu}_L = \eta^{\mu\nu} - \frac{p^\mu p^\nu}{p^2} - P^{\mu\nu}_T \,, \tag{6.75b}$$

which yields

$$-\bar{D}^{ab}_{\mu\nu} = -d_{\mu\nu}\bar{D}^{ab} = \bar{D}^{ab}_L P^L_{\mu\nu} + \bar{D}^{ab}_T P^T_{\mu\nu} + \xi \Delta^{ab}_0 \frac{p_\mu p_\nu}{p^2} \,. \tag{6.76}$$

This decomposition has the advantage that Eq. (6.74) splits into two separate pieces due to the orthogonality of the projectors, one for the longitudinal component and one for the transverse one, without any remaining Lorentz indices, allowing to solve for the full propagator analytically with the solution

$$\bar{D}^{R/A}_{L/T} = \frac{1}{(\Delta^{R/A})^{-1} + \Pi^{R/A}_{L/T}} . \tag{6.77}$$

For practical calculations it is often useful to work with the 11-component of the exact propagator instead of the advanced or retarded one.[3] To work out the explicit form, one can use Eq. (6.27a) and the fact that, in equilibrium, the correlated propagator is related to the retarded and advanced propagators via the fluctuation-dissipation theorem [395, 396]

$$\bar{D}^C_{\mu\nu}(p) = [1 + 2f_B(|p^0|)]\mathrm{sgn}(p^0)\left[\bar{D}^R_{\mu\nu}(p) - \bar{D}^A_{\mu\nu}(p)\right] \,. \tag{6.78}$$

---

[3] The 22-component can be simply be obtained from the 11-part through complex conjugation.

The resummed propagator can then be written in the compact form:

$$\bar{D}^{11}_{L/T} = \frac{\Omega_{L,T}}{\Omega^2_{L,T} + \Gamma^2_{L,T}} - i[1 + 2f_B(|p^0|)]\mathrm{sgn}(p^0)\frac{\Gamma_{L,T}}{\Omega^2_{L,T} + \Gamma^2_{L,T}}, \tag{6.79a}$$

with the abbreviations

$$\Omega^{L,T} = p^2 + \mathrm{Re}\,\Pi^{L/T}_R\,, \tag{6.80a}$$

$$\Gamma^{L,T} = \mathrm{Im}\,\Pi^{L,T}_R\,. \tag{6.80b}$$

It is understood Eq. (6.79a) should be replaced by the causality-respecting ϵ-prescription if the imaginary part of the retarded self-energy vanishes for kinematic reasons, i.e., by the propagator in Eq. (6.61a).

6.4 Thermal Integrals

In thermal field theory calculations within the real-time formalism one often encounters integrals of the forms

$$K^\mu(P) = 2g^2 \int \frac{\mathrm{d}^4k}{(2\pi)^3} k^\mu \frac{\delta(k^2 - m^2) f_D(|k^0|)}{(P+k)^2 - m^2 + i\epsilon}\,, \tag{6.81a}$$

$$K^{\mu\nu}(P) = 2g^2 \int \frac{\mathrm{d}^4k}{(2\pi)^3} k^\mu k^\nu \frac{\delta(k^2 - m^2) f_D(|k^0|)}{(P+k)^2 - m^2 + i\epsilon} \tag{6.81b}$$

with a generic coupling $g \ll \sqrt{4\pi}$ depending on the external momentum P and (implicitly) on the mass scale m. The purpose of this section is therefore to evaluate these “thermal integrals” as far as possible such that only one integral over the energy $\omega = |k^0| = \sqrt{\mathbf{k}^2 + m^2}$ remains. For this computation, $\mathbf{P}$ is chosen as reference direction and the corresponding unit vector is denoted by $\hat{\mathbf{P}}$. The integration variable can then be parameterized via

$$\mathbf{k} = |\mathbf{k}|(\cos\vartheta \hat{\mathbf{P}} + \cos\varphi \sin\vartheta \hat{\mathbf{e}}_1 + \sin\varphi \sin\vartheta \hat{\mathbf{e}}_2), \tag{6.82}$$

where, together, $\hat{\mathbf{P}}$ and the two unit vectors $\hat{\mathbf{e}}_1$ and $\hat{\mathbf{e}}_2$ form a complete orthogonal basis.

The contributions from $\hat{\mathbf{e}}_1$ and $\hat{\mathbf{e}}_2$ to the spatial components of K^μ vanish after the azimuthal φ-integration, resulting in

$$\mathbf{K} = \frac{\mathbf{P}}{|\mathbf{P}|^3} \frac{g^2}{(4\pi)^2} \int_m^\infty \mathrm{d}\omega \left[P^2 \ell_1(\omega, P) + 2\omega P_0 \ell_2(\omega, P) - 8|\mathbf{k}||\mathbf{P}|\right] f_D(\omega), \tag{6.83}$$

where the two functions

$$\ell_1(\omega, P) = \ln\left|\frac{(P^2 + 2|\mathbf{k}||\mathbf{P}|)^2 - 4P_0^2\omega^2}{(P^2 - 2|\mathbf{k}||\mathbf{P}|)^2 - 4P_0^2\omega^2}\right|, \tag{6.84a}$$

$$\ell_2(\omega, P) = \ln\left|\frac{P^4 - 4(P_0\omega + |\mathbf{P}||\mathbf{k}|)^2}{P^4 - 4(P_0\omega - |\mathbf{P}||\mathbf{k}|)^2}\right| \tag{6.84b}$$

arise from the integration over $\cos\vartheta$. Correspondingly,

$$K^0 = \frac{g^2}{8\pi^2|\mathbf{P}|}\int_m^\infty \mathrm{d}\omega\,\omega\,\ell_2(\omega,P)f_D(\omega) \tag{6.85}$$

is the remaining, temporal component of K^μ.

For $K^{\mu\nu}$, after application of the completeness relation $\delta^{ij} = \hat{P}^i\hat{P}^j + \sum_{k=1,2}\hat{e}^i_k\hat{e}^j_k$, the spatial components become

$$K^{ij} = \hat{P}^i\hat{P}^j G_1 + (\delta^{ij} - \hat{P}^i\hat{P}^j)(I_2 - I_1/2), \tag{6.86}$$

with the two auxiliary functions

$$I_1 = \frac{g^2}{2(2\pi)^2|\mathbf{P}|^3}\int_m^\infty \mathrm{d}\omega\,\left[(P^4 + 4P_0^2\omega^2)\ell_1(\omega,P) + 4P^2P_0\,\omega\,\ell_2(\omega,P) - 8|\mathbf{P}||\mathbf{k}|P^2\right]f_D(\omega), \tag{6.87a}$$

$$I_2 = \frac{g^2}{(4\pi)^2|\mathbf{P}|}\int_m^\infty \mathrm{d}\omega\,|\mathbf{k}|^2\ell_1(\omega,P)f_D(\omega). \tag{6.87b}$$

The remaining components with at least one index being zero are

$$K^{00}(P) = \frac{g^2}{8\pi^2|\mathbf{P}|}\int_m^\infty \mathrm{d}\omega\,\omega^2\,\ell_1(\omega,P)f_D(\omega), \tag{6.88a}$$

$$K^{0i} = \frac{g^2\hat{P}^i}{(4\pi)^2|\mathbf{P}|^2}\int_m^\infty \mathrm{d}\omega\,\omega\,\left[2P_0\omega\ell_1(\omega,P) + P^2\ell_2(\omega,P)\right]f_D(\omega). \tag{6.88b}$$

The remaining single integral over ω has to be evaluated numerically.

The HTL Approximation The hard thermal loop (HTL) approximation [397] is a very successful scheme to analytically approximate integrals like K^μ and $K^{\mu\nu}$. It is based on the assumption that the quantities in such integrals can be separated into hard $\mathcal{O}(\pi T)$ and soft scales $\mathcal{O}(gT)$. This is achieved by taking the external momentum P to be soft and therefore negligible compared to the loop momentum k whose hard contribution is supposed to dominate the integral. In addition, $m \ll T$ is assumed such that the mass m is taken to be zero. These assumptions then reduce the two auxiliary logarithmic functions to

$$\ell_1(\omega,P) \overset{\text{HTL}}{\approx} -2\frac{|\mathbf{P}|}{|\mathbf{k}|}, \quad \ell_2(\omega,P) \overset{\text{HTL}}{\approx} 2\ln\left|\frac{P_0 + |\mathbf{P}|}{P_0 - |\mathbf{P}|}\right|, \tag{6.89}$$

where the symbol $\overset{\text{HTL}}{\approx}$ is used to denote the HTL limit. In all cases, this leaves an integral over ω that can be performed analytically through

$$\int_0^\infty \mathrm{d}\omega\,\omega\,f_D(\omega) = \frac{\pi^2T^2}{12}. \tag{6.90}$$

6.5 The Photon Self-Energy in the Real-Time Formalism

A crucial ingredient in the NLO improved calculation of N_{eff} in the Standard Model in Ch. 7 is the photon self-energy. Therefore, an exact derivation at the one-loop level within the Keldysh-Schwinger formalism is presented in this section, making use of the previously calculated integrals and assuming electrons in thermal equilibrium with vanishing chemical potentials. In addition, from there, the resummed photon propagator can be extracted. While exact expressions for this self-energy have been long known in the simplified scenarios wherein $m_e = 0$ [398] or in the HTL approximation (see, e.g., [360, 396]), these assumptions are removed here instead and a photon self-energy valid for all values of the electron mass m_e and photon momenta P is derived. Note that, while Ref. [399] also studied the photon self-energy beyond the HTL approximation (and accounting for non-zero electron chemical potentials), no explicit formulae were provided.

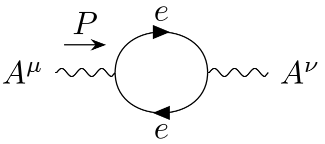

Figure 6.5: One-loop electron contribution to the photon self-energy.

At the one-loop level, the photon self-energy in the real-time formalism, displayed in Fig. 6.5 and only accounting for the electron contribution, reads

$$-i\Pi^{\mu\nu}_{ab}(P) = (-1)^{a+b}e^2 \int \frac{\mathrm{d}^4k}{(2\pi)^4} \mathrm{Tr}\left[iS^{ab}_e(k)\gamma^\mu iS^{ba}_e(k-P)\gamma^\nu\right] . \tag{6.91}$$

Nonetheless, it is straightforward to extend the calculation to other electrically charged particles in the loop. By gauge invariance, the self-energy can always be split into a longitudinal and a transverse part,

$$\Pi^{\mu\nu}_{ab} = \Pi^L_{ab}P^{\mu\nu}_L + \Pi^T_{ab}P^{\mu\nu}_T , \tag{6.92}$$

through the projectors defined in Eq. (6.75). Writing the self-energy in this form makes also manifest that $\Pi^{\mu\nu}_{ab}$ fulfills the Ward-Takahashi identity $P_\mu\Pi^{\mu\nu}_{ab} = 0$. The longitudinal projector can alternatively be expressed through the heat bath four-velocity $U^\mu = \delta^\mu_0$ (in its rest frame) as $P^{\mu\nu}_L = \tilde{U}^\mu\tilde{U}^\nu/\tilde{U}^2$ with $\tilde{U}^\mu = P^2U^\mu - (U\cdot P)P^\mu$, so that the transverse projector becomes $P^{\mu\nu}_T = \eta^{\mu\nu} - \frac{P^\mu P^\nu}{P^2} - P^{\mu\nu}_L$.

In the following, only the derivation of $\Pi^{\mu\nu}_{11}$ and $\Pi^{\mu\nu}_{12}$ is highlighted, since the remaining two self-energy components can be related to the first two via the bosonic KMS relation $\Pi^{\mu\nu}_{21}(P) = e^{P_0/T}\Pi^{\mu\nu}_{12}(P)$ derived in Eq. (6.57) and $\Pi^{\mu\nu}_{22}(P) = -(\Pi^{\mu\nu}_{11}(P))^*$ which follows from inspection of Eq. (6.91) under complex conjugation.

Starting with the diagonal components, $\Pi^{\mu\nu}_{11}$ splits into the vacuum self-energy

$$\Pi^{\mu\nu}_2 = ie^2\int_k \frac{i}{k^2 - m_e^2 + i\epsilon}\frac{i}{(k+P)^2 - m_e^2 + i\epsilon}\mathrm{Tr}\left[(\not{k} + m_e)\gamma^\mu(\not{k} + \not{P} + m_e)\gamma^\nu\right] \tag{6.93}$$

and the finite-temperature part $\Pi^{\mu\nu}_{11,T\neq 0}$. The renormalized vacuum part $\Pi^{\mu\nu}_2(P) = (\alpha_{\mathrm{em}}/\pi)(P^2\eta^{\mu\nu} - P^\nu P^\mu)\Pi_2(P^2)$ can be, e.g., computed using the Passarino-Veltmann reduction procedureand, in the $\overline{\mathrm{MS}}$-scheme, reads

$$\Pi_2(P^2) = \frac{2}{3}\ln\left(\frac{\mu}{m_e}\right) + \frac{5}{9} + \frac{\tau}{3} + \frac{1}{3}\left(1 + \frac{\tau}{2}\right)\sqrt{1-\tau}\ln\left(\frac{\sqrt{1-\tau}-1}{\sqrt{1-\tau}+1}\right) \tag{6.94a}$$

$$\longrightarrow \frac{1}{3}\ln\left(\frac{\mu^2}{-P^2}\right) + \frac{5}{9} \quad \text{for } m_e \to 0, \tag{6.94b}$$

with $\tau = 4m_e^2/P^2$ and in agreement with Ref. [400].

The finite-temperature part can be written in terms of the integrals K^μ and $K^{\mu\nu}$ computed in Sec. 6.4 such that the corresponding real part reads

$$\begin{aligned}\operatorname{Re}\Pi^{\mu\nu}_{11,T\neq 0} &= \operatorname{Tr}\left[(\not{K} + m_e)\gamma^\mu(\not{K} + \not{P} + m_e)\gamma^\nu\right] \\ &= 4(-\eta^{\mu\nu}K\cdot P + 2K^{\mu\nu} + K^\mu P^\nu + K^\nu P^\mu). \end{aligned} \tag{6.95}$$

After collecting all the terms according to the projectors defined in Eq. (6.75), one obtains for the longitudinal part

$$\operatorname{Re}\Pi^{L}_{11,T\neq 0} = \frac{\alpha_{\mathrm{em}}P^2}{\pi|\mathbf{P}|^3}\int_{m_e}^{\infty}\mathrm{d}\omega\left[8|\mathbf{k}||\mathbf{P}| - \ell_1(\omega,P)(P^2+4\omega^2) - 4\ell_2(\omega,P)P_0\omega\right]f_D(\omega) \tag{6.96a}$$

$$\overset{\mathrm{HTL}}{\approx} -3m_\gamma^2\left(1-\frac{P_0^2}{|\mathbf{P}|^2}\right)\left[1-\frac{P_0}{2|\mathbf{P}|}\ln\left|\frac{P_0+|\mathbf{P}|}{P_0-|\mathbf{P}|}\right|\right] \longrightarrow -3m_\gamma^2 \ \text{ for } P_0 = 0\,. \tag{6.96b}$$

It is remarkable that this result shows that even in the static limit $P_0 \to 0$, the longitudinal excitations of the photon field, which are also sometimes referred to as "plasmons", obtain an electric mass $m_\gamma = eT/3$ just through interactions with the thermal electron bath whereas the corresponding expression for the transverse part

$$\begin{aligned}\operatorname{Re}\Pi^{T}_{11,T\neq 0} = \frac{\alpha_{\mathrm{em}}}{\pi|\mathbf{P}|^3}\int_{m_e}^{\infty}\mathrm{d}\omega\Bigg[&2\ell_2(\omega,P)P_0P^2\omega - 4|\mathbf{k}||\mathbf{P}|(P_0^2+|\mathbf{P}|^2) \\ &+ \ell_1(\omega,P)\left(|\mathbf{P}|^2P^2 + 2P_0^2\omega^2 - 2|\mathbf{k}|^2|\mathbf{P}|^2 + \frac{1}{2}P^4\right)\Bigg]f_D(\omega)\end{aligned} \tag{6.97a}$$

$$\overset{\mathrm{HTL}}{\approx} -\frac{3}{2}m_\gamma^2\frac{P_0^2}{|\mathbf{P}|^2}\left[1-\left(1-\frac{|\mathbf{P}|^2}{P_0^2}\right)\frac{P_0}{2|\mathbf{P}|}\ln\left|\frac{P_0+|\mathbf{P}|}{P_0-|\mathbf{P}|}\right|\right] \longrightarrow 0, \ \text{ for } P_0 = 0\,, \tag{6.97b}$$

shows no such behavior. The (purely imaginary) off-diagonal component $\Pi^{\mu\nu}_{12}$, on the other hand, reads

$$\begin{aligned}\Pi^{\mu\nu}_{12} = i(ie)^2\int\frac{\mathrm{d}^4k}{(2\pi)^4}16\pi^2\delta\left(k^2-m_e^2\right)(f_D(|k^0|)-\Theta(k^0))\delta\left((k+P)^2-m_e^2\right)& \\ \times\left(f_D(|k^0+P^0|)-\Theta(-k^0-P^0)\right)A^{\mu\nu},&\end{aligned} \tag{6.98}$$

where the minus sign from the fermionic loop and the one from the fact that a type-1 and a type-2 vertex occur cancel out, and $A^{\mu\nu} = -\eta^{\mu\nu}k\cdot P + 2k^\mu k^\nu + k^\nu P^\mu + k^\mu P^\nu$.

For the evaluation of the integrals, the decomposition of $\mathbf{k}$ shown in Eq. (6.82) is used again. The additional δ-function here (compared to the diagonal case) fixes then the polar angle θ to the value

$$\cos\theta^*_\pm = \frac{P^2 \pm 2\omega P_0}{2|\mathbf{k}||\mathbf{P}|}. \tag{6.99}$$

With that, the tensor $A^{\mu\nu}$ separates into a transverse and a longitudinal part according to

$$A^{\mu\nu}_\pm = \frac{P^2}{2}(P_T^{\mu\nu}+P_L^{\mu\nu}) - |\mathbf{k}|^2\sin^2\theta^*_\pm P_T^{\mu\nu} - \frac{P^2}{2|\mathbf{P}|^2}(P_0\pm 2\omega)^2P_L^{\mu\nu}. \tag{6.100}$$

The final result then reads

$$\Pi_{12}^{\mu\nu} = -i\frac{2\alpha_{\mathrm{em}}}{|\mathbf{P}|}\int_{m_e}^{\infty} \mathrm{d}\omega \sum_{\pm} \Theta(1-|\cos\theta_\pm^*|)(f_D(\omega)-\Theta(k^0))(f_D(|k^0+P^0|)-\Theta(-k^0-P^0))A_\pm^{\mu\nu}, \tag{6.101}$$

where the sum runs over positive and negative energies $k^0 = \pm\omega$. In the HTL limit, Eq. (6.101) becomes

$$\Pi_{12}^{L} \overset{\mathrm{HTL}}{\approx} -i\frac{\pi e^2 P^2 T^3}{3|\mathbf{P}|^3}\Theta(|\mathbf{P}|-|P^0|), \tag{6.102a}$$

$$\Pi_{12}^{T} \overset{\mathrm{HTL}}{\approx} i\frac{\pi e^2 P^2 T^3}{6|\mathbf{P}|^3}\Theta(|\mathbf{P}|-|P^0|), \tag{6.102b}$$

where the integral $\int_0^\infty \mathrm{d}k\, k^2 f_D(k)\,[1-f_D(k)] = \pi^2 T^3/6$ has been used. Note that the off-diagonal contributions (6.102) vanish for timelike external momenta, $P^2 > 0$.

For the calculation of the dressed photon propagator, it is convenient to compute the retarded and advanced photon self-energy which can be written as

$$\begin{aligned}\Pi_{R/A}^{T/L} = \Pi_{11}^{T/L} - \Pi_{12/21}^{T/L} &= \mathrm{Re}\,\Pi_{11}^{T/L} \mp \frac{1}{2}\left(\Pi_{12}^{T/L} - \Pi_{21}^{T/L}\right)\\ &= \mathrm{Re}\,\Pi_{11}^{T/L} \mp \frac{1}{2}\left(1-e^{P_0/T}\right)\Pi_{12}^{T/L},\end{aligned} \tag{6.103}$$

using $\mathrm{Im}\,\Pi_{11} = \frac{1}{2i}(\Pi_{12}+\Pi_{21})$ in the second equality and the KMS relation (6.58) in the last one. In particular, Eq. (6.103) implies that $\mathrm{Im}\,\Pi_R^{T/L} = -\mathrm{Im}\,\Pi_A^{T/L}$.

Given that $\Pi_{R,A}^{L/T} \overset{\mathrm{HTL}}{\approx} \mathrm{Re}\,\Pi_{11}^{L/T} \pm \frac{P^0}{2T}\Pi_{12}^{L/T}$ in the HTL limit, these results for the advanced and the retarded transverse photon self-energies in the HTL limit agree with Refs. [360, 396] apart from an opposite minus sign in the imaginary part due to the slightly different definition of the physical self-energies in Eq. (6.40).

It is noted in passing that the self-energy (6.101) leads to the unphysical process of photon decay $\gamma \to e^+e^-$ at high enough temperatures, where m_γ exceeds $2m_e$ [399]. In practice, this could be resolved by employing the dressed electron propagator. For the calculation of N_{eff} in Ch. 7, however, the relevant dynamics happen at temperatures much below that threshold, such that the resummation of the electron propagator for this reason is not necessary.

In Fig. 6.6, the finite-temperature contribution to the real and the imaginary parts of the retarded transverse and longitudinal propagators are displayed for $T = 2m_e$ and various choices of $|\mathbf{P}|/T$. The exact finite-temperature contribution to the real and the imaginary parts of the retarded transverse and longitudinal one-loop photon self-energy is compared in Fig. 6.6 numerically for $T = 2m_e$ and various choices of $|\mathbf{P}|/T$ to (i) the equivalent self-energy in the limit $m_e \to 0$, and (ii) the equivalent self-energy in the HTL limit. Similarly, in Fig. 6.7, the impact of the temperature on the photon self-energy is examined. It can be observed that the effect of the finite electron mass m_e, while small for large temperatures $T/m_e \sim 5$, remains sizeable for temperatures around $T/m_e \sim 2$ where neutrino decoupling occurs.

Another quantity of interest derived from the photon self-energy is the dispersion relation $P_0 = w(|\mathbf{P}|)$, i.e., solutions of the equation $P^2 + \mathrm{Re}\,\Pi_R^{T/L}(P) = 0$, which have to be obtained numerically and are shown for the $T = 2m_e$ benchmark in Fig. 6.8.

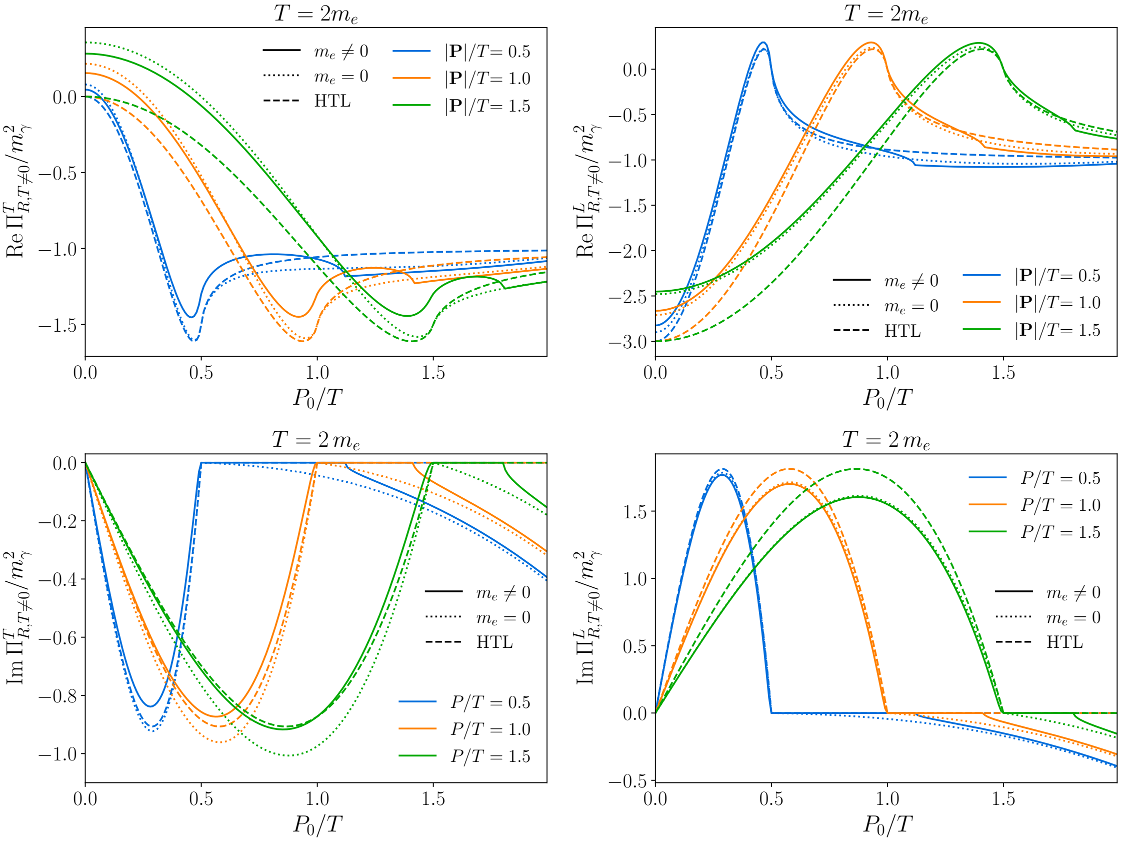

Figure 6.6: Comparison between the finite-temperature part of the retarded photon self-energy at the one-loop level with and without the HTL approximation at $T = 2m_e$ and for various choices of $|\mathbf{P}|/T$.

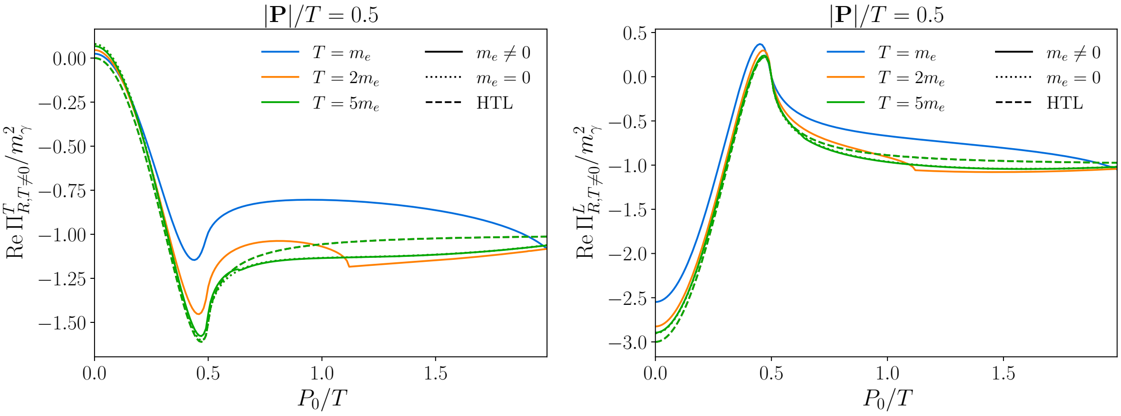

Figure 6.7: Comparison between the finite-temperature part of the retarded photon self-energy at the one-loop level with and without the HTL approximation for different temperatures $T \in \{m_e, 2m_e, 5m_e\}$ at a fixed $|\mathbf{P}|/T = 0.5$.

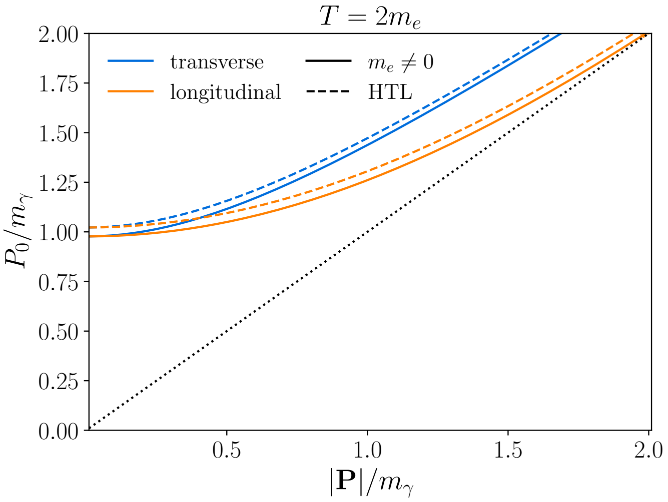

Figure 6.8: One-loop dispersion laws for transverse (blue lines) and longitudinal (orange lines) photons at $T = 2m_e$ with (continuous lines) and without (dashed lines) the HTL approximation. The black dotted line shows the dispersion relation at zero temperature, i.e., $P_0 = |\mathbf{P}|$.

Chapter 7

The Thermal Neutrino Interaction rate at NLO and Its Impact on $N_{\mathrm{eff}}^{\mathrm{SM}}$

While the previous sections dealt with precision calculations beyond the SM, the discussion shifts now towards a precision calculation *in* the SM based on Ref. [401], namely of the effective number of neutrinos N_{eff} whose primary role is to fix the universal expansion rate at $T \lesssim 1\,\mathrm{MeV}$ up to the end of the radiation-domination epoch, in particular since its observable consequences are many—from setting the primordial light element abundances, to influencing the correlation statistics of the CMB anisotropies and the large-scale matter distribution, pinning down its value both theoretically and observationally has enjoyed an unwavering interest for over four decades [17, 402]. This is reinforced by the fact that many BSM scenarios predict N_{eff}-like effects (e.g., light sterile neutrinos [403, 404], axions [405, 406], gravitational waves [407], hidden sectors [408, 409], etc.).

From a theoretical perspective, as shown in Sec. 2.5, the expected value of N_{eff} in the context of the SM of particle physics is under the most restrictive assumptions 3, for the three neutrino flavors. The value receives percent-level corrections due to residual energy transfer between the QED plasma and the neutrino sector during neutrino decoupling [336, 410–414] as well as deviations of the QED plasma itself from an ideal gas [415–420]. Historical estimates of these corrections have ranged from 0.011 to 0.052 [411, 421–424]. Detailed modeling [339, 425–427] over the last five years, however, have significantly narrowed the range. The current state-of-the-art prediction is $N_{\mathrm{eff}}^{\mathrm{SM}} = 3.0440 \pm 0.0002$ from a fully momentum-dependent transport calculation that includes (i) neutrino oscillations, (ii) finite-temperature corrections to the QED equation of state to $\mathcal{O}(e^3)$, and (iii) a first estimate of finite-temperature corrections due to thermal mass shifts in the weak interaction rates. The effects of the different contributions are summarized in Tab. 7.1. In particular, the uncertainty of $N_{\mathrm{eff}}^{\mathrm{SM}}$ is primarily attributed to discretization errors and uncertainties in the measured neutrino mixing angles. Impressively, this result aligns perfectly with the independent calculation of Ref. [426] which models the same physics to five significant digits in the central value and with a similar error margin. Thus, the accurate calculation of $N_{\mathrm{eff}}^{\mathrm{SM}}$ seems to have reached convergence, albeit in a limited sense.

There are, however, reasons to be cautious since as of yet missing is a systematic study of possible higher-order corrections to the weak rates that may be at least equally important. This means that the computations [426, 427] are, at least conceptually, incomplete. The two works [428, 429] have

Standard-model corrections to $N_{\text{eff}}^{\text{SM}}$	Leading-digit contribution
m_e/T_d correction	$+0.04$
$\mathcal{O}(e^2)$ FTQED correction to the QED EoS	$+0.01$
Non-instantaneous decoupling+spectral distortion	-0.006
$\mathcal{O}(e^3)$ FTQED correction to the QED EoS	-0.001
Flavor oscillations	$+0.0005$
Thermal mass corrections to the weak rates	$\lesssim 10^{-4}$
Sources of uncertainty	
Numerical solution by FortEPiaNO	± 0.0001
Input solar neutrino mixing angle θ_{12}	± 0.0001

Table 7.1: Leading-digit contributions from various SM corrections, in order of importance, thus far accounted that make up the final $N_{\text{eff}}^{\text{SM}} - 3 = 0.0440 \pm 0.0002$ [426, 427].

taken a first step towards filling this gap by considering the next-to-leading order corrections in finite-temperature QED to the neutrino interaction rate. Ref. [428] took the rate corrections for $e^+e^- \to \nu_\alpha \bar{\nu}_\alpha$ from [430], computed originally in the context of energy loss in a stellar plasma within the real-time formalism, but neglects (i) corrections to elastic scattering reactions like $\nu_\alpha e \to \nu_\alpha e$, (ii) Pauli blocking effects, as well as (iii) corrections due to the diagram in Fig. 7.2d (the "closed fermion loop"), claiming in the end a quite substantial correction to $N_{\text{eff}}^{\text{SM}}$ at the ~ 0.001 level. The neglect of the diagram containing the closed fermion loop is particularly worrisome, since it contains a t-channel enhancement, and should therefore, at least naïvely, dominate the rate correction. In contrast, Ref. [429] considered all diagrams in the imaginary-time formalism of thermal field theory along with hadronic corrections to the diagram in Fig. 7.2d but assumed a negligible electron mass by setting $m_e = 0$, even though this is not necessitated by the formalism. The final result is stated as corrections to the thermal neutrino interaction rate. While Ref. [429] confirms the expected t-channel enhancement and does not report the corresponding change in $N_{\text{eff}}^{\text{SM}}$, the corrections to the rate are found to be of order 0.2 to 0.3 % such that it is clear that corrections of this magnitude cannot effect a shift in N_{eff} as sizable as that claimed in Ref. [428]. As Ref. [429] employs the imaginary-time formalism, that only applies to equilibrium systems, the generalization of the computation to nonequilibrium neutrino phase space distributions is rather difficult.

The purpose of this chapter is therefore to clarify whether or not QED corrections to the neutrino interaction rate can alter the Standard Model $N_{\text{eff}}^{\text{SM}}$ at the ~ 0.001 level. Although this correction is small compared to the expected sensitivity of the upcoming CMB-S4 program to N_{eff}, $\sigma(N_{\text{eff}}) \simeq 0.02 - 0.03$ [346], having a precise theoretical prediction for $N_{\text{eff}}^{\text{SM}}$ with per-mille level accuracy is still important to justify ignoring the theoretical uncertainty in cosmological parameter inference. In contrast to Ref. [429] this calculation is performed in the closed time path formalism reviewd in Ch. 6 which automatically takes care of both vacuum and finite-temperature corrections like the imaginary-time formalism but has the advantage that it can easily be extended to nonequilibrium situations [357, 431], while in equilibrium situations the two formalisms are exactly equivalent [392]. This aspect is important to pave the way for incorporating NLO effects into neutrino decoupling codes such as FortEPiaNNO [339]. For the purpose of estimating the neutrino interaction rate, however, the same equilibrium conditions as in Ref. [429] are assumed. In addition, a finite electron mass m_e is retained as the $m_e = 0$ approximation made in Ref. [429] is not well justified in the vicinity of neutrino decoupling happening at temperatures $T \sim 1\,\mathrm{MeV}$. It should also be immensely stressed that in contrast to vacuum field theory, NLO calculations in the closed time path formalism are still in their early stages, since there is, e.g., so far no KLN-like theorem guaranteeing an infrared finite result or numerical libraries for "thermal" integrals of the type calculated in Sec. 6.4 resembling the by now well-known Passarino-Veltmann integrals from Sec. 4.2.2. However, first approaches towards full NLO calculations in the real-time formalism have been undertaken in the context of stellar physics [430], leptogenesis [368, 374] and dark matter [97, 98, 381].

This chapter is organized as follows. In Sec. 7.1 the ingredients going into the current $N_{\text{eff}}^{\text{SM}}$ state-of-the-art prediction are sketched. Section 7.2 shows how the thermal neutrino interaction rate can be defined in the real-time formalism while Sec. 7.3 contains the derivation of the neutrino-electron interaction according to an effective Fermi theory. Section 7.4 deals with the calculation of the leading order rate while Sec. 7.5 outlines the computation of QED corrections to the neutrino damping rate due to the t-channel enhanced diagram. The shift in $N_{\text{eff}}^{\text{SM}}$ due to these corrections is presented in Sec. 7.6, and Sec. 7.7 contains the conclusions.

7.1 State of the Art $N_{\text{eff}}^{\text{SM}}$ Calculation

The precision calculation of $N_{\text{eff}}^{\text{SM}}$ requires to track the evolution of the neutrino and photon energy densities, ρ_ν and ρ_γ, simultaneously across the time frame of neutrino decoupling, i.e., across photon temperatures $T \sim \mathcal{O}(10) \to \mathcal{O}(0.01)$ MeV. This is generally accomplished by solving two sets of evolution equations: (i) a continuity equation that tracks the total energy density of the Universe, and (ii) a generalized Boltzmann equation—commonly known as the quantum kinetic equations (QKEs)—which describe the nonequilibrium behavior in the neutrino sector during the decoupling process.

Continuity Equation At the time of neutrino decoupling, the total energy density and the total pressure in the continuity equation (2.6) are given by $\rho = \rho_{\text{QED}} + \rho_\nu$ and $P = P_{\text{QED}} + P_\nu$, where $\rho_{\text{QED}} = \rho_\gamma + \rho_e$ subsumes the photon and the electron/positron energy densities, and similarly for P_{QED}. The QED sector can be safely assumed to be in a state of thermodynamic equilibrium in the time frame of interest meaning that the standard thermodynamic relation $\rho_{\text{QED}} = -P_{\text{QED}} + T\,(\partial/\partial T)P_{\text{QED}}$ applies. Then, the finite-temperature corrections to the QED equation of state summarized in Tab. 7.1 can be simply implemented as corrections to the QED partition function Z_{QED} and hence $P_{\text{QED}} = (T/V)\ln Z_{\text{QED}}$ that alter $\rho_{\text{QED}} + P_{\text{QED}} = T\,(\partial/\partial T)P_{\text{QED}}$ from its ideal-gas value. Corrections to Z_{QED} are known to $\mathcal{O}(e^3)$ for arbitrary m_e and chemical potential μ [432] and to $\mathcal{O}(e^5)$ for vanishing electron mass and chemical potential [433, 434]. In Refs. [416, 419, 420] their effects on $N_{\text{eff}}^{\text{SM}}$ have been estimated up to $\mathcal{O}(e^4)$.

Quantum Kinetic Equations To account for neutrino oscillations, state of the art neutrino decoupling calculations are formulated on the level of the one-particle reduced density matrix of the neutrino ensemble, $\varrho = \varrho(p,t)$. In terms of this matrix, the quantum kinetic equations take schematically the form [435]

$$\partial_t \varrho - pH\partial_p \varrho = -\mathrm{i}[\mathbb{H}, \varrho] + \mathcal{I}[\varrho]\,, \tag{7.1}$$

where the effective Hamiltonian $\mathbb{H} = \mathbb{H}(p,t) = \mathbb{H}_{\text{vac}} + \mathbb{V}$ incorporates vacuum flavor oscillations through $\mathbb{H}_{\text{vac}}$ and in-medium corrections from forward scattering trough $\mathbb{V}$. Depending on context, these modifications to the in-medium quasiparticle dispersion relations are known as thermal masses, matter potentials or refractive indices. At the current level of precision [427],

$$\mathcal{I}[\varrho] = \frac{1}{2}\Big((\mathbb{1} - \varrho)\mathbb{\Gamma}^{<}(p,t) - \varrho\,\mathbb{\Gamma}^{>}(p,t)\Big) + \text{h.c.} \tag{7.2}$$

is nothing but the semi-classical collision term from Eq. (2.12) encapsulating the non-unitary gains $\mathbb{\Gamma}^{<}$ and losses $\mathbb{\Gamma}^{>}$ of ϱ from weak $2 \to 2$ tree-level scattering processes wherein at least one neutrino appears in either the initial or final state. More precisely, $\mathcal{I}[\varrho]$ contains the processes involving (i) two neutrinos and two electrons any way distributed in the initial and final states, and (ii) neutrino-neutrino scattering. The leading-order $\mathbb{\Gamma}^{\gtrless}$ for these processes are well known, see, e.g., Ref. [411], and take the form of the two-dimensional momentum integral (B.12) already encountered within dark matter annihilation in Ch. 5. Within the Standard Model, the quantities ϱ, $\mathbb{H}$, and $\mathbb{\Gamma}^{\gtrless}$ can be seen as 3×3 hermitian matrices in flavor space, with the diagonal entries of ϱ corresponding to the phase space distribution functions $f_\alpha(p,t) \equiv \{\varrho(p,t)\}_{\alpha\alpha}$ with $\alpha = e, \mu, \tau$ denoting the neutrino flavor. Strictly speaking, this identification is only valid in the basis in which $\mathbb{H}$ is diagonal, i.e., in the mass basis, rather than the interaction basis. However, this distinction is unimportant for estimating the neutrino decoupling temperature, and therefore, in accordance with common practice, $\{\varrho(p,t)\}_{ee}$ is referred to as the electron neutrino phase space distribution function in the following and so on. Under the assumption of a CP-symmetric Universe, which is well justified if the lepton sector mirrors the baryon asymmetry in the observable Universe [436], it is sufficient to consider only one set of QKEs for neutrinos since the corresponding antineutrinos evolve identically.

The current benchmark $N_{\text{eff}}^{\text{SM}} = 3.0440 \pm 0.0002$ was then obtained with the purpose-built neutrino decoupling code FortEPiaNNO [339, 427], which solves numerically the continuity equation (2.6) and the three-flavor QKEs (7.1) in their entirety.

7.2 The Thermal Neutrino Interaction Rate in the Real-Time Formalism

In the framework of the real-time formalism and without neutrino oscillations, i.e., $\Gamma_\alpha^{\gtrless} = \mathbb{\Gamma}_{\alpha\alpha}^{\gtrless}$, the kinetic equation (7.1) is obtained from the gradient expanded Kadanoff-Baym equation (6.69). This means that the production $\Gamma_\alpha^{<}$ and destruction rates $\Gamma_\alpha^{>}$ at the momentum p can be extracted from the α-flavored neutrino self-energies $\Sigma_\alpha^{\gtrless}$ via

$$\Gamma_\alpha^{\gtrless}(p) = \mp\frac{1}{2p^0}\,\mathrm{Tr}\left[-i\Sigma_\alpha^{\gtrless}\not{p}\right]\Big|_{p^0 = |\mathbf{p}|}\,. \tag{7.3}$$

For completeness, the neutrino distribution function $f_\alpha(p)$ belonging to ν_α follows then the generalized Boltzmann equation

$$\frac{\mathrm{d}f_\alpha(p)}{\mathrm{d}t} = [1 - f_\alpha(p)]\Gamma^<_\alpha(p) - f_\alpha(p)\Gamma^>_\alpha(p)\,. \tag{7.4}$$

The usual diffusion term in a FLRW background on the right-hand side of Eq. (7.1) involving the Hubble rate is recovered in Eq. (7.4) by recalling that p corresponds to the physical momentum from Eq. (2.8). The total thermal neutrino interaction rate is then given by the sum $\Gamma_\alpha = \Gamma^>_\alpha(p) + \Gamma^<_\alpha(p)$. In thermal equilibrium, detailed balance is established by the KMS relation (6.70) such that the mode-dependent interactino rate can also be written as

$$\Gamma_\alpha(p) = \frac{1}{2p^0}\,\mathrm{Tr}\left[-i(\Sigma^<_\alpha - \Sigma^>_\alpha)\not{p}\right]\Big|_{p^0=E_p} = \frac{1}{2p^0 f_D(p^0)}\,\mathrm{Tr}\left[-i\Sigma^<_\alpha\not{p}\right]\Big|_{p^0=E_p}\,. \tag{7.5}$$

The first equality follows also from the fact that Γ_α can be related to the discontinuity of the retarded neutrino self-energy evaluated at the quasiparticle pole, $-\mathrm{disc}\, i\Sigma^R_\alpha = 2\,\mathrm{Im}\Sigma^R_\alpha = i(\Sigma^<_\alpha - \Sigma^>_\alpha)$, in accordance with the optical theorem at finite temperature. While the KMS relation makes explicit use of the fact that the $\Sigma^{\gtrless}_\alpha$ are computed in thermal equilibrium, Eq. (7.3) coupled with Eq. (7.4) extends to to nonequilibrium situations in a straightforward manner [431]. More specifically, this involves substituting the equilibrium distribution in Eq. (6.63) between the statistical and spectral propagators with a dynamical function, and adjusting all other propagators correspondingly. For further discussion, see, e.g., Refs. [373, 437]. Where there is no confusion, the flavor index α is dropped in the following.

7.3 The Effective Lagrangian in Fermi Theory

To compute the QED corrections to the weak processes $\nu_\alpha e \leftrightarrow \nu_\alpha e$ and $\nu_\alpha\bar{\nu}_\alpha \leftrightarrow e^+e^-$ at temperatures of $\mathcal{O}(\mathrm{MeV})$, it is adequate to work in the Fermi limit where the weak bosons decouple. To arrive at the effective Lagrangian, one can write down the corresponding amplitudes according to the Feynman rules of the weak interaction which can, e.g., be found in Ref. [438]. After neglecting the propagator momentum and replacing the $\mathrm{SU}(2)_L$ coupling g through the Fermi constant $G_F = \frac{\sqrt{2}}{8}\frac{g^2}{m_W^2}$ with the W-mass $m_W = m_Z\cos\theta_W$, one obtains

$$\mathcal{M}_Z = i\left(G_F\frac{4}{\sqrt{2}}\right)\left[\bar{\psi}_\alpha\gamma^\mu P_L\psi_\alpha\right]\left[\bar{\psi}_e\gamma_\mu(P_L\tilde{g}_L + P_R g_R)\psi_e\right]\,, \tag{7.6a}$$

$$\mathcal{M}_W = i\left(G_F\frac{4}{\sqrt{2}}\right)\delta^{\alpha e}\left[\bar{\psi}_\alpha\gamma^\mu P_L\psi_e\right]\left[\bar{\psi}_e\gamma_\mu P_L\psi_\alpha\right] \tag{7.6b}$$

with the first one being the charged current contribution coming from the exchange of a W-boson; the second one being the neutral current part from a Z as intermediate state; the couplings $\tilde{g}_L = -\frac{1}{2} + \sin^2\theta_W$ and $g_R = \sin^2\theta_W$. These two amplitudes can be combined in the sum $\mathcal{M}_{4F} = \mathcal{M}_Z + \mathcal{M}_W$ by using the Fierz identity [439]

$$\left[\bar{\psi}_1\gamma^\mu P_L\psi_2\right]\left[\bar{\psi}_3\gamma_\mu P_L\psi_4\right] = \left[\bar{\psi}_1\gamma^\mu P_L\psi_4\right]\left[\bar{\psi}_3\gamma_\mu P_L\psi_2\right] \tag{7.7}$$

involving the four arbitrary spinors ψ_i such that one can immediately read off the effective four-fermion Lagrangian and write it as

$$\mathcal{L}_{4\mathrm{F}} = \frac{4G_F}{\sqrt{2}} \left[\bar{\psi}_\alpha \gamma_\mu P_L \psi_\alpha\right] \left[g_L^\alpha J_L^\mu + g_R J_R^\mu\right] . \tag{7.8}$$

This combination yields the flavor-dependent left-handed coupling $g_L^\alpha = \tilde{g}_L + \delta^{\alpha e}$ and $J^\mu_{L/R} = \bar{\psi}_e \gamma^\mu P_{L/R} \psi_e$ are the left- and right-handed electron current operators. The interaction of neutrinos with quarks is also well described by a Lagrangian of the form (7.8), with the couplings g_L^α and g_R updated for the quarks of interest. However, for the purpose of calculating the thermal neutrino interaction rate one can safely omit the contributions from free quarks as at the $\mathcal{O}(1\,\mathrm{MeV})$ temperatures of interest these contributions are Boltzmann-suppressed. Hadronic effect are in principle relevant and could be included through appropriate Wilson coefficients, see, e.g., Ref. [440]. As QED is a vector-like theory, it is convenient to additionally introduce the vector-axial couplings

$$g^\alpha_{V,A} = \frac{1}{2}(g_L^\alpha \pm g_R) \tag{7.9}$$

as an alternative notation.

7.4 The Leading Order Rate

The leading order contribution to the thermal neutrino interaction rate in Fermi theory is given by the two-loop neutrino self-energy shown in Fig. 7.1 which will be evaluated in the following and allows to estimate the leading order neutrino decoupling temperature.

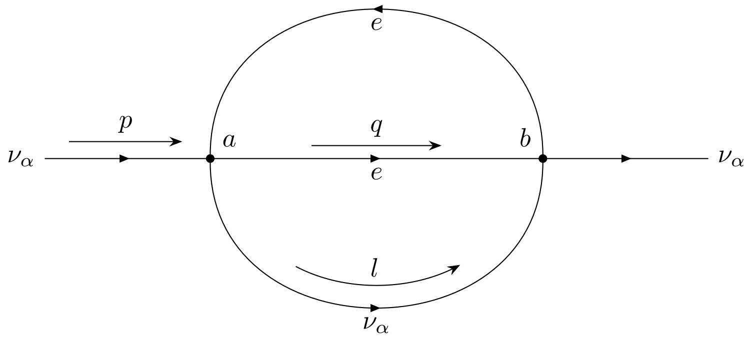

Figure 7.1: Leading order neutrino-self energy in Fermi theory. Labeled are the momenta (p, q and l), real-time labels (a and b) and particles (e and ν_α)

According to the effective neutrino-electron interaction Lagrangian (7.8), the graph in Fig. 7.1 evaluates to

$$\begin{aligned}\mathrm{Tr}\left[i\Sigma^{ba}_{(\mathrm{LO})}\not{p}\right] = (-1)^{a+b}\left(\frac{4G_F}{\sqrt{2}}\right)^2 \int \frac{\mathrm{d}^4 l}{(2\pi)^4}\frac{\mathrm{d}^4 q}{(2\pi)^4} \mathrm{Tr}\left[\not{p}\gamma^\rho P_L i S^{ba}_{\nu_\alpha}(l)\gamma^\sigma P_L\right] \\ \times \mathrm{Tr}\left[iS_e^{ba}(p+q-l)\gamma_\sigma(P_L g_L^\alpha + P_R g_R) i S_e^{ab}(q)\gamma_\rho(P_L g_L^\alpha + P_R g_R)\right] ,\end{aligned} \tag{7.10}$$

where the traces are over the Clifford algebra and the definitions of the thermal propagators can be found in Sec. 6.1.5. As the interaction rate (7.5) is given by $\Sigma^<_\alpha$, the external contour indices are set to $a = 2$ and $b = 1$. The generalized Boltzmann equation (7.4) suggests that the self-energy in Eq. (7.10) can be brought into the form of the semi-classical Boltzmann collision integral in Eq. (2.12). To do so, the four-momenta p, l, q in Fig. 7.1 are first identified with the momenta p_1, p_2, p_3, p_4 of the external neutrinos and electrons of the underlying $2 \to 2$ process via the reassignments

$$p_1 = p, \qquad p_2 = -l, \qquad p_3 = q + p - l, \qquad p_4 = -q. \tag{7.11}$$

Then, writing out the propagators $iS_e^{12/21}$ and $iS_\nu^{12/21}$ explicitly, the self-energy (7.10) can be brought into the form

$$\begin{aligned}\mathrm{Tr}\left[i\Sigma^<_{(\mathrm{LO})}\not{p}\right] = -\int \frac{\mathrm{d}^4 p_2}{(2\pi)^3}\frac{\mathrm{d}^4 p_3}{(2\pi)^3}\frac{\mathrm{d}^4 p_4}{(2\pi)^3}\,\delta(p_2^2)\,\delta(p_3^2 - m_e^2)\,\delta(p_4^2 - m_e^2)&\\ \times (2\pi)^4 \delta^{(4)}(p_1 + p_2 - p_3 - p_4)\,\mathcal{F}(p_2^0, p_3^0, p_4^0)\,\mathcal{T}_{\mathrm{LO}}(p_1, p_2, p_3, p_4)\,.&\end{aligned} \tag{7.12}$$

The equilibrium phase space distributions of the three integrated external particles are contained in the population factor

$$\mathcal{F}(p_2^0, p_3^0, p_4^0) = \left[f_D(|p_2^0|) - \Theta(p_2^0)\right]\left[f_D(|p_3^0|) - \Theta(-p_3^0)\right]\left[f_D(|p_4^0|) - \Theta(-p_4^0)\right] \tag{7.13}$$

and the remaining piece coming from the traces over the γ-matrices given by

$$\mathcal{T}_{\mathrm{LO}}(p_1, p_2, p_3, p_4) = 2^7 G_F^2 \left[(g_L^\alpha)^2\,(p_1 \cdot p_4)^2 + g_R^2\,(p_2 \cdot p_4)^2 + g_L^\alpha g_R m_e^2\,(p_1 \cdot p_2)\right] \tag{7.14}$$

is nothing but the squared matrix element $|\mathcal{M}_{4F}|^2$ from Eq. (7.6) summed over all spin configurations. Therefore, the real-time formalism reproduces at $\mathcal{O}\big(\alpha_{\mathrm{em}}^0\big)$ exactly the standard semi-classical Boltzmann collision term. Their equivalence has also been demonstrated in Ref. [420] in the full electroweak theory.

7.5 The Rate at NLO

At next-to-leading order in the electromagnetic coupling, the four diagrams in Fig. 7.2 contribute to the thermal neutrino interaction rate. The dominant QED correction to Γ_α is expected to come from the diagram in Fig. 7.2d in the regime where the photon propagator is on-shell due to the resulting t-channel enhancement. This expectation has been confirmed in Ref. [429].

7.5.1 Evaluation of the Closed Fermion Loop

As only the last diagram is computed, the corresponding self-energy is simply denoted with $\Sigma^{ba}_{(\mathrm{NLO})}$. For notational convenience, $\Sigma^{ba}_{(\mathrm{NLO})}$ is further split into the sum $\Sigma^{ba}_{(\mathrm{NLO})} = \sum_{c,d=1,2} \Sigma^{ba,cd}$ over the internal real-time indices c and d. The partial self-energies $\Sigma^{ba,cd}$ are then given by

$$\mathrm{Tr}\left[i\Sigma^{ba,cd}\not{p}\right] = (-1)^{a+b+c+d}(ie)^2\left(\frac{i4G_F}{\sqrt{2}}\right)^2$$

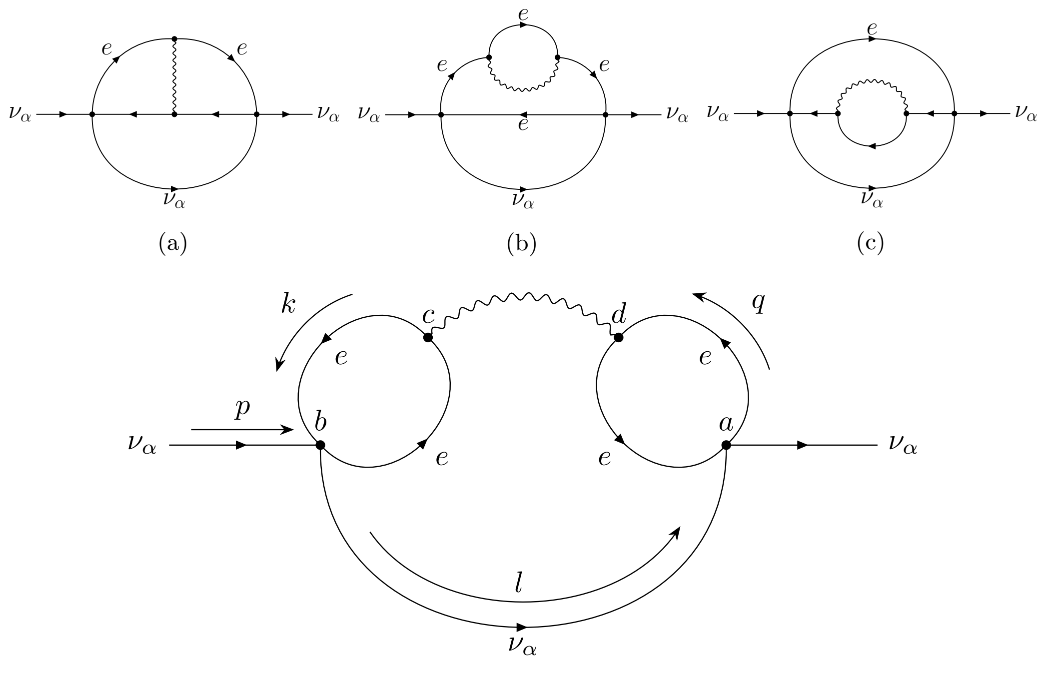

(a) (b) (c)

(d)

Figure 7.2: The three-loop neutrino self-energies containing the $\mathcal{O}(e^2)$ QED corrections to the thermal neutrino interaction rate. For the last diagram with the closed fermion loops, explicitly labeled are the external (a and b) and summed (c and d) real-time contour indices and the momenta (k, l, p and q) whereas particles (e and ν_α) are labeled in all diagrams.

$$\begin{aligned}\times \int \frac{\mathrm{d}^4 l}{(2\pi)^4}\frac{\mathrm{d}^4 q}{(2\pi)^4}\frac{\mathrm{d}^4 k}{(2\pi)^4}\mathrm{Tr}\left[iS_e^{ad}(q)\gamma_\rho(P_L g_L^\alpha + P_R g_R) iS_e^{da}(q+p-l)\gamma^\mu\right] iD^{cd}_{\mu\nu}(p-l)\\ \times \mathrm{Tr}\left[\not{p}\gamma^\rho P_L iS_\alpha^{ba}(l)\gamma^\sigma P_L\right]\mathrm{Tr}\left[iS_e^{cb}(k)\gamma^\nu iS_e^{bc}(k+p-l)\gamma_\sigma(P_L g_L^\alpha + P_R g_R)\right]. \quad (7.15)\end{aligned}$$

Again, only $\Sigma^{12}_{(\mathrm{NLO})}$ is needed for the equilibrium interaction rate (7.5). Then, the contributions $\mathrm{Tr}\left[i\Sigma^{12,21}\not{p}\right]$ and $\mathrm{Tr}\left[i\Sigma^{12,12}\not{p}\right]$, which correspond to setting both the photon and neutrino lines on-shell, vanish by momentum conservation (see also footnote 1). Of the remaining "11" and "22" contributions, the transformation behavior of the thermal propagators under hermitian conjugation dictates that $\mathrm{Tr}\left[i\Sigma^{12,11}\not{p}\right] = \mathrm{Tr}\left[i\Sigma^{12,22}\not{p}\right]^*$. It then follows that the NLO interaction rate from the diagram in Fig. 7.2d can be determined entirely through the real part of the diagonal "11" contribution, i.e.,

$$\mathrm{Tr}\left[i\Sigma^{12}_{(\mathrm{NLO})}\not{p}\right] = 2\mathrm{Re}\,\mathrm{Tr}\left[i\Sigma^{12,11}\not{p}\right]. \quad (7.16)$$

Using the same momentum reassignments as in Eq. (7.11), one finds that Eq. (7.16) can be brought in the same form as the leading order self-energy (7.12) with $\mathcal{T}_{\mathrm{LO}}$ replaced by the quantity $\mathcal{T}_{\mathrm{NLO}}$ which plays the role of the QED corrections to the LO squared matrix element and contains the remaining loop integral over k. It can be stated in terms of the thermal one-loop photon self-energy $\Pi^{\mu\nu}_{ab}$ calculated in Sec. 6.5 as

$$\mathcal{T}_{\mathrm{NLO}} = -16G_F^2 g_V^\alpha \mathrm{Re}\Big\{\mathrm{Tr}\left[(\not{p}_3 + m_e)\gamma^\mu\ (m_e - \not{p}_4)\gamma^\rho\,(g_L^\alpha P_L + g_R P_R)\right]$$

$$\times \mathrm{Tr}\left[\not{p}_1\gamma_\rho P_L \not{p}_2 \gamma_\sigma P_L\right] D^{11}_{\mu\nu}(P)\Pi^{\nu\sigma}_{11}(P)\Big\}\,, \tag{7.17}$$

where the photon momentum gets the additional label $P = p_1 + p_2$.

Since $\mathcal{T}_{\rm NLO}$ has the interpretation of a squared matrix element, one can split it into a vacuum and a thermal part according to their temperature dependence,

$$\mathcal{T}_{\rm NLO} = \mathcal{T}_{\rm vac} + \mathcal{T}_{\rm th}. \tag{7.18}$$

The vacuum virtual correction $\mathcal{T}_{\rm vac}$ can be recovered from a cut through one closed electron loop and the internal neutrino line and has no intrinsic temperature dependence in the sense that it makes no explicit reference to the temperature or to any phase space distribution. It is simply the correction to the weak matrix elements arising from the interference of the closed fermion loop diagram shown in Fig. 7.3 with the LO graph in standard $T = 0$ quantum field theory, and can be expressed in terms of the vacuum photon self-energy as

$$\mathcal{T}_{\rm vac} = -2^{10} G_F^2\, \alpha_{\rm em}\,[(g_V^\alpha)^2/(4\pi)]\left[m_e^2(p_1\cdot p_2) + 2(p_1\cdot p_4)^2\right] \mathrm{Re}\,\Pi_2(P^2)\,, \tag{7.19}$$

where the form factor Π_2 is defined in Eq. (6.94). The simplicity of the expression follows from the fact that the integration domain is symmetric under the exchange $p_3 \leftrightarrow p_4$. This symmetry, along with momentum conservation, also ensures the absence of all antisymmetric terms containing Levi-Civita symbols. The vacuum QED corrections to the neutrino-electron scattering cross section were also previously computed in Ref. [441].

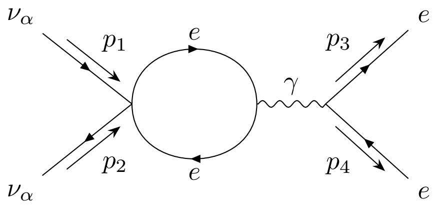

Figure 7.3: The "closed fermion loop" vacuum correction.

The thermal correction $\mathcal{T}_{\rm th}$, on the other hand, can be thought of as a temperature-dependent correction to the squared matrix element as it depends explicitly on equilibrium phase space distribution, f_D or f_B, of the internal particles. These originate in the thermal "11" part of the tree-level propagators containing a Dirac δ-function along with the corresponding distribution function and, where this part is applied, effectively puts an internal line of the closed fermion loop diagram in Fig. 7.3 on-shell. Purely from counting, there are altogether seven possible ways to put one, two, or all three internal lines of the diagram in Fig. 7.3 on-shell. However, not all combinations contribute to $\mathcal{T}_{\rm NLO}$: The terms proportional to the Bose distribution f_B correspond to putting the photon line on-shell, which are forbidden for kinematic reasons [399, 442]. Similarly, putting both internal electrons on-shell leads to a purely imaginary contribution that is irrelevant to the real part of the self-energy required for the neutrino interaction rate. The only surviving two combinations correspond to putting either internal electron line on-shell, and are proportional to $f_D(|k^0|)$ and $f_D(|k^0 + P^0|)$ respectively.

Importantly, the t-channel contribution from elastic $\nu_\alpha e$ scattering in $\mathcal{T}_{\rm NLO}$, i.e., if $p_2^0 < 0$, is logarithmically divergent for soft photon momenta. This divergence comes from the fact that the finite-temperature photon self-energy scales not as P^2 like in vacuum, but as T^2 in the HTL limit which do not compensate anymore for the $1/P^2$ behavior of the photon propagator. In addition, soft photons are Bose-enhanced. To remedy the problem, the tree-level photon propagator $D^{cd}_{\mu\nu}$ in

Eq. (7.17) is replaced with the fully-resummed photon propagator $\bar{D}^{ab}_{\mu\nu}$.[1] Furthermore, because both $\bar{D}^{ab}_{\mu\nu}$ and $\Pi^{\nu\sigma}_{11}$ split into a longitudinal ("L") and a transverse ("T") part, the same decomposition applies also to $\mathcal{T}_{\rm th}$, i.e., $\mathcal{T}_{\rm th} = \mathcal{T}^{L}_{\rm th} + \mathcal{T}^{T}_{\rm th}$, where $\mathcal{T}^{L,T}_{\rm th}$ can be brought into the form

$$\begin{aligned}\mathcal{T}^{L/T}_{\rm th} = -2^8 G_F^2 (g_V^\alpha)^2 \mathrm{Re}\, \bar{D}^{L/T}_R(P) \mathrm{Re}\, \Pi^{L/T}_{R,T\neq 0}(P) \Big[2(p_1 \cdot p_4) P^{1,4}_{L/T} \\ + (p_1 \cdot p_2)(a_{L/T}(p_1 \cdot p_2) + P^{2,2}_{L,T} + P^{4,4}_{L/T}) \Big] . \quad (7.20)\end{aligned}$$

Here, $\bar{D}_R$ denotes the retarded resummed photon propagator; $\Pi_{R,T\neq 0}$ is the retarded thermal photon self-energy comprising the $f_D(|k^0|)$ and $f_D(|k^0 + P^0|)$ terms described above; the shorthand notation $P^{i,j}_{L/T} = P^{\mu\nu}_{L/T} p_{i,\mu} p_{j,\nu}$; and $a_{L,T} = (3 \mp 1)/4$ further differentiates between the longitudinal and the transverse contribution.

Note that the imaginary part of the photon propagator, $\mathrm{Im}\, \bar{D}^{L,T}_{11}$, does not appear in Eq. (7.20) because it is formally of higher-order in $\alpha_{\rm em}$ and we only compute the $\mathcal{O}(\alpha_{\rm em})$ corrections. The resummed photon propagator is only used in the IR divergent t-channel contribution; where the divergence is absent, i.e., in the s-channel $\bar{D}_R \to D_R$ is set, where D_R is the un-resummed counterpart of $\bar{D}_R$. In addition, note that the vacuum contribution (6.94) to the photon self-energy is numerically irrelevant for the resummed photon propagator, since it vanishes in the soft photon exchange limit $P^2 \to 0$, and is therefore discarded in the resummed phton propagator. The final expressions for $\mathrm{Re}\, \Pi^{L/T}_{11,T\neq 0}$ and $\mathrm{Re}\, \bar{D}^{L/T}_{11}$ are given in equations (6.96b), (6.97b) and (6.79a), which can be easily mapped to $\mathrm{Re}\, \Pi^{L/T}_{R,T\neq 0}$ and $\mathrm{Re}\, \bar{D}_R$ via $\mathrm{Re}\, \bar{D}^{L/T}_R = \mathrm{Re}\, \bar{D}^{L/T}_{11}$ and $\mathrm{Re}\, \Pi^{L/T}_R = \mathrm{Re}\, \Pi^{L/T}_{11}$.

7.5.2 Numerical Results for the NLO Rate and $T_{d(\alpha)}$

The evaluation of the self-energy (7.12) for both the LO rate as well as the corresponding correction and hence the neutrino interaction rate (7.5) is performed by parametrizing the momentum integrals following App. B.1.1. Given that the the leading order matrix element (7.14) as well as the NLO contributions (7.19) and (7.20) are a quadratic polynomial in the angle $z = \cos\alpha$ between $\mathbf{p}_1$ and $\mathbf{p}_2$, the integration over z can be performed analytically following the strategy outlined in App. B.1.1. In all cases, the remaining three integrals are calculated numerically by using the Cuhre algorithm for multi-dimensional integration from the CUBA-4.2.2 [277] library. To guarantee the reproduciblity of these results it makes sense to report the input parameter values. These are set to the experimentally-determined values reported by the Particle Data Group [317]:

- Fermi's constant: $G_F = 1.166\,378\,8(6)\,\mathrm{MeV}^{-2}$,
- Electron mass: $m_e = 0.510\,998\,950\,00(15)\,\mathrm{MeV}$,
- Electromagnetic fine-structure constant: $\alpha^{-1}_{\rm em}(0) = 137.035\,999\,180(10)$, and
- Weinberg angle: $\sin^2\theta_W(0)_{\overline{\rm MS}} = 0.238\,63(5)$.

The renormalization scale μ_R appearing in the photon self-energy of the vacuum contribution is identified with the electron mass, $\mu_R = m_e$. In addition, the results are cross checked using the

---

[1] Resumming the photon propagator opens up an additional cut through the photon and the internal neutrino lines, corresponding to the so-called plasmon process $\gamma \to \nu\bar{\nu}$, even if the imaginary part of the photon self-energy is neglected. This can be seen in Eq. (6.79a), which exhibits an on-shell δ-function in the limit of vanishing width (6.80b). However, the plasmon process contributes at $\mathcal{O}(\alpha^2_{\rm em})$ [399], which can be understood as a phase space suppression from $m_\gamma \sim \alpha_{\rm em} T$ and is therefore not included.

alternative phase space parametrization presented in App. B.1.2 which is found to converge about 100 times faster than the one from App. B.1.1 for the tree-level result but hardly converges for the NLO rate.

Figure 7.4 shows the closed fermion loop corrections to the damping rates $\Gamma_e(p)$ and $\Gamma_{\mu,\tau}(p)$ at the mean momentum $p = 3.15T$. Relative to their respective LO rates, the corrections at temperatures $T \sim 1 \to 3$ MeV fall in the range $-0.2 \to +0.1\%$ and $-0.0005 \to +0.0002\%$, respectively, for ν_e and $\nu_{\mu,\tau}$. It should also be noted that:

1. At $T \sim 2\,\text{MeV}$, the vacuum and the thermal contributions to the correction are roughly equal in magnitude (green versus blue lines in Fig. 7.4), in contrast to the findings of Ref. [428], where finite-temperature corrections were determined to be subdominant. However, a direct comparison is not possible because Ref. [428] investigated the type of corrections contained in the diagrams shown in Figs. (7.2a) to (7.2c) —as opposed to the closed fermion loop correction examined here.

2. Ref. [428] also found no significant flavor dependence in the rate corrections since their Γ_e and $\Gamma_{\mu,\tau}$ corrections differ by less than 1% in the temperature regime around neutrino decoupling. Figure 7.4 on the other hand shows in agreement with Ref. [429] a strong flavor-dependence by more than two orders of magnitude. This behavior can be traced back to the fact that electron neutrinos experience charged current interactions while $\nu_{\mu,\tau}$ interact only via Z-exchange with the $e^{\pm}$ thermal bath. This difference renders the corresponding vector couplings, $g_V^e \sim 0.49$ and $g_V^{\mu,\tau} \sim -0.012$, very roughly two orders of magnitude apart from one another.

3. Figure 7.4 shows the NLO contributions to the interaction rates in two different approximations: (i) retaining the full dependence on the electron mass (solid lines in Fig. 7.4), and (ii) in the limit $m_e \to 0$ (dashed lines). The massless calculation aims to quantify the effect of the $m_e = 0$ approximation employed in Ref. [429], along with the HTL approximation of the photon propagator.

   One observes that the error from neglecting the electron mass is relatively minor for $T \gtrsim 3m_e$, but becomes sizable at low temperatures. In particular, in the limit $T \to 0$ the ratio $\Gamma_\alpha^{\text{NLO}}/\Gamma_\alpha^{\text{LO}}$ vanishes for $m_e > 0$, but diverges for $m_e = 0$ because of the Boltzmann suppression of the LO rates. Precision computations of $N_{\text{eff}}^{\text{SM}}$ track the evolution of neutrinos down to temperatures much below m_e [426,427]. Thus, although it is commonly understood that (electron) neutrino decoupling occurs at relativistic temperatures $T \sim (2 \to 3) \times m_e$, a finite m_e in the NLO rate computations may yet have some impact on N_{eff} (see Sec. 7.6.2).

Figure 7.5 focuses on the t-channel contribution to the interaction rate, where the enhancement near the photon mass-shell occurs to compare four versions of the resummed photon propagator: (i) the complete one-loop result including a finite m_e everywhere, (ii) the complete one-loop result in the limit $m_e \to 0$, (iii) using the HTL photon propagator (which does not depend on the electron mass), but with m_e everywhere else,[2] and (iv) using the HTL photon propagator and setting $m_e = 0$ everywhere. As expected, (ii) and (iv) match to a very good approximation. Indeed, since the scattering rates are dominated by the kinematic region around the t-channel singularity where

---

[2] Even though it is physically inconsistent to keep m_e in the electron propagators and not in the photon one, (iii) is nonetheless helpful as it isolates the dependence of the rate corrections to the 1PI-resummed versus the HTL propagator.

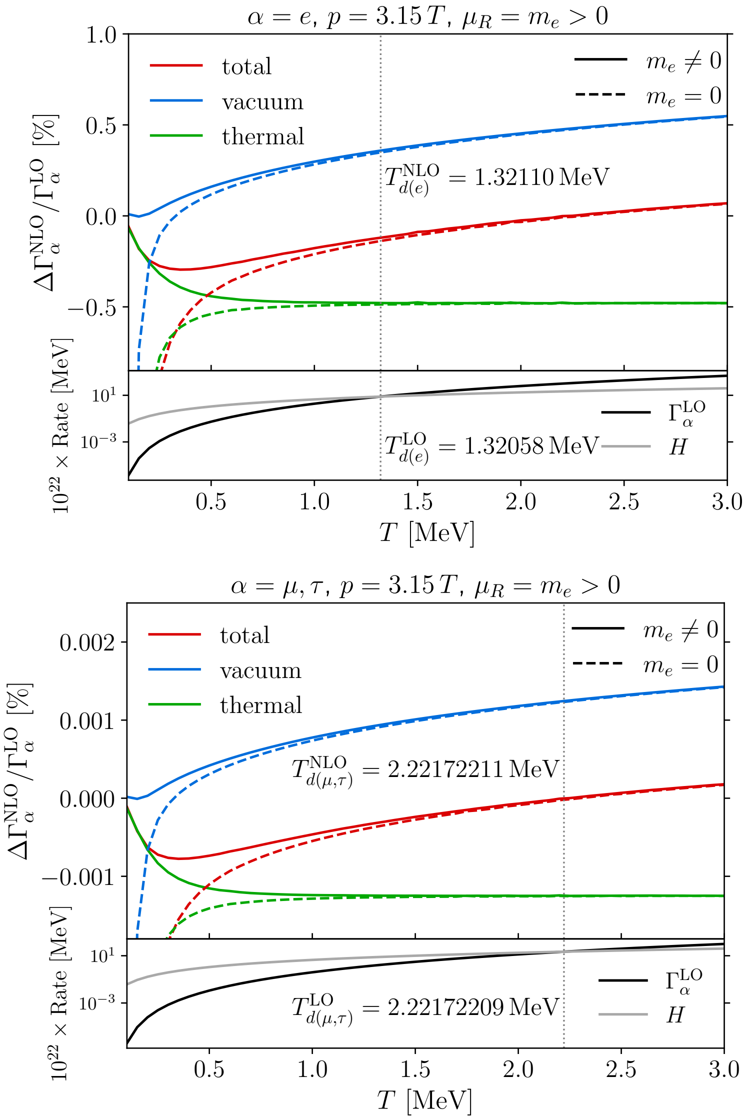

Figure 7.4: *Top*: NLO contributions to the ν_e interaction rate from the closed fermion loop with a finite electron mass (solid) or $m_e = 0$ (dashed) at different temperatures for the mean neutrino momentum $p = 3.15T$. For comparison we normalize all curves to the LO rate (without QED corrections), which we always evaluate with $m_e \neq 0$ to ensure a common normalization. The total rate correction (red) is further split into the vacuum (blue) and the thermal contribution (green). At $T \gg m_e$, the green curve flattens out as the thermal correction contains no scale besides the temperature in this region, while the vacuum correction retains a mild dependence on the renormalization scale μ_R. The lower panel shows again for better comparability the LO neutrino interaction rate compared to the Hubble rate, and T_d indicates the decoupling temperature, defined via $\Gamma_\alpha(T_{d(e)}) = H(T_{d(e)})$. *Bottom*: Same as top, but for $\nu_{\mu,\tau}$.

photons are soft, the 1PI-resummed propagator is well-approximated by the HTL one when, in addition, $m_e = 0$ is set. On the other hand, visible differences can be discerned between (i) and (iii) at $T \lesssim 1\,\mathrm{MeV}$, which can be explained by the fact that the HTL approximation only holds for $T \gg m_e$. In the lower panel of Fig. 7.5, the impact of m_e is highlighted by displaying the ratio of (i) to (iv).

7.5.3 NLO Decoupling Temperatures

While the upper panels of the two plots in Fig. 7.4 show the correction to electron neutrino and muon/tau neutrino interaction rates, the lower panels demonstrate the corresponding leading order rates juxtaposed with the Hubble expansion rate. Within the time frame of interest, the latter is given by $H^2(T) = (\rho_{\mathrm{QED}} + \rho_\nu)/(3M_{\mathrm{Pl}}^2)$.

Solving the equation $\Gamma_\alpha^{\mathrm{LO}}(T_{d(\alpha)}) = H(T_{d(\alpha)})$ for the flavor-dependent decoupling temperatures $T_{d(\alpha)}$, yields the LO decoupling temperatures

$$T_{d(e)}^{\mathrm{LO}} \simeq 1.320\,58\,\mathrm{MeV}\,, \tag{7.21a}$$

$$T_{d(\mu,\tau)}^{\mathrm{LO}} \simeq 2.221\,722\,09\,\mathrm{MeV}\,. \tag{7.21b}$$

The first number differs from the estimate $T_{d(e)}^{\mathrm{LO}} \simeq 1.3453\,\mathrm{MeV}$ from Ref. [420], which might be traced back to a different choise of the input parameter value for the Weinberg angle. Incorporating the QED corrections to the damping rates, the decoupling temperatures shift to

$$T_{d(e)}^{\mathrm{NLO}} \simeq 1.321\,10\,\mathrm{MeV}, \tag{7.22a}$$

$$T_{d(\mu,\tau)}^{\mathrm{NLO}} \simeq 2.221\,722\,11\,\mathrm{MeV} \tag{7.22b}$$

corresponding to an increase of $\sim 0.04\,\%$ for ν_e and of $\sim 8 \times 10^{-7}\,\%$ for $\nu_{\mu,\tau}$. Around the muon neutrino decoupling temperature, the vacuum and thermal contributions to the NLO rates approximately cancel, explaining the smallness of the correction to $T_{d(\mu,\tau)}^{\mathrm{NLO}}$.

Given that Ref. [429] computed the NLO weak rates assuming $m_e = 0$, it is also of interest to study how such an assumption modifies the decoupling temperature shifts. Using the $m_e = 0$ rate corrections from Fig. 7.4 (but with the $m_e \neq 0$ LO rates), the corresponding NLO decoupling temperatures turn out to be

$$T_{d(e)}^{\mathrm{NLO},m_e=0} \simeq 1.321\,18\,\mathrm{MeV}, \tag{7.23a}$$

$$T_{d(\mu,\tau)}^{\mathrm{NLO},m_e=0} \simeq 2.221\,722\,23\,\mathrm{MeV}, \tag{7.23b}$$

i.e., a $0.05\,\%$ and $6 \times 10^{-6}\,\%$ shift for ν_e and $\nu_{\mu,\tau}$, respectively, relative to their corresponding LO decoupling temperature (7.21).

7.6 NLO Effects on $N_{\mathrm{eff}}^{\mathrm{SM}}$

Having computed the correction from the diagram in Fig. 7.2d to the interaction rate Γ_α, it is now possible to estimate its effect on $N_{\mathrm{eff}}^{\mathrm{SM}}$. With the equilibrium rates at hand, two avenues are available:

Method	$\delta N_{\text{eff}}/N_{\text{eff}}^{\text{LO}}$	$\delta N_{\text{eff}}^{m_e=0}/N_{\text{eff}}^{\text{LO}}$
Entropy conservation (common decoupling)	-1.1×10^{-5}	-1.2×10^{-5}
Entropy conservation (flavour-dependent decoupling)	-5.4×10^{-6}	-6.1×10^{-6}
Boltzmann damping approximation (mean momentum)	-7.8×10^{-6}	-1.6×10^{-5}
Boltzmann damping approximation (full momentum)	-7.9×10^{-6}	-2.6×10^{-5}

Table 7.2: Estimates of the relative correction to $N_{\text{eff}}^{\text{SM}}$ due to NLO weak rate corrections, with and without the electron mass, using different methods.

- Based on the computed correction to the neutrino decoupling temperature T_d, defined via $\Gamma_\alpha(T_d) = H(T_d)$, one can, under the assumption of instantaneous neutrino decoupling, estimate the change to $N_{\text{eff}}^{\text{SM}}$, $\delta N_{\text{eff}} \equiv N_{\text{eff}}^{\text{NLO}} - N_{\text{eff}}^{\text{LO}}$, through entropy conservation arguments.
- One may also compute δN_{eff} by solving directly the continuity equation (2.6) and the (Boltzmann) evolution equation (7.4) for the neutrino densities, however, in the damping approximation which entails that all neutrino species are assumed to be in thermal equilibrium with the QED bath besides that a single momentum mode.

Both approaches are considered in the following. The corresponding estimates for δN_{eff} are summarized in Tab. 7.2.

7.6.1 Entropy Conservation

The entropy conservation argument has already been presented in Sec. 2.5 to obtain the standard $N_{\text{eff}}^{\text{SM}} = 3$ estimate. However, here it makes sense to drop the ultra-relativistic assumption to account for a finite m_e and also allow for flavor-dependent decoupling temperatures. To do so, it is convenient to parameterize the entropy density of the QED+ν_β plasma as

$$s(a) = \frac{2\pi^2}{45} h_{\text{eff}}(a) T(a)^3 \tag{7.24}$$

via the effective entropy degree of freedom parameter h_{eff} which in the ideal gas approximation at the time of neutrino decoupling is given by

$$h_{\text{eff}}(a) = g_\gamma + \frac{45}{2\pi^4} \frac{g_e}{T^4(a)} \int_0^\infty \mathrm{d}p\, p^2 \left(E_e + \frac{p^2}{3E_e} \right) f_D(E_e, T(a), \mu = 0) + \frac{7}{8} \sum_{\beta \neq \alpha} g_{\nu_\beta} \tag{7.25}$$

with $E_e = \sqrt{p^2 + m_e^2}$. For the purpose of estimating δN_{eff} due to NLO contributions to the weak rates, it suffices to use the ideal-gas h_{eff}. Note however that the QED entropy density at $T_d \sim \mathcal{O}(1\,\text{MeV})$ is subject in principle to a sizable finite-temperature correction to the QED equation of state, which needs to be included in precision calculations of $N_{\text{eff}}^{\text{SM}}$ [420].

Then, following the same considerations as in Sec. 2.5 with the full h_{eff} from Eq. (7.25) however, the neutrino-to-photon temperature ratio at the later time a_2 becomes

$$\frac{T_{\nu_\alpha}(a_2)}{T(a_2)} = \left[\frac{h_{\text{eff}}(a_2)}{h_{\text{eff}}(a_d^+)} \right]^{1/3} . \tag{7.26}$$

This temperature ratio is used in the following to provide two estimates of $\delta N_{\rm eff}$ due to the NLO contributions.

Common Decoupling Temperature Within the first estimate, as in Sec. 2.5, all neutrino flavors are assumed to decouple effectively at the same time, i.e., again, $a_1 = a_d^+$ corresponds to the time immediately after ν_e decoupling and a_2 to a time significantly after $e^\pm$ annihilation such that $h_{\rm eff}(a_2) = g_\gamma = 2$, while for the former one has

$$h_{\rm eff}(a_d^+) = g_\gamma + \frac{45}{\pi^4 T_{d(e)}^4} \int_0^\infty {\rm d}p\, p^2 \left(E_e + \frac{p^2}{3E_e}\right) f_D(E_e, T_{d(e)}). \tag{7.27}$$

Then, using the temperature ratio (7.26) and the ideal-gas relations $\rho_\gamma \propto g_\gamma T^4$ and $\rho_{\nu_\alpha} \propto (7/8) g_{\nu_\alpha} T_{\nu_\alpha}^4$ from Eq. (2.16b), one finds

$$\left.\frac{\rho_\nu}{\rho_\gamma}\right|_{T/m_e \to 0} = \sum_\alpha \frac{\rho_{\nu_\alpha}(a_2)}{\rho_\gamma(a_2)} = 3 \times \frac{7}{8} \left[\frac{2}{h_{\rm eff}(a_d^+)}\right]^{4/3} \tag{7.28}$$

which is equivalent to

$$N_{\rm eff} = 3 \times \left[\frac{11}{4} \frac{2}{h_{\rm eff}(a_d^+)}\right]^{4/3}. \tag{7.29}$$

The LO and NLO electron neutrino decoupling temperatures in Eqs. (7.21) and (7.22) respectively, yield a fractional shift of $\delta N_{\rm eff}/N_{\rm eff}^{\rm LO} \simeq -1.1 \times 10^{-5}$ due to the rate corrections. If the $m_e = 0$ NLO decoupling temperatures from Eq. (7.23) are used instead, the resulting shift in $N_{\rm eff}$ would have been $\delta N_{\rm eff}^{m_e=0}/N_{\rm eff}^{\rm LO} \simeq -1.2 \times 10^{-5}$. Therefore, while setting $m_e = 0$ causes an approximate 10% change in the estimate of $\delta N_{\rm eff}$, its overall effect on $N_{\rm eff}^{\rm SM}$ seems to be minor, at least within the framework of entropy conservation. These findings are summarized in Tab. 7.2.

Flavor-Dependent Decoupling In the absence of neutrino oscillations, electron neutrinos decouple later than $\nu_{\mu,\tau}$, i.e., at different temperatures $T_{d(e)}$ and $T_{d(\mu,\tau)} > T_{d(e)}$. Consequently, the estimation of $N_{\rm eff}^{\rm SM}$ requires considering entropy conservation across four epochs: the time immediately after $\nu_{\mu,\tau}$ decoupling $a_1 = a_{d(\mu,\tau)}^+$; immediately before ν_e decoupling at $a_2 = a_{d(e)}^-$; immediately after ν_e decoupling $a_3 = a_{d(e)}^+$; and significantly after $e^\pm$ annihilation a_4. The associated effective number of entropy degrees of freedom are

$$h_{\rm eff}(a_{d(\mu,\tau)}^+) = g_\gamma + \frac{45}{\pi^4 T_{d(\mu,\tau)}^4} \int_0^\infty {\rm d}p\, p^2 \left(E_e + \frac{p^2}{3E_e}\right) f_D(E_e, T_{d(\mu,\tau)}) + \frac{7}{8} g_{\nu_e}, \tag{7.30a}$$

$$h_{\rm eff}(a_{d(e)}^-) = g_\gamma + \frac{45}{\pi^4 T_{d(e)}^4} \int_0^\infty {\rm d}p\, p^2 \left(E_e + \frac{p^2}{3E_e}\right) f_D(E_e, T_{d(e)}) + \frac{7}{8} g_{\nu_e}, \tag{7.30b}$$

$$h_{\rm eff}(a_{d(e)}^+) = g_\gamma + \frac{45}{\pi^4 T_{d(e)}^4} \int_0^\infty {\rm d}p\, p^2 \left(E_e + \frac{p^2}{3E_e}\right) f_D(E_e, T_{d(e)}), \tag{7.30c}$$

and $h_{\rm eff}(a_4) = 2$. An estimate of the ν_e-to-photon energy density ratio at the time corresponding to a_4 follows straightforwardly from the temperature ratio in Eq. (7.26) and the ideal-gas relations in Eq. (2.16):

$$\frac{\rho_{\nu_e}(a_4)}{\rho_\gamma(a_4)} = \frac{7}{8} \left[\frac{h_{\rm eff}(a_4)}{h_{\rm eff}(a_{d(e)}^+)}\right]^{4/3} = \frac{7}{8} \left[\frac{2}{h_{\rm eff}(a_{d(e)}^+)}\right]^{4/3}. \tag{7.31}$$

For the ratio $\rho_{\nu_{\mu,\tau}}(a_4)/\rho_\gamma(a_4)$, note that the decoupling of ν_e at $a_{d(e)}$ introduces a discontinuity in the degrees of freedom $h_{\rm eff}$, thereby leading to a more complicated energy density ratio at a_4,

$$\frac{\rho_{\nu_{\mu,\tau}}(a_4)}{\rho_\gamma(a_4)} = \frac{7}{8}\left[\frac{2}{h_{\rm eff}(a^+_{d(e)})}\frac{h_{\rm eff}(a^-_{d(e)})}{h_{\rm eff}(a^+_{d(\mu,\tau)})}\right]^{4/3} . \tag{7.32}$$

Then, combining Eqs. (7.31) and (7.32) to form $\rho_\nu = \sum_\alpha \rho_{\nu_\alpha}$, yields

$$N_{\rm eff} = \left(\frac{11}{4}\frac{2}{h_{\rm eff}(a^+_{d(e)})}\right)^{4/3}\left[1 + 2\times\left(\frac{h_{\rm eff}(a^-_{d(e)})}{h_{\rm eff}(a^+_{d(\mu,\tau)})}\right)^{4/3}\right] \tag{7.33}$$

for the flavor-dependent decoupling estimate.

Evaluating Eq. (7.33) at the LO and NLO decoupling temperatures from Eqs. (7.21) and (7.22) gives a fractional change in $N_{\rm eff}$ of $\delta N_{\rm eff}/N_{\rm eff}^{\rm LO} \simeq -5.4\times10^{-6}$ for the $m_e \neq 0$ corrections, or $\delta N_{\rm eff}^{m_e=0}/N_{\rm eff}^{\rm LO} \simeq -6.1\times10^{-6}$ for the $m_e = 0$ corrections. In comparison with the common-decoupling estimates shown in Tab. 7.2, it is evident that the flavor-dependent decoupling estimates of $\delta N_{\rm eff}/N_{\rm eff}^{\rm LO}$ are typically about half as large, for both the $m_e = 0$ and $m_e \neq 0$ scenarios. This discrepancy is anticipated, as the QED corrections to the $\nu_{\mu,\tau}$ interaction rates are minimal in contrast to the corrections to the ν_e rates. Nonetheless, both estimates are very rough approximations: the actual shift in $\delta N_{\rm eff}$ is likely to lie somewhere in-between.

7.6.2 Solving the Neutrino Boltzmann Equations and the Continuity Equation

Ideally, the QED corrections should be incorporated into a neutrino decoupling code such as FortEPiaNNO to estimate their impact on $N_{\rm eff}^{\rm SM}$. As a first pass, however, one can resort to the damping approximation, which allows to make use of the equilibrium rates by making the simplifying assumption that all particle species—except for neutrinos at one particular momentum mode p represented by $f_\alpha(p)$—are in thermal equilibrium with the QED plasma with temperature T. Then, defining the deviation from equilibrium as $\delta f_\alpha = f_\alpha(p) - f_D(p)$ the generalized Boltzmann equation (7.4) can be expanded to linear order in δf_α resulting in

$$\frac{{\rm d}f_\alpha(p)}{{\rm d}t} \simeq -\Gamma_\alpha(p,T)\left[f_\alpha(p) - f_D(p)\right] . \tag{7.34}$$

To actually solve the approximate Boltzmann equation (7.34) along with the continuity equation (2.6), one can follow Ref. [419] and introduce the comoving quantities $x = m_e\, a$, $y = a\, p$, and $z = T\, a$ since this allows to rewrite the continuity equation as a differential equation for z which is nothing but the photon-to-neutrino temperature ratio:

$$\frac{{\rm d}z}{{\rm d}x} = \frac{\frac{x}{z}J(x/z) - \frac{1}{2z^3}\frac{{\rm d}\bar\rho_\nu}{{\rm d}x} + G_1(x/z)}{\frac{x^2}{z^2}J(x/z) + Y(x/z) + \frac{2\pi^2}{15} + G_2(x/z)} . \tag{7.35}$$

In case of instantaneous neutrino decoupling, the asymptotic value of z results to the value $(11/4)^{1/3}$. Here, the functions

$$J(\tau) = \frac{1}{\pi^2}\int_0^\infty \mathrm{d}\omega\,\omega^2 \frac{\exp\big(\sqrt{\omega^2+\tau^2}\big)}{[\exp\big(\sqrt{\omega^2+\tau^2}\big)+1]^2}, \tag{7.36a}$$

$$Y(\tau) = \frac{1}{\pi^2}\int_0^\infty \mathrm{d}\omega\,\omega^4 \frac{\exp\big(\sqrt{\omega^2+\tau^2}\big)}{[\exp\big(\sqrt{\omega^2+\tau^2}\big)+1]^2}, \tag{7.36b}$$

describe the ideal-gas behavior of the QED plasma, while the other two functions $G_{1,2}(\tau)$ account for finite-temperature QED corrections. To $\mathcal{O}\big(e^2\big)$ these are given by

$$\begin{aligned} G_1(\tau) = 2\pi\alpha_{\mathrm{em}}&\Bigg[\frac{1}{\tau}\left(\frac{K(\tau)}{3} + 2K^2(\tau) - \frac{J(\tau)}{6} - K(\tau)J(\tau)\right) \\ &+ \left(\frac{K'(\tau)}{6} - K(\tau)K'(\tau) + \frac{J'(\tau)}{6} + J'(\tau)K(\tau) + J(\tau)K'(\tau)\right)\Bigg], \end{aligned} \tag{7.37a}$$

$$\begin{aligned} G_2(\tau) = -8\pi\alpha_{\mathrm{em}}&\left(\frac{K(\tau)}{6} + \frac{J(\tau)}{6} - \frac{1}{2}K^2(\tau) + K(\tau)J(\tau)\right) \\ &+ 2\pi\alpha_{\mathrm{em}}\left(\frac{K'(\tau)}{6} - K(\tau)K'(\tau) + \frac{J'(\tau)}{6} + J'(\tau)K(\tau) + J(\tau)K'(\tau)\right), \end{aligned} \tag{7.37b}$$

while the corresponding expressions at $\mathcal{O}\big(e^3\big)$ can be found in Ref. [420]. The $'$ in Eq. (7.37) denotes the first derivative with respect to τ and the auxiliary function $K(\tau)$ is defined as

$$K(\tau) = \frac{1}{\pi^2}\int_0^\infty \mathrm{d}u\;\frac{u^2}{\sqrt{u^2+\tau^2}}\;\frac{1}{\exp\left(\sqrt{u^2+\tau^2}\right)+1}\,. \tag{7.38}$$

Equation (7.35) also requires as input the total time derivative of the comoving neutrino energy density $\bar{\rho}_\nu \equiv \rho_\nu a^4$, which according to Eq. (2.13b) can be constructed from neutrino occupation numbers via

$$\frac{\mathrm{d}\bar{\rho}_\nu}{\mathrm{d}x} = \frac{1}{\pi^2}\int \mathrm{d}y\,y^3 \sum_\alpha \frac{\mathrm{d}f_\alpha(x,y)}{\mathrm{d}x}\,. \tag{7.39}$$

The derivative $\frac{\mathrm{d}f_\alpha(x,y)}{\mathrm{d}x}$ in Eq. (7.39) corresponds to the approximate Boltzmann equation (7.34) which in terms of the new variables reads

$$\frac{\mathrm{d}f_\alpha(x,y)}{\mathrm{d}x} \simeq -\frac{\Gamma_\alpha(x,y)}{xH(x)}\left[f_\alpha(x,y) - f_D((y/z)T)\right]. \tag{7.40}$$

Equation (7.40) can now be solved together with the continuity equation (7.35) for a range of momenta y covering the majority of the neutrino population. A typical range is $y \in [0.01, 30]$ and this procedure is referred to in the following as the "full-momentum" approach. Alternatively, Eq. (7.40) can be simplified further by adopting the ansatz that all neutrino species still maintain an equilibrium shape but with a different number of total neutrinos. This corresponds to

$$f_\alpha(y) = f_\alpha(\langle y\rangle)\frac{f_D(yT)}{f_D(\langle y\rangle T)}, \tag{7.41}$$

and $\Gamma_\alpha(y) = \Gamma_\alpha(\langle y\rangle)$. A reasonable choice for $\langle y\rangle$ is the mean momentum mode $y_0 = 3.15\,z(T_0)$ where T_0 is the photon temperature at initialization which is still equal to the neutrino temperature at that time. In this approximation, Eq. (7.39) can be rewritten as

$$\frac{\mathrm{d}\bar{\rho}_\nu}{\mathrm{d}x} = -\frac{7\pi^2}{120xH(x)}\left[\sum_\alpha \Gamma_\alpha(\langle y\rangle)\left(\frac{f_\alpha(x,\langle y\rangle)}{f_D(\langle y\rangle T)} - z^3(x)\right)\right] . \tag{7.42}$$

This alternative is referred to as the "mean-momentum" approach.

Irrespective of whether the full-momentum or the mean-momentum approach is used, the final value for $N_{\text{eff}}^{\text{SM}}$ can be estimated from the solutions to ρ_ν and z in the limit $x \to \infty$ by using the definition of $N_{\text{eff}}^{\text{SM}}$ in Eq. (2.21). In terms of the rescaled variables one has

$$N_{\text{eff}}^{\text{SM}} = \frac{8}{7}\left(\frac{11}{4}\right)^{4/3}\frac{30}{2\pi^2}\left[\frac{z(T_0)}{z(x)}\right]^4 \bar{\rho}_\nu(x)\bigg|_{x\to\infty} . \tag{7.43}$$

Table 7.2 shows the estimates of $\delta N_{\text{eff}}/N_{\text{eff}}^{\text{LO}}$ due to QED corrections to the neutrino interaction rates using both the full-momentum and the mean-momentum approaches, with and without the electron mass in the correction.

As is evident form Tab. 7.2, the full-momentum and the mean-momentum calculations for a finite electron mass $m_e \neq 0$, $\delta N_{\text{eff}}/N_{\text{eff}}^{\text{LO}} \simeq (-7.8 \to -7.9) \times 10^{-6}$, both align fairly well with their counterpart obtained in Sec. 7.6.1 from entropy conservation arguments: in fact they fall between the common-decoupling and flavor-dependent decoupling estimates. However, the calculations assuming a vanishing electron mass $m_e = 0$ show a 50 % difference between the full-momentum ($\delta N_{\text{eff}}^{m_e=0}/N_{\text{eff}}^{\text{LO}} \simeq -2.6 \times 10^{-5}$) and the mean-momentum ($\delta N_{\text{eff}}^{m_e=0}/N_{\text{eff}}^{\text{LO}} \simeq -1.6 \times 10^{-5}$) methods, and are in addition ~ 30 % up to four times larger than those derived from entropy methods. This result is in line with expectations. As previously shown in Figs. 7.4 and 7.5, the rate corrections under the $m_e = 0$ assumption diverge as $T \to 0$ compared to the LO rate, whereas the $m_e \neq 0$ counterpart approaches zero. Given that neutrino decoupling in the early Universe is gradual and reaches into the $e^\pm$-annihilation era at $T \sim m_e$, any calculation of δN_{eff} that considers non-instantaneous decoupling will be somewhat sensitive to the assumptions made for m_e in the $T \lesssim 3m_e$ range. Indeed, the low temperature impact of m_e on $\delta N_{\text{eff}}/N_{\text{eff}}^{\text{LO}}$ is not captured by entropy conservation arguments, which rely on a single point estimate, i.e., the decoupling temperatures at $T > m_e$, where the $m_e \neq 0$ and $m_e = 0$ rate corrections differ by less than 10 %. Conversely, the full-momentum approach, covering the widest temperature range, exhibits the strongest dependence on the electron mass assumption for $\delta N_{\text{eff}}/N_{\text{eff}}^{\text{LO}}$. Consequently, while the impact of rate corrections on $N_{\text{eff}}^{\text{SM}}$ is minor, one can deduce that ignoring m_e in these calculations is an inadequate approximation in high-precision evaluations of $N_{\text{eff}}^{\text{SM}}$.

7.7 Conclusions

In this chapter, the QED corrections to the neutrino-electron interaction rates near neutrino decoupling have been calculated and their impact on the effective number of neutrinos in the Standard Model, $N_{\text{eff}}^{\text{SM}}$, has been assessed. The focus was on the diagram from Fig. 7.2d, due to its expected t-channel enhancement, leading to its dominance over the other three diagrams. Similar corrections have been examined in Refs. [428, 429]. The former analysis [428] suggested a shift in $N_{\text{eff}}^{\text{SM}}$ from the benchmark value of 3.044 [426, 427] to 3.043. Contrary to these findings, the ab initio calculation presented here shows that the QED corrections to the neutrino interaction rate are minimal. Within the temperature range $T \sim 1 \to 3$ MeV, the corrections to the electron neutrino interaction rate range from $-0.2 \to +0.1\%$ relative to the LO rate. For muon and tau neutrinos, the effect is even smaller, ranging from $-0.0005 \to +0.0002\%$. These results are consistent with the findings from Ref. [429], despite differing formalisms (imaginary time versus real-time) and assumptions (zeroth versus finite m_e). The significant contrast in the relative corrections for ν_e and $\nu_{\mu,\tau}$, spanning over two orders of magnitude, confirms the strong flavor dependence noted in Ref. [429] but not in Ref. [428]. Employing the QED-corrected neutrino interaction rates, the resulting change in $N_{\text{eff}}^{\text{SM}}$ has been estimated using various approximations and methods: via entropy conservation arguments which assume instantaneous decoupling, and by solving the Boltzmann equation along with the continuity equation in the damping approximation. Depending on the method/approximation, the relative change in $N_{\text{eff}}^{\text{SM}}$ lies within $\delta N_{\text{eff}}/N_{\text{eff}}^{\text{LO}} \simeq (-0.5 \to -1.1) \times 10^{-5}$. Thus, relative to the current SM benchmark of $N_{\text{eff}}^{\text{SM}} = 3.0440 \pm 0.0002$ [426, 427], the QED corrections to the neutrino interaction rates could shift the value negatively in the fifth decimal place, thereby remaining completely within the reported uncertainties. While this confirms the sign of δN_{eff} calculated in Ref. [428], even the most optimistic estimate is roughly 30 times smaller than their claimed correction.

Notably, assuming $m_e = 0$ in rate corrections can have an $\mathcal{O}(1)$ impact on $\delta N_{\text{eff}}/N_{\text{eff}}^{\text{LO}}$, despite that the rate corrections at $T \sim 1 \to 3$ MeV differ by less than 10 %. This arises because corrections assuming $m_e = 0$ deviate from their $m_e \neq 0$ counterparts at $T \lesssim 3m_e$, as they diverge in the $T \to 0$ limit while the $m_e \neq 0$ corrections vanish. Since neutrino decoupling in the early Universe is not instantaneous, these $T \lesssim 3m_e$ effects will influence $N_{\text{eff}}^{\text{SM}}$, despite the common understanding that neutrino decoupling occurs at $T \sim 1\,\text{MeV}$. Therefore, even though the QED corrections to the weak rates effect $N_{\text{eff}}^{\text{SM}}$ negligibly, disregarding the electron mass for high-precision $N_{\text{eff}}^{\text{SM}}$ calculations is not a good approximation.

To conclude, these findings strongly indicate that the SM benchmark value $N_{\text{eff}}^{\text{SM}} = 3.0440 \pm 0.0002$ [426, 427] remains correct within the stated uncertainties. Ideally, a comprehensive numerical solution of the QKEs using a dedicated neutrino decoupling code like FortEPiaNO [339] incorporating all NLO contributions shown in Fig. 7.2 in the collision integral would be desirable. However, unless there is a new effect that has not yet been taken into account so far, it's unlikely that a more detailed examination of NLO effects on the neutrino interaction rate will lead to a departure from the existing SM benchmark $N_{\text{eff}}^{\text{SM}}$ that is large enough to be relevant for cosmological observations in the near future.

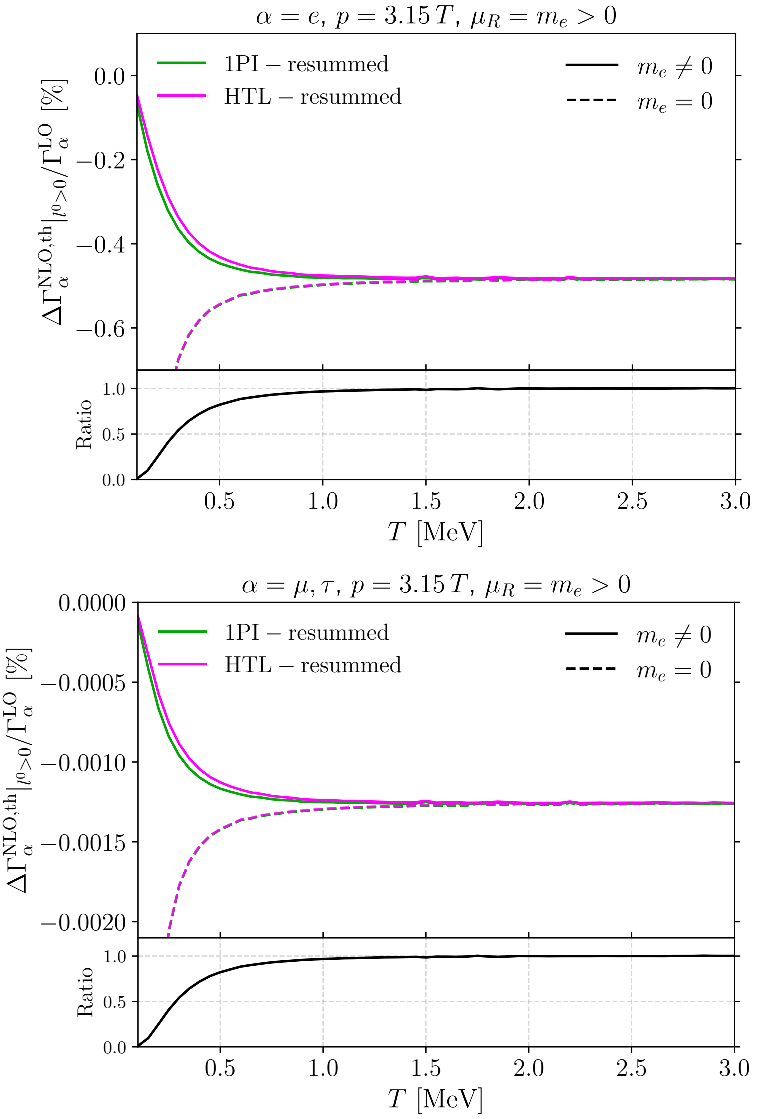

Figure 7.5: *Top:* The t-channel contribution ($l^0 > 0$) to the NLO electron neutrino interaction rate at the mean momentum $p = 3.15T$ in different approximations, namely, using 1PI-resummed (green) and HTL (magenta) photon propagators, in each case with $m_e \neq 0$ (solid lines) or $m_e = 0$ (dashed lines) in both electron loops of the self-energy diagram of Fig. 7.2d. As in Fig. 7.4, all curves are normalized to the LO rate, which we always evaluate with $m_e \neq 0$. The lower panel shows the ratio of the 1PI result for $m_e \neq 0$ to the HTL result for $m_e = 0$ as a function of the temperature. *Bottom*: Same as top, but for $\alpha \neq e$.

Chapter 8

Conclusion and Outlook

While the Standard Model of particle physics combined with general relativity seems to be widely consistent with observations, it remains mandatory to precisely calculate observables in those theories to match the (future) experimental resolution. This extends to theories that go beyond the Standard Model to explain, e.g., dark matter, to reliably draw conclusions on the viability of such models. In this spirit, this thesis investigated higher-order SUSY-QCD corrections to dark matter (co)annihilation cross sections in the context of neutralino dark matter in the MSSM and the precision code DM@NLO. The corresponding calculations do not only allow to constrain the MSSM parameter space more reliably, but can also serve as guidelines for other models. In more detail, the methods of (dimensional) regularization and renormalization have been presented to treat the UV divergences appearing in the virtual corrections, providing a selection of (stable) renormalization schemes for the MSSM region relevant for stop coannihilation. Also, an extension of the dipole subtraction method to massive initial-states has been performed and verified through comparison with the space phase space slicing method. As an example, the $\mathcal{O}(\alpha_s)$ corrections to stop-antistop annihilation into gluons and light quarks have been calculated including the Sommerfeld enhancement effect. Generally, throughout the DM@NLO history, the strong corrections are found to shift the neutralino relic density in the stop coannihilation region by at most $\sim 50\,\%$. In terms of another angle, the effect on the dark matter relic abundance was examined within a simplified dark matter model featuring forbidden DM annihilations into SM leptons if the assumption of kinetic equilibrium between dark matter and the Standard Model in the standard freeze-out scenario is lifted. The resulting changes in the final DM abundance were much more severe than due to the higher-order corrections, finding shifts by more than an order of magnitude, that in turn severely change current exclusion limits on the investigated model.

While the previous refinements of the dark matter freeze-out calculation were all done using vacuum QFT matrix elements due to the non-relativistic nature of the the problem, a precise description of neutrino decoupling requires the inclusion of finite-temperature effects which necessitated a relatively large review of the closed time path formalism of nonequilibrium quantum field theory, as particle physics was for a long time dominated by collider experiments and thermal effects were if only relevant in the context of the quark-gluon plasma. This then allowed to calculate the dominant next-to-leading order QED corrections to the weak rates determining $N_{\mathrm{eff}}^{\mathrm{SM}}$ with the result that the current benchmark for N_{eff} in the Standard Model remains unchanged within the reported uncertainties.

There are now several possibilities to extend the work presented in this thesis: In the context of DM@NLO there is the obvious path of including radiative corrections to not yet implemented processes like gluino coannihilation. Another direction would be the addition of other models beyond the MSSM like the Inert Doublet Model or the NMSSM. An orthogonal direction is the inclusion of other so far missing non-perturbative effects like bound-state formation which is, e.g., relevant for stop-anstistop annihilation, or the inclusion of more argument sets for one-loop integrals with a vanishing Gram determinant in DM@NLO's loop library since these are relevant for the computation of direct and indirect detection signals in general. In the context of a precision calculation of N_{eff} in the Standard Model, the closed fermion loop still needs to be supplemented by hadronic contributions. Also the evaluation of the remaining three identified diagrams yielding the $\mathcal{O}(e^2)$ corrections needs to be completed followed by the subsequent implementation of the NLO contributions into the neutrino decoupling code FortEPianNO, however, only after the generalization of the thermal rates to nonequilibrium phase space distribution functions for the different neutrino flavors. In addition, similar to dark matter bound-state formation, one may include non-perturbative physics that could be taking place in the QED plasma like the formation of positronium out of non-relativistic electron–positron pairs.

Appendix A

Collection of Calculations and Results for the Dipole Method

In this part of the appendix, calculations and results related to the extension of the dipole method to massive initial states are collected.

A.1 Derivation of the Phase Space Factorization

A.1.1 Final-State Emitter and Initial-State Spectator

The phase space element for $m+1$ particles in the final state in $D = 4-2\varepsilon$ dimensions is given by [443]

$$\begin{aligned} \mathrm{d}\phi_{m+1}(p_i, p_j, p_k; p_a + p_b) = (2\pi)\delta^{(D)}(p_a + p_b - p_i - p_j - \sum_k p_k)\frac{\mathrm{d}^D p_i}{(2\pi)^{D-1}}\delta_+(p_i^2 - m_i^2) \\ \times \frac{\mathrm{d}^D p_j}{(2\pi)^{D-1}}\delta_+(p_j^2 - m_j^2)\prod_k \frac{\mathrm{d}^D p_k}{(2\pi)^{D-1}}\delta_+(p_k^2 - m_k^2), \quad \text{(A.1)} \end{aligned}$$

where the modified Dirac delta distribution contains the Heaviside step function $\theta(x)$ and is defined as $\delta_+(p^2 - m^2) = \delta(p^2 - m^2)\theta(p^0)$. The momentum of the spectator is p_a, while the emitter $\widetilde{ij}$ splits into two particles with the momenta p_i and p_j. The momenta of the remaining final state particles other than i or j are labelled as p_k. The $(m+1)$-particle phase space is factorized exactly into a m-particle phase space and a two-particle phase space through a convolution of the form

$$\mathrm{d}\phi_{m+1}(p_i, p_j, p_k; p_a + p_b) = \frac{\mathrm{d}m_P^2}{2\pi}\ \mathrm{d}\phi_m(P, p_k; p_a + p_b)\mathrm{d}\phi_2(p_i, p_j; P), \quad \text{(A.2)}$$

where $m_P^2 = P^2$ acts as the squared invariant mass related to the momentum $P = p_i + p_j$. As the dipole splitting functions are expressed as functions of x and z_i, it makes sense to replace the integration over m_P^2 with an integration over x by using the relation in Eq. (4.64) and turn the integration over the two-particle phase space

$$\mathrm{d}\phi_2(p_i, p_j; P) = (2\pi)^D\delta^{(D)}(P - p_i - p_j)\frac{\mathrm{d}^D p_i}{(2\pi)^{D-1}}\delta_+(p_i^2 - m_i^2)\frac{\mathrm{d}^D p_j}{(2\pi)^{D-1}}\delta_+(p_j^2 - m_j^2) \quad \text{(A.3)}$$

into an integration over z_i. As a first step towards the parametrization through z_i, two Dirac delta functions are integrated out which gives

$$\mathrm{d}\phi_2(p_i,p_j;P) = \frac{\mathrm{d}^{D-1}p_i}{(2\pi)^{D-2}2E_i}\delta_+((P-p_i)^2 - m_j^2). \tag{A.4}$$

It is convenient to work in the c.m. frame of p_i and p_j from now on, i.e., in the rest frame of P, which sets the time and spatial components of p_i and p_j to the well-known expressions [443]:

$$E_i = \frac{P^2 + m_i^2 - m_j^2}{2\sqrt{P^2}}, \quad E_j = \frac{P^2 + m_j^2 - m_i^2}{2\sqrt{P^2}}, \quad |\mathbf{p}_i| = |\mathbf{p}_j| = \frac{\sqrt{\lambda(P^2, m_i^2, m_j^2)}}{2\sqrt{P^2}}. \tag{A.5}$$

The components of momentum p_a become

$$E_a = \frac{p_a \cdot P}{\sqrt{P^2}} = \frac{-\bar{Q}^2}{2x\sqrt{P^2}}, \quad |\mathbf{p}_a| = \sqrt{\frac{(p_a\cdot P)^2}{P^2} - m_a^2} = \frac{1}{2\sqrt{P^2}}\frac{\sqrt{\lambda_{aj}}R(x)}{x}, \tag{A.6}$$

where Eq. (4.64) was used to replace the product $p_a \cdot P$. The expressions in Eq. (A.5) can be used to write the remaining Dirac δ-function in Eq. (A.4) as a function of the absolute value of the momentum $\mathbf{p}_i$

$$\delta_+(P^2 - 2P\cdot p_i + m_i^2 - m_j^2) = \frac{E_i}{2\sqrt{P^2}|\mathbf{p}_i|}\delta_+\left(|\mathbf{p}_i| - \frac{1}{2\sqrt{P^2}}\sqrt{\lambda(P^2,m_i^2,m_j^2)}\right). \tag{A.7}$$

Inserting polar coordinates in $D-1$ dimensions

$$\mathrm{d}^{D-1}p_i = \mathrm{d}|\mathbf{p}_i|\ |\mathbf{p}_i|^{D-2}\ \mathrm{d}\Omega_{D-2}\ \mathrm{d}\cos\theta\,\sin^{D-4}\theta \tag{A.8}$$

allows to integrate out the remaining delta function and the phase space measure becomes

$$\mathrm{d}\phi_2(p_i,p_j;P) = \frac{\mathrm{d}\Omega_{D-2}}{(2\pi)^{D-2}}\mathrm{d}\cos\theta\,\sin^{D-4}\theta\ \ \frac{1}{2}\left(4P^2\right)^{\frac{2-D}{2}}\ \lambda^{\frac{D-3}{2}}(P^2,m_i^2,m_j^2), \tag{A.9}$$

where the angle θ is defined as the angle between $\mathbf{p}_a$ and $\mathbf{p}_i$, so that $\cos\theta$ is given by

$$\cos\theta = \frac{E_iE_a - p_i\cdot p_a}{|\mathbf{p}_i||\mathbf{p}_a|}. \tag{A.10}$$

The integration over $\cos\theta$ can now be turned easily into an integration over the desired variable z_i as E_i, E_a, $|\mathbf{p}_i|$ and $|\mathbf{p}_a|$ do not depend on z_i. In order to express $\sin\theta$ through z_i, the integration limits

$$z_\pm = \frac{E_iE_a \pm |\mathbf{p}_i||\mathbf{p}_a|}{P\cdot p_a}, \tag{A.11}$$

which are given in Eq. (4.71) in terms of x and Q^2 for $m_i = 0$, can be used to write

$$\sin^2\theta = (1-\cos\theta)(1+\cos\theta) = \left(\frac{P\cdot p_a}{|\mathbf{p}_i||\mathbf{p}_a|}\right)^2(z_i - z_-)(z_+ - z_i). \tag{A.12}$$

Due to O(3) invariance of the matrix element squared around the axis given by $\mathbf{p}_a$, the integration over the solid angle Ω_{D-2} can already be performed using

$$\int \mathrm{d}\Omega_{D-2} = \frac{2\pi^{\frac{D-2}{2}}}{\Gamma(\frac{D-2}{2})} \,. \tag{A.13}$$

After defining the jacobian from the transition from m_P^2 to x into the dipole phase space $\left[\mathrm{d}p_i\left(Q^2, x, z_i\right)\right]$, one arrives at Eq. (4.70).

A.1.2 Initial-State Emitter and Initial-State Spectator

As in the previous section, the form of the measure $[\mathrm{d}p_i\,(s, x, y)]$ is derived by considering a convolution of the form

$$\begin{aligned} \mathrm{d}\phi_{m+1}(p_i, p_k; p_a + p_b) = \frac{\mathrm{d}m_P^2}{2\pi} \prod_k \frac{\mathrm{d}^D p_k}{(2\pi)^{D-1}} \delta_+(p_k^2 - m_k^2) \\ \times (2\pi)^D \delta^{(D)}(p_a + p_b - p_i - \sum_k p_k) \mathrm{d}\phi_2(p_i, P; p_a + p_b)\,, \end{aligned} \tag{A.14}$$

where m_P acts as the invariant mass of the momentum $P = p_a + p_b - p_i$. By using the facts that the dipole momenta obey the mass-shell relations $\tilde{p}_k = m_k^2$ and momentum conservation $p_a + p_b - p_i - \sum_k p_k = \tilde{p}_{ai} + p_b - \sum_k \tilde{p}_k$ by construction and that a Lorentz transformation $\tilde{p}_k^\mu = \Lambda^\mu{}_\nu p_k^\nu$ leaves the measure $\mathrm{d}^D p_k$ invariant, the remaining momentum integrations in Eq. (A.14) can be expressed through a m-particle phase space with initial momentum $\tilde{p}_{ai} + p_b$ and final momenta $\tilde{p}_k$:

$$\mathrm{d}\phi_{m+1}(p_i, p_k; p_a + p_b) = \frac{\mathrm{d}m_P^2}{2\pi} \mathrm{d}\phi_m(\tilde{p}_k; \tilde{p}_{ai} + p_b) \mathrm{d}\phi_2(p_i, P; p_a + p_b). \tag{A.15}$$

Following the same line of thought as in App. A.1.1 and working in the c.m. frame of p_a and p_b, the integration over the two-particle phase space for $m_i = 0$

$$\mathrm{d}\phi_2(P, p_i; p_a + p_b) = \frac{\mathrm{d}^D p_i}{(2\pi)^{D-1}} \delta_+(p_i^2) \frac{\mathrm{d}^D P}{(2\pi)^{D-1}} \delta_+(P^2 - m_P^2) (2\pi)^D \delta^{(D)}(p_a + p_b - P - p_i) \tag{A.16}$$

can be turned into an integration over y

$$\begin{aligned} \mathrm{d}\phi_2(P, p_i; p_a + p_b) &= \frac{\mathrm{d}\Omega_{D-2}}{2(2\pi)^{D-2}}\ \mathrm{d}|\mathbf{p_i}||\mathbf{p_i}|^{D-3}\ \mathrm{d}\cos\theta \sin^{D-4}\theta\ \delta_+(s - 2|\mathbf{p_i}|\sqrt{s} - P^2) \\ &= \frac{\mathrm{d}\Omega_{D-2}}{2(2\pi)^{D-2}} (2\sqrt{s})^{2-D} (s - P^2)^{D-3}\ \mathrm{d}\cos\theta \sin^{D-4}\theta \\ &= \frac{\bar{s}^{1-2\varepsilon}}{2(4\pi)^{2-2\varepsilon}} \frac{(4s)^{-\varepsilon}}{\sqrt{\lambda_{ab}}^{1-2\varepsilon}}\ \mathrm{d}\Omega_{D-2}\ \mathrm{d}y\, [(y_+ - y)(y - y_-)]^{-\varepsilon}\,. \end{aligned} \tag{A.17}$$

The angle θ is defined as the angle between $\mathbf{p}_i$ and $\mathbf{p}_a$ and therefore determined through

$$p_a \cdot p_i = |\mathbf{p}_i| E_a - |\mathbf{p}_a||\mathbf{p}_i| \cos\theta. \tag{A.18}$$

A simple substitution from m_P^2 to x via Eq. (4.113) yields the dipole phase space $[\mathrm{d}p_i\,(s,x,y)]$ given in Eq. (4.110).

A.2 Computation of the Relevant Integrals

The expansion in ε of the integrals $I_1(z;\varepsilon)$ and $I_2(z;\varepsilon)$ up to $\mathcal{O}(\varepsilon)$ is obtained by inserting the ansatz

$$u(z) = r(z) + \varepsilon s(z) + \mathcal{O}\big(\varepsilon^2\big) \tag{A.19}$$

into the hypergeometric equation [444]

$$z(1-z)u''(z) + (c-(a+b+1)z)u'(z) - abu(z) = 0\,, \tag{A.20}$$

whose general solution for the initial condition $u(0) = 1$ is the hypergeometric function $u = {}_2F_1(a,b;c;z)$. Solving the resulting system of equations order by order while enforcing the boundary conditions $r(0) = 1$ and $s(0) = 0$ yields the functions $r(z)$ and $s(z)$. Note that the Euler beta function $\beta(a,b) = \frac{1}{b}\,{}_2F_1(a,1-b,a+1;1)$ is just a special case of the hypergeometric function.

For the computation of the integrals $\mathcal{I}_1\,(y_0;\varepsilon)$ and $\mathcal{I}_2\,(y_0;\varepsilon)$, the integral

$$\int_0^\infty \mathrm{d}t\, t^{\alpha-1}\,{}_2F_1(a,b;c;-t) = \frac{\Gamma(\alpha)\Gamma(c)\Gamma(a-\alpha)\Gamma(b-\alpha)}{\Gamma(a)\Gamma(b)\Gamma(c-\alpha)} \tag{A.21}$$

is used. It can be computed by inserting the integral representation of the hypergeometric function followed by factorizing the double integral into two beta functions

$$\begin{aligned}\int_0^\infty \mathrm{d}t \int_0^1 \mathrm{d}t'\, t^{\alpha-1}t'^{b-1}(1-t')^{c-b-1}(1+tt')^{-a}& \\ = \int_0^1 \mathrm{d}x\,(1-x)^{\alpha-1}x^{a-\alpha-1}\int_0^1 \mathrm{d}t'\,(1-t')^{c-b-1}t'^{b-\alpha-1}& \\ = \beta(\alpha,a-\alpha)\beta(c-b,b-\alpha)&\end{aligned} \tag{A.22}$$

through the substitution $x = 1/(1+tt')$. The remaining step for the computation of $\mathcal{I}_1\,(y_0;\varepsilon)$ is to separate the integral into a part giving the divergences for $y \to 0$ and a finite part

$$\begin{aligned}\mathcal{I}_1(y_0;\varepsilon) = \beta(1-\varepsilon,1-\varepsilon)\Bigg(\frac{1}{y_0^{1+\varepsilon}}\int_0^1 \mathrm{d}t\, t^\varepsilon\,{}_2F_1\left(1,1-\varepsilon;2-2\varepsilon;-\frac{t}{y_0}\right)& \\ -\int_0^\infty \mathrm{d}t\, t^\varepsilon\,{}_2F_1\left(1,1-\varepsilon;2-2\varepsilon;-t\right)\Bigg)\,.&\end{aligned} \tag{A.23}$$

The last part contains the divergent piece and is evaluated with the help of Eq. (A.21)

$$\int_0^\infty \mathrm{d}t\, t^\varepsilon\,{}_2F_1(1,1-\varepsilon;2-2\varepsilon;-t) = \frac{1}{2\varepsilon^2} - \frac{1}{\varepsilon} + \mathcal{O}(\varepsilon)\,, \tag{A.24}$$

whereas the first integral is finite and can be evaluated for $\varepsilon = 0$

$$\int_0^1 \mathrm{d}t\, t^{\varepsilon}\, {}_2F_1\left(1, 1-\varepsilon; 2-2\varepsilon; -\frac{t}{y_0}\right) = -y_0 \,\mathrm{Li}_2\left(-\frac{1}{y_0}\right) + \mathcal{O}(\varepsilon). \tag{A.25}$$

The calculation of $\mathcal{I}_2\left(y_0; \varepsilon\right)$ proceeds in an analogous way.

A.3 The Integrated Dipoles

A.3.1 Final-State Emitter and Initial-State Spectator

The integrated counterparts I^a_{ij} according to Eq. (4.81) read:

$$\begin{aligned}
I^a_{gq}\left(x; \varepsilon\right) = {} & \frac{2C_F}{vR(x)x^2}\frac{1}{(1-x)^{1+2\varepsilon}} \\
& \times \left(\eta_j x + (1-x)\right)^{2\varepsilon}\left(\frac{-\bar{Q}^2}{P^2}\right)^{\varepsilon}\left[\left(\frac{\sqrt{\lambda_{aj}}R(x)}{\bar{Q}^2} + \frac{1}{4}h_g^{\mathrm{RS}} z_-(z_+ - z_-)\right)\beta(1-\varepsilon, 1-\varepsilon)\right. \\
& \left. + \frac{1}{4}h_g^{\mathrm{RS}}(z_+ - z_-)^2\beta(1-\varepsilon, 2-\varepsilon) - I_1(-A(x); \varepsilon)\right], \qquad \text{(A.26)} \\
\hat{I}^a_{gq}\left(x; \varepsilon\right) = {} & \frac{2C_F}{x^{2-\varepsilon}}\frac{1}{(1-x)^{1+\varepsilon}}\left[\left(\frac{1}{8}h_g^{\mathrm{RS}}(1-R(x)) - 1\right)\beta(1-\varepsilon, 1-\varepsilon)\right. \\
& \left. + \frac{1}{4}h_g^{\mathrm{RS}}R(x)\beta(1-\varepsilon, 2-\varepsilon) - \frac{1}{R(x)}I_1(-A(x); \varepsilon)\right], \qquad \text{(A.27)} \\
I^a_{g\tilde{q}}\left(x; \varepsilon\right) = {} & \frac{2C_F}{vR(x)x^2}\frac{1}{(1-x)^{1+2\varepsilon}}\left(\eta_j x + (1-x)\right)^{2\varepsilon} \\
& \times \left(\frac{-\bar{Q}^2}{P^2}\right)^{\varepsilon}\left[\left(\frac{\sqrt{\lambda_{aj}}R(x)}{\bar{Q}^2}\right)\beta(1-\varepsilon, 1-\varepsilon) - I_1(-A(x); \varepsilon)\right], \qquad \text{(A.28)} \\
I^a_{gg}\left(x; \varepsilon\right) = {} & -\frac{2C_A}{R(x)x^{2-\varepsilon}}\frac{1}{(1-x)^{1+\epsilon}}\left[I_1\left(-A(x); \varepsilon\right) - I_1(\tilde{A}(x); \varepsilon)\right. \\
& \left. -\frac{h_g^{\mathrm{RS}}}{2(1-\varepsilon)}R(x)^3\beta\left(2-\varepsilon, 2-\varepsilon\right) + 2R(x)\beta\left(1-\varepsilon, 1-\varepsilon\right)\right], \qquad \text{(A.29)} \\
I^a_{q\bar{q}}\left(x; \varepsilon\right) = {} & \frac{T_F}{x^{2-\varepsilon}}\frac{1}{(1-x)^{1+\epsilon}}\left(\beta(1-\varepsilon, 1-\varepsilon) - \frac{2}{1-\varepsilon}R(x)^2\beta(2-\varepsilon, 2-\varepsilon)\right). \qquad \text{(A.30)}
\end{aligned}$$

Note that in the massless case $m_j = 0$ the variables A and $\tilde{A}$ are related through $A(x) = \tilde{A}(x)/(1-\tilde{A}(x))$ which allows to simplify the difference of the I_1 functions in Eq. (A.29)

$$I_1\left(-A(x); \varepsilon\right) - I_1(\tilde{A}(x); \varepsilon) = 2I_1\left(-A(x); \varepsilon\right) \tag{A.31}$$

by employing the identity $I_1\left(z; \varepsilon\right) = -I_1\left(z/(z-1); \varepsilon\right)$ which follows directly from the Pfaff transformation

$${}_2F_1\left(a, b; c; z\right) = (1-z)^{-a}\, {}_2F_1\left(a, c-b; c; \frac{z}{z-1}\right). \tag{A.32}$$

A.3.2 Initial-State Emitter and Final-State Spectator

The integrated counterparts $I_j^{a,\widetilde{ai}}$ according to Eq. (4.95) read:

$$\begin{aligned} I_j^{\tilde{q}\tilde{q}}(x;\varepsilon) = {} & \frac{2C_F}{vR(x)x^2}\frac{1}{(1-x)^{1+2\varepsilon}}\left(\eta_j x+(1-x)\right)^{2\varepsilon}\left(\frac{-\bar{Q}^2}{P^2}\right)^{\varepsilon} \\ & \times\left(I_1(-A(x);\varepsilon)-xI_1(-B(x);\varepsilon)+2\eta_a x^2\frac{(\eta_j-1)x+1}{1-vR(x)}I_2(-B(x);\varepsilon)\right)\,, \end{aligned} \tag{A.33}$$

$$\hat{I}_j^{\tilde{q}\tilde{q}}(x;\varepsilon) = \frac{2C_F}{R(x)x^{2-\varepsilon}}\frac{1}{(1-x)^{1+\varepsilon}}\Big(I_1\left(-A(x);\varepsilon\right)-xI_1\left(-B(x);\varepsilon\right)+\frac{x}{2}(R(x)+1)I_2\left(-B(x);\varepsilon\right)\Big)\,. \tag{A.34}$$

Appendix B

Parametrization of 2 → 2 Collision Terms

In this part of the appendix, three parametrizations of the collision term for 2 → 2 processes given by

$$\hat{C}[f_a] = \frac{1}{16(2\pi)^5 g_a} \int \mathrm{d}^3\mathbf{p}_b \, \mathrm{d}^3\mathbf{p}_1 \, \mathrm{d}^3\mathbf{p}_2 \, \delta^{(4)}(p_a + p_b - p_1 - p_2) \frac{|\mathcal{M}_{ab\to 12}|^2}{E_b E_1 E_2} \mathcal{P}(f_a, f_b, f_1, f_2) \tag{B.1}$$

are presented, two for the case where the corresponding matrix element $|\mathcal{M}_{ab\to 12}|^2$ possesses an arbitrary angular dependence such that there remain in total four integrals without any further assumptions on the matrix element and one for the specific case where the matrix element depends only on a single Mandelstam variable so that three integrals remain and one more integral can be done analytically for a wide range of tree-level scattering matrix elements. In either case, the population factor $\mathcal{P}$ containing the phase space densities is expected to depend solely on the energies

$$E_a = \sqrt{\mathbf{p}_a^2 + m_a^2} \qquad E_1 = \sqrt{\mathbf{p}_1^2 + m_1^2} \tag{B.2a}$$

$$E_b = \sqrt{\mathbf{p}_b^2 + m_b^2} \qquad E_2 = \sqrt{\mathbf{p}_2^2 + m_2^2} \tag{B.2b}$$

defined in the cosmic rest frame which is justified through the isotropy of the FLRW spacetime.

B.1 For a Generic Matrix Element

In the following, two parametrizations for a 2 → 2 matrix element with an arbitrary angular dependence are presented with the first one being better suited for the solution of momentum-dependent Boltzmann equations since in this context at least one phase space density is only available in discretized form.

B.1.1 Parametrization in the Cosmic Rest Frame

Using the integral replacement

$$\int \frac{\mathrm{d}^3\mathbf{p}_2}{2E_2} = \int \mathrm{d}^3\mathbf{p}_2\,\mathrm{d}E_2\,\delta(E_2^2 - \mathbf{p}_2^2 - m_2^2)\theta(E_2)\,, \tag{B.3}$$

choosing $\mathbf{p}_a$ along the z-direction through the spherical coordinates

$$\mathbf{p}_a = |\mathbf{p}_a|(0,0,1)\,, \tag{B.4a}$$

$$\mathbf{p}_b = |\mathbf{p}_b|(0,\sin\alpha,\cos\alpha)\,, \tag{B.4b}$$

$$\mathbf{p}_1 = |\mathbf{p}_1|(\sin\beta\sin\theta,\cos\beta\sin\theta,\cos\theta) \tag{B.4c}$$

yields after removal of the four-momentum conserving δ-function through p_2-integration the remaining integration measures

$$\mathrm{d}^3\mathbf{p}_b = \mathbf{p}_b^2\,\mathrm{d}|\mathbf{p}_b|\,\mathrm{d}\!\cos\alpha\,\mathrm{d}\beta\ , \tag{B.5a}$$

$$\mathrm{d}^3\mathbf{p}_1 = \mathbf{p}_1^2\,\mathrm{d}|\mathbf{p}_1|\,\mathrm{d}\!\cos\theta\,\mathrm{d}\varphi\ . \tag{B.5b}$$

The δ-function in Eq. (B.3) fixes the angle β to

$$\cos\beta = -\left(|\mathbf{p}_1||\mathbf{p}_b|\sin\alpha\sin\theta\right)^{-1}\left(\frac{\bar{t}}{2} + E_aE_b - E_1E_b + \cos\alpha|\mathbf{p}_b|\left(\cos\theta|\mathbf{p}_1| - |\mathbf{p}_a|\right)\right) \tag{B.6}$$

with the abbreviation $\bar{t} = t + m_b^2 - m_2^2$, where

$$s = (p_a + p_b)^2 = m_a^2 + m_b^2 + 2E_aE_b - 2|\mathbf{p}_a||\mathbf{p}_b|\cos\alpha\,, \tag{B.7a}$$

$$t = (p_a - p_1)^2 = m_a^2 + m_1^2 - 2E_aE_1 + 2|\mathbf{p}_a||\mathbf{p}_1|\cos\theta \tag{B.7b}$$

are the two independent Mandelstam variables. The integration domain of $z \equiv \cos\alpha$ is bounded trough the requirement $|\cos\beta| \leq 1$ which translates into the condition

$$az^2 + bz + c \geq 0\,, \tag{B.8}$$

where the corresponding polynomial coefficients read

$$a = -4\mathbf{p}_b^2|\mathbf{p_a} - \mathbf{p}_1|^2\,, \tag{B.9a}$$

$$b = -8|\mathbf{p}_b|\left(E_bE_1 - E_aE_b - \frac{\bar{t}}{2}\right)(|\mathbf{p}_a| - |\mathbf{p}_1|\cos\theta)\,, \tag{B.9b}$$

$$c = 4\mathbf{p}_b^2\mathbf{p}_1^2\sin^2\theta - 4\left(E_bE_1 - E_aE_b - \frac{\bar{t}}{2}\right)^2\ . \tag{B.9c}$$

The inequality (B.8) then imposes the integration limits

$$z_\pm = \frac{-b \pm \sqrt{\Delta}}{2a} \tag{B.10}$$

on z with the abbreviation

$$\Delta = b^2 - 4ac = 64\mathbf{p}_b^2\mathbf{p}_1^2 \sin^2\theta \left[\mathbf{p}_b^2|\mathbf{p}_a - \mathbf{p}_1|^2 - \left(E_bE_1 - E_aE_b - \frac{\bar{t}}{2}\right)^2\right] . \tag{B.11}$$

The existence of the limits $z_\pm$ imposes the additional condition $\Delta > 0$ on the integration domain which is enforced through a Heaviside step function in the final generic parametrization for the $2 \to 2$ collision term given by [327, 336]

$$\hat{C}\,[f_a] = \frac{1}{4(2\pi)^4 g_a} \int_{m_b}^{\infty} \mathrm{d}E_b\,|\mathbf{p}_b| \int_{m_1}^{\infty} \mathrm{d}E_1\,|\mathbf{p}_1| F(E_a, E_b, E_1)\mathcal{P}(f_a, f_b, f_1, f_2)\,, \tag{B.12}$$

where the two angular integrals are contained in the auxiliary function

$$F(E_a, E_b, E_1) = \int_{-1}^{1} \mathrm{d}\!\cos\theta \int_{z_-}^{z_+} \mathrm{d}z\, \frac{|\mathcal{M}_{ab\to12}|^2}{\sqrt{a(z-z_-)(z-z_+)}}\Theta(b^2 - 4ac)\,. \tag{B.13}$$

If the matrix element $|\mathcal{M}_{ab\to12}|^2$ is a quadratic polynomial in z, the z-integration can be performed analytically using the integrals

$$\int_{z_-}^{z_+} \frac{1}{\sqrt{(z-z_-)(z_+-z)}} = \pi\,, \tag{B.14a}$$

$$\int_{z_-}^{z_+} \frac{z}{\sqrt{(z-z_-)(z_+-z)}} = -\frac{\pi b}{2a}\,, \tag{B.14b}$$

$$\int_{z_-}^{z_+} \frac{z^2}{\sqrt{(z-z_-)(z_+-z)}} = \pi\frac{3b^2 - 4ca}{8a^2} \tag{B.14c}$$

which can all be traced back to the Euler β-function.

Before concluding this section, it's important to draw attention to certain caveats associated with the numerical evaluation of the collision term in Eq. (B.12). Even if double precision numbers are used, it is recommended to use the simplified expression for Δ provided in Eq. (B.11), as a plain usage of $b^2 - 4ac$ may lead to a wrong sign of Δ at the boundaries $\cos\theta = \pm 1$ through round-off errors. The usage of quadruple-precision floating-point numbers would be a suitable alternative.

B.1.2 Parametrization with a Lorentz Boost

Another possible reduction of the phase space integrals to a numerically accessible form proceeds through application of a Lorentz boost Λ that transforms a four-momentum q into the rest frame of the timelike four-momentum p: $[\Lambda p]^i = 0$, $i = 1, 2, 3$. The transformed four-vector is denoted by $\hat{q} = \Lambda q$ with the components

$$\hat{q}^0 = \gamma(q^0 + \beta\mathbf{e}\cdot\mathbf{q})\,, \tag{B.15a}$$

$$\hat{\mathbf{q}} = \mathbf{q} - (\mathbf{e}\cdot\mathbf{q})\,\mathbf{e} + \gamma(\beta q^0 + \mathbf{e}\cdot\mathbf{q})\,\mathbf{e}\,, \tag{B.15b}$$

where

$$\beta = -\frac{|\mathbf{p}|}{p^0}\,, \quad \gamma = \frac{1}{\sqrt{1-\beta^2}}\,, \quad \mathbf{e} = \frac{\mathbf{p}}{|\mathbf{p}|}\,. \tag{B.16}$$

The parametrization then proceeds by writing a Lorentz invariant subpart of the phase space integration in the rest frame of $p_a + p_b$, i.e., $\hat{\mathbf{p}}_a + \hat{\mathbf{p}}_b = 0$:

$$\hat{C}[f_a] = \frac{1}{2(2\pi)^5 g_a} \int \frac{\mathrm{d}^3\mathbf{p}_b}{2E_b} \left\{ \int \frac{\mathrm{d}^3\hat{\mathbf{p}}_1}{2\hat{E}_1} \frac{\mathrm{d}^3\hat{\mathbf{p}}_2}{2\hat{E}_2} \delta^{(3)}(\hat{\mathbf{p}}_1 + \hat{\mathbf{p}}_2) \right.$$
$$\left. \times \delta(\hat{E}_a + \hat{E}_b - \hat{E}_1 - \hat{E}_2) |\mathcal{M}_{ab\to12}|^2 \mathcal{P}(f_a, f_b, f_1, f_2) \right\}_{\hat{V}=\Lambda V} . \tag{B.17}$$

For this, the energies in the phase space densities have to be rewritten in the covariant form through $u = (1, \mathbf{0})$ as $E_a = u \cdot p_a = \hat{u} \cdot \hat{p}$ and so on. The first Dirac delta function is used to integrate out $\hat{\mathbf{p}}_2$ while the second eliminates the integration over $|\hat{\mathbf{p}}_1|$ via

$$\int \frac{\mathrm{d}|\hat{\mathbf{p}}_1|\, \hat{\mathbf{p}}_1^2}{\sqrt{\hat{\mathbf{p}}_1^2 + m_1^2}\sqrt{\hat{\mathbf{p}}_1^2 + m_2^2}} \delta\left(\sqrt{\hat{\mathbf{p}}_1^2 + m_1^2} + \sqrt{\hat{\mathbf{p}}_1^2 + m_2^2} - \hat{E}\right) = \Theta(\hat{E} - m_1 - m_2) \frac{\lambda^{\frac{1}{2}}(\hat{E}^2, m_1^2, m_2^2)}{2\hat{E}^2} \tag{B.18}$$

with $\hat{E} = \hat{E}_a + \hat{E}_b$ and the Källén function λ. For the remaining integrals over $\mathbf{p}_b$ and $\mathrm{d}\Omega_{\hat{\mathbf{p}}_1}$, the explicit coordinate system

$$\mathbf{p}_a = |\mathbf{p}_a|(0, 0, 1)\,, \tag{B.19a}$$
$$\mathbf{p}_b = |\mathbf{p}_b|(\sin\theta, 0, \cos\theta) \tag{B.19b}$$

is chosen and the angular element $\mathrm{d}\Omega_{\hat{\mathbf{p}}_1}$ is expressed through the spherical coordinates $\hat{\theta}$ and $\hat{\varphi}$ such that $\hat{\mathbf{p}}_1$ becomes

$$\hat{\mathbf{p}}_1 = |\hat{\mathbf{p}}_1| \begin{pmatrix} e_3 \sin\hat{\theta}\cos\hat{\varphi} + e_1\cos\hat{\theta} \\ \sin\hat{\theta}\sin\hat{\varphi} \\ e_3\cos\hat{\theta} - e_1\sin\hat{\theta}\cos\hat{\varphi} \end{pmatrix} . \tag{B.20}$$

Recall that the absolute value of $\hat{\mathbf{p}}_1$ is fixed through $|\hat{\mathbf{p}}_1| = \lambda^{\frac{1}{2}}(\hat{E}^2, m_1^2, m_2^2)/(2\hat{E})$ and that the unit vector $\mathbf{e}$ in Eq. (B.20) has the value $(\mathbf{p}_a + \mathbf{p}_b)/|\mathbf{p}_a + \mathbf{p}_b|$. The final collision term thus becomes [445]

$$\hat{C}[f_a] = \frac{1}{16(2\pi)^4 g_a} \int_{m_b}^{\infty} \mathrm{d}E_b\, |\mathbf{p}_b| \int_{-1}^{1} \mathrm{d}\cos\theta$$
$$\times \left\{ \int_{-1}^{1} \mathrm{d}\cos\hat{\theta} \int_0^{2\pi} \mathrm{d}\hat{\varphi}\, \frac{\lambda^{\frac{1}{2}}(\hat{E}^2, m_1^2, m_2^2)}{2\hat{E}^2} |\mathcal{M}_{ab\to12}|^2 \mathcal{P}(f_a, f_b, f_1, f_2) \right\} . \tag{B.21}$$

If the integrand is a second order polynomial in $\cos\hat{\varphi}$ of the form $f(\hat{\varphi}) = a + b\cos\hat{\varphi} + c\cos^2\hat{\varphi}$, the φ-integration can be performed analytically:

$$\int_0^{2\pi} \mathrm{d}\hat{\varphi}\, f(\hat{\varphi}) = \pi \left[f\left(\frac{\pi}{4}\right) + f\left(\frac{3\pi}{4}\right) \right] . \tag{B.22}$$

B.2 For a *t*-Channel Matrix Element

For the parametrization of the collision term for a matrix element $|\mathcal{M}_{ab\to12}|^2$ which depends only on one Mandelstam variable, the strategy outlined in Refs. [330, 331] is adopted. Without loss of generality, this Mandelstam variable is chosen to be $t = (p_1 - p_a)^2 = (p_b - p_2)^2$ with the corresponding three-momentum

$$\mathbf{k} = \mathbf{p}_1 - \mathbf{p}_a = \mathbf{p}_b - \mathbf{p}_2, \tag{B.23}$$

which is used as reference direction to define the explicit coordinate system:

$$\begin{aligned} \mathbf{k} &= |\mathbf{k}|(0,0,1), && \text{(B.24a)} \\ \mathbf{p}_a &= |\mathbf{p}_a|(0,\sin\eta,\cos\eta), && \text{(B.24b)} \\ \mathbf{p}_b &= |\mathbf{p}_b|(\cos\varphi\sin\vartheta,\sin\varphi\sin\vartheta,\cos\vartheta). && \text{(B.24c)} \end{aligned}$$

The four-momentum p_2 is integrated out using four-momentum conservation

$$\begin{aligned} \int \frac{\mathrm{d}^3\mathbf{p}_2}{2E_2}\delta^{(4)}(p_a+p_b-p_1-p_2) &= \Theta(E_a+E_b-E_1-m_2) \\ &\times \frac{1}{2|\mathbf{k}||\mathbf{p}_b|}\delta\left(\cos\vartheta - \frac{|\mathbf{p}_b|^2+\mathbf{k}^2+m_2^2-(E_a+E_b-E_1)^2}{2|\mathbf{p}_b|k}\right), \end{aligned} \tag{B.25}$$

where the remaining δ-function sets p_2 on-shell. The absolute value of $\mathbf{p}_2$ is then fixed by energy conservation. The spatial components of p_1 are turned into the integration variable $\mathbf{k}$, giving

$$\begin{aligned} \int \frac{\mathrm{d}^3\mathbf{p}_1}{2E_1} &= \int \mathrm{d}^3\mathbf{k}\,\mathrm{d}E_1\,\delta(E_1^2-|\mathbf{k}+\mathbf{p}_a|^2-m_1^2)\Theta(E_1-m_1) && \text{(B.26)} \\ &= \int \mathrm{d}^3\mathbf{k}\,\mathrm{d}E_1\,\frac{1}{2|\mathbf{k}||\mathbf{p}_a|}\delta\left(\cos\eta - \frac{E_1^2-\mathbf{k}^2-|\mathbf{p}_a|^2-m_1^2}{2|\mathbf{p}_a||\mathbf{k}|}\right)\Theta(E_1-m_1). && \text{(B.27)} \end{aligned}$$

Averaging over the direction of the incoming particle with momentum p_a via $\int \mathrm{d}\cos\eta/2$ and performing the trivial angular integrals results in

$$\begin{aligned} \hat{C}[f_a] = \frac{1}{128\pi^3|\mathbf{p}_a|g_a} &\int \mathrm{d}E_1\,\mathrm{d}E_b\,\mathrm{d}|\mathbf{k}|\,\mathrm{d}\cos\vartheta\,\mathrm{d}\cos\eta\,\delta\left(\cos\eta-\dots\right)\delta\left(\cos\vartheta-\dots\right) \\ &\times |\mathcal{M}_{ab\to12}|^2\mathcal{P}(f_a,f_b,f_1,f_2)\Theta(E_1-m_1)\Theta(E_a+E_b-E_1-m_2)\,. \end{aligned} \tag{B.28}$$

The two delta functions can be used to constrain the integration domain of $|\mathbf{k}|$ such that one obtains the integration limits

$$k_- \equiv \max(||\mathbf{p}_a|-|\mathbf{p}_1||,||\mathbf{p}_b|-|\mathbf{p}_2||) \le |\mathbf{k}| \le \min(|\mathbf{p}_a|+|\mathbf{p}_1|,|\mathbf{p}_b|+|\mathbf{p}_2|) \equiv k_+\,, \tag{B.29}$$

so that the final form of the collision term reads

$$\hat{C}[f_a] = \frac{1}{128\pi^3|\mathbf{p}_a|g_a}\int_{m_1}^{\infty}\mathrm{d}E_1\int_{\max(m_b,E_1-E_a+m_2)}^{\infty}\mathrm{d}E_b\,\Pi(E_a,E_b,E_1)\mathcal{P}(f_a,f_b,f_1,f_2) \tag{B.30}$$

with the collision kernel

$$\Pi(E_a,E_b,E_1) = \Theta(k_+-k_-)\int_{k_-}^{k_+}\mathrm{d}|\mathbf{k}|\,|\mathcal{M}_{ab\to12}|^2. \tag{B.31}$$

Appendix C

Options for the DM@NLO User Interface

C.1 The DM@NLO Configuration File

In this part of the appendix, the options available in a DM@NLO configuration file are described. Such an input file consists out of a series of keywords that can be set to user defined values. These keywords are given by:

- `slha = <string>`: path to the SLHA input file defining the SUSY scenario to investigate (mass spectrum, mixing matrices, decay widths, *etc.*).
- `muR = <double>`: renormalisation scale μ_R in GeV.
- `renscheme = <int>`: renormalisation scheme according to the numbering scheme introduced in Sec. 4.2.4. The mixed $\overline{\text{DR}}$-OS scheme no. 1 is the recommended option.
- `choosesol = <int>`: solutions for $M_{\tilde{Q}}$, $M_{\tilde{U}}$, $M_{\tilde{D}}$ as explained in Sec. 4.2.4.
- `particleA = <int>` and `particleB = <int>`: PDG numbers of the first and second particle in the initial state.
- `particle1 = <int>` and `particle2 = <int>`: PDG numbers of the first and second particle in the final state.
- `pcm = <double>`: centre-of-mass momentum in GeV.
- `result = <string>`: defines whether the output should contain the total cross σ corresponding to the value `s` or the total cross section times relative velocity σv defined through the value `sv`.
- `formfactor = <int>`: sets the scalar nuclear form factors f^N_{Tq} to one of the sets of values in Tab. 4.6.

C.2 Available Options in the Command Line Interface

The DM@NLO program can be run with several command line options by typing in a shell

```
./dmnlo <input-file> [options]
```

The keyword `<input-file>` provides the path to a configuration file specifying the details of the computation to be achieved according to the standard defined in App. C.1. The following options are allowed:

- `--help`, prints a help message to the screen, indicating how to execute the code.
- `--slha`, followed by a string sets the path to the SLHA 2 parameter file containing the numerical values of masses, mixing angles, decay widths, *etc.*
- `--muR`, followed by a double-precision number sets the value of the renormalisation scale in GeV.
- `--renscheme`, followed by an integer number sets the renormalisation scheme according to the numbering scheme introduced in Sec. 4.2.4.
- `--choosesol`, followed by an integer number defines which solution to use for $M_{\tilde{Q}}$, $M_{\tilde{U}}$, $M_{\tilde{D}}$ as explained in Sec. 4.2.4.
- `--legacy`, defines the weak mixing angle θ_W and the W-mass as in the default MSSM model file in MicrOMEGAs 2.4.1.
- `--lo`, returns the result at LO accuracy.
- `--nlo`, returns the result at NLO accuracy.
- `--sommerfeld`, returns the Sommerfeld enhanced cross section.
- `--full`, returns the NLO result matched to the Sommerfeld enhancement if the latter is available. Otherwise the output is identical to `--nlo`.
- `--particleA` and `--particleB`, followed by integer numbers defines the nature of the two initial-state particles through their PDG numbers.
- `--particle1` and `--particle2`, followed by integer numbers defines the nature of the two final-state particles through their PDG numbers.
- `--pcm`, followed by a double-precision number sets the centre-of-mass momentum p_{cm} in GeV.
- `--result`, followed by a string corresponding to `s` for the total cross σ or `sv` for the total cross section times the relative velocity σv.
- `--DD`, enables the direct detection module. This option supersedes (co)annihilation settings.
- `--formfactor`, followed by an integer number ranging from zero to two sets the scalar nuclear form factors f^N_{Tq} to one of the value sets shown in Tab. 4.6 with zero for DM@NLO and two for MicrOMEGAs.

Bibliography

[1] J.D. Hunter, *Matplotlib: A 2D Graphics Environment*, *Comput. Sci. Eng.* **9** (2007) 90.

[2] J. Ellis, *TikZ-Feynman: Feynman diagrams with TikZ*, *Comput. Phys. Commun.* **210** (2017) 103 [`1601.05437`].

[3] C.R. Harris et al., *Array programming with NumPy*, *Nature* **585** (2020) 357 [`2006.10256`].

[4] P. Virtanen et al., *SciPy 1.0–Fundamental Algorithms for Scientific Computing in Python*, *Nature Meth.* **17** (2020) 261 [`1907.10121`].

[5] S.M. Carroll, *Spacetime and Geometry: An Introduction to General Relativity*, Cambridge University Press (7, 2019), 10.1017/9781108770385.

[6] E.W. Kolb and M.S. Turner, *The Early Universe*, vol. 69 (1990), 10.1201/9780429492860.

[7] PLANCK collaboration, *Planck 2018 results. VI. Cosmological parameters*, *Astron. Astrophys.* **641** (2020) A6 [`1807.06209`].

[8] J. Bernstein, *Kinetic Theory in the Expanding Universe*, Cambridge Monographs on Mathematical Physics, Cambridge University Press (1988), 10.1017/CBO9780511564185.

[9] A.H. Guth, *The Inflationary Universe: A Possible Solution to the Horizon and Flatness Problems*, *Phys. Rev. D* **23** (1981) 347.

[10] A.D. Linde, *A New Inflationary Universe Scenario: A Possible Solution of the Horizon, Flatness, Homogeneity, Isotropy and Primordial Monopole Problems*, *Phys. Lett. B* **108** (1982) 389.

[11] P.F. de Salas, M. Lattanzi, G. Mangano, G. Miele, S. Pastor and O. Pisanti, *Bounds on very low reheating scenarios after Planck*, *Phys. Rev. D* **92** (2015) 123534 [`1511.00672`].

[12] V.A. Kuzmin, V.A. Rubakov and M.E. Shaposhnikov, *On the Anomalous Electroweak Baryon Number Nonconservation in the Early Universe*, *Phys. Lett. B* **155** (1985) 36.

[13] M. Fukugita and T. Yanagida, *Baryogenesis Without Grand Unification*, *Phys. Lett. B* **174** (1986) 45.

[14] M. D'Onofrio and K. Rummukainen, *Standard model cross-over on the lattice*, *Phys. Rev. D* **93** (2016) 025003 [`1508.07161`].

[15] Y. Aoki, G. Endrodi, Z. Fodor, S.D. Katz and K.K. Szabo, *The Order of the quantum chromodynamics transition predicted by the standard model of particle physics*, *Nature* **443** (2006) 675 [`hep-lat/0611014`].

[16] PTOLEMY collaboration, *PTOLEMY: A Proposal for Thermal Relic Detection of Massive Neutrinos and Directional Detection of MeV Dark Matter*, `1808.01892`.

[17] G. Steigman, D.N. Schramm and J.E. Gunn, *Cosmological Limits to the Number of Massive Leptons*, *Phys. Lett. B* **66** (1977) 202.

[18] D.J. Fixsen, *The Temperature of the Cosmic Microwave Background*, *Astrophys. J.* **707** (2009) 916 [`0911.1955`].

[19] D.J. Fixsen, E.S. Cheng, J.M. Gales, J.C. Mather, R.A. Shafer and E.L. Wright, *The Cosmic Microwave Background spectrum from the full COBE FIRAS data set*, *Astrophys. J.* **473** (1996) 576 [`astro-ph/9605054`].

[20] WMAP collaboration, *Nine-Year Wilkinson Microwave Anisotropy Probe (WMAP) Observations: Cosmological Parameter Results*, *Astrophys. J. Suppl.* **208** (2013) 19 [`1212.5226`].

[21] J.R. Pritchard and A. Loeb, *21-cm cosmology*, *Rept. Prog. Phys.* **75** (2012) 086901 [`1109.6012`].

[22] V. Mukhanov, *Physical Foundations of Cosmology*, Cambridge University Press, Oxford (2005), 10.1017/CBO9780511790553.

[23] G. Bertone, D. Hooper and J. Silk, *Particle dark matter: Evidence, candidates and constraints*, *Phys. Rept.* **405** (2005) 279 [`hep-ph/0404175`].

[24] K. Garrett and G. Duda, *Dark Matter: A Primer*, *Adv. Astron.* **2011** (2011) 968283 [`1006.2483`].

[25] M. Klasen, M. Pohl and G. Sigl, *Indirect and direct search for dark matter*, *Prog. Part. Nucl. Phys.* **85** (2015) 1 [`1507.03800`].

[26] K. Freese, *Status of Dark Matter in the Universe*, *Int. J. Mod. Phys.* **1** (2017) 325 [`1701.01840`].

[27] M. Cirelli, A. Strumia and J. Zupan, *Dark Matter*, `2406.01705`.

[28] G. Bertone and D. Hooper, *History of dark matter*, *Rev. Mod. Phys.* **90** (2018) 045002 [`1605.04909`].

[29] J.H. Oort, *The force exerted by the stellar system in the direction perpendicular to the galactic plane and some related problems*, *Bulletin of the Astronomical Institutes of the Netherlands, Vol. 6, p. 249* **6** (1932) 249.

[30] V.C. Rubin and W.K. Ford, Jr., *Rotation of the Andromeda Nebula from a Spectroscopic Survey of Emission Regions*, *Astrophys. J.* **159** (1970) 379.

[31] V.C. Rubin, W.K. Ford, Jr. and N. Thonnard, *Extended rotation curves of high-luminosity spiral galaxies. IV. Systematic dynamical properties, Sa through Sc*, *Astrophys. J. Lett.* **225** (1978) L107.

[32] F. Zwicky, *Die Rotverschiebung von extragalaktischen Nebeln*, *Helv. Phys. Acta* **6** (1933) 110.

[33] F. Zwicky, *On the Masses of Nebulae and of Clusters of Nebulae*, *Astrophys. J.* **86** (1937) 217.

[34] D. Clowe, M. Bradac, A.H. Gonzalez, M. Markevitch, S.W. Randall, C. Jones et al., *A direct empirical proof of the existence of dark matter*, *Astrophys. J. Lett.* **648** (2006) L109 [`astro-ph/0608407`].

[35] J. Hamann, S. Hannestad, M.S. Sloth and Y.Y.Y. Wong, *How robust are inflation model and dark matter constraints from cosmological data?*, *Phys. Rev. D* **75** (2007) 023522 [`astro-ph/0611582`].

[36] T. Bringmann, F. Kahlhoefer, K. Schmidt-Hoberg and P. Walia, *Converting nonrelativistic dark matter to radiation*, *Phys. Rev. D* **98** (2018) 023543 [`1803.03644`].

[37] SDSS collaboration, *Baryon Acoustic Oscillations in the Sloan Digital Sky Survey Data Release 7 Galaxy Sample*, *Mon. Not. Roy. Astron. Soc.* **401** (2010) 2148 [`0907.1660`].

[38] BOSS collaboration, *The clustering of galaxies in the SDSS-III Baryon Oscillation Spectroscopic Survey: baryon acoustic oscillations in the Data Releases 10 and 11 Galaxy samples*, *Mon. Not. Roy. Astron. Soc.* **441** (2014) 24 [`1312.4877`].

[39] V. Springel et al., *Simulating the joint evolution of quasars, galaxies and their large-scale distribution*, *Nature* **435** (2005) 629 [`astro-ph/0504097`].

[40] A. Klypin, S. Trujillo-Gomez and J. Primack, *Halos and galaxies in the standard cosmological model: results from the Bolshoi simulation*, *Astrophys. J.* **740** (2011) 102 [`1002.3660`].

[41] M. Milgrom, *A Modification of the Newtonian dynamics as a possible alternative to the hidden mass hypothesis*, *Astrophys. J.* **270** (1983) 365.

[42] R.B. Tully and J.R. Fisher, *A New method of determining distances to galaxies*, *Astron. Astrophys.* **54** (1977) 661.

[43] J.D. Bekenstein, *Relativistic gravitation theory for the MOND paradigm*, *Phys. Rev. D* **70** (2004) 083509 [`astro-ph/0403694`].

[44] S. Boran, S. Desai, E.O. Kahya and R.P. Woodard, *GW170817 Falsifies Dark Matter Emulators*, *Phys. Rev. D* **97** (2018) 041501 [`1710.06168`].

[45] K. Pardo and D.N. Spergel, *What is the price of abandoning dark matter? Cosmological constraints on alternative gravity theories*, *Phys. Rev. Lett.* **125** (2020) 211101 [`2007.00555`].

[46] Super-Kamiokande collaboration, *Evidence for oscillation of atmospheric neutrinos*, *Phys. Rev. Lett.* **81** (1998) 1562 [`hep-ex/9807003`].

[47] SNO collaboration, *Measurement of the rate of $\nu_e + d \to p + p + e^-$ interactions produced by ^8B solar neutrinos at the Sudbury Neutrino Observatory*, *Phys. Rev. Lett.* **87** (2001) 071301 [`nucl-ex/0106015`].

[48] S. Tremaine and J.E. Gunn, *Dynamical Role of Light Neutral Leptons in Cosmology*, *Phys. Rev. Lett.* **42** (1979) 407.

[49] K. Griest, *Galactic Microlensing as a Method of Detecting Massive Compact Halo Objects*, *Astrophys. J.* **366** (1991) 412.

[50] B. Carr, F. Kuhnel and M. Sandstad, *Primordial Black Holes as Dark Matter*, *Phys. Rev. D* **94** (2016) 083504 [`1607.06077`].

[51] G.R. Farrar, *Stable Sexaquark*, `1708.08951`.

[52] M. Moore and T.R. Slatyer, *Cosmology and terrestrial signals of sexaquark dark matter*, *Phys. Rev. D* **110** (2024) 023515 [`2403.03972`].

[53] G. Jungman, M. Kamionkowski and K. Griest, *Supersymmetric dark matter*, *Phys. Rept.* **267** (1996) 195 [`hep-ph/9506380`].

[54] H.-C. Cheng, J.L. Feng and K.T. Matchev, *Kaluza-Klein dark matter*, *Phys. Rev. Lett.* **89** (2002) 211301 [`hep-ph/0207125`].

[55] H.P. Nilles, *Supersymmetry, Supergravity and Particle Physics*, *Phys. Rept.* **110** (1984) 1.

[56] A.H. Chamseddine, R.L. Arnowitt and P. Nath, *Locally Supersymmetric Grand Unification*, *Phys. Rev. Lett.* **49** (1982) 970.

[57] ATLAS collaboration, *The quest to discover supersymmetry at the ATLAS experiment*, `2403.02455`.

[58] G.F. Giudice and A. Masiero, *A Natural Solution to the mu Problem in Supergravity Theories*, *Phys. Lett. B* **206** (1988) 480.

[59] M. Cirelli, N. Fornengo and A. Strumia, *Minimal dark matter*, *Nucl. Phys. B* **753** (2006) 178 [`hep-ph/0512090`].

[60] L.J. Hall, K. Jedamzik, J. March-Russell and S.M. West, *Freeze-In Production of FIMP Dark Matter*, *JHEP* **03** (2010) 080 [`0911.1120`].

[61] B. Holdom, *Two U(1)'s and Epsilon Charge Shifts*, *Phys. Lett. B* **166** (1986) 196.

[62] C. Dvorkin, T. Lin and K. Schutz, *Making dark matter out of light: freeze-in from plasma effects*, *Phys. Rev. D* **99** (2019) 115009 [`1902.08623`].

[63] C.E. Yaguna, *The Singlet Scalar as FIMP Dark Matter*, *JHEP* **08** (2011) 060 [`1105.1654`].

[64] R.D. Peccei and H.R. Quinn, *CP Conservation in the Presence of Instantons*, *Phys. Rev. Lett.* **38** (1977) 1440.

[65] J. Preskill, M.B. Wise and F. Wilczek, *Cosmology of the Invisible Axion*, *Phys. Lett. B* **120** (1983) 127.

[66] M. Bauer, M. Neubert and A. Thamm, *Collider Probes of Axion-Like Particles*, *JHEP* **12** (2017) 044 [`1708.00443`].

[67] S. Dodelson and L.M. Widrow, *Sterile-neutrinos as dark matter*, *Phys. Rev. Lett.* **72** (1994) 17 [`hep-ph/9303287`].

[68] X.-D. Shi and G.M. Fuller, *A New dark matter candidate: Nonthermal sterile neutrinos*, *Phys. Rev. Lett.* **82** (1999) 2832 [`astro-ph/9810076`].

[69] Z.-j. Tao, *Radiative seesaw mechanism at weak scale*, *Phys. Rev. D* **54** (1996) 5693 [`hep-ph/9603309`].

[70] E. Ma, *Verifiable radiative seesaw mechanism of neutrino mass and dark matter*, *Phys. Rev. D* **73** (2006) 077301 [`hep-ph/0601225`].

[71] N.G. Deshpande and E. Ma, *Pattern of Symmetry Breaking with Two Higgs Doublets*, *Phys. Rev. D* **18** (1978) 2574.

[72] R. Barbieri, L.J. Hall and V.S. Rychkov, *Improved naturalness with a heavy Higgs: An Alternative road to LHC physics*, *Phys. Rev. D* **74** (2006) 015007 [`hep-ph/0603188`].

[73] G. Arcadi, M. Dutra, P. Ghosh, M. Lindner, Y. Mambrini, M. Pierre et al., *The waning of the WIMP? A review of models, searches, and constraints*, *Eur. Phys. J. C* **78** (2018) 203 [`1703.07364`].

[74] G. Arcadi, D. Cabo-Almeida, M. Dutra, P. Ghosh, M. Lindner, Y. Mambrini et al., *The Waning of the WIMP: Endgame?*, `2403.15860`.

[75] Y. Tang and Y.-L. Wu, *On Thermal Gravitational Contribution to Particle Production and Dark Matter*, *Phys. Lett. B* **774** (2017) 676 [`1708.05138`].

[76] M. Drees, F. Hajkarim and E.R. Schmitz, *The Effects of QCD Equation of State on the Relic Density of WIMP Dark Matter*, *JCAP* **06** (2015) 025 [`1503.03513`].

[77] K. Griest and D. Seckel, *Three exceptions in the calculation of relic abundances*, *Phys. Rev. D* **43** (1991) 3191.

[78] T. Binder, L. Covi, A. Kamada, H. Murayama, T. Takahashi and N. Yoshida, *Matter Power Spectrum in Hidden Neutrino Interacting Dark Matter Models: A Closer Look at the Collision Term*, *JCAP* **11** (2016) 043 [`1602.07624`].

[79] B.W. Lee and S. Weinberg, *Cosmological lower bound on heavy-neutrino masses*, *Phys. Rev. Lett.* **39** (1977) 165.

[80] P. Gondolo and G. Gelmini, *Cosmic abundances of stable particles: Improved analysis*, *Nucl. Phys. B* **360** (1991) 145.

[81] J. Edsjö and P. Gondolo, *Neutralino relic density including coannihilations*, *Phys. Rev. D* **56** (1997) 1879 [`hep-ph/9704361`].

[82] L.G. van den Aarssen, T. Bringmann and Y.C. Goedecke, *Thermal decoupling and the smallest subhalo mass in dark matter models with Sommerfeld-enhanced annihilation rates*, *Phys. Rev. D* **85** (2012) 123512 [`1202.5456`].

[83] T. Binder, T. Bringmann, M. Gustafsson and A. Hryczuk, *Early kinetic decoupling of dark matter: when the standard way of calculating the thermal relic density fails*, *Phys. Rev. D* **96** (2017) 115010 [`1706.07433`].

[84] T. Binder, T. Bringmann, M. Gustafsson and A. Hryczuk, *Dark matter relic abundance beyond kinetic equilibrium*, *Eur. Phys. J. C* **81** (2021) 577 [`2103.01944`].

[85] M. Hindmarsh and O. Philipsen, *WIMP dark matter and the QCD equation of state*, *Phys. Rev. D* **71** (2005) 087302 [`hep-ph/0501232`].

[86] G. Steigman, B. Dasgupta and J.F. Beacom, *Precise Relic WIMP Abundance and its Impact on Searches for Dark Matter Annihilation*, *Phys. Rev. D* **86** (2012) 023506 [`1204.3622`].

[87] M. Laine and M. Meyer, *Standard Model thermodynamics across the electroweak crossover*, *JCAP* **07** (2015) 035 [`1503.04935`].

[88] S. Borsanyi et al., *Calculation of the axion mass based on high-temperature lattice quantum chromodynamics*, *Nature* **539** (2016) 69 [`1606.07494`].

[89] K. Saikawa and S. Shirai, *Precise WIMP Dark Matter Abundance and Standard Model Thermodynamics*, *JCAP* **08** (2020) 011 [`2005.03544`].

[90] A. Arbey and F. Mahmoudi, *SUSY constraints from relic density: High sensitivity to pre-BBN expansion rate*, *Phys. Lett. B* **669** (2008) 46 [`0803.0741`].

[91] Y. Cui, M. Lewicki, D.E. Morrissey and J.D. Wells, *Probing the pre-BBN universe with gravitational waves from cosmic strings*, *JHEP* **01** (2019) 081 [`1808.08968`].

[92] C.E. Yaguna, *Large contributions to dark matter annihilation from three-body final states*, *Phys. Rev. D* **81** (2010) 075024 [`1003.2730`].

[93] T. Bringmann and F. Calore, *Significant Enhancement of Neutralino Dark Matter Annihilation from Electroweak Bremsstrahlung*, *Phys. Rev. Lett.* **112** (2014) 071301 [`1308.1089`].

[94] B. von Harling and K. Petraki, *Bound-state formation for thermal relic dark matter and unitarity*, *JCAP* **12** (2014) 033 [`1407.7874`].

[95] J. Ellis, F. Luo and K.A. Olive, *Gluino Coannihilation Revisited*, *JHEP* **09** (2015) 127 [`1503.07142`].

[96] T. Wizansky, *Finite temperature corrections to relic density calculations*, *Phys. Rev. D* **74** (2006) 065007 [`hep-ph/0605179`].

[97] M. Beneke, F. Dighera and A. Hryczuk, *Relic density computations at NLO: infrared finiteness and thermal correction*, *JHEP* **10** (2014) 045 [`1409.3049`].

[98] P. Butola, D. Indumathi and P. Sen, *NLO thermal corrections to dark matter annihilation cross sections: A novel approach*, *Phys. Rev. D* **110** (2024) 036006 [`2404.15987`].

[99] A. Aboubrahim, M. Klasen and L.P. Wiggering, *Forbidden dark matter annihilation into leptons with full collision terms*, *JCAP* **08** (2023) 075 [`2306.07753`].

[100] H.E.S.S. collaboration, *Search for Dark Matter Annihilation Signals in the H.E.S.S. Inner Galaxy Survey*, *Phys. Rev. Lett.* **129** (2022) 111101 [`2207.10471`].

[101] VERITAS collaboration, *Dark Matter Constraints from a Joint Analysis of Dwarf Spheroidal Galaxy Observations with VERITAS*, *Phys. Rev. D* **95** (2017) 082001 [`1703.04937`].

[102] MAGIC collaboration, *A search for dark matter in Triangulum II with the MAGIC telescopes*, *Phys. Dark Univ.* **28** (2020) 100529 [`2003.05260`].

[103] CTA collaboration, *Sensitivity of the Cherenkov Telescope Array to a dark matter signal from the Galactic centre*, *JCAP* **01** (2021) 057 [`2007.16129`].

[104] Fermi-LAT collaboration, *Searching for Dark Matter Annihilation from Milky Way Dwarf Spheroidal Galaxies with Six Years of Fermi Large Area Telescope Data*, *Phys. Rev. Lett.* **115** (2015) 231301 [`1503.02641`].

[105] HAWC collaboration, *Dark Matter Limits From Dwarf Spheroidal Galaxies with The HAWC Gamma-Ray Observatory*, *Astrophys. J.* **853** (2018) 154 [`1706.01277`].

[106] Hess, HAWC, VERITAS, MAGIC, H.E.S.S., Fermi-LAT collaboration, *Combined dark matter searches towards dwarf spheroidal galaxies with Fermi-LAT, HAWC, H.E.S.S., MAGIC, and VERITAS*, *PoS* **ICRC2021** (2021) 528 [`2108.13646`].

[107] HESS collaboration, *Search for γ-Ray Line Signals from Dark Matter Annihilations in the Inner Galactic Halo from 10 Years of Observations with H.E.S.S.*, *Phys. Rev. Lett.* **120** (2018) 201101 [`1805.05741`].

[108] MAGIC collaboration, *Search for Gamma-Ray Spectral Lines from Dark Matter Annihilation up to 100 TeV toward the Galactic Center with MAGIC*, *Phys. Rev. Lett.* **130** (2023) 061002 [`2212.10527`].

[109] F. Calore, M. Cirelli, L. Derome, Y. Genolini, D. Maurin, P. Salati et al., *AMS-02 antiprotons and dark matter: Trimmed hints and robust bounds*, *SciPost Phys.* **12** (2022) 163 [`2202.03076`].

[110] IceCube collaboration, *Search for Neutrinos from Dark Matter Self-Annihilations in the center of the Milky Way with 3 years of IceCube/DeepCore*, *Eur. Phys. J. C* **77** (2017) 627 [`1705.08103`].

[111] Super-Kamiokande collaboration, *Indirect search for dark matter from the Galactic Center and halo with the Super-Kamiokande detector*, *Phys. Rev. D* **102** (2020) 072002 [`2005.05109`].

[112] ANTARES collaboration, *Search for dark matter towards the Galactic Centre with 11 years of ANTARES data*, *Phys. Lett. B* **805** (2020) 135439 [`1912.05296`].

[113] KM3NeT collaboration, *Letter of intent for KM3NeT 2.0*, *J. Phys. G* **43** (2016) 084001 [`1601.07459`].

[114] K. Abe et al., *Letter of Intent: The Hyper-Kamiokande Experiment — Detector Design and Physics Potential —*, `1109.3262`.

[115] IceCube-PINGU collaboration, *Letter of Intent: The Precision IceCube Next Generation Upgrade (PINGU)*, `1401.2046`.

[116] Particle Data Group collaboration, *Review of particle physics*, *Phys. Rev. D* **110** (2024) 030001.

[117] IceCube collaboration, *Search for annihilating dark matter in the Sun with 3 years of IceCube data*, *Eur. Phys. J. C* **77** (2017) 146 [`1612.05949`].

[118] D.G. Cerdeno and A.M. Green, *Direct detection of WIMPs*, `1002.1912`.

[119] PandaX-4T collaboration, *Dark Matter Search Results from the PandaX-4T Commissioning Run*, *Phys. Rev. Lett.* **127** (2021) 261802 [`2107.13438`].

[120] XENON collaboration, *Search for Light Dark Matter Interactions Enhanced by the Migdal Effect or Bremsstrahlung in XENON1T*, *Phys. Rev. Lett.* **123** (2019) 241803 [`1907.12771`].

[121] XENON collaboration, *First Dark Matter Search with Nuclear Recoils from the XENONnT Experiment*, *Phys. Rev. Lett.* **131** (2023) 041003 [`2303.14729`].

[122] LZ collaboration, *First Dark Matter Search Results from the LUX-ZEPLIN (LZ) Experiment*, *Phys. Rev. Lett.* **131** (2023) 041002 [`2207.03764`].

[123] DarkSide-50 collaboration, *Search for low-mass dark matter WIMPs with 12 ton-day exposure of DarkSide-50*, *Phys. Rev. D* **107** (2023) 063001 [`2207.11966`].

[124] DEAP collaboration, *Search for dark matter with a 231-day exposure of liquid argon using DEAP-3600 at SNOLAB*, *Phys. Rev. D* **100** (2019) 022004 [`1902.04048`].

[125] SuperCDMS collaboration, *Results from the Super Cryogenic Dark Matter Search Experiment at Soudan*, *Phys. Rev. Lett.* **120** (2018) 061802 [`1708.08869`].

[126] SuperCDMS collaboration, *Search for Low-Mass Dark Matter with CDMSlite Using a Profile Likelihood Fit*, *Phys. Rev. D* **99** (2019) 062001 [`1808.09098`].

[127] DAMIC collaboration, *Results on low-mass weakly interacting massive particles from a 11 kg-day target exposure of DAMIC at SNOLAB*, *Phys. Rev. Lett.* **125** (2020) 241803 [`2007.15622`].

[128] CRESST collaboration, *First results from the CRESST-III low-mass dark matter program*, *Phys. Rev. D* **100** (2019) 102002 [`1904.00498`].

[129] DARWIN collaboration, *DARWIN: towards the ultimate dark matter detector*, *JCAP* **11** (2016) 017 [`1606.07001`].

[130] S.E. Vahsen et al., *CYGNUS: Feasibility of a nuclear recoil observatory with directional sensitivity to dark matter and neutrinos*, `2008.12587`.

[131] XENON collaboration, *Constraining the spin-dependent WIMP-nucleon cross sections with XENON1T*, *Phys. Rev. Lett.* **122** (2019) 141301 [`1902.03234`].

[132] CRESST collaboration, *Results on MeV-scale dark matter from a gram-scale cryogenic calorimeter operated above ground*, *Eur. Phys. J. C* **77** (2017) 637 [`1707.06749`].

[133] CRESST collaboration, *First results on sub-GeV spin-dependent dark matter interactions with*^{7}*Li*, *Eur. Phys. J. C* **79** (2019) 630 [`1902.07587`].

[134] EDELWEISS collaboration, *Searching for low-mass dark matter particles with a massive Ge bolometer operated above-ground*, *Phys. Rev. D* **99** (2019) 082003 [`1901.03588`].

[135] CDEX collaboration, *Limits on Light Weakly Interacting Massive Particles from the First 102.8 kg × day Data of the CDEX-10 Experiment*, *Phys. Rev. Lett.* **120** (2018) 241301 [`1802.09016`].

[136] CDEX collaboration, *Constraints on sub-GeV dark matter boosted by cosmic rays from the CDEX-10 experiment at the China Jinping Underground Laboratory*, *Phys. Rev. D* **106** (2022) 052008 [`2201.01704`].

[137] CDMS collaboration, *Exclusion limits on the WIMP-nucleon cross section from the first run of the Cryogenic Dark Matter Search in the Soudan Underground Laboratory*, *Phys. Rev. D* **72** (2005) 052009 [`astro-ph/0507190`].

[138] SuperCDMS collaboration, *Low-mass dark matter search with CDMSlite*, *Phys. Rev. D* **97** (2018) 022002 [`1707.01632`].

[139] UK Dark Matter collaboration, *Limits on WIMP cross-sections from the NAIAD experiment at the Boulby Underground Laboratory*, *Phys. Lett. B* **616** (2005) 17 [`hep-ex/0504031`].

[140] COSINE-100 collaboration, *Searching for low-mass dark matter via the Migdal effect in COSINE-100*, *Phys. Rev. D* **105** (2022) 042006 [`2110.05806`].

[141] PICO collaboration, *Dark Matter Search Results from the Complete Exposure of the PICO-60* C_3F_8 *Bubble Chamber*, *Phys. Rev. D* **100** (2019) 022001 [`1902.04031`].

[142] R. Bernabei et al., *First model independent results from DAMA/LIBRA-phase2*, *Nucl. Phys. Atom. Energy* **19** (2018) 307 [`1805.10486`].

[143] COSINE-100 collaboration, *Comparison between DAMA/LIBRA and COSINE-100 in the light of Quenching Factors*, *JCAP* **11** (2019) 008 [`1907.04963`].

[144] OPAL collaboration, *Search for stable and longlived massive charged particles in e+ e- collisions at s**(1/2) = 130-GeV to 209-GeV*, *Phys. Lett. B* **572** (2003) 8 [`hep-ex/0305031`].

[145] A. De Simone and T. Jacques, *Simplified models vs. effective field theory approaches in dark matter searches*, *Eur. Phys. J. C* **76** (2016) 367 [`1603.08002`].

[146] ATLAS collaboration, *The ATLAS Experiment at the CERN Large Hadron Collider*, *JINST* **3** (2008) S08003.

[147] CMS collaboration, *The CMS Experiment at the CERN LHC*, *JINST* **3** (2008) S08004.

[148] ATLAS collaboration, *Search for invisible Higgs-boson decays in events with vector-boson fusion signatures using 139 fb^{-1} of proton-proton data recorded by the ATLAS experiment*, *JHEP* **08** (2022) 104 [`2202.07953`].

[149] CMS collaboration, *Search for invisible decays of the Higgs boson produced via vector boson fusion in proton-proton collisions at s=13 TeV*, *Phys. Rev. D* **105** (2022) 092007 [`2201.11585`].

[150] J.D. Bjorken, S. Ecklund, W.R. Nelson, A. Abashian, C. Church, B. Lu et al., *Search for Neutral Metastable Penetrating Particles Produced in the SLAC Beam Dump*, *Phys. Rev. D* **38** (1988) 3375.

[151] G. Krnjaic, G. Marques-Tavares, D. Redigolo and K. Tobioka, *Probing Muonphilic Force Carriers and Dark Matter at Kaon Factories*, *Phys. Rev. Lett.* **124** (2020) 041802 [`1902.07715`].

[152] D. d'Enterria, *Physics at the FCC-ee*, in *17th Lomonosov Conference on Elementary Particle Physics*, pp. 182–191, 2017, DOI [`1602.05043`].

[153] ILC collaboration, *The International Linear Collider. A Global Project*, `1901.09829`.

[154] CEPC Physics Study Group collaboration, *The Physics potential of the CEPC. Prepared for the US Snowmass Community Planning Exercise (Snowmass 2021)*, in *Snowmass 2021*, 5, 2022 [`2205.08553`].

[155] FCC collaboration, *FCC-hh: The Hadron Collider: Future Circular Collider Conceptual Design Report Volume 3*, *Eur. Phys. J. ST* **228** (2019) 755.

[156] C. Accettura et al., *Towards a muon collider*, *Eur. Phys. J. C* **83** (2023) 864 [`2303.08533`].

[157] A. Freitas, *Radiative corrections to co-annihilation processes*, *Phys. Lett. B* **652** (2007) 280 [`0705.4027`].

[158] B. Herrmann and M. Klasen, *SUSY-QCD Corrections to Dark Matter Annihilation in the Higgs Funnel*, *Phys. Rev. D* **76** (2007) 117704 [`0709.0043`].

[159] N. Baro, F. Boudjema and A. Semenov, *Full one-loop corrections to the relic density in the MSSM: A Few examples*, *Phys. Lett. B* **660** (2008) 550 [`0710.1821`].

[160] N. Baro, F. Boudjema and A. Semenov, *Automatised full one-loop renormalisation of the MSSM. I. The Higgs sector, the issue of tan(beta) and gauge invariance*, *Phys. Rev. D* **78** (2008) 115003 [`0807.4668`].

[161] N. Baro and F. Boudjema, *Automatised full one-loop renormalisation of the MSSM II: The chargino-neutralino sector, the sfermion sector and some applications*, *Phys. Rev. D* **80** (2009) 076010 [`0906.1665`].

[162] B. Herrmann, M. Klasen and K. Kovařík, *Neutralino Annihilation into Massive Quarks with SUSY-QCD Corrections*, *Phys. Rev. D* **79** (2009) 061701 [`0901.0481`].

[163] B. Herrmann, M. Klasen and K. Kovařík, *SUSY-QCD effects on neutralino dark matter annihilation beyond scalar or gaugino mass unification*, *Phys. Rev. D* **80** (2009) 085025 [`0907.0030`].

[164] J. Harz, B. Herrmann, M. Klasen, K. Kovařík and Q.L. Boulc'h, *Neutralino-stop coannihilation into electroweak gauge and Higgs bosons at one loop*, *Phys. Rev. D* **87** (2013) 054031 [`1212.5241`].

[165] J. Harz, B. Herrmann, M. Klasen and K. Kovařík, *One-loop corrections to neutralino-stop coannihilation revisited*, *Phys. Rev. D* **91** (2015) 034028 [`1409.2898`].

[166] B. Herrmann, M. Klasen, K. Kovařík, M. Meinecke and P. Steppeler, *One-loop corrections to gaugino (co)annihilation into quarks in the MSSM*, *Phys. Rev. D* **89** (2014) 114012 [`1404.2931`].

[167] J. Harz, B. Herrmann, M. Klasen, K. Kovařík and M. Meinecke, *SUSY-QCD corrections to stop annihilation into electroweak final states including Coulomb enhancement effects*, *Phys. Rev. D* **91** (2015) 034012 [`1410.8063`].

[168] T. Bringmann, A.J. Galea and P. Walia, *Leading QCD Corrections for Indirect Dark Matter Searches: a Fresh Look*, *Phys. Rev. D* **93** (2016) 043529 [`1510.02473`].

[169] S. Schmiemann, J. Harz, B. Herrmann, M. Klasen and K. Kovařík, *Squark-pair annihilation into quarks at next-to-leading order*, *Phys. Rev. D* **99** (2019) 095015 [`1903.10998`].

[170] J. Branahl, J. Harz, B. Herrmann, M. Klasen, K. Kovařík and S. Schmiemann, *SUSY-QCD corrected and Sommerfeld enhanced stau annihilation into heavy quarks with scheme and scale uncertainties*, *Phys. Rev. D* **100** (2019) 115003 [`1909.09527`].

[171] M. Klasen, K. Kovařík and L.P. Wiggering, *Radiative corrections to stop-antistop annihilation into gluons and light quarks*, *Phys. Rev. D* **106** (2022) 115032 [`2210.05260`].

[172] G. Bélanger, V. Bizouard, F. Boudjema and G. Chalons, *One-loop renormalization of the NMSSM in SloopS: The neutralino-chargino and sfermion sectors*, *Phys. Rev. D* **93** (2016) 115031 [`1602.05495`].

[173] G. Bélanger, V. Bizouard, F. Boudjema and G. Chalons, *One-loop renormalization of the NMSSM in SloopS. II. The Higgs sector*, *Phys. Rev. D* **96** (2017) 015040 [`1705.02209`].

[174] S. Banerjee, F. Boudjema, N. Chakrabarty, G. Chalons and H. Sun, *Relic density of dark matter in the inert doublet model beyond leading order: The heavy mass case*, *Phys. Rev. D* **100** (2019) 095024 [`1906.11269`].

[175] S. Banerjee, F. Boudjema, N. Chakrabarty and H. Sun, *Relic density of dark matter in the inert doublet model beyond leading order for the low mass region: 1. Renormalisation and constraints*, *Phys. Rev. D* **104** (2021) 075002 [`2101.02165`].

[176] R. Iengo, *Sommerfeld enhancement: General results from field theory diagrams*, *JHEP* **05** (2009) 024 [`0902.0688`].

[177] M. Beneke, A. Bharucha, F. Dighera, C. Hellmann, A. Hryczuk, S. Recksiegel et al., *Relic density of wino-like dark matter in the MSSM*, *JHEP* **03** (2016) 119 [`1601.04718`].

[178] J. Harz and K. Petraki, *Higgs Enhancement for the Dark Matter Relic Density*, *Phys. Rev. D* **97** (2018) 075041 [`1711.03552`].

[179] J. Harz and K. Petraki, *Radiative bound-state formation in unbroken perturbative non-Abelian theories and implications for dark matter*, *JHEP* **07** (2018) 096 [`1805.01200`].

[180] S. Biondini, *Bound-state effects for dark matter with Higgs-like mediators*, *JHEP* **06** (2018) 104 [`1805.00353`].

[181] J. Harz and K. Petraki, *Higgs-mediated bound states in dark-matter models*, *JHEP* **04** (2019) 130 [`1901.10030`].

[182] J. Harz, B. Herrmann, M. Klasen, K. Kovarik and P. Steppeler, *Theoretical uncertainty of the supersymmetric dark matter relic density from scheme and scale variations*, *Phys. Rev. D* **93** (2016) 114023 [`1602.08103`].

[183] A. Hryczuk and R. Iengo, *The one-loop and Sommerfeld electroweak corrections to the Wino dark matter annihilation*, *JHEP* **01** (2012) 163 [`1111.2916`].

[184] A. Hryczuk, I. Cholis, R. Iengo, M. Tavakoli and P. Ullio, *Indirect Detection Analysis: Wino Dark Matter Case Study*, *JCAP* **07** (2014) 031 [`1401.6212`].

[185] M. Baumgart, T. Cohen, I. Moult, N.L. Rodd, T.R. Slatyer, M.P. Solon et al., *Resummed Photon Spectra for WIMP Annihilation*, *JHEP* **03** (2018) 117 [`1712.07656`].

[186] M. Baumgart, T. Cohen, E. Moulin, I. Moult, L. Rinchiuso, N.L. Rodd et al., *Precision Photon Spectra for Wino Annihilation*, *JHEP* **01** (2019) 036 [`1808.08956`].

[187] M. Drees and M.M. Nojiri, *New contributions to coherent neutralino - nucleus scattering*, *Phys. Rev. D* **47** (1993) 4226 [`hep-ph/9210272`].

[188] M. Drees and M. Nojiri, *Neutralino - nucleon scattering revisited*, *Phys. Rev. D* **48** (1993) 3483 [`hep-ph/9307208`].

[189] J. Hisano, S. Matsumoto, M.M. Nojiri and O. Saito, *Direct detection of the Wino and Higgsino-like neutralino dark matters at one-loop level*, *Phys. Rev. D* **71** (2005) 015007 [`hep-ph/0407168`].

[190] A. Berlin, D.S. Robertson, M.P. Solon and K.M. Zurek, *Bino variations: Effective field theory methods for dark matter direct detection*, *Phys. Rev. D* **93** (2016) 095008 [`1511.05964`].

[191] M. Klasen, K. Kovarik and P. Steppeler, *SUSY-QCD corrections for direct detection of neutralino dark matter and correlations with relic density*, *Phys. Rev. D* **94** (2016) 095002 [`1607.06396`].

[192] S. Bisal, A. Chatterjee, D. Das and S.A. Pasha, *Radiative corrections to aid the direct detection of the Higgsino-like neutralino dark matter: Spin-independent interactions*, *Phys. Rev. D* **110** (2024) 023043 [`2311.09937`].

[193] S. Bisal, A. Chatterjee, D. Das and S.A. Pasha, *Confronting electroweak MSSM through one-loop renormalized neutralino-Higgs interactions for dark matter direct detection and the muon g-2*, *Phys. Rev. D* **110** (2024) 015021 [`2311.09938`].

[194] M. Klasen, C.E. Yaguna and J.D. Ruiz-Alvarez, *Electroweak corrections to the direct detection cross section of inert higgs dark matter*, *Phys. Rev. D* **87** (2013) 075025 [`1302.1657`].

[195] T. Abe and R. Sato, *Quantum corrections to the spin-independent cross section of the inert doublet dark matter*, *JHEP* **03** (2015) 109 [`1501.04161`].

[196] D. Azevedo, M. Duch, B. Grzadkowski, D. Huang, M. Iglicki and R. Santos, *One-loop contribution to dark-matter-nucleon scattering in the pseudo-scalar dark matter model*, *JHEP* **01** (2019) 138 [`1810.06105`].

[197] K. Ishiwata and T. Toma, *Probing pseudo Nambu-Goldstone boson dark matter at loop level*, *JHEP* **12** (2018) 089 [`1810.08139`].

[198] K. Ghorbani and P.H. Ghorbani, *Leading Loop Effects in Pseudoscalar-Higgs Portal Dark Matter*, *JHEP* **05** (2019) 096 [`1812.04092`].

[199] T. Abe, M. Fujiwara and J. Hisano, *Loop corrections to dark matter direct detection in a pseudoscalar mediator dark matter model*, *JHEP* **02** (2019) 028 [`1810.01039`].

[200] S. Glaus, M. Mühlleitner, J. Müller, S. Patel and R. Santos, *Electroweak corrections to dark matter direct detection in the dark singlet phase of the N2HDM*, *Phys. Lett. B* **833** (2022) 137342 [`2204.13145`].

[201] S. Glaus, M. Mühlleitner, J. Müller, S. Patel and R. Santos, *Electroweak Corrections to Dark Matter Direct Detection in a Vector Dark Matter Model*, *JHEP* **10** (2019) 152 [`1908.09249`].

[202] T. Biekötter, P. Gabriel, M.O. Olea-Romacho and R. Santos, *Direct detection of pseudo-Nambu-Goldstone dark matter in a two Higgs doublet plus singlet extension of the SM*, *JHEP* **10** (2022) 126 [`2207.04973`].

[203] A. Berlin, D. Hooper and S.D. McDermott, *Dark matter elastic scattering through Higgs loops*, *Phys. Rev. D* **92** (2015) 123531 [`1508.05390`].

[204] F. Ertas and F. Kahlhoefer, *Loop-induced direct detection signatures from CP-violating scalar mediators*, *JHEP* **06** (2019) 052 [`1902.11070`].

[205] C. Borschensky, G. Coniglio, B. Jäger, J. Jochum and V. Schipperges, *Direct detection of dark matter: Precision predictions in a simplified model framework*, *Eur. Phys. J. C* **81** (2021) 44 [`2008.04253`].

[206] U. Haisch and F. Kahlhoefer, *On the importance of loop-induced spin-independent interactions for dark matter direct detection*, *JCAP* **04** (2013) 050 [`1302.4454`].

[207] A. Crivellin, F. D'Eramo and M. Procura, *New Constraints on Dark Matter Effective Theories from Standard Model Loops*, *Phys. Rev. Lett.* **112** (2014) 191304 [`1402.1173`].

[208] P. Gondolo, J. Edsjo, P. Ullio, L. Bergstrom, M. Schelke and E.A. Baltz, *DarkSUSY: Computing supersymmetric dark matter properties numerically*, *JCAP* **07** (2004) 008 [`astro-ph/0406204`].

[209] T. Bringmann, J. Edsjö, P. Gondolo, P. Ullio and L. Bergström, *DarkSUSY 6 : An Advanced Tool to Compute Dark Matter Properties Numerically*, *JCAP* **07** (2018) 033 [`1802.03399`].

[210] A. Arbey and F. Mahmoudi, *SuperIso Relic: A Program for calculating relic density and flavor physics observables in Supersymmetry*, *Comput. Phys. Commun.* **181** (2010) 1277 [`0906.0369`].

[211] A. Arbey and F. Mahmoudi, *SuperIso Relic v3.0: A program for calculating relic density and flavour physics observables: Extension to NMSSM*, *Comput. Phys. Commun.* **182** (2011) 1582.

[212] A. Arbey, F. Mahmoudi and G. Robbins, *SuperIso Relic v4: A program for calculating dark matter and flavour physics observables in Supersymmetry*, *Comput. Phys. Commun.* **239** (2019) 238 [`1806.11489`].

[213] G. Belanger, F. Boudjema, A. Pukhov and A. Semenov, *MicrOMEGAs: A Program for calculating the relic density in the MSSM*, *Comput. Phys. Commun.* **149** (2002) 103 [`hep-ph/0112278`].

[214] G. Belanger, F. Boudjema, A. Pukhov and A. Semenov, *MicrOMEGAs 2.0: A Program to calculate the relic density of dark matter in a generic model*, *Comput. Phys. Commun.* **176** (2007) 367 [`hep-ph/0607059`].

[215] G. Bélanger, F. Boudjema, A. Goudelis, A. Pukhov and B. Zaldivar, *micrOMEGAs5.0 : Freeze-in*, *Comput. Phys. Commun.* **231** (2018) 173 [`1801.03509`].

[216] G. Alguero, G. Belanger, F. Boudjema, S. Chakraborti, A. Goudelis, S. Kraml et al., *micrOMEGAs 6.0: N-component dark matter*, *Comput. Phys. Commun.* **299** (2024) 109133 [`2312.14894`].

[217] M. Backovic, K. Kong and M. McCaskey, *MadDM v.1.0: Computation of Dark Matter Relic Abundance Using MadGraph5*, *Physics of the Dark Universe* **5-6** (2014) 18 [`1308.4955`].

[218] F. Ambrogi, C. Arina, M. Backovic, J. Heisig, F. Maltoni, L. Mantani et al., *MadDM v.3.0: a Comprehensive Tool for Dark Matter Studies*, *Phys. Dark Univ.* **24** (2019) 100249 [`1804.00044`].

[219] J. Wess and B. Zumino, *A Lagrangian Model Invariant Under Supergauge Transformations*, *Phys. Lett. B* **49** (1974) 52.

[220] J. Wess and B. Zumino, *Supergauge Transformations in Four-Dimensions*, *Nucl. Phys. B* **70** (1974) 39.

[221] S. Dimopoulos and H. Georgi, *Softly Broken Supersymmetry and SU(5)*, *Nucl. Phys. B* **193** (1981) 150.

[222] M. Drees, R. Godbole and P. Roy, *Theory And Phenomenology Of Sparticles: An Account Of Four-dimensional N=1 Supersymmetry In High Energy Physics*, World Scientific Publishing Company (2005).

[223] I.J.R. Aitchison, *Supersymmetry in Particle Physics. An Elementary Introduction*, Cambridge University Press, Cambridge (2007), 10.1017/CBO9780511619250.

[224] H.E. Haber and G.L. Kane, *The Search for Supersymmetry: Probing Physics Beyond the Standard Model*, *Phys. Rept.* **117** (1985) 75.

[225] S.P. Martin, *A Supersymmetry primer*, *Adv. Ser. Direct. High Energy Phys.* **18** (1998) 1 [`hep-ph/9709356`].

[226] J.A. Aguilar-Saavedra et al., *Supersymmetry parameter analysis: SPA convention and project*, *Eur. Phys. J. C* **46** (2006) 43 [`hep-ph/0511344`].

[227] MSSM Working Group collaboration, *The Minimal supersymmetric standard model: Group summary report*, in *GDR (Groupement De Recherche) - Supersymetrie*, 12, 1998 [`hep-ph/9901246`].

[228] W. Pauli and F. Villars, *On the Invariant regularization in relativistic quantum theory*, *Rev. Mod. Phys.* **21** (1949) 434.

[229] G. 't Hooft, *Lattice regularization of gauge theories without loss of chiral symmetry*, *Phys. Lett. B* **349** (1995) 491 [`hep-th/9411228`].

[230] M.E. Peskin and D.V. Schroeder, *An Introduction to quantum field theory*, Addison-Wesley, Reading, USA (1995), 10.1201/9780429503559.

[231] G. 't Hooft and M.J.G. Veltman, *Regularization and Renormalization of Gauge Fields*, *Nucl. Phys. B* **44** (1972) 189.

[232] W. Siegel, *Supersymmetric Dimensional Regularization via Dimensional Reduction*, *Phys. Lett. B* **84** (1979) 193.

[233] W. Siegel, *Inconsistency of Supersymmetric Dimensional Regularization*, *Phys. Lett. B* **94** (1980) 37.

[234] D. Stöckinger, *Regularization by dimensional reduction: consistency, quantum action principle, and supersymmetry*, *JHEP* **03** (2005) 076 [`hep-ph/0503129`].

[235] L. Mihaila, *Precision Calculations in Supersymmetric Theories*, *Adv. High Energy Phys.* **2013** (2013) 607807 [`1310.6178`].

[236] A. Signer and D. Stöckinger, *Using Dimensional Reduction for Hadronic Collisions*, *Nucl. Phys. B* **808** (2009) 88 [`0807.4424`].

[237] F. Jegerlehner, *Facts of life with gamma(5)*, *Eur. Phys. J. C* **18** (2001) 673 [`hep-th/0005255`].

[238] P. Breitenlohner and D. Maison, *Dimensional Renormalization and the Action Principle*, *Commun. Math. Phys.* **52** (1977) 11.

[239] G. Passarino and M.J.G. Veltman, *One Loop Corrections for e+ e- Annihilation Into mu+ mu- in the Weinberg Model*, *Nucl. Phys. B* **160** (1979) 151.

[240] A. Denner, *Techniques for calculation of electroweak radiative corrections at the one loop level and results for W physics at LEP-200*, *Fortsch. Phys.* **41** (1993) 307 [`0709.1075`].

[241] S. Dittmaier, *Separation of soft and collinear singularities from one loop N point integrals*, *Nucl. Phys. B* **675** (2003) 447 [`hep-ph/0308246`].

[242] R.K. Ellis and G. Zanderighi, *Scalar one-loop integrals for QCD*, *JHEP* **02** (2008) 002 [`0712.1851`].

[243] A. Denner and S. Dittmaier, *Scalar one-loop 4-point integrals*, *Nucl. Phys. B* **844** (2011) 199 [`1005.2076`].

[244] T. Hahn and M. Perez-Victoria, *Automatized one loop calculations in four-dimensions and D-dimensions*, *Comput. Phys. Commun.* **118** (1999) 153 [`hep-ph/9807565`].

[245] A. van Hameren, *OneLOop: For the evaluation of one-loop scalar functions*, *Comput. Phys. Commun.* **182** (2011) 2427 [`1007.4716`].

[246] A. Denner, S. Dittmaier and L. Hofer, *Collier: a fortran-based Complex One-Loop LIbrary in Extended Regularizations*, *Comput. Phys. Commun.* **212** (2017) 220 [`1604.06792`].

[247] S. Carrazza, R.K. Ellis and G. Zanderighi, *QCDLoop: a comprehensive framework for one-loop scalar integrals*, *Comput. Phys. Commun.* **209** (2016) 134 [`1605.03181`].

[248] J. Harz, B. Herrmann, M. Klasen, K. Kovařík and L.P. Wiggering, *Precision predictions for dark matter with DM@NLO in the MSSM*, *Eur. Phys. J. C* **84** (2024) 342 [`2312.17206`].

[249] S. Heinemeyer, H. Rzehak and C. Schappacher, *Proposals for Bottom Quark/Squark Renormalization in the Complex MSSM*, *Phys. Rev. D* **82** (2010) 075010 [`1007.0689`].

[250] S. Heinemeyer and F. von der Pahlen, *Automated choice for the best renormalization scheme in BSM models*, *Eur. Phys. J. C* **83** (2023) 865 [`2302.12187`].

[251] K. Kovařík, *Hitchhiker's Guide To Renormalization* (2020).

[252] W. Beenakker, R. Hopker, M. Spira and P.M. Zerwas, *Squark and gluino production at hadron colliders*, *Nucl. Phys. B* **492** (1997) 51 [`hep-ph/9610490`].

[253] T. Binoth, D. Goncalves Netto, D. Lopez-Val, K. Mawatari, T. Plehn and I. Wigmore, *Automized Squark-Neutralino Production to Next-to-Leading Order*, *Phys. Rev. D* **84** (2011) 075005 [`1108.1250`].

[254] A. Sommerfeld, *Über die Beugung und Bremsung der Elektronen*, *Annalen Phys.* **403** (1931) 257.

[255] A.D. Sakharov, *Interaction of an Electron and Positron in Pair Production*, *Zh. Eksp. Teor. Fiz.* **18** (1948) 631.

[256] J. Abdallah et al., *Simplified Models for Dark Matter Searches at the LHC*, *Phys. Dark Univ.* **9-10** (2015) 8 [`1506.03116`].

[257] M. Becker, E. Copello, J. Harz, K.A. Mohan and D. Sengupta, *Impact of Sommerfeld effect and bound state formation in simplified t-channel dark matter models*, *JHEP* **08** (2022) 145 [`2203.04326`].

[258] T. Kinoshita, *Mass singularities of Feynman amplitudes*, *J. Math. Phys.* **3** (1962) 650.

[259] S. Frixione, Z. Kunszt and A. Signer, *Three jet cross-sections to next-to-leading order*, *Nucl. Phys. B* **467** (1996) 399 [`hep-ph/9512328`].

[260] S. Catani and M.H. Seymour, *A General algorithm for calculating jet cross-sections in NLO QCD*, *Nucl. Phys. B* **485** (1997) 291 [`hep-ph/9605323`].

[261] S. Catani, S. Dittmaier, M.H. Seymour and Z. Trocsanyi, *The Dipole formalism for next-to-leading order QCD calculations with massive partons*, *Nucl. Phys. B* **627** (2002) 189 [`hep-ph/0201036`].

[262] W.T. Giele and E.W.N. Glover, *Higher order corrections to jet cross-sections in e+ e- annihilation*, *Phys. Rev. D* **46** (1992) 1980.

[263] K. Fabricius, I. Schmitt, G. Kramer and G. Schierholz, *Higher Order Perturbative QCD Calculation of Jet Cross-Sections in e+ e- Annihilation*, *Z. Phys. C* **11** (1981) 315.

[264] G. Kramer and B. Lampe, *Jet Cross-Sections in e+ e- Annihilation*, *Fortsch. Phys.* **37** (1989) 161.

[265] B.W. Harris and J.F. Owens, *The Two cutoff phase space slicing method*, *Phys. Rev. D* **65** (2002) 094032 [`hep-ph/0102128`].

[266] S. Dittmaier, *A General approach to photon radiation off fermions*, *Nucl. Phys. B* **565** (2000) 69 [`hep-ph/9904440`].

[267] P. Kotko, *General Mass Scheme for Jet Production in QCD (revised version)*, Ph.D. thesis, Jagiellonian U. (main), 2012.

[268] P. Kotko and W. Slominski, *General Mass Scheme for Jet Production in DIS*, *Phys. Rev. D* **86** (2012) 094008 [`1206.4024`].

[269] F. Krauss and D. Napoletano, *Towards a fully massive five-flavor scheme*, *Phys. Rev. D* **98** (2018) 096002 [`1712.06832`].

[270] T.O. Eynck, E. Laenen, L. Phaf and S. Weinzierl, *Comparison of phase space slicing and dipole subtraction methods for* $\gamma^* \to Q\bar{Q}$, *Eur. Phys. J. C* **23** (2002) 259 [`hep-ph/0109246`].

[271] J. Harz, M. Klasen, M.Y. Sassi and L.P. Wiggering, *Dipole formalism for massive initial-state particles and its application to dark matter calculations*, *Phys. Rev. D* **107** (2023) 056020 [`2210.03409`].

[272] G. Altarelli and G. Parisi, *Asymptotic freedom in parton language*, *Nuclear Physics B* **126** (1977) 298.

[273] S. Catani, M.H. Seymour and Z. Trocsanyi, *Regularization scheme independence and unitarity in QCD cross-sections*, *Phys. Rev. D* **55** (1997) 6819 [`hep-ph/9610553`].

[274] W. Porod, *SPheno, a program for calculating supersymmetric spectra, SUSY particle decays and SUSY particle production at e+ e- colliders*, *Comput. Phys. Commun.* **153** (2003) 275 [`hep-ph/0301101`].

[275] W. Porod and F. Staub, *SPheno 3.1: Extensions including flavour, CP-phases and models beyond the MSSM*, *Comput. Phys. Commun.* **183** (2012) 2458 [`1104.1573`].

[276] G.P. Lepage, *A New Algorithm for Adaptive Multidimensional Integration*, *J. Comput. Phys.* **27** (1978) 192.

[277] T. Hahn, *CUBA: A Library for multidimensional numerical integration*, *Comput. Phys. Commun.* **168** (2005) 78 [`hep-ph/0404043`].

[278] T. Hahn, *New features in FormCalc 4*, *Nucl. Phys. B Proc. Suppl.* **135** (2004) 333 [`hep-ph/0406288`].

[279] ATLAS collaboration, *Summary of the ATLAS experiment's sensitivity to supersymmetry after LHC Run 1 — interpreted in the phenomenological MSSM*, *JHEP* **10** (2015) 134 [`1508.06608`].

[280] S. Profumo and C.E. Yaguna, *A Statistical analysis of supersymmetric dark matter in the MSSM after WMAP*, *Phys. Rev. D* **70** (2004) 095004 [`hep-ph/0407036`].

[281] C. Boehm, A. Djouadi and M. Drees, *Light scalar top quarks and supersymmetric dark matter*, *Phys. Rev. D* **62** (2000) 035012 [`hep-ph/9911496`].

[282] J.R. Ellis, K.A. Olive and Y. Santoso, *Calculations of neutralino stop coannihilation in the CMSSM*, *Astropart. Phys.* **18** (2003) 395 [`hep-ph/0112113`].

[283] M.A. Ajaib, T. Li and Q. Shafi, *Stop-Neutralino Coannihilation in the Light of LHC*, *Phys. Rev. D* **85** (2012) 055021 [`1111.4467`].

[284] J. Ellis, K.A. Olive and J. Zheng, *The Extent of the Stop Coannihilation Strip*, *Eur. Phys. J. C* **74** (2014) 2947 [`1404.5571`].

[285] J. Ellis, J.L. Evans, F. Luo, K.A. Olive and J. Zheng, *Stop Coannihilation in the CMSSM and SubGUT Models*, *Eur. Phys. J. C* **78** (2018) 425 [`1801.09855`].

[286] D. Feldman, Z. Liu and P. Nath, *Gluino NLSP, Dark Matter via Gluino Coannihilation, and LHC Signatures*, *Phys. Rev. D* **80** (2009) 015007 [`0905.1148`].

[287] M. Drees and M.M. Nojiri, *The Neutralino relic density in minimal $N = 1$ supergravity*, *Phys. Rev. D* **47** (1993) 376 [`hep-ph/9207234`].

[288] ATLAS collaboration, *Observation of a new particle in the search for the Standard Model Higgs boson with the ATLAS detector at the LHC*, *Phys. Lett. B* **716** (2012) 1 [`1207.7214`].

[289] CMS collaboration, *Observation of a New Boson at a Mass of 125 GeV with the CMS Experiment at the LHC*, *Phys. Lett. B* **716** (2012) 30 [`1207.7235`].

[290] A. Arbey, M. Battaglia, A. Djouadi and F. Mahmoudi, *An update on the constraints on the phenomenological MSSM from the new LHC Higgs results*, *Phys. Lett. B* **720** (2013) 153 [`1211.4004`].

[291] J. Rosiek, *Complete Set of Feynman Rules for the Minimal Supersymmetric Extension of the Standard Model*, *Phys. Rev. D* **41** (1990) 3464 [`hep-ph/9511250`].

[292] M. Beneke, P. Falgari and C. Schwinn, *Soft radiation in heavy-particle pair production: All-order colour structure and two-loop anomalous dimension*, *Nucl. Phys. B* **828** (2010) 69 [`0907.1443`].

[293] A.J. MacFarlane, A. Sudbery and P.H. Weisz, *On Gell-Mann's lambda-matrices, d- and f-tensors, octets, and parametrizations of SU(3)*, *Commun. Math. Phys.* **11** (1968) 77.

[294] C. Becchi, A. Rouet and R. Stora, *Renormalization of gauge theories*, *Annals of Physics* **98** (1976) 287.

[295] T. Kugo and I. Ojima, *Manifestly Covariant Canonical Formulation of Yang-Mills Field Theories. 1. The Case of Yang-Mills Fields of Higgs-Kibble Type in Landau Gauge*, *Prog. Theor. Phys.* **60** (1978) 1869.

[296] J. Ellis, K.A. Olive, V.C. Spanos and I.D. Stamou, *The CMSSM survives Planck, the LHC, LUX-ZEPLIN, Fermi-LAT, H.E.S.S. and IceCube*, *Eur. Phys. J. C* **83** (2023) 246 [`2210.16337`].

[297] T. Hahn, *Generating Feynman diagrams and amplitudes with FeynArts 3*, *Comput. Phys. Commun.* **140** (2001) 418 [`hep-ph/0012260`].

[298] V. Shtabovenko, R. Mertig and F. Orellana, *Feyncalc 9.3: New features and improvements*, *Computer Physics Communications* **256** (2020) 107478.

[299] M. Jamin and M.E. Lautenbacher, *TRACER: Version 1.1: A Mathematica package for gamma algebra in arbitrary dimensions*, *Comput. Phys. Commun.* **74** (1993) 265.

[300] T. Hahn, *Automatic loop calculations with FeynArts, FormCalc, and LoopTools*, *Nucl. Phys. B Proc. Suppl.* **89** (2000) 231 [`hep-ph/0005029`].

[301] K. Hagiwara, Y. Sumino and H. Yokoya, *Bound-state Effects on Top Quark Production at Hadron Colliders*, *Phys. Lett. B* **666** (2008) 71 [`0804.1014`].

[302] Y. Kiyo, J.H. Kuhn, S. Moch, M. Steinhauser and P. Uwer, *Top-quark pair production near threshold at LHC*, *Eur. Phys. J. C* **60** (2009) 375 [`0812.0919`].

[303] M. Beneke, P. Falgari and C. Schwinn, *Threshold resummation for pair production of coloured heavy (s)particles at hadron colliders*, *Nucl. Phys. B* **842** (2011) 414 [`1007.5414`].

[304] J. Fan, M. Reece and L.-T. Wang, *Non-relativistic effective theory of dark matter direct detection*, *JCAP* **11** (2010) 042 [`1008.1591`].

[305] R.J. Hill and M.P. Solon, *Standard Model anatomy of WIMP dark matter direct detection I: weak-scale matching*, *Phys. Rev. D* **91** (2015) 043504 [`1401.3339`].

[306] R.J. Hill and M.P. Solon, *Standard Model anatomy of WIMP dark matter direct detection II: QCD analysis and hadronic matrix elements*, *Phys. Rev. D* **91** (2015) 043505 [`1409.8290`].

[307] J. Hisano, R. Nagai and N. Nagata, *Effective Theories for Dark Matter Nucleon Scattering*, *JHEP* **05** (2015) 037 [`1502.02244`].

[308] M.A. Shifman, A.I. Vainshtein and V.I. Zakharov, *Remarks on Higgs Boson Interactions with Nucleons*, *Phys. Lett. B* **78** (1978) 443.

[309] M. Hoferichter, J. Ruiz de Elvira, B. Kubis and U.-G. Meißner, *High-Precision Determination of the Pion-Nucleon σ Term from Roy-Steiner Equations*, *Phys. Rev. Lett.* **115** (2015) 092301 [`1506.04142`].

[310] J. Gasser, H. Leutwyler and M.E. Sainio, *Sigma term update*, *Phys. Lett. B* **253** (1991) 252.

[311] B. Fuks, M. Klasen, D.R. Lamprea and M. Rothering, *Precision predictions for electroweak superpartner production at hadron colliders with Resummino*, *Eur. Phys. J. C* **73** (2013) 2480 [`1304.0790`].

[312] J. Fiaschi, B. Fuks, M. Klasen and A. Neuwirth, *Electroweak superpartner production at 13.6 Tev with Resummino*, *Eur. Phys. J. C* **83** (2023) 707 [`2304.11915`].

[313] T. Hahn, *SUSY Les Houches Accord 2 I/O made easy*, *Comput. Phys. Commun.* **180** (2009) 1681 [`hep-ph/0605049`].

[314] P.Z. Skands et al., *SUSY Les Houches accord: Interfacing SUSY spectrum calculators, decay packages, and event generators*, *JHEP* **07** (2004) 036 [`hep-ph/0311123`].

[315] B.C. Allanach et al., *SUSY Les Houches Accord 2*, *Comput. Phys. Commun.* **180** (2009) 8 [`0801.0045`].

[316] A. Buckley, *PySLHA: a Pythonic interface to SUSY Les Houches Accord data*, *Eur. Phys. J. C* **75** (2015) 467 [`1305.4194`].

[317] Particle Data Group collaboration, *Review of Particle Physics*, *PTEP* **2022** (2022) 083C01.

[318] T. Abe, *Effect of the early kinetic decoupling in a fermionic dark matter model*, *Phys. Rev. D* **102** (2020) 035018 [`2004.10041`].

[319] T. Abe, *Early kinetic decoupling and a pseudo-Nambu-Goldstone dark matter model*, *Phys. Rev. D* **104** (2021) 035025 [`2106.01956`].

[320] G.D. Moore and T. Prokopec, *How fast can the wall move? A Study of the electroweak phase transition dynamics*, *Phys. Rev. D* **52** (1995) 7182 [`hep-ph/9506475`].

[321] R.T. D'Agnolo and J.T. Ruderman, *Light Dark Matter from Forbidden Channels*, *Phys. Rev. Lett.* **115** (2015) 061301 [`1505.07107`].

[322] A. Delgado, A. Martin and N. Raj, *Forbidden Dark Matter at the Weak Scale via the Top Portal*, *Phys. Rev. D* **95** (2017) 035002 [`1608.05345`].

[323] R.T. D'Agnolo, D. Liu, J.T. Ruderman and P.-J. Wang, *Forbidden dark matter annihilations into Standard Model particles*, *JHEP* **06** (2021) 103 [`2012.11766`].

[324] Y. Liu, X. Liu and B. Zhu, *Early kinetic decoupling effect on the forbidden dark matter annihilations into standard model particles*, *Phys. Rev. D* **107** (2023) 115009 [`2301.12199`].

[325] K. Ala-Mattinen and K. Kainulainen, *Precision calculations of dark matter relic abundance*, *JCAP* **09** (2020) 040 [`1912.02870`].

[326] F. Brümmer, *Coscattering in next-to-minimal dark matter and split supersymmetry*, *JHEP* **01** (2020) 113 [`1910.01549`].

[327] Y. Du, F. Huang, H.-L. Li, Y.-Z. Li and J.-H. Yu, *Revisiting dark matter freeze-in and freeze-out through phase-space distribution*, *JCAP* **04** (2022) 012 [`2111.01267`].

[328] K. Ala-Mattinen, M. Heikinheimo, K. Kainulainen and K. Tuominen, *Momentum distributions of cosmic relics: Improved analysis*, *Phys. Rev. D* **105** (2022) 123005 [`2201.06456`].

[329] A. Hryczuk and M. Laletin, *Impact of dark matter self-scattering on its relic abundance*, *Phys. Rev. D* **106** (2022) 023007 [`2204.07078`].

[330] S. Hannestad, R.S. Hansen, T. Tram and Y.Y.Y. Wong, *Active-sterile neutrino oscillations in the early Universe with full collision terms*, *JCAP* **08** (2015) 019 [`1506.05266`].

[331] F. Hahn-Woernle, M. Plumacher and Y.Y.Y. Wong, *Full Boltzmann equations for leptogenesis including scattering*, *JCAP* **08** (2009) 028 [`0907.0205`].

[332] A. Ghosh and S. Mukhopadhyay, *Momentum distribution of dark matter produced in inflaton decay: Effect of inflaton mediated scatterings*, *Phys. Rev. D* **106** (2022) 043519 [`2205.03440`].

[333] S. De Curtis, L.D. Rose, A. Guiggiani, A.G. Muyor and G. Panico, *Bubble wall dynamics at the electroweak phase transition*, *JHEP* **03** (2022) 163 [`2201.08220`].

[334] S. Kim and M. Laine, *Langevin simulation of dark matter kinetic equilibration*, *JCAP* **05** (2023) 003 [`2302.05129`].

[335] J. Herms, S. Jana, V.P. Kovilakam and S. Saad, *Minimal Realization of Light Thermal Dark Matter*, *Phys. Rev. Lett.* **129** (2022) 091803 [`2203.05579`].

[336] S. Hannestad and J. Madsen, *Neutrino decoupling in the early universe*, *Phys. Rev. D* **52** (1995) 1764 [`astro-ph/9506015`].

[337] E. Cervantes and A. Hryczuk, *Freezing-in Cannibal Dark Sectors*, `2407.12104`.

[338] D. Blas, J. Lesgourgues and T. Tram, *The Cosmic Linear Anisotropy Solving System (CLASS) II: Approximation schemes*, *JCAP* **07** (2011) 034 [`1104.2933`].

[339] S. Gariazzo, P.F. de Salas and S. Pastor, *Thermalisation of sterile neutrinos in the early Universe in the 3+1 scheme with full mixing matrix*, *JCAP* **07** (2019) 014 [`1905.11290`].

[340] M.C. Galassi, J. Davies, J. Theiler, B. Gough, G. Jungman, P. Alken et al., *GNU Scientific Library*, Network Theory, Ltd. (8, 2019).

[341] A.C. Hindmarsh, P.N. Brown, K.E. Grant, S.L. Lee, R. Serban, D.E. Shumaker et al., *SUNDIALS: Suite of nonlinear and differential/algebraic equation solvers*, *ACM Transactions on Mathematical Software (TOMS)* **31** (2005) 363.

[342] D.J. Gardner, D.R. Reynolds, C.S. Woodward and C.J. Balos, *Enabling new flexibility in the SUNDIALS suite of nonlinear and differential/algebraic equation solvers*, *ACM Transactions on Mathematical Software (TOMS)* (2022) .

[343] R. Balian and J. Zinn-Justin, eds., *Methods in Field Theory. Les Houches Summer School in Theoretical Physics. Session 28, July 28-September 6, 1975*, North-Holland Pub. Co. (1976).

[344] F. Kahlhoefer, K. Schmidt-Hoberg, M.T. Frandsen and S. Sarkar, *Colliding clusters and dark matter self-interactions*, *Mon. Not. Roy. Astron. Soc.* **437** (2014) 2865 [`1308.3419`].

[345] T.R. Slatyer, *Indirect dark matter signatures in the cosmic dark ages. I. Generalizing the bound on s-wave dark matter annihilation from Planck results*, *Phys. Rev. D* **93** (2016) 023527 [`1506.03811`].

[346] CMB-S4 collaboration, *CMB-S4 Science Book, First Edition*, `1610.02743`.

[347] L. Marsicano, M. Battaglieri, A. Celentano, R. De Vita and Y.-M. Zhong, *Probing Leptophilic Dark Sectors at Electron Beam-Dump Facilities*, *Phys. Rev. D* **98** (2018) 115022 [`1812.03829`].

[348] BDX collaboration, *Light Dark Matter search in a beam-dump experiment: BDX at Jefferson Lab*, *EPJ Web Conf.* **142** (2017) 01005.

[349] Y. Kahn, G. Krnjaic, N. Tran and A. Whitbeck, *M^3: a new muon missing momentum experiment to probe $(g-2)_\mu$ and dark matter at Fermilab*, *JHEP* **09** (2018) 153 [`1804.03144`].

[350] S.N. Gninenko, N.V. Krasnikov and V.A. Matveev, *Muon g-2 and searches for a new leptophobic sub-GeV dark boson in a missing-energy experiment at CERN*, *Phys. Rev. D* **91** (2015) 095015 [`1412.1400`].

[351] C.-Y. Chen, J. Kozaczuk and Y.-M. Zhong, *Exploring leptophilic dark matter with NA64-μ*, *JHEP* **10** (2018) 154 [`1807.03790`].

[352] K.J. Kim and Y.-S. Tsai, *Improved Weizsäcker-Williams Method and Its Application to Lepton and W-Boson Pair Production*, *Phys. Rev. D* **8** (1973) 3109.

[353] J. Liu, L.-T. Wang, X.-P. Wang and W. Xue, *Exposing the dark sector with future Z factories*, *Phys. Rev. D* **97** (2018) 095044 [`1712.07237`].

[354] BaBar collaboration, *Search for Invisible Decays of a Dark Photon Produced in e^+e^- Collisions at BaBar*, *Phys. Rev. Lett.* **119** (2017) 131804 [`1702.03327`].

[355] Belle-II collaboration, *Belle II Technical Design Report*, `1011.0352`.

[356] M.J. Dolan, T. Ferber, C. Hearty, F. Kahlhoefer and K. Schmidt-Hoberg, *Revised constraints and Belle II sensitivity for visible and invisible axion-like particles*, *JHEP* **12** (2017) 094 [`1709.00009`].

[357] J. Berges, *Introduction to nonequilibrium quantum field theory*, *AIP Conf. Proc.* **739** (2004) 3 [`hep-ph/0409233`].

[358] M. Drewes, *Quantum aspects of early universe thermodynamics*, other thesis, 3, 2010, 10.3204/DESY-THESIS-2010-010.

[359] A.K. Das, *Finite Temperature Field Theory*, World Scientific, New York (1997).

[360] M.L. Bellac, *Thermal Field Theory*, Cambridge Monographs on Mathematical Physics, Cambridge University Press (3, 2011), 10.1017/CBO9780511721700.

[361] T. Matsubara, *A New approach to quantum statistical mechanics*, *Prog. Theor. Phys.* **14** (1955) 351.

[362] J.S. Schwinger, *Brownian motion of a quantum oscillator*, *J. Math. Phys.* **2** (1961) 407.

[363] L.V. Keldysh, *Diagram technique for nonequilibrium processes*, *Zh. Eksp. Teor. Fiz.* **47** (1964) 1515.

[364] H. Umezawa, H. Matsumoto and M. Tachiki, *Thermo field dynamics and condensed states* (1982).

[365] A. Riotto, *Towards a nonequilibrium quantum field theory approach to electroweak baryogenesis*, *Phys. Rev. D* **53** (1996) 5834 [`hep-ph/9510271`].

[366] W. Buchmuller and S. Fredenhagen, *Quantum mechanics of baryogenesis*, *Phys. Lett. B* **483** (2000) 217 [`hep-ph/0004145`].

[367] V. Cirigliano, C. Lee, M.J. Ramsey-Musolf and S. Tulin, *Flavored Quantum Boltzmann Equations*, *Phys. Rev. D* **81** (2010) 103503 [`0912.3523`].

[368] A. Salvio, P. Lodone and A. Strumia, *Towards leptogenesis at NLO: the right-handed neutrino interaction rate*, *JHEP* **08** (2011) 116 [`1106.2814`].

[369] T. Prokopec, M.G. Schmidt and S. Weinstock, *Transport equations for chiral fermions to order h bar and electroweak baryogenesis. Part 1*, *Annals Phys.* **314** (2004) 208 [`hep-ph/0312110`].

[370] T. Prokopec, M.G. Schmidt and S. Weinstock, *Transport equations for chiral fermions to order h-bar and electroweak baryogenesis. Part II*, *Annals Phys.* **314** (2004) 267 [`hep-ph/0406140`].

[371] M. Beneke, B. Garbrecht, M. Herranen and P. Schwaller, *Finite Number Density Corrections to Leptogenesis*, *Nucl. Phys. B* **838** (2010) 1 [`1002.1326`].

[372] C. Fidler, M. Herranen, K. Kainulainen and P.M. Rahkila, *Flavoured quantum Boltzmann equations from cQPA*, *JHEP* **02** (2012) 065 [`1108.2309`].

[373] B. Garbrecht and M. Garny, *Finite Width in out-of-Equilibrium Propagators and Kinetic Theory*, *Annals Phys.* **327** (2012) 914 [`1108.3688`].

[374] B. Garbrecht, F. Glowna and M. Herranen, *Right-Handed Neutrino Production at Finite Temperature: Radiative Corrections, Soft and Collinear Divergences*, *JHEP* **04** (2013) 099 [`1302.0743`].

[375] M. Drewes, B. Garbrecht, D. Gueter and J. Klaric, *Leptogenesis from Oscillations of Heavy Neutrinos with Large Mixing Angles*, *JHEP* **12** (2016) 150 [`1606.06690`].

[376] P.F. Depta, A. Halsch, J. Hütig, S. Mendizabal and O. Philipsen, *Complete leading-order standard model corrections to quantum leptogenesis*, *JHEP* **09** (2020) 036 [`2005.01728`].

[377] K. Kainulainen, *CP-violating transport theory for electroweak baryogenesis with thermal corrections*, *JCAP* **11** (2021) 042 [`2108.08336`].

[378] J. Yokoyama and A.D. Linde, *Is warm inflation possible?*, *Phys. Rev. D* **60** (1999) 083509 [`hep-ph/9809409`].

[379] X. Tong, Y. Wang and S. Zhou, *Unsuppressed primordial standard clocks in warm quasi-single field inflation*, *JCAP* **06** (2018) 013 [`1801.05688`].

[380] M. Drewes, Y. Georis, J. Klaric and P. Klose, *Upper bound on thermal gravitational wave backgrounds from hidden sectors*, *JCAP* **06** (2024) 073 [`2312.13855`].

[381] A. Czarnecki, M. Kamionkowski, S.K. Lee and K. Melnikov, *Charged Particle Decay at Finite Temperature*, *Phys. Rev. D* **85** (2012) 025018 [`1110.2171`].

[382] T. Binder, L. Covi and K. Mukaida, *Dark Matter Sommerfeld-enhanced annihilation and Bound-state decay at finite temperature*, *Phys. Rev. D* **98** (2018) 115023 [`1808.06472`].

[383] H. Eberl, I.D. Gialamas and V.C. Spanos, *Gravitino thermal production revisited*, *Phys. Rev. D* **103** (2021) 075025 [`2010.14621`].

[384] T. Binder, B. Blobel, J. Harz and K. Mukaida, *Dark matter bound-state formation at higher order: a non-equilibrium quantum field theory approach*, *JHEP* **09** (2020) 086 [`2002.07145`].

[385] W.-Y. Ai, A. Beniwal, A. Maggi and D.J.E. Marsh, *From QFT to Boltzmann: freeze-in in the presence of oscillating condensates*, *JHEP* **02** (2024) 122 [`2310.08272`].

[386] A. Abada, G. Arcadi, M. Lucente, G. Piazza and S. Rosauro-Alcaraz, *Thermal effects in freeze-in neutrino dark mater production*, *JHEP* **11** (2023) 180 [`2308.01341`].

[387] M. Becker, E. Copello, J. Harz and C. Tamarit, *Dark matter freeze-in from non-equilibrium QFT: towards a consistent treatment of thermal effects*, `2312.17246`.

[388] M.D. Schwartz, *Quantum Field Theory and the Standard Model*, Cambridge University Press (3, 2014).

[389] G. Baym and L.P. Kadanoff, *Conservation Laws and Correlation Functions*, *Phys. Rev.* **124** (1961) 287.

[390] L. Kadanoff and G. Baym, *Quantum Statistical Mechanics: Green's Function Methods in Equilibrium and Nonequilibrium Problems*, W.A. Benjamin (1962).

[391] A. Anisimov, W. Buchmüller, M. Drewes and S. Mendizabal, *Quantum Leptogenesis I*, *Annals Phys.* **326** (2011) 1998 [`1012.5821`].

[392] N.P. Landsman and C.G. van Weert, *Real and Imaginary Time Field Theory at Finite Temperature and Density*, *Phys. Rept.* **145** (1987) 141.

[393] T.S. Evans and A.C. Pearson, *Real time thermal propagators for massive gauge bosons*, *Z. Phys. C* **65** (1995) 123 [`hep-ph/9307229`].

[394] A. Rebhan, *Hard thermal loops and QCD thermodynamics*, in *Cargese Summer School on QCD Perspectives on Hot and Dense Matter*, pp. 327–351, 11, 2001 [`hep-ph/0111341`].

[395] H.B. Callen and T.A. Welton, *Irreversibility and generalized noise*, *Phys. Rev.* **83** (1951) 34.

[396] M.E. Carrington, D.-f. Hou and M.H. Thoma, *Equilibrium and nonequilibrium hard thermal loop resummation in the real time formalism*, *Eur. Phys. J. C* **7** (1999) 347 [`hep-ph/9708363`].

[397] E. Braaten and R.D. Pisarski, *Soft Amplitudes in Hot Gauge Theories: A General Analysis*, *Nucl. Phys. B* **337** (1990) 569.

[398] A. Peshier, K. Schertler and M.H. Thoma, *One loop selfenergies at finite temperature*, *Annals Phys.* **266** (1998) 162 [`hep-ph/9708434`].

[399] E. Braaten and D. Segel, *Neutrino energy loss from the plasma process at all temperatures and densities*, *Phys. Rev. D* **48** (1993) 1478 [`hep-ph/9302213`].

[400] M. Vanderhaeghen, J.M. Friedrich, D. Lhuillier, D. Marchand, L. Van Hoorebeke and J. Van de Wiele, *QED radiative corrections to virtual Compton scattering*, *Phys. Rev. C* **62** (2000) 025501 [`hep-ph/0001100`].

[401] M. Drewes, Y. Georis, M. Klasen, L.P. Wiggering and Y.Y.Y. Wong, *Towards a precision calculation of N_{eff} in the Standard Model. Part III. Improved estimate of NLO contributions to the collision integral*, *JCAP* **06** (2024) 032 [`2402.18481`].

[402] Planck collaboration, *Planck 2018 results. VI. Cosmological parameters*, *Astron. Astrophys.* **641** (2020) A6 [`1807.06209`].

[403] R. Barbieri and A. Dolgov, *Neutrino oscillations in the early universe*, *Nucl. Phys. B* **349** (1991) 743.

[404] A.M. Abdullahi et al., *The present and future status of heavy neutral leptons*, *J. Phys. G* **50** (2023) 020501 [`2203.08039`].

[405] L. Di Luzio, J. Martin Camalich, G. Martinelli, J.A. Oller and G. Piazza, *Axion-pion thermalization rate in unitarized NLO chiral perturbation theory*, *Phys. Rev. D* **108** (2023) 035025 [`2211.05073`].

[406] F. D'Eramo, F. Hajkarim and S. Yun, *Thermal QCD Axions across Thresholds*, *JHEP* **10** (2021) 224 [`2108.05371`].

[407] C. Caprini and D.G. Figueroa, *Cosmological Backgrounds of Gravitational Waves*, *Class. Quant. Grav.* **35** (2018) 163001 [`1801.04268`].

[408] A. Aboubrahim, M. Klasen and P. Nath, *Analyzing the Hubble tension through hidden sector dynamics in the early universe*, *JCAP* **04** (2022) 042 [`2202.04453`].

[409] P. Agrawal et al., *Feebly-interacting particles: FIPs 2020 workshop report*, *Eur. Phys. J. C* **81** (2021) 1015 [`2102.12143`].

[410] S. Dodelson and M.S. Turner, *Nonequilibrium neutrino statistical mechanics in the expanding universe*, *Phys. Rev. D* **46** (1992) 3372.

[411] A.D. Dolgov, S.H. Hansen and D.V. Semikoz, *Nonequilibrium corrections to the spectra of massless neutrinos in the early universe*, *Nucl. Phys. B* **503** (1997) 426.

[412] A.D. Dolgov, S.H. Hansen and D.V. Semikoz, *Nonequilibrium corrections to the spectra of massless neutrinos in the early universe: Addendum*, *Nucl. Phys. B* **543** (1999) 269.

[413] S. Esposito, G. Miele, S. Pastor, M. Peloso and O. Pisanti, *Nonequilibrium spectra of degenerate relic neutrinos*, *Nucl. Phys. B* **590** (2000) 539.

[414] J. Froustey and C. Pitrou, *Incomplete neutrino decoupling effect on big bang nucleosynthesis*, *Phys. Rev. D* **101** (2020) 043524 [`1912.09378`].

[415] D.A. Dicus, E.W. Kolb, A.M. Gleeson, E.C.G. Sudarshan, V.L. Teplitz and M.S. Turner, *Primordial Nucleosynthesis Including Radiative, Coulomb, and Finite Temperature Corrections to Weak Rates*, *Phys. Rev. D* **26** (1982) 2694.

[416] A. Heckler, *Astrophysical applications of quantum corrections to the equation of state of a plasma*, *Phys. Rev. D* **49** (1994) 611.

[417] N. Fornengo, C. Kim and J. Song, *Finite temperature effects on the neutrino decoupling in the early universe*, *Phys. Rev. D* **56** (1997) 5123 [`hep-ph/9702324`].

[418] R.E. Lopez and M.S. Turner, *An Accurate Calculation of the Big Bang Prediction for the Abundance of Primordial Helium*, *Phys. Rev. D* **59** (1999) 103502 [`astro-ph/9807279`].

[419] G. Mangano, G. Miele, S. Pastor and M. Peloso, *A Precision calculation of the effective number of cosmological neutrinos*, *Phys. Lett. B* **534** (2002) 8 [`astro-ph/0111408`].

[420] J.J. Bennett, G. Buldgen, M. Drewes and Y.Y.Y. Wong, *Towards a precision calculation of the effective number of neutrinos $N_{\rm eff}$ in the Standard Model I: the QED equation of state*, *JCAP* **03** (2020) 003 [`1911.04504`].

[421] G. Mangano, G. Miele, S. Pastor, T. Pinto, O. Pisanti and P.D. Serpico, *Relic neutrino decoupling including flavor oscillations*, *Nucl. Phys. B* **729** (2005) 221 [`hep-ph/0506164`].

[422] J. Birrell, C.-T. Yang and J. Rafelski, *Relic Neutrino Freeze-out: Dependence on Natural Constants*, *Nucl. Phys. B* **890** (2014) 481 [`1406.1759`].

[423] E. Grohs, G.M. Fuller, C.T. Kishimoto, M.W. Paris and A. Vlasenko, *Neutrino energy transport in weak decoupling and big bang nucleosynthesis*, *Phys. Rev. D* **93** (2016) 083522 [`1512.02205`].

[424] P.F. de Salas and S. Pastor, *Relic neutrino decoupling with flavour oscillations revisited*, *JCAP* **07** (2016) 051 [`1606.06986`].

[425] K. Akita and M. Yamaguchi, *A precision calculation of relic neutrino decoupling*, *JCAP* **08** (2020) 012 [`2005.07047`].

[426] J. Froustey, C. Pitrou and M.C. Volpe, *Neutrino decoupling including flavour oscillations and primordial nucleosynthesis*, *JCAP* **12** (2020) 015 [`2008.01074`].

[427] J.J. Bennett, G. Buldgen, P.F. De Salas, M. Drewes, S. Gariazzo, S. Pastor et al., *Towards a precision calculation of $N_{\rm eff}$ in the Standard Model II: Neutrino decoupling in the presence of flavour oscillations and finite-temperature QED*, *JCAP* **04** (2021) 073 [`2012.02726`].

[428] M. Cielo, M. Escudero, G. Mangano and O. Pisanti, *Neff in the Standard Model at NLO is 3.043*, *Phys. Rev. D* **108** (2023) L121301 [`2306.05460`].

[429] G. Jackson and M. Laine, *QED corrections to the thermal neutrino interaction rate*, *JHEP* **05** (2024) 089 [`2312.07015`].

[430] S. Esposito, G. Mangano, G. Miele, I. Picardi and O. Pisanti, *Neutrino energy loss rate in a stellar plasma*, *Nucl. Phys. B* **658** (2003) 217 [`astro-ph/0301438`].

[431] K.-c. Chou, Z.-b. Su, B.-l. Hao and L. Yu, *Equilibrium and Nonequilibrium Formalisms Made Unified*, *Phys. Rept.* **118** (1985) 1.

[432] J.I. Kapusta and C. Gale, *Finite-temperature field theory: Principles and applications*, Cambridge Monographs on Mathematical Physics, Cambridge University Press (2011), 10.1017/CBO9780511535130.

[433] C. Coriano and R.R. Parwani, *The Three loop equation of state of QED at high temperature*, *Phys. Rev. Lett.* **73** (1994) 2398 [`hep-ph/9405343`].

[434] R.R. Parwani and C. Coriano, *Higher order corrections to the equation of state of QED at high temperature*, *Nucl. Phys. B* **434** (1995) 56 [`hep-ph/9409269`].

[435] G. Sigl and G. Raffelt, *General kinetic description of relativistic mixed neutrinos*, *Nucl. Phys. B* **406** (1993) 423.

[436] L. Canetti, M. Drewes and M. Shaposhnikov, *Matter and Antimatter in the Universe*, *New J. Phys.* **14** (2012) 095012 [`1204.4186`].

[437] M. Drewes, S. Mendizabal and C. Weniger, *The Boltzmann Equation from Quantum Field Theory*, *Phys. Lett. B* **718** (2013) 1119 [`1202.1301`].

[438] F. Halzen and A. Martin, *Quarks & Leptons: An introductory course in modern particle physics*, John Wiley & Sons, New York, USA (1984).

[439] J.F. Nieves and P.B. Pal, *Generalized Fierz identities*, *Am. J. Phys.* **72** (2004) 1100 [`hep-ph/0306087`].

[440] R.J. Hill and O. Tomalak, *On the effective theory of neutrino-electron and neutrino-quark interactions*, *Phys. Lett. B* **805** (2020) 135466 [`1911.01493`].

[441] O. Tomalak and R.J. Hill, *Theory of elastic neutrino-electron scattering*, *Phys. Rev. D* **101** (2020) 033006 [`1907.03379`].

[442] E. Braaten, *Neutrino emissivity of an ultrarelativistic plasma from positron and plasmino annihilation*, *Astrophys. J.* **392** (1992) 70.

[443] E. Byckling and K. Kajantie, *Particle Kinematics*, A Wiley-Interscience publication, Wiley (1973).

[444] N. Lebedev and R. Silverman, *Special Functions and Their Applications*, Dover Books on Mathematics, Dover Publications (1972).

[445] T. Asaka, M. Laine and M. Shaposhnikov, *Lightest sterile neutrino abundance within the nuMSM*, *JHEP* **01** (2007) 091 [`hep-ph/0612182`].